

# **For Reference**

---

**NOT TO BE TAKEN FROM THIS ROOM**



Ex libris  
UNIVERSITATIS  
ALBERTAENSIS













THE UNIVERSITY of ALBERTA

RELEASE FORM

NAME OF AUTHOR Ewe Hin Choot.....  
TITLE OF THESIS Spectral Characterization, Evaluation, and  
Fundamental Studies of Mixed Gas  
Inductively Coupled Plasmas.....  
DEGREE FOR WHICH THIS THESIS WAS PRESENTED Ph.D.....  
YEAR THIS DEGREE GRANTED 1983.....

Permission is hereby granted to THE UNIVERSITY OF  
ALBERTA LIBRARY to reproduce single copies of this  
thesis and to lend or sell such copies for private,  
scholarly or scientific research purposes only.

The author reserves other publication rights, and  
neither the thesis nor extensive extracts from it may  
be printed or otherwise reproduced without the author's  
written permission.






THE UNIVERSITY OF ALBERTA

SPECTRAL CHARACTERIZATION, EVALUATION, AND FUNDAMENTAL  
STUDIES OF MIXED GAS INDUCTIVELY COUPLED PLASMAS

by

EWE HIN CHOOT

A THESIS

SUBMITTED TO THE FACULTY OF GRADUATE STUDIES AND RESEARCH  
IN PARTIAL FULFILLMENT OF THE REQUIREMENTS FOR THE DEGREE  
OF DOCTOR OF PHILOSOPHY

DEPARTMENT OF CHEMISTRY

EDMONTON, ALBERTA

SPRING, 1983





THE UNIVERSITY OF ALBERTA  
FACULTY OF GRADUATE STUDIES AND RESEARCH

The undersigned certify that they have read, and  
recommend to the Faculty of Graduate Studies and Research,  
for acceptance, a thesis entitled .....  
SPECTRAL CHARACTERIZATION,  
EVALUATION, AND FUNDAMENTAL STUDIES OF MIXED GAS INDUCTIVELY  
.....  
COUPLED PLASMAS  
.....  
submitted by ...EWE HIN CHOOT.....  
in partial fulfillment of the requirements for the degree of  
Doctor of Philosophy in Analytical Chemistry.



## DEDICATION

To my parents and my wife Nee





## ABSTRACT

Most inductively coupled plasmas (ICPs) utilized for analytical spectroscopy are based on argon, although some systems employing gas combinations have been used. Such combinations include Ar-N<sub>2</sub>, Ar-He, Ar-O<sub>2</sub> and Ar-air where upwards of 95% of the argon is replaced by the alternate gas. A detailed evaluation and characterization of such mixed gas ICPs has been carried out. It has been found that the shape of the plasma and the relative and absolute intensities of analyte emission lines are strongly dependent on the concentration of the foreign (non-argon) gas. In general, as foreign gas is added to replace argon, the plasma decreases in size and analyte ion line emission is enhanced relative to neutral atom emission. Overall, the analytical studies have shown that under optimal operating conditions, mixed gas ICPs are comparable or superior to the conventional argon discharge in terms of stability, sensitivity, tolerance of organic solvents, freedom from interference effects and operational cost.

One of the key plasma parameters that is likely to be altered by the addition of a foreign gas is electron density. A detailed study of the spatial distribution of electron density over a range of operating parameters such as plasma power, aerosol flow rate, and plasma gas





composition has been carried out. Electron density was measured using the Stark broadened width of the  $H_{\beta}$  line. It was found that regions of high electron density in the aerosol channel correlate well with maximum analyte emission. In addition, the analyte emission and the electron density showed similar spatial characteristics in mixed gas ICPs.



## ACKNOWLEDGEMENTS

I would like to express my grateful thanks for the help and advice given me by Dr. Gary Horlick. Without his encouragement and faith, this thesis might have remained just another dream.

I would also like to express my deepest appreciation to my fellow colleagues for their invaluable and helpful advice.

Finally, I would like to express my love to my wife Nee for her understanding, support and patience, without whom this work would have been possible but not much fun.



## TABLE OF CONTENTS

CHAPTER		PAGE
I	INTRODUCTION	1
	A. Introduction	1
	B. Plasma	4
	1. The Fourth State of Matter	4
	2. Definition	5
	C. Inductively Coupled Plasma	8
	1. History	8
	2. Generating and Sustaining the Plasma	11
	3. Mixed Gas ICPs	15
	D. Measurements of Temperature and Electron Density in Mixed Gas ICPs	23
	1. Temperatures	23
	2. Electron Density	26
	E. Excitation and Ionization Mechanisms in Mixed Gas ICPs	30
II	EXPERIMENTAL	35
	A. ICP Instrumentation	35
	1. ICP Source	35
	2. Plasma Torch	38
	3. Nebulizing System	40
	B. The Optical System	42
	C. Gas Mixing	45





CHAPTER		PAGE
	D. The Detection Systems	45
	1. Detection System for Spectral Characterization and Evaluation of Mixed Gas ICPs	46
	2. Detection System for Spatial Profile Measurements	48
	E. Control and Data Acquisition System	50
	F. Preparation of Chemical Solutions	55
III	EXPERIMENTAL OBSERVATIONS OF MIXED GAS ICPs	56
	A. Introduction	56
	B. Experimental Procedures for Lighting a Mixed Gas ICP	56
	C. Experimental Observations	57
	D. Conclusions	62
IV	VERTICAL SPATIAL PROFILES OF ANALYTE EMISSION FROM A N <sub>2</sub> -AR MIXED GAS PLASMA	63
	A. Introduction	63
	B. Experimental	64
	C. Effect of Nitrogen on the Vertical Profiles	66
	D. Effects of Aerosol Flow Rate and Power on the Vertical Profiles	75
	E. Effect of Nitrogen in the Aerosol Flow on the Vertical Profiles	91
	F. Conclusions	96



CHAPTER		PAGE
V	ANALYTICAL AND SPECTRAL CHARACTERISTICS OF N <sub>2</sub> -AR, O <sub>2</sub> -AR, AIR-AR, AND HE-AR MIXED GAS PLASMAS	98
	A. Introduction	98
	B. Experimental	101
	C. Characterization of Emission Noise with a Photodiode Array Spectrometer	103
	D. Spectral Characteristics and Evaluation of Mixed Gas Plasmas (spectral region centered at 373 nm)	108
	1. Nitrogen-Argon Mixed Gas Plasmas	108
	2. Oxygen-Argon Mixed Gas Plasmas	115
	3. Air-Argon Mixed Gas Plasmas	119
	4. Helium-Argon Mixed Gas Plasmas	123
	5. Final Comparisons of the Mixed Gas Plasmas (spectral region centered at 373 nm)	127
	E. Spectral Characteristics and Evaluation of Mixed Gas Plasmas (spectral region centered at 228 nm)	129
	1. Nitrogen-Argon Mixed Gas Plasmas	130
	2. Oxygen-Argon Mixed Gas Plasmas	137
	3. Air-Argon mixed Gas Plasmas	142
	4. Helium-Argon Mixed Gas Plasmas	147
	5. Final Comparisons of the Mixed Gas Plasmas (spectral region centered at 228 nm)	152
	F. Conclusions	157



CHAPTER		PAGE
VI	EVALUATION OF THE ANALYTICAL PERFORMANCE OF MIXED GAS PLASMAS	159
	A. Introduction	159
	B. Experimental	162
	C. Signal-to-Noise Evaluation of Mixed Gas Plasmas as a function of Plasma Power, Aerosol Flow Rate and Observation Height	163
	1. Conventional Argon ICPs	164
	2. Nitrogen-Argon Mixed Gas ICPs	167
	3. Oxygen-Argon Mixed Gas ICPs	171
	4. Air-Argon Mixed Gas ICPs	174
	5. Helium-Argon Mixed Gas ICPs	174
	D. Interference Studies of the Mixed Gas ICPs	179
	1. Phosphate on Calcium Emission, Solute Vaporization Interference	179
	2. Potassium on Calcium Emission, Effect of Easily Ionizable Element (EIE)	184
	E. Analytical Calibration Curves	189
	F. Conclusions	193
VII	ELECTRON DENSITY MEASUREMENTS IN ICPs USING A PHOTODIODE ARRAY DETECTION SYSTEM	195
	A. Introduction	195
	B. Excitation and Ionization Mechanisms in Mixed Gas ICPs	196
	C. Electron Density Measurements	206





CHAPTER		PAGE
	1. Microwave Probe	207
	2. Optical Interferometry	207
	3. Background Continuum Method	208
	4. Intensity Ratios	209
	5. Line Merging Method	210
	6. Measurement of Line Profile	212
	D. Line Broadening	213
	1. Doppler Effect	215
	2. Stark Effect	216
	E. Experimental	227
	1. Experimental Conditions	227
	2. Background Subtraction: "Slope" Method	229
	3. Transformation of Lateral Intensity into Radial Intensity by Abel Inversion	234
	4. Experimental Procedure for Electron Density Measurements	246
	F. Results and Discussion	251
	G. Conclusions	263
VIII	SPATIAL DISTRIBUTION OF ELECTRON DENSITIES IN ARGON, NITROGEN-ARGON, AND OXYGEN-ARGON MIXED GAS PLASMAS	265
	A. Introduction	265
	B. Experimental	267
	C. Spatial Distribution of Electron Density in an ICP source	267



CHAPTER		PAGE
	1. Effects of rf Power on Electron Density Distribution	277
	2. Effects of Aerosol Flow Rate on Electron Density Distribution	279
	3. Effects of Foreign Gases in the Coolant Stream on the Electron Density Distribution	280
	a. 10% Nitrogen Cooled ICP	281
	b. 100% Nitrogen Cooled ICP	287
	c. 10% Oxygen Cooled ICP	288
	d. 100% Oxygen Cooled ICP	294
	D. Conclusions	295
IX	CORRELATION OF ANALYTE EMISSION WITH ELECTRON DENSITY IN MIXED GAS ICPs	297
	A. Introduction	297
	B. Experimental	299
	C. Results and Discussion	299
	1. Comparison of Horizontal Lateral and Radial Emission Profiles of Cadmium Neutral Atom and Ion Lines	299
	2. Complete Radial Emission Maps for Cadmium Neutral Atom and Ion Lines	303
	3. Effects of Foreign Gases (N <sub>2</sub> and O <sub>2</sub> ) in the Coolant Stream on the Complete Radial Emission Maps	313
	a. 10% and 100% Nitrogen Cooled ICPs	314
	b. 10% and 100% Oxygen Cooled ICPs	316



CHAPTER		PAGE
	4. Correlation of Analyte Radial Emission with Electron Density Measured at 2, 10, and 20mm Above the Load Coil	318
	5. Correlation of Analyte Radial Emission from Mixed Gas ICPs with Electron Density in the Aerosol Channel	326
	D. Conclusions	339
X	SUMMARY	344
	BIBLIOGRAPHY	348
	APPENDIX A	363





## LIST OF TABLES

Table	Description	Page
I.1	ICP operating parameters for mixed gas studies N <sub>2</sub> - Ar mixed gas ICPs.	19
II.1	ICP system specifications.	36
II.2	Measurement system.	44
III.1	Typical operating conditions for mixed gas ICPs.	58
IV.1	Excitation potentials and ionization potentials for analyte atom and ion lines.	72
IV.2	Excitation potentials and peak positions for some analyte lines.	90
V.1	Precision tests for the photodiode array detection system.	107
V.2	Signal-to-noise ratios for N <sub>2</sub> -Ar mixed gas plasmas (CaII 393.4 nm).	113
V.3	Signal-to-noise ratios for O <sub>2</sub> -Ar mixed gas plasmas (CaII 393.4 nm).	117
V.4	Signal-to-noise ratios for Air-Ar mixed gas plasmas (CaII 393.4 nm).	121
V.5	Signal-to-noise ratios for He-Ar mixed gas plasmas (CaII 393.4 nm).	125
V.6	Comparison of signal-to-noise ratios for mixed gas plasmas (CaII 393.4 nm).	128
V.7	Signal-to-noise ratios for N <sub>2</sub> -Ar mixed gas plasmas: a. CdII 214.4 nm, and b. CdI 228.8 nm.	135
V.8	Signal-to-noise ratios for O <sub>2</sub> -Ar mixed gas plasmas: a. CdII 214.4 nm, and b. CdI 228.8 nm.	140
V.9	Signal-to-noise ratios for Air-Ar mixed gas plasmas: a. CdII 214.4 nm, and b. CdI 228.8 nm.	145



Table	Description	Page
V.10	Signal-to-noise ratios for He-Ar mixed gas plasmas: a. CdII 214.4 nm, and b. CdI 228.8 nm.	150
V.11	Comparison of signal-to-noise ratios for mixed gas plasmas: CdI 228.8 nm, CdII 226.5 nm, and CdII 214.4 nm.	154
VI.1	Signal-to-noise ratios of CaII 393.37 nm for argon plasmas as a function of power and aerosol flow rate (15 mm above the load coil).	165
VI.2	Signal-to-noise ratios of CaII 393.37 nm for argon plasmas as a function of power and aerosol flow rate (10 mm above the load coil).	165
VI.3	Signal-to-noise ratios of CaII 393.37 nm for argon plasmas as a function of power and aerosol flow rate (5 mm above the load coil).	166
VI.4	Signal-to-noise ratios of CaII 393.37 nm for argon plasmas as a function of power and aerosol flow rate (2 mm above the load coil).	166
VI.5	Signal-to-noise ratios of CaII 393.37 nm for 10% N <sub>2</sub> cooled plasmas as a function of power and aerosol flow rate (10mm above the load coil).	169
VI.6	Signal-to-noise ratios of CaII 393.37 nm for 20% N <sub>2</sub> cooled plasmas as a function of power and aerosol flow rate (5 mm above the load coil).	169
VI.7	Signal-to-noise ratios of CaII 393.37 nm for 100% N <sub>2</sub> cooled plasmas as a function of power and aerosol flow rate (2 mm above the load coil).	170
VI.8	Signal-to-noise ratios of CaII 393.37 nm for 10% O <sub>2</sub> cooled plasmas as a function of power and aerosol flow rate (10mm above the load coil).	172
VI.9	Signal-to-noise ratios of CaII 393.37 nm for 20% O <sub>2</sub> cooled plasmas as a function of power and aerosol flow rate (5 mm above the load coil).	172
VI.10	Signal-to-noise ratios of CaII 393.37 nm for 100% O <sub>2</sub> cooled plasmas as a function of power	173



Table	Description	Page
	and aerosol flow rate (2 mm above the load coil).	
VI.11	Signal-to-noise ratios of CaII 393.37 nm for 10% air cooled plasmas as a function of power and aerosol flow rate (10mm above the load coil).	175
VI.12	Signal-to-noise ratios of CaII 393.37 nm for 20% air cooled plasmas as a function of power and aerosol flow rate (5 mm above the load coil).	175
VI.13	Signal-to-noise ratios of CaII 393.37 nm for 100% air cooled plasmas as a function of power and aerosol flow rate (2 mm above the load coil).	176
VI.14	Signal-to-noise ratios of CaII 393.37 nm for 10% He cooled plasmas as a function of power and aerosol flow rate (10mm above the load coil).	177
VI.15	Signal-to-noise ratios of CaII 393.37 nm for 20% He cooled plasmas as a function of power and aerosol flow rate (5 mm above the load coil).	177
VI.16	Signal-to-noise ratios of CaII 393.37 nm for 70% He cooled plasmas as a function of power and aerosol flow rate (2 mm above the load coil).	178
VII.1	Calculated Doppler and Stark half-widths of $H_{\beta}$ line for some typical temperatures and electron densities.	223
VII.2	Transformation of lateral data into radial data by (a) Bockasten's, and by (b) Nestor and Olson's method.	240
VII.3	Data pairs for half-width of $H_{\beta}$ line versus electron density measurements.	253
VII.4	Survey of electron density in an Ar-ICP.	258
IX.1	Wavelengths, excitation potentials and sum of excitation potentials and ionization potentials for Cd.	335





## LIST OF FIGURES

Figure	Description	Page
1.	Main features of the ICP discharge.	12
2.	ICP torch (nomenclature).	37
3.	ICP torch (dimensions in mm).	39
4.	ICP torch, spray chamber and nebulizer assembly.	41
5.	Block diagram of ICP instrumentation.	43
6.	Schematic diagram of Czerny-Turner type monochromator with a photodiode array detector for spectral measurements.	47
7.	Schematic diagram of Czerny-Turner type monochromator with a photodiode array detector for spatial profile measurements.	49
8.	Block diagram of computer controlled photodiode array measurement system.	52
9.	Signal conditioning electronics for photodiode array.	53
10.	Photos of (A) Ar-ICP; (B) 10% N <sub>2</sub> Cooled ICP; (C) 100% N <sub>2</sub> Cooled ICP, operated at 2.0 Kw power and 1.0 L/min aerosol flow rate.	60
11.	Spatial profiles of (a) MgI 285.2nm, (b) MgII 279.6nm, (c) CdI 228.8nm, and (d) CdII 226.5nm as a function of N <sub>2</sub> -Ar mixed gas composition. (curve a, 0%; curve b, 10%; curve c, 20%; curve d, 50%; and curve e, 100% nitrogen cooled ICP).	68
12.	Spatial profiles of (a) ZnI 213.9nm, (b) ZnII 202.6nm, (c) MnI 403.1nm, and (d) MnII 257.6nm as a function of N <sub>2</sub> -Ar mixed gas composition.	69
13.	Spatial profiles of (a) CuI 324.7nm, (b) CuII 224.7nm, (c) CrI 425.4nm, and (d) CrII 267.7nm as a function of N <sub>2</sub> -Ar mixed gas composition.	70



Figure	Description	Page
14.	Spatial profiles of (a) SrI 460.7nm, (b) SrII 407.6nm, (c) CoI 345.4nm, and (d) CoII 228.6nm as a function of N <sub>2</sub> -Ar mixed gas composition.	71
15.	Spatial profiles of ArI 415.8 nm as a function of N <sub>2</sub> -Ar mixed gas plasmas. Percentages of N <sub>2</sub> in the coolant flow: (a) 0%, (b) 10%, (c) 20%, (d) 50%, and (e) 100%.	74
16.	Vertical spatial profiles for SrII 407.8nm and SrI 460.7nm (Ar-ICP). Aerosol flow rates: (I) 0.8 L/min, (II) 1.0 L/min, and (III) 1.2 L/min. RF power: (1) 2.25 Kw, (2) 2.00 Kw, (3) 1.75 Kw, (4) 1.50 Kw, and (5) 1.25 Kw.	76
17.	Vertical spatial profiles for SrII 407.8nm and SrI 460.7nm (10% N <sub>2</sub> Cooled ICP). Aerosol flow rates: (I) 0.8 L/min, (II) 1.0 L/min, and (III) 1.2 L/min. RF power: (1) 2.25 Kw, (2) 2.00 Kw, (3) 1.75 Kw, (4) 1.50 Kw, and (5) 1.25 Kw.	77
18.	Vertical spatial profiles for SrII 407.8nm and SrI 460.7nm (100% N <sub>2</sub> Cooled ICP). Aerosol flow rates: (I) 0.8 L/min, (II) 1.0 L/min, and (III) 1.2 L/min. RF power: (1) 2.25 Kw, (2) 2.00 Kw, (3) 1.75 Kw, (4) 1.50 Kw, and (5) 1.25 Kw.	78
19.	Vertical spatial profiles for CrII 267.7nm and CrI 425.4nm (Ar-ICP). Aerosol flow rates: (I) 0.8 L/min, (II) 1.0 L/min, and (III) 1.2 L/min. RF power: (1) 2.25 Kw, (2) 2.00 Kw, (3) 1.75 Kw, (4) 1.50 Kw, and (5) 1.25 Kw.	79
20.	Vertical spatial profiles for CrII 267.7nm and CrI 425.4nm (10% N <sub>2</sub> Cooled ICP). Aerosol flow rates: (I) 0.8 L/min, (II) 1.0 L/min, and (III) 1.2 L/min. RF power: (1) 2.25 Kw, (2) 2.00 Kw, (3) 1.75 Kw, (4) 1.50 Kw, and (5) 1.25 Kw.	80



Figure	Description	Page
21.	Vertical spatial profiles for CrII 267.7nm and CrI 425.4nm (100% N <sub>2</sub> Cooled ICP). Aerosol flow rates: (I) 0.8 L/min, (II) 1.0 L/min, and (III) 1.2 L/min. RF power: (1) 2.25 Kw, (2) 2.00 Kw, (3) 1.75 Kw, (4) 1.50 Kw, and (5) 1.25 Kw.	81
22.	Vertical spatial profiles for MnII 257.6nm and MnI 403.1nm (Ar-ICP). Aerosol flow rates: (I) 0.8 L/min, (II) 1.0 L/min, and (III) 1.2 L/min. RF power: (1) 2.25 Kw, (2) 2.00 Kw, (3) 1.75 Kw, (4) 1.50 Kw, and (5) 1.25 Kw.	82
23.	Vertical spatial profiles for MnII 257.6nm and MnI 403.1nm (10% N <sub>2</sub> Cooled ICP). Aerosol flow rates: (I) 0.8 L/min, (II) 1.0 L/min, and (III) 1.2 L/min. RF power: (1) 2.25 Kw, (2) 2.00 Kw, (3) 1.75 Kw, (4) 1.50 Kw, and (5) 1.25 Kw.	83
24.	Vertical spatial profiles for MnII 257.6nm and MnI 403.1nm (100% N <sub>2</sub> Cooled ICP). Aerosol flow rates: (I) 0.8 L/min, (II) 1.0 L/min, and (III) 1.2 L/min. RF power: (1) 2.25 Kw, (2) 2.00 Kw, (3) 1.75 Kw, (4) 1.50 Kw, and (5) 1.25 Kw.	84
25.	Vertical spatial profiles for MgII 279.6nm and MgI 285.2nm (Ar-ICP). Aerosol flow rates: (I) 0.8 L/min, (II) 1.0 L/min, and (III) 1.2 L/min. RF power: (1) 2.25 Kw, (2) 2.00 Kw, (3) 1.75 Kw, (4) 1.50 Kw, and (5) 1.25 Kw.	85
26.	Vertical spatial profiles for MgII 279.6nm and MgI 285.2nm (10% N <sub>2</sub> Cooled ICP). Aerosol flow rates: (I) 0.8 L/min, (II) 1.0 L/min, and (III) 1.2 L/min. RF power: (1) 2.25 Kw, (2) 2.00 Kw, (3) 1.75 Kw, (4) 1.50 Kw, and (5) 1.25 Kw.	86
27.	Vertical spatial profiles for MgII 279.6nm and MgI 285.2nm (100% N <sub>2</sub> Cooled ICP). Aerosol flow rates: (I) 0.8 L/min, (II) 1.0 L/min, and (III) 1.2 L/min. RF power: (1) 2.25 Kw,	87





Figure	Description	Page
	(2) 2.00 Kw, (3) 1.75 Kw, (4) 1.50 Kw, and (5) 1.25 Kw.	
28.	Vertical spatial profiles for CaII 393.4nm (Ar-ICP and 100% N <sub>2</sub> cooled ICP). Percentage of N <sub>2</sub> in the aerosol flow: (1) 0%, (2) 20%, and (3) 50%.	94
29.	Background emission spectra for N <sub>2</sub> -Ar mixed gas plasmas at 2 mm and 10 mm above load coil (spectral region centered at 373 nm).	109
30.	Background emission spectra for O <sub>2</sub> -Ar mixed gas plasmas at 2 mm and 10 mm above load coil (spectral region centered at 373 nm).	116
31.	Background emission spectra for Air-Ar mixed gas plasmas at 2 mm and 10 mm above load coil (spectral region centered at 373 nm).	120
32.	Background emission spectra for He-Ar mixed gas plasmas at 2 mm and 10 mm above load coil (spectral region centered at 373 nm).	124
33.	Background emission spectra for N <sub>2</sub> -Ar mixed gas plasmas at 2 mm and 10 mm above load coil (spectral region centered at 228 nm).	132
34.	Background subtracted spectra of CdI and CdII lines as a function of N <sub>2</sub> -Ar gas composition and observation height.	133
35.	Background emission spectra for O <sub>2</sub> -Ar mixed gas plasmas at 2 mm and 10 mm above load coil (spectral region centered at 228 nm).	138
36.	Background subtracted spectra of CdI and CdII lines as a function of O <sub>2</sub> -Ar gas composition and observation height.	139
37.	Background emission spectra for Air-Ar mixed gas plasmas at 2 mm and 10 mm above load coil (spectral region centered at 228 nm).	143
38.	Background subtracted spectra of CdI and CdII	144



Figure	Description	Page
	lines as a function of Air-Ar gas composition and observation height.	
39.	Background emission spectra for He-Ar mixed gas plasmas at 2 mm and 10 mm above load coil (spectral region centered at 228 nm).	148
40.	Background subtracted spectra of CdI and CdII lines as a function of He-Ar gas composition and observation height.	149
41.	Comparison of background subtracted spectra of CdI and CdII lines for optimized mixed gas plasmas.	153
42.	Comparison of Cd emission spectra for mixed gas plasmas at observation heights of 2mm, 5mm, 10mm, 15mm and 20 mm above the load coil. Coolant gas composition : 100% Ar, 10% N <sub>2</sub> , 10% O <sub>2</sub> , 10% Air and 10% He.	156
43.	Effect of PO <sub>4</sub> <sup>3-</sup> interference on CaII 393.4nm emission in N <sub>2</sub> -Ar mixed gas ICPs, at observation heights of 2mm, 10mm, and 18 mm above the load coil. Percentage of N <sub>2</sub> in coolant gas flow: (a) 0%, (b) 10%, (c) 20%, and (d) 100%.	181
44.	Effect of PO <sub>4</sub> <sup>3-</sup> interference on CaII 393.4nm emission in O <sub>2</sub> -Ar mixed gas ICPs, at observation heights of 2mm, 10mm, and 18mm above the load coil. Percentage of O <sub>2</sub> in coolant gas flow: (a) 0%, (b) 10%, (c) 20%, and (d) 100%.	182
45.	Effect of K interference on CaII 393.4nm emission in N <sub>2</sub> -Ar mixed gas ICPs, at observation heights of 2mm, 10mm, and 18mm above the load coil. Percentage of N <sub>2</sub> in coolant gas flow: (a) 0%, (b) 10%, (c) 20%, and (d) 100%.	186
46.	Effect of K interference on CaII 393.4nm emission in O <sub>2</sub> -Ar mixed gas ICPs, at observation heights of 2mm, 10mm, and 18mm above the load coil. Percentage of O <sub>2</sub> in coolant gas flow: (a) 0%, (b) 10%, (c) 20%, and (d) 100%.	187



Figure	Description	Page
47.	Effect of N <sub>2</sub> -Ar mixed gas ICPs on the analytical calibration curves for CaII 393.4nm line. Coolant gas composition and observation height above the load coil: (1) 100% Ar at 18mm, (2) 10% N <sub>2</sub> - 90% Ar at 10mm, (3) 20% N <sub>2</sub> - 80% Ar at 5mm, and (4) 100% N <sub>2</sub> at 2 mm.	190
48.	Effect of O <sub>2</sub> -Ar mixed gas ICPs on the analytical calibration curves for CaII 393.4nm line. Coolant gas composition and observation height above the load coil: (1) 100% Ar (18mm), (2) 10% O <sub>2</sub> - 90% Ar (10mm), (3) 20% O <sub>2</sub> - 80% Ar (5mm), and (d) 100% O <sub>2</sub> (2mm).	191
49.	Effect of N <sub>2</sub> -Ar mixed gas ICPs on the analytical calibration curves for MnII 257.6nm line. Coolant gas composition and observation height above the load coil: (1) 100% Ar (18mm), (2) 5% N <sub>2</sub> -95% Ar (10mm), (3) 10% N <sub>2</sub> -90% Ar (10mm), (4) 20% N <sub>2</sub> -80% Ar (5mm), (5) 50% N <sub>2</sub> -50% Ar (2mm), and (6) 100% N <sub>2</sub> (2mm).	192
50.	Theoretical profiles for H <sub>β</sub> 486.1 nm line. Electron density (a) 10 <sup>14</sup> cm <sup>-3</sup> , and (b) 10 <sup>16</sup> cm <sup>-3</sup> . (The data are found in H.R. Griem's "Plasma spectroscopy", McGraw Hill Book Company, 1964).	219
51.	Experimental profile for H <sub>β</sub> line emission as measured with a photodiode array detector.	221
52.	Calculated log(half-width) of the H <sub>β</sub> emission as a function of log(electron density) for the temperature range from 5000 to 20000 K.	226
53.	Spectra illustrating the power of electronic background subtraction. (a) original emission spectrum, (b) background emission spectrum, and (c) electronic background subtracted spectrum.	230
54.	Schematic representation of the background subtraction using "slope" method.	231
55.	Schematic representation of the lateral and radial variables involved with Abel inversion.	237





Figure	Description	Page
56.	(a) Radial intensities calculated from lateral test data with smoothing. (b) Lateral test data (c) Radial intensities calculated from lateral test data without smoothing.	245
57.	Schematic diagram of the lateral $H_{\beta}$ line emission profiles measured with a photodiode array system.	248
58.	Schematic representation of the lateral and radial variables involved with the half-width determination of the line emission profile: (a) measured lateral data, (b) expanded lateral data, (c) calculated radial data via Abel inversion, and (d) calculated half-width for electron density measurements.	249
59.	Radial emission profile for $H_{\beta}$ 486.1 nm at 2 mm above the load coil.	252
60.	Plot of log(half-width) versus log(electron density).	254
61.	Radial electron density profiles of an Ar-ICP as a function of observation height: (a) 2 mm, (b) 5 mm, (c) 10 mm, (d) 15 mm, and (d) 20 mm above the load coil.	256
62.	Vertical electron density profile for an Ar-ICP.	260
63.	Vertical electron density profiles of an Ar-ICP as a function of distance off the plasma central axis: (a) 0.0 mm, (b) 2.0 mm, and (c) 4.0 mm off the central aerosol channel.	261
64.	Electron density map of an Ar-ICP (solid line marks torch edge).	262
65.	Radial electron density profiles of an Ar-ICP as a function of observation height: (a) 2 mm, (b) 5 mm, (c) 10 mm, (d) 15 mm, and (e) 20 mm above the load coil, operated at 2.0 Kw power and 1.0 L/min aerosol flow rate.	271





Figure	Description	Page
66.	Electron density map for an Ar-ICP (solid line marks torch edge), operated at 2.0 Kw power and 1.0 L/min aerosol flow rate.	272
67.	Radial electron density profiles of an Ar-ICP as a function of observation height: (a) 2 mm, (b) 5 mm, (c) 10 mm, (d) 15 mm, and (e) 20 mm above the load coil, operated at 1.5 Kw power and 1.0 L/min aerosol flow rate.	273
68.	Electron density map for an Ar-ICP, operated at 1.5 Kw power and 1.0 L/min aerosol flow rate.	274
69.	Radial electron density profiles of an Ar-ICP as a function of observaton height: (a) 2 mm, (b) 5 mm, (c) 10 mm, (d) 15 mm, and (d) 20 mm above the load coil, operated at 2.0 Kw power and 1.5 L/min aerosol flow rate.	275
70.	Electron density map for an Ar-ICP, operated at 2.0 Kw power and 1.5 L/min aerosol flow rate.	276
71.	Radial electron density profiles of a 10% N <sub>2</sub> - 90% Ar cooled ICP as a function of observation height: (a) 2 mm, (b) 5 mm, (c) 10 mm, (d) 15 mm, and (E) 20 mm above the load coil, operated at 2.0 Kw power and 1.0 L/min aerosol flow rate.	283
72.	Electron density map for a 10% N <sub>2</sub> cooled ICP, operated at 2.0 Kw power and 1.0 L/min aerosol flow rate.	284
73.	Radial electron density profiles of a 100% N <sub>2</sub> cooled ICP as a function of observation height: (a) 2 mm, (b) 5 mm, (c) 10 mm, (d) 15 mm, and (E) 20 mm above the load coil, operated at 2.0 Kw power and 1.0 L/min aerosol flow rate.	285
74.	Electron density map for a 100% N <sub>2</sub> cooled ICP, operated at 2.0 Kw power and 1.0 L/min aerosol flow rate.	286
75.	Radial electron density profiles of a 10% O <sub>2</sub> - 90% Ar cooled ICP as a function of observatfon height: (a) 2 mm, (b) 5 mm, (c) 10 mm, (d) 15	290



Figure	Description	Page
	mm, and (E) 20 mm above the load coil, operated at 2.0 Kw power and 1.0 L/min aerosol flow rate.	
76.	Electron density map for a 10% O <sub>2</sub> cooled ICP, operated at 2.0 Kw power and 1.0 L/min aerosol flow rate.	291
77.	Radial electron density profiles of a 100% O <sub>2</sub> cooled ICP as a function of observation height: (a) 2 mm, (b) 5 mm, (c) 10 mm, (d) 15 mm, and (E) 20 mm above the load coil, operated at 2.0 Kw power and 1.0 L/min aerosol flow rate.	292
78.	Electron density map for a 100% O <sub>2</sub> cooled ICP, operated at 2.0 Kw power and 1.0 L/min aerosol flow rate.	293
79.	Lateral and radial emission profiles for CdI 228.8 nm line at 2 mm above the load coil.	301
80.	Lateral and radial emission profiles for CdII 226.5 nm line at 2 mm above the load coil.	302
81.	Complete radial emission map of an Ar-ICP for CdI 228.8 nm and CdII 226.5 nm, operated at 2.0 Kw power and 1.0 L/min aerosol flow rate.	304
82.	Complete radial emission map of an Ar-ICP for CdI 228.8 nm and CdII 226.5 nm, operated at 1.5 Kw power and 1.0 L/min aerosol flow rate.	305
83.	Complete radial emission map of an Ar-ICP for CdI 228.8 nm and CdII 226.5 nm, operated at 2.0 Kw power and 1.5 L/min aerosol flow rate.	306
84.	Complete radial emission map of a 10% N <sub>2</sub> - 90% Ar cooled ICP for CdI 228.8 nm and CdII 226.5 nm, operated at 2.0 Kw power and 1.0 L/min aerosol flow rate.	307
85.	Complete radial emission map of a 100% N <sub>2</sub> cooled ICP for CdI 228.8 nm and CdII 226.5 nm, operated at 2.0 L/min power and 1.0 L/min aerosol flow rate.	308
86.	Complete radial emission map of a 10% O <sub>2</sub> - 90% Ar cooled ICP for CdI 228.8 nm and CdII 226.5 nm,	309





Figure	Description	Page
	operated at 2.0 Kw power and 1.0 L/min aerosol flow rate.	
87.	Complete radial emission map of a 100% O <sub>2</sub> cooled ICP for CdI 228.8 nm and CdII 226.5 nm, operated 2.0 Kw power and 1.0 L/min aerosol flow rate.	310
88.	Correlation of electron density with radial emission for CdI 228.8 nm, CdII 226.5 nm, and CdII 214.4 nm at 2 mm above the load coil.	320
89.	Correlation of electron density with radial emission for CdI 228.8 nm, and CdII 226.5 nm at 10 mm above the load coil.	321
90.	Correlation of electron density with radial emission for CdI 228.8 nm and CdII 226.5 nm at 20 mm above the load coil.	322
91.	Correlation of electron density with radial emission for CdI 228.8 nm and CdII 226.5 nm at 10 mm above the load coil (dotted line = Ar-ICP, solid line = 10% N <sub>2</sub> -90% Ar cooled ICP).	325
92.	Correlation of electron density with vertical spatial emission for CdI 228.8 nm and CdII 226.5 nm as a function of plasma power, curve a, 2.0 Kw; curve b, 1.50 Kw.	328
93.	Correlation of electron density with vertical spatial emission profiles for CdI 228.8 nm and CdII 226.5 nm as a function of aerosol flow rate, curve a, 1.0 L/min; curve b, 1.5 L/min.	229
94.	Correlation of electron density with vertical spatial emission profiles for CdI 228.8 nm and CdII 226.5 nm as a function of N <sub>2</sub> -Ar mixed gas composition, curve a, 100% Ar; curve b, 10% N <sub>2</sub> - 90% Ar; and curve c, 100% N <sub>2</sub> cooled ICP.	330
95.	Correlation of electron density with vertical spatial emission profiles for CdI 228.8 nm and CdII 226.5 nm as a function of O <sub>2</sub> -Ar mixed gas composition, curve a, 100% Ar; curve b, 10% O <sub>2</sub> - 90% Ar; and curve c, 100% O <sub>2</sub> cooled ICP.	331





## CHAPTER I

### INTRODUCTION

#### A. Introduction

One of the major goals of an analytical chemist is the development of analytical techniques for the solution of specific analytical problems of current interest. Very frequently, an already established technique suitable for the solution of a particular task cannot be found. In that instance, one is confronted with the need of establishing, modifying, choosing and/or developing a new technique to solve the particular problem. In today's modern analytical chemistry, the design of a system suitable for a particular chemical measurement requires a familiarity with both a basic understanding of the principles involved and the capabilities of the technique being developed. Therefore, in order to ensure the ultimate success of a particular technique, one has to investigate in parallel both the construction of new instrumentation and the fundamental aspects of the system.

Classical methods for elemental analysis often have the advantages of high precision and accuracy, however these advantages are just as often offset by the disadvantages of



extensive sample pretreatment and the need to separate interfering substances i.e., lack of specificity. Therefore, instrumental methods of analysis such as atomic emission spectrometry seem to be more appropriate for elemental analysis; they provide ease and speed of operation, and usually require relatively simple or no sample pretreatment. Atomic emission spectroscopy is widely used for both qualitative and quantitative analysis. The high sensitivity and the possibility of simultaneous excitation of many elements make emission spectroscopy especially suitable for rapid elemental analysis.

Among several excitation sources available for emission spectroscopy, the inductively coupled plasma (ICP) is perhaps the most promising emission source. This source is a relatively recent development, the first commercial ICP system became available in 1974, but research on this source has been going on since the early 1960's (1-4). The ICP source enable attaining high sensitivity, low detection limits, wide dynamic range and relative freedom from chemical interferences. These advantages, coupled with the high temperature and inert atmosphere of the discharge, make the ICP an almost ideal source for emission spectrochemical analysis.

Most of the inductively coupled plasmas currently utilized for analytical spectroscopy are based on pure



argon. One of the major disadvantages in both the commercial and research Ar-ICP systems is the large consumption of expensive argon gas. While much interest has been focused on modifications in the Ar-ICP instrumentation in order to cut down on the operating cost, comparatively little research has been carried out on replacing the expensive argon gas with cheaper gases such as nitrogen, oxygen or air. The purpose of this work is to study and evaluate the analytical capabilities of the mixed gas ICPs. In addition, the performance-to-cost ratio of the conventional argon and the mixed gas ICPs under similar operating conditions will be evaluated.

The second part of this work is a study of the spatial distribution of analyte species and electron density in mixed gas ICPs. The results of the investigations are used to speculate on the nature of the excitation and ionization processes in the plasma discharge. In addition, they are used to rationalize and clarify some of the physical and spectral observations of the mixed gas plasmas. However, before proceeding into the discussion of the mixed gas plasmas, a brief introduction to the inductively coupled plasma is warranted.





## B. Plasma

### 1. The Fourth State of Matter

Matter can exist in a variety of stable forms which are governed by their physical environments. The most common classification of stable states is that of solid, liquid or gas. However for a number of years, the plasma state has been considered to be a fourth state of matter. What is the unique property that separates a plasma from solid, liquid or gaseous states? A plasma looks like a gas and in many ways behaves like a gas. But there is a major distinction, i.e., a plasma is a gas that conducts electricity, that is, an ionized gas.

At sufficiently high temperatures, gases experience an increase in kinetic energy resulting in an increase in collision frequency. Upon colliding with other gases, they release their electrons and become ions. The gas is said to be ionized which means that some of the gas molecules have been divided into positively charged ions and negatively charged electrons. This state of ionized gases was classified as the fourth state of matter by Sir William Crookes (5) while performing experiments demonstrating the passage of electricity through gases. In 1929, Langmuir (6) began using the term "plasma" to describe the state of





matter in discharge tubes.

A plasma can be completely or partially ionized. In most cases, a high temperature plasma consists of a mixture of neutral atoms, molecules, electrons and ions. Perhaps the most significant and fundamental aspect of a plasma is its tendency to remain electrically neutral. Therefore, in general, a plasma as a whole is in a quasi-neutral state where there is no surplus of opposite charge in a given volume (7).

## 2. Definition

The most notable feature of a plasma is that some of the particles are charged and therefore interactions with each other are governed by coulombic forces. The coulombic force, which is inversely proportional to the square of the distance between particles, falls off with distance. Hence, every charged particle in a plasma interacts with its neighbors, giving the plasma a cohesiveness which is often compared to that of a mold or jelly. Since charged particles have tendencies to rearrange themselves in order to effectively shield any electrostatic effects due to a charge within the plasma, this shielding effect which cancels out any electrostatic fields has to occur within a sphere. The correlation of electron position with respect to the



neighboring positive ion is expressed as Debye length, DL (8). For a plasma consisting of singly charged ions and electrons, the Debye length is given by,

$$DL = \left( \frac{kT}{4 \pi N_e e^2} \right)^{1/2} = 6.90 \left( \frac{T}{N_e} \right)^{1/2} \quad (1)$$

where  $T$  = temperature, K.

$N_e$  = electron number density, particles/cm<sup>3</sup>.

Unlike the solid metal conductor, where current is carried by electrons while the ions are fixed in the lattice, both electrons and ions in the plasma are free to move. However the density of electrons in a plasma is so large that even a small displacement of the electron with respect to the ion will give rise to a very intense electric field. Therefore, for the plasma to remain in the quasi-neutral state, the large electrostatic force due to charge separation will have to build up sufficiently to prevent charge separation. In this case, the ions and electrons in the plasma are constrained to move more or less together.

Since one of the major characteristics of the plasma is the maintenance of charge neutrality, the number of



electrons inside the Debye sphere with radius  $DL$  must be greater or equal to unity. Beyond the Debye sphere, there is a charge unbalance. Conversely, thermal and electrical forces are in balance within the Debye sphere.

Martin A. Uman (9) defined plasma as "a collection of mobile positively and negatively charged particles for which the Debye length is much less than the physical size of the plasma". If we consider a cube with sides of length  $x$ , where  $x$  is much smaller than Debye length, then inside this cube the number of ions may in fact be very different from the number of electrons. This cube cannot be classified as a plasma even though it contains some ionized particles.

It is worth noting that the concept of Debye length was first introduced in connection with the properties exhibited by a strong electrolyte. A strong electrolyte is in actual fact a liquid plasma (9,10).

The sun and all the stars are nothing more than gigantic globes of ultra high temperature plasmas. Although plasma is commonly found in the universe, it is rarely found on earth. With the recent interest and demand in ultra-high temperature technology and plasma energy sources, physicists, chemists and engineers in many fields have become more involved in economically generating plasma and developing practical applications.

Laboratory or man-made plasmas can be created by





several methods: combustion flames and explosion produced by chemical reactions of high specific energy (10), controlled nuclear reactions (11,12), electrically heated furnaces (10), shock waves (10) and electrical discharges (13). The type of plasma reported in this work was generated by an electrical discharge. The plasma discharge for analytical emission spectroscopy can be produced by a variety of methods, namely, d.c. current (14-19), microwave induction (20-24), and radio frequency inductive coupling (25-30). Each of these discharges excites a sample in a different way and by a slightly different mechanism, thus the instrumentation also differs considerably. The type of plasma discharge under study in this work is the high frequency inductively coupled plasma.

## C. Inductively Coupled Plasma

### 1. History

In 1941, G.I. Babat succeeded in obtaining an electrodeless discharge at atmospheric pressure though it only lasted for a few seconds (13,31). He designed and used for the first time the multi-turn coil inductor. He was not only the first to obtain a discharge at atmospheric



pressure, but he also applied for the first time a continuous gas flow through the discharge, which is the basic operating principle of today's high frequency plasma torch. Unfortunately his important work was hindered by the outbreak of the Second World War. After the war, research and interest in this form of discharge disappeared for a long time until, in 1961, Reed proposed a convenient design of a plasma torch which was capable of sustaining a stable discharge at atmospheric pressure (32,33). In his design, heat shielding of the walls was accomplished by introducing a gas jet between the wall and the plasma. Vortex gas stabilization has been used quite frequently for the plasma discharge. It is difficult to say who proposed this idea first in connection with the ICP. Tangential gas feeds are found in several references (32,34,35). Thus, the development of reliable methods for heat shielding and vortex stabilization of electrical discharges at atmospheric pressure makes it possible to sustain and control a plasma over a wide range of powers and frequencies. It was quickly recognized by two groups of workers that Reed's type of plasma could be a useful source for analytical spectroscopy. These groups led by Greenfield (1) and by Fassel (2), took separate routes at an early stage : the former used a high power nitrogen cooled argon ICP and the latter employed a one hundred percent argon ICP.



Early investigators encountered some difficulties in introducing aerosols or powdered samples into the plasma (36,37) because, with their designs, the aerosols or powdered samples simply reflected from or passed along the outer surface of the plasma. Taking advantage of the skin depth effect of induction heating, Dickinson and Fassel (37) designed and developed a plasma torch which consisted of two concentric tubes and a central aerosol channel, resulting in a doughnut (toroidal) like discharge. The plasma was operated at 30 MHz and an argon flow of 1.7 L/min passed through the central aerosol injection orifice. They also employed tangential coolant gas inlets to achieve vortex stabilization of the plasma. At that time, their reported detection limits for many metals were two to four orders of magnitude superior to the best detection values reported by users of flame atomic absorption or other emission techniques. Since then, ICP technology has been rapidly developed and is widely regarded by analytical spectroscopists as the most important and promising emission spectroscopic source today.

Applications of ICP-Atomic Emission Spectroscopy (ICP-AES) come from many disciplines which include the analysis of trace metals in biological materials (29,38-41), the determination of impurities in alloy steel (42-43), and toxicological investigations. ICP-AES can also be applied to





the analysis of metals in organic media like lubricating oils, fuel, edible oils, coal liquification products and tar sand (44,45). For good historical and application reviews of plasmas as spectrochemical sources, the reader is referred to Greenfield (25-27), Barnes (28) and Boumans (30).

## 2. Generating and Sustaining the Plasma.

A schematic drawing of an assembly of three concentric quartz tubes used for generating an ICP is showned in Figure 1. This assembly of concentric tubes is called the "plasma torch", which is surrounded by a three turned water cooled induction coil connected to a high radio frequency (rf) current generator. The plasma torch itself is described in Chapter II. Gases are made to flow tangentially through these tubes. To initiate the plasma, argon gas is made electrically conductive and partially ionized by Tesla sparks. This can be represented as,



The resulting charged particles (ions and electrons) are induced to flow in a circular motion due to their interaction with the applied magnetic field produced as a result of rf power applied to the induction coil. The





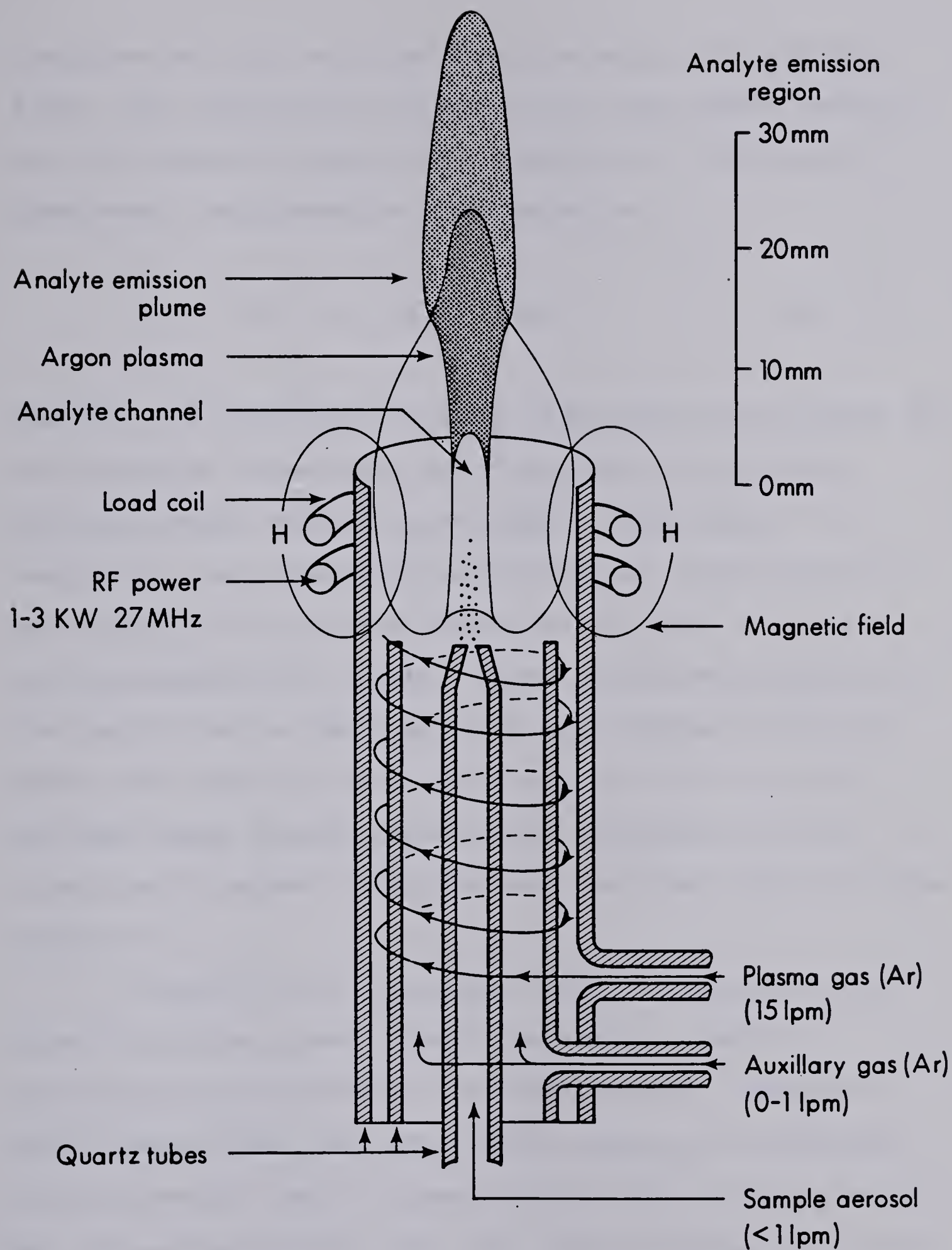


Figure 1. Main features of the ICP discharge.



electrons and ions are then accelerated in this magnetic field. The accelerated electrons have high enough energies to ionize neutral argon atoms, creating an "avalanche" of electrons. The process is represented as,



However, the accelerated charged particles can also meet the resistance of the coolant gas flow producing an ohmic heating effect, which in turn leads to additional ionization, as represented in Equation(2). Since power is continuously fed into the induction coil from a high rf current generator at 1.0 to 2.5 Kw, the plasma generated is then maintained by the continuous application of that rf power. The cooler doughnut-hole entry provided by the toroidal shape plasma presents less resistance to the injection of aerosol particles into the inner regions of the plasma (37).

Samples may be introduced into the plasma in the form of liquids, gases, powders or solids. Special techniques are required to introduce gaseous, powdered or solid samples into the ICP. Hydride generation techniques can be commonly used to convert some metals, such as Se, As, Sn, Pb, and Ge (46-48) into their metal hydrides by reaction with sodium borohydride. The hydride gases are then



transported into the plasma with the aerosol carrier gas. Solids are introduced into the plasma as powders, vapors or metal aerosols. Generation of powders or metal aerosols can be achieved by direct laser vaporization (49) or electrothermal vaporization of the solid samples (50-53). Salin and Horlick designed a novel device which is capable of introducing the solid sample in the form of powders directly into the plasma. This technique is known as the "Direct Sample Insertion" technique (54). However, the analysis of samples in solution form is by far the most common approach because it reduces problems associated with the inhomogeneity of samples. Liquid sample (solution) is introduced into the plasma in the form of a nebulized aerosol. The generation of this aerosol gas is described in Chapter II. The aerosol is carried by an argon carrier gas to the base of the plasma. This aerosol/gas combination will then "punch a hole" through the base of the plasma forming an analyte channel. The temperature in this analyte channel is high enough for the samples to become volatilized, desolvated, atomized, ionized, excited and subsequently to emit radiation.





### 3. Mixed Gas ICPs

Modifications in ICP instrumentation are regularly reported in the literature (55-60). These modifications give rise to many differences in operating conditions among the various ICPs currently used. However, there is only one really essential distinction which classifies ICPs into three main categories:

1. Argon ICPs
2. Mixed Gas ICPs
3. 100% non-Argon ICPs

The argon ICPs for analytical spectroscopy developed first by Fassel et al. (2,4) were produced with torches of 18 mm i.d., in the outer tube. The argon plasmas are usually operated with only argon in the coolant, the auxiliary and the aerosol carrier gas flows. They are normally operated at a frequency of 27 or 40 MHz with the input power between 0.5 to 1.5 Kw. Greenfield and his co-workers (1) were the first to introduce a mixture of argon and non-argon gases ( $N_2$ ,  $O_2$ , Air or He) into the outer coolant or the inner aerosol gas flows. The mixed gas plasmas were usually operated at a lower frequency, 7 MHz, extremely high power, 10 Kw, and very high flow rates. Recently, Barnes and Meyer (61)



reported that they can sustain a 100% nitrogen ICP with operating conditions similar to those described above for the conventional argon plasma. However, they did not provide any information on the performance of this discharge except that the nitrogen plasma was used to verify the validity of calculated predictions in an earlier paper (62).

Argon has been commonly employed as the operating gas for analytical plasma spectrometry, however the major disadvantage of both the commercial and the research Ar-ICP units is the large consumption of expensive argon gas. In recent years, several proposals and modifications in the plasma torch have been made to decrease the consumption of argon gas. Most notably, Savage and Hieftje (56) utilized a mini-torch with an outer coolant tube of 13 mm i.d., to decrease the amount of argon gas consumption to less than 8 L/min. Another approach was taken by Kornblum et al. (57) They designed a water cooled jacketed plasma torch which reduced the argon consumption to 2 L/min. However, the tenfold reduction in argon consumption required an equal reduction of the sample carrier gas flow to about 0.1 L/min (58). Currently available pneumatic nebulizers described in Chapter II do not operate at such a low flow rates. Ripson and de Galan (58) recently described a new sample introduction system for an ICP operating on an argon carrier gas flow of 0.1 L/min. However, it is unfortunate that such



a nebulization system incorporated with the water cooled ICP torch does not show any net gain in detection powers. In fact, the detection limits for Ca, Ba and Mg reported in their paper are two to three orders of magnitude smaller as compared to the detection limits obtained with the conventional Ar-ICP torch.

A more practical solution to this problem is to replace the expensive argon gas by cheaper gases such as  $N_2$ ,  $O_2$  or air. In the past, Greenfield and co-workers have introduced various diatomic gases ( $N_2$ ,  $O_2$ ) into the coolant or nebulizer flow of the ICP torch. But the mixed gas ICPs with which they operated required a very high power to sustain the plasma and also required a large volume of diatomic gas to prevent melt down of the plasma torch (1,25-27,64-71). The configurations operated by Greenfield and his co-workers did not demonstrate any net reduction in operating cost of the ICPs, and their reported detection limits, dynamic range and complicated molecular background spectra for the mixed gas plasmas did not show any advantages over the argon plasmas. Therefore, the mixed gas plasmas obtained only limited recognition among both commercial and academic ICP users.

Unfortunately, it also became a general belief that mixed gas plasmas could only be operated at higher power than conventional argon plasmas. This excess energy was





believed to be required to break the bonds of diatomic molecules. However in the past few years, experimental and theoretical investigations have been described for a variety of torches, generators, and mixed gas plasmas (57-59,72). Most research on mixed gas plasmas focused only on the N<sub>2</sub>-Ar mixed gas ICPs (59,73-78,82). Only limited research has been carried out on the evaluation and characterization of O<sub>2</sub>-Ar, Air-Ar and He-Ar mixed gas ICPs.

A brief summary of the various ICP operating parameters used for analytical studies of the N<sub>2</sub>-Ar mixed gas ICP is presented in Table I.1. Many of the operating conditions for the N<sub>2</sub>-Ar mixed gas ICPs reported prior to 1970 used extremely high coolant and auxiliary flow rates. In addition, the mixed gas plasmas required very high power. Although argon is widely preferred as an operating gas for ICP-AES because of its inert atmosphere, Greenfield et al. (1,64-67) have argued for argon discharges cooled with nitrogen because of the ease of operation and relatively low operating cost.

The first studies of the mixed gas ICPs (O<sub>2</sub>-Ar, Air-Ar and He-Ar) for spectrochemical analysis were also reported by Greenfield et al. (64-71). They reported that a 20% O<sub>2</sub>-80% Ar mixed gas ICP yielded better sensitivity than a 100 % argon discharge. Boumans and de Boer (79) later compared the signal-to-background ratios of some ion lines



TABLE I.1

ICP OPERATING PARAMETERS FOR MIXED GAS STUDIES  
N<sub>2</sub> - Ar MIXED GAS ICPS

	Coolant (L/min)	Auxiliary (L/min)	Aerosol (L/min)	Power (Kw)	Frequency (MHz)
S. Greenfield (1964-1971)	64 (N <sub>2</sub> )	15.0 (Ar)	2.0 (Ar)	10.5	7
D. Truitt (1970)	22 (N <sub>2</sub> )	0.5 (Ar)	0.8 (Ar)	2.0	8
V.A. Fassel (1978)	16 to 0 (Ar) 0 to 16 (N <sub>2</sub> )	1.5 (Ar)	1.0 (Ar)	1.1	27
K. Ohls (1979)	24 (N <sub>2</sub> )	16.0 (Ar)	0.03 (Ar)	3.0	27
G. Horlick (1979)	15 to 0 (Ar) 0 to 15 (N <sub>2</sub> )	1.0 (Ar)	1.0 (Ar)	0.5 to 2.75	27
A. Montaser (1980)	13.5 (Ar) +1.5 (N <sub>2</sub> )	1.5 (Ar)	1.0 (Ar)	1.2	27
L. Ebdon (1980)	4.6 (N <sub>2</sub> )	10.0 (Ar)	0.4 (Ar)	3.0	27
S. Greenfield (1980)	7.5 (N <sub>2</sub> )	7.5 (Ar)	1.0 (Ar)	2.5	36



observed in their Ar-ICP under compromise conditions for simultaneous multielement analysis (1.1 Kw) with values reported by Greenfield for a 6 Kw mixed gas ICP. Their report noted differences of one to two orders of magnitude in favor of the argon discharge. It is difficult to draw generalized conclusions on this comparative analytical performance of the argon and mixed gas ICPs because the investigation was conducted under significantly different operating conditions for each plasma.

In contrast to the system utilized by Greenfield and his co-workers (1,64-67), and Truitt and Robinson (80,81) in the late 1960's, the mixed gas plasmas investigated recently by Zalewski ( $N_2$ -Ar) (75), by Montaser and Mortazavi ( $N_2$ -Ar) (74), and by Choot and Horlick ( $N_2$ -Ar,  $O_2$ -Ar, Air-Ar and He-Ar) (82,83) have been demonstrated to be operable at similar plasma power and flow rate levels as those used in most Ar-ICP systems today. Typical conditions for the mixed gas plasmas operated in this laboratory are a coolant flow rate of 15 L/min, auxiliary (Ar) flow rate of 1.0 L/min, nebulizing flow rate (Ar) of 1.0 L/min, and rf power of 1.5 to 2.0 Kw.

Investigations on the effect of nitrogen in the outer flow on the net analyte emission intensities were reported by Montaser and Mortazavi (74), and Montaser et al. (76) who concluded that the analytical performance of the 5





to 10 % nitrogen cooled plasma was superior to that of the conventional argon discharge. However, when the outer flow was converted to 100 % nitrogen, the detection limits deteriorated sharply. These comparisons were conducted at 1.0, 1.2 and 1.4 Kw plasma power, at the "optimal" observation height of 10 mm for the N<sub>2</sub>-Ar mixed gas plasmas and at 10 and 15 mm for the conventional argon discharge.

Applications of the low powered mixed gas plasmas have been carried out in this laboratory. In Lau's dissertation (84), he reported the observation of very intense cyanogen molecular emission spectra when organic samples were aspirated into the N<sub>2</sub>-Ar mixed gas plasma. His reported results did not indicate any advantage in using a N<sub>2</sub>-Ar plasma to improve elemental determinations in organic matrices over the conventional Ar-ICP. However, when O<sub>2</sub> was introduced into the plasma, the detection limits for various elements and the analytical capabilities of the O<sub>2</sub>-Ar mixed gas plasma with the organic environments appeared to be an order of magnitude superior compared to the conventional Ar-ICPs. Work by Ng and Horlick (85) using mixed gas ICPs with a Fourier-Transform spectrometer in the near infrared and visible regions has demonstrated a tremendous advantageous decrease in background intensities. In addition, the N<sub>2</sub>-Ar mixed gas ICP was reported to be more stable than the conventional Ar-ICP. The use of a mixed gas



plasma to improve the analytical performance of the ICP-Fourier Transform spectrometer system is described in Ng's dissertation (85).

Recently, Ohls and Sommer (77,78) studied the analytical application of an air-argon and nitrogen-argon ICP source. The air cooled plasma was operated at 27.12 MHz and 3.0 Kw plasma power. Although higher coolant and auxiliary flows were used (28 L/min air and 15 L/min Ar respectively), their results for determinations in aqueous media indicated that an air cooled plasma performed slightly better than either a nitrogen or argon cooled ICP.

Many studies on mixed gas plasmas have been carried out on the characteristics of the ICPs. While much interest has been centered on applications and detection limit studies of mixed gas plasmas, comparatively little work has been carried out on evaluating the effect of gas composition, plasma power, and aerosol flow rate on the analytical capability of the mixed gas ICPs. In addition, little fundamental research has been carried out on spatial emission structures and excitation mechanisms in the mixed gas plasmas.

The purpose of this study is to provide a comprehensive investigation of the effect of plasma operating parameters on the spectral emission background and analyte emission signals. It is also the intent of this work



to compare the analytical capabilities of the plasma discharge operated in argon and mixed gas atmospheres.

#### D. Measurements of Temperature and Electron Density in Mixed Gas ICPs

The second part of this work includes a study of the excitation and ionization processes in mixed gas plasmas. The goal of this study is to optimize the plasma discharge for spectrochemical analysis from a fundamental point of view. Such a study is capable of rationalizing the experimental data available about analytical plasmas.

Electron density and plasma temperature are two of the major physical parameters that govern the excitation and ionization processes in the ICP (86,87,88). The values of plasma temperature available in the literature vary as much as 2500 K (122) depending on the plasma operating parameters used.

##### 1. Temperatures

For a source which is in local thermal equilibrium (LTE), all temperatures measured have equal values. Studies of the Ar-ICP source indicate that complete thermal equilibrium, where every temperature is the same, does not





prevail in the ICP. As a consequence of the non-local thermal equilibrium (non-LTE) state of the plasma, no single temperature may be defined for the plasma discharge. The non-LTE state of the plasma discharge leads to the possibility of several different kinds of temperatures, namely :

- (1) excitation temperature ( $T_{\text{exc}}$ ), which is a measure of the energy distribution among the various particles of a discharge and of energy distribution within the various energy levels of individual particles. This temperature is defined by the Boltzmann distribution (91).
- (2) ionization temperature ( $T_{\text{ion}}$ ), the distribution of atoms and ionization products in the discharge described by the Saha-Eggert relation which is a function of ionization temperature (92).
- (3) radiation temperature ( $T_{\text{rad}}$ ), the radiative field that provides a radiation density which depends only upon the temperature defined by Planck function.
- (4) rotational-vibrational temperature ( $T_{\text{rot}}$ ), which is a measure of energy distribution among the populations of excited rotational or vibrational states of molecules. This temperature is similarly defined as the excitation temperature. Due to the weak energy



needed to obtain these spectra, the rotational temperature is considered to be close to the gas kinetic temperature (87), i.e., the macroscopic temperature of the plasma.

- (5) electron temperature ( $T_e$ ), which is the temperature of the free electrons and which is governed by Maxwell equation.

For a source which is in LTE, all temperatures measured have equal values, i.e.,

$$T_{\text{exc}} = T_{\text{ion}} = T_{\text{rad}} = T_{\text{rot}} = T_e \quad (4)$$

However, the ICP used for analytical spectroscopy is generally considered not to be in LTE (79,88,93-97). The results of Kornblum and de Galan (88) obtained for an Ar-ICP operating at 50 MHz indicated that:

$$T_{\text{rot}} < T_{\text{exc}}(X) < T_{\text{exc}}(X^+) < T_{\text{ion}} \quad (5)$$

Most workers in the field of plasma spectroscopy recognize the use of spatial distribution of temperature and electron density to study the excitation and ionization mechanisms in the plasma discharge. In this laboratory, spatially resolved excitation temperature measurements have been utilized to



explain the characteristic emission patterns of some neutral atom and ion lines (93,120). The plasma "temperatures" reported in the literature show a wide range of values because of non-LTE condition. However, the major criterion for all temperature measurements in the plasma source is that the plasma must be "assumed" to be in LTE. In addition, the transition probabilities available in the literature for the "temperature" measurements show a range of values. Depending on the set and operating conditions used, calculated "temperature" can vary as much as 2500 K (122). While much interest has been focused on source "temperature", comparatively little fundamental work has been carried out on the distribution of electron density in the plasma discharge. For these reasons, no attempt has been made to measure the plasma temperatures in this work. Instead, this work will focus primarily on the distribution of electron density in the mixed gas ICPs in order to unveil the excitation and ionization mechanisms in the mixed gas plasmas.

## 2. Electron Density

The second important physical parameter that governs the excitation and ionization processes in the ICP is electron density. At a specific region in the discharge





there are several different types of temperatures because of non-LTE conditions, but there is only one electron density. Unfortunately, there is no simple way to calculate electron density in the plasma discharge but it can be measured in several ways. The electron density may be derived from the absolute continuum intensity (98):

$$I_c = 8.058 \times 10^{-31} N_e^2 T_e^{-\frac{1}{2}} \quad (6)$$

where:

$I_c$  = the absolute continuum intensity  
( $\text{erg s}^{-1} \text{ cm}^{-3} \text{ sr}^{-1} \mu\text{m}^{-1}$ ),

$N_e$  = the electron density in  $\text{cm}^{-3}$ , and

$T_e$  = the electron temperature in K.

Using the continuum method, Kornblum et al. (98) reported values of electron density for an atmospheric pressure Ar-ICP between  $5 \times 10^{14}$  and  $2 \times 10^{15} \text{ cm}^{-3}$ . The basic assumption of this continuum method is that the plasma be in an LTE state where  $T_e = T_{\text{ion}}$ ; the value of  $T_{\text{ion}}$  was derived from Saha-Eggert equation described below.

The most convenient method for the determination of electron density is to measure the ion-to-atom emission intensity ratio for some probe analyte species using the Saha-Eggert equation:



$$N_e = 4.83 \times 10^{15} \frac{I_i (gA)_i v_i}{I_a (gA)_a v_a} T^{3/2} e^{-(E_i - E_a - E_i^0 + \Delta E)} \quad (7)$$

where:

$N_e$  = electron density in  $\text{cm}^{-3}$ ,

$I_i, I_a$  = intensity of ion and atom emission,

$(gA)_i, (gA)_a$  = product of degeneracy and transition probability for upper states of ion and atom,

$v_i, v_a$  = frequency of spectral line emitted by ion and atom,

$E_i, E_a$  = energy of upper state of ionic and neutral atom transitions,

$E_i^0$  = ionization energy of the neutral atom,

$\Delta E$  = plasma ionization correction, and

$T$  = ionization temperature, K.

When the Saha-Eggert equation is used to calculate  $N_e$ ,  $T_{\text{ion}}$  is assumed to be  $T_{\text{exc}}$ , while  $T_{\text{exc}}$  is derived from argon lines. Results obtained by Mermet (93), Boumans et al. (99), and Kalnicky et al. (94) using Saha-Eggert equation were  $2 \times 10^{13}$ ,  $2 \times 10^{14}$  and  $10^{15} \text{cm}^{-3}$  respectively. The values of  $N_e$



obtained by this method show a range of values due to the differences in the "assumed"  $T_{ion}$  as well as the uncertainty in the ratio of atom-ion line intensities. Although this method fits the majority of analytical spectrochemical conditions very well, it has the serious drawback of being indirect; it requires not only the known inaccurate transition probabilities but also the computation of electron density from the Saha-Eggert equation. Since LTE does not prevail in the plasma source, the major drawback of this line ratio method is the requirement that the plasma be in LTE.

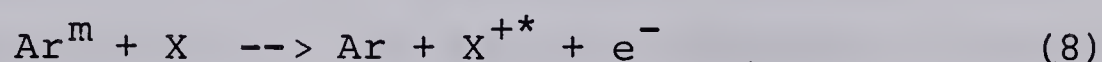
A more accurate method of electron density measurement is that of measuring the Stark broadening of spectral lines emitted by argon or hydrogen. This technique is largely independent of the temperature and any assumptions about the existence of LTE conditions since the lines are broadened electrostatically. Theory and practical aspects of this technique will be discussed in Chapter VII. Using this technique for the argon lines, Mermet (93) found that axial values of electron density decreased from  $1.1 \times 10^{16}$  to  $3 \times 10^{15} \text{ cm}^{-3}$  with increasing observation height (10 to 20 mm). Other values derived from the  $H_{\beta}$  line vary from  $3 \times 10^{15}$  to  $2.7 \times 10^{16} \text{ cm}^{-3}$  (13,100).





## E. Excitation and Ionization Mechanisms in Mixed Gas ICPs

Several mechanisms have been proposed by different authors to explain the observed emission intensities in the ICP source. Boumans and de Boer (79) published an in-depth study into the possible nonthermal mechanism in the plasma discharge involving argon metastable interactions. Their work is based on the Penning ionization mechanism proposed by Mermet (101).



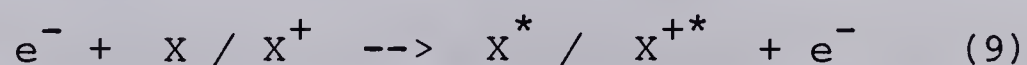
This reaction is possible when the combined energies of excitation and ionization of the analyte, X, is less than the excitation energy of the argon metastable. Metastable states are excited states which are quantum mechanically forbidden from radiative decay. In their hypothesis, the metastable levels were considered to be easily ionizable with an ionization potential of only 4.21 eV. Since transitions between the excited metastable states and the ground state are forbidden, the argon metastables have considerably longer lifetimes than the radiative decay. Because of this long lifetime, these metastable states would act as a very effective energy buffer for the analyte



species and thus influence the excitation characteristics of the ICP. In addition, the metastable states are about 11.5 eV above the ground state, therefore they are capable of ionizing and exciting a large fraction of analyte introduced into the plasma.

Although the lifetimes of argon metastables in vacuum (low pressure) are greater than 1.3 s (102) their lifetime in the atmospheric plasma is considerably smaller due to high electron density and the frequency of collisions in the source . Therefore, a high electron density will considerably reduce the importance of analyte ionization via a Penning process as the dominant ionization process (103). Most recently, Alder et al. have proposed that analyte excitation and ionization in the ICP are primarily dominated by electron impact (96). In fact, many reactions may occur by electron collisions i.e.

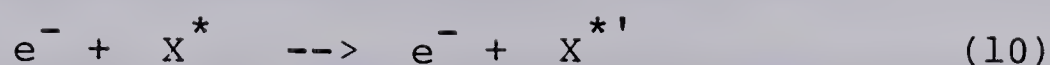
(1) excitation from the ground state



where  $X^{*}$  and  $X^{+*}$  are the excited states of atom and ion species,

(2) excitation from another excited state





(3) by superelastic collisions, and ionization to  $X^{+}$  and  $X^{2+}$ .

It is unlikely that any of these proposed mechanisms dominates the excitation and ionization mechanisms in the ICP. Among them, the energy transfer from excited electrons to the analyte seems to provide a reasonable prediction of the excitation and ionization mechanisms in the plasma source, but the role of excited argon metastables or other excited species cannot be neglected. In addition, several of the mechanisms may be acting simultaneously to produce the excited or ionized states.

A study of spatially resolved analyte emission and electron density will certainly provide an important set of data to distinguish which of these mechanisms can be considered the most probable excitation and ionization mechanisms in analytical ICP spectroscopy. The correlation study will then be used to provide a rational explanation on the nature of ion line advantages in the mixed gas ICPs. In addition, certain qualitative observations will also be employed to assess the role of electrons in the ionization and excitation mechanisms in the mixed gas plasmas.





Although the photomultiplier tube (PMT) is the most widely used detector for spectrochemical measurements in the uv-visible spectral regions, the 1024 element photodiode array detection system is used throughout this study because it is capable of simultaneously measuring over 50 nm of continuous spectral information anywhere from 200 to 1000 nm. The tedious process of measuring the hydrogen line profile and accurately extracting line intensity by a conventional PMT based system is significantly facilitated using the 1024 element photodiode array system (104).

The acquisition of detailed spatial profiles with a photodiode array system has been successfully accomplished in several studies involving measurement of emission intensity information from the Ar-ICP (105, 106-108). This approach has been used to acquire all the horizontal spatial data presented in this work. The measurement systems will be described in the following chapter.

This thesis is divided into two parts: the first deals with the investigation and evaluation of the spectral characteristics and analytical performance of the mixed gas ICPs; the second part deals with the electron density measurements in the mixed gas ICPs by means of hydrogen line broadening. Included in the second part is the correlation of the analyte emission intensity with the electron density in mixed gas plasma discharges and a summary of the



experimental evidence for the excitation and ionization processes of analytes with energetic electrons.

The results of such a study are important from the analytical point of view not only from the discussions presented above but also because of several potential advantages offered by the mixed gas plasmas, namely

- (a) lower operating cost,
  - (b) improvement in signal-to-noise ratios,
  - (c) improvement in signal-to-background ratios,
  - (d) achievement of different analytical capabilities,
- and (e) action as a possible probe to study the excitation and ionization processes in the plasma discharge.



## CHAPTER II

### EXPERIMENTAL

#### A. ICP Instrumentation

##### 1. ICP Source

The ICP system used for generating and sustaining the plasma discharge was a model HFP-2500D 2.5 Kw rf generator (Plasma Therm Inc. Kreston, N.J.). The system also included a model ADC5-3 automatic power control, and a model PT-2500E automatic matching network. The specifications for this system are listed in Table II.1.

The rf generator is of a crystal controlled type operating at a frequency of 27.12 MHz. This rf generator allows power output be varied from 0 to 2.75 Kw. Power from the rf generator is coupled via an automatic matching and tuning network to the ICP source. The tuning network allows efficient power transfer to the plasma by adjusting the matching network to a proper impedance in order to establish a stable plasma discharge. The three turn load coil (induction coil) surrounds the top of the plasma torch and serves to couple rf power to the plasma source (Figure 2). The load coil is constructed from a 8.5 mm copper tubing with 1 mm spacing between turns. Water is continuously fed





TABLE II.1  
ICP SYSTEM SPECIFICATIONS

Component	Specification
r.f. generator frequency	27.12 MHz (crystal control)
Rated output power	2.75 Kw
Envelope ripple	less than 5 %
Generator (output impedance)	50 $\Omega$
Matching network (input impedance)	50 $\Omega$
Matching network (output Impedance)	wide range
Load coil	3 turn



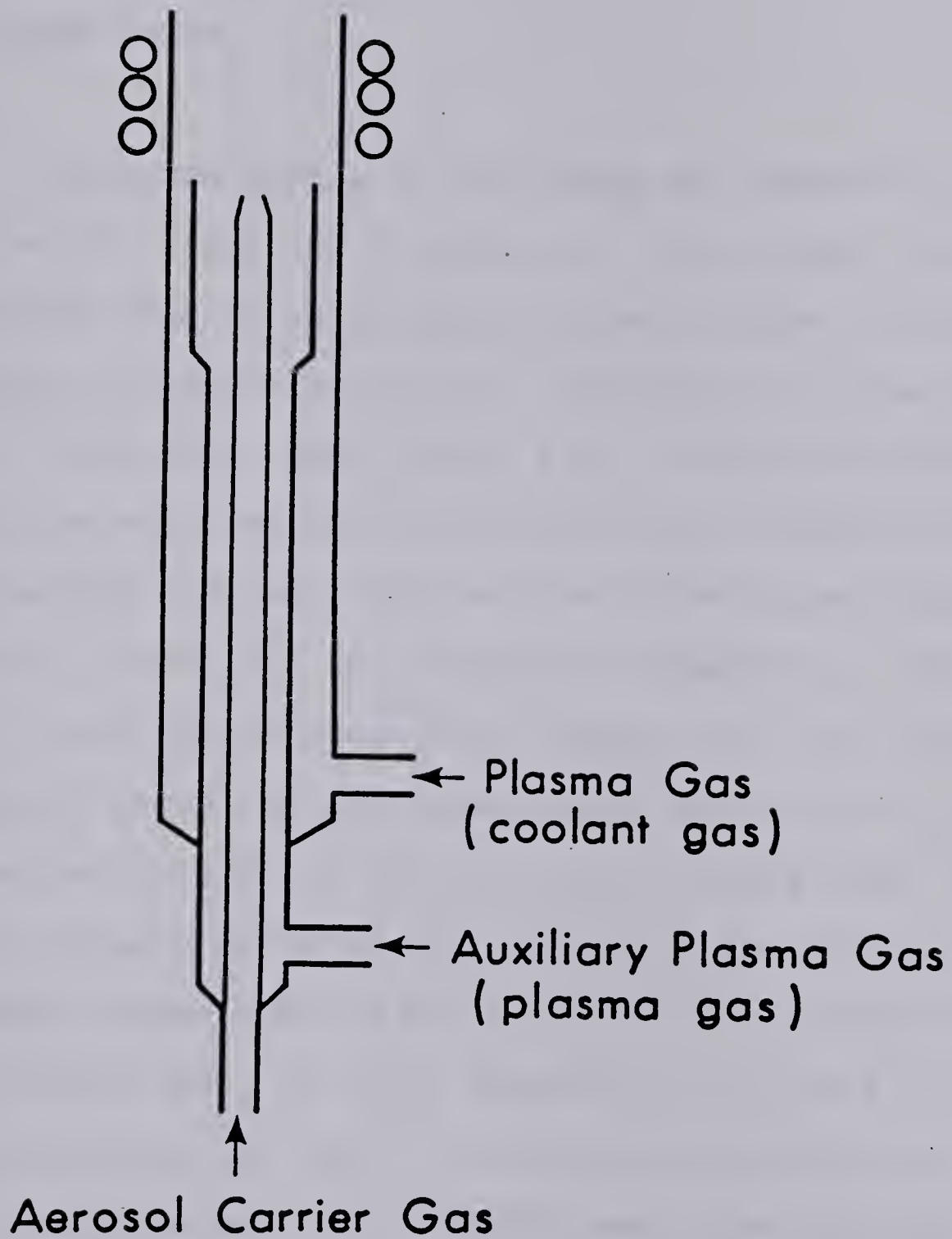


Figure 2. ICP torch (nomenclature).



through the copper tubing in order to keep it cool during the experiment.

## 2. Plasma Torch

The basic design of the torch was similar to that suggested by Fassel and Kniseley (2). The plasma torch was constructed from three concentric quartz tubes. A diagram of the torch configuration and its dimensions is given in Figure 3. The outer tube, 18 mm i.d., is the coolant or plasma tube which serves to introduce the coolant or the plasma supporting gas into the plasma discharge region. Ordinarily, argon gas is introduced tangentially into the base of the outer coolant tube. However, in this study mixtures of argon and non-argon gases ( $\text{Ar-N}_2$ ,  $\text{Ar-O}_2$ ,  $\text{Ar-Air}$  or  $\text{Ar-He}$ ) were injected into the base of this tube. The coolant gas also prevents the melting of the plasma torch. The middle quartz tube is tulip shaped and is known as the auxiliary gas tube. It has a dimension of 12 mm i.d., and is used to direct a low flow of argon gas at the base of the plasma discharge once it is established. The auxiliary gas, introduced tangentially into the base of the middle tube, serves to lift the plasma discharge slightly and prevent the inner tube from melting. The inner or aerosol tube is 3 mm i.d., and its exit is constricted to 1.5 mm i.d. This tube





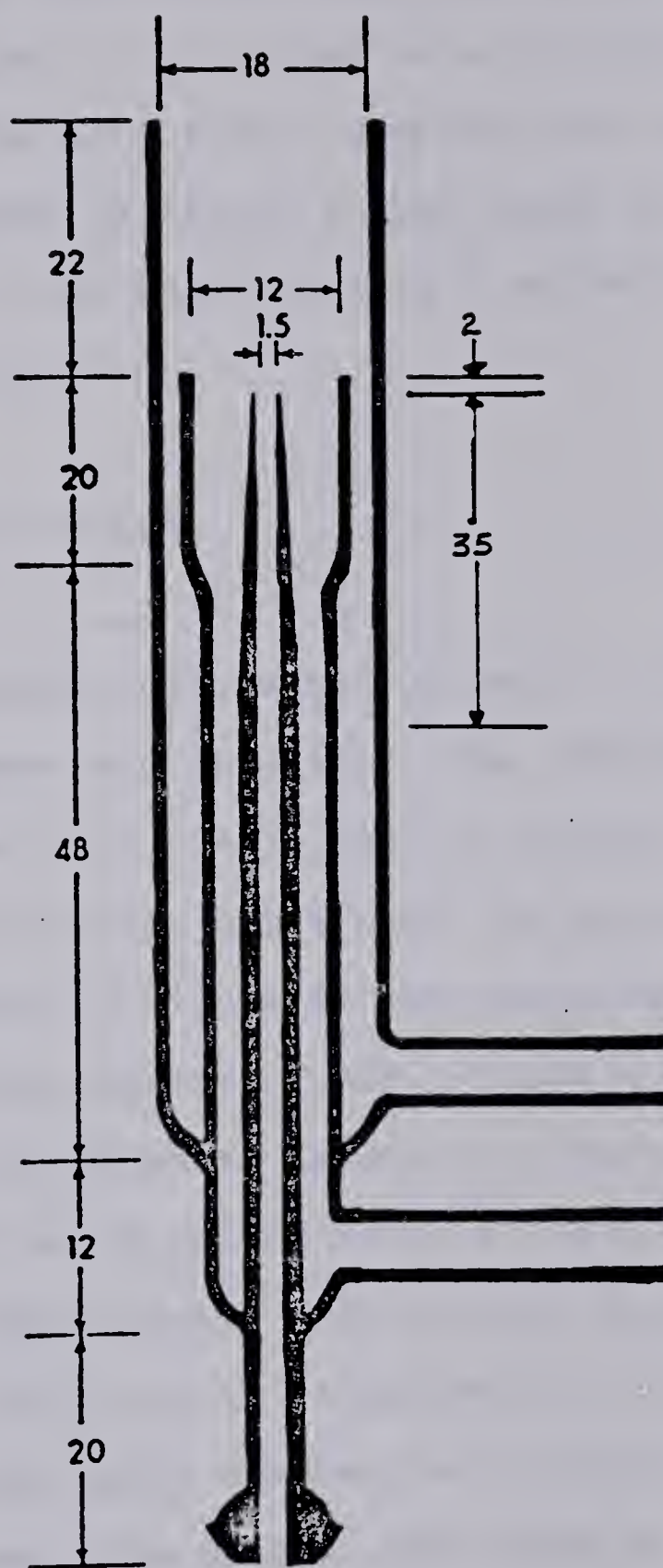


Fig. 3. ICP torch (dimensions in mm).



is used to feed the analyte aerosol into the center of the plasma discharge. It is joined to a 5/12 ball joint at the torch base. This ball joint, coupled with the aerosol spray chamber, is shown in Figure 4. The torch is positioned such that the tip of the inner tube is 2 mm below the bottom of the induction coil.

### 3. Nebulizing System

The nebulizing system consists of two major parts, the spray chamber and nebulizer. The nebulizer converts the sample solution into a fine mist or aerosol. It is inserted into a Teflon carrying block which is attached to a spray chamber as shown in Figure 4. The nebulizer used in this study was of the pneumatic type. It was a model TR-30-A1 supplied by J.E. Meinhard Associates, Santa Ana, California. The nebulizer has an uptake rate of 0.8 ml/min.

The spray chamber used in this study was of the Scott design (109) and is illustrated in Figure 4. The main function of this spray chamber is to allow only the smaller droplets to reach the plasma. Less than 3-5 % of the nebulized sample solution actually reaches the plasma. The majority settles out in the spray chamber and goes down the drain.



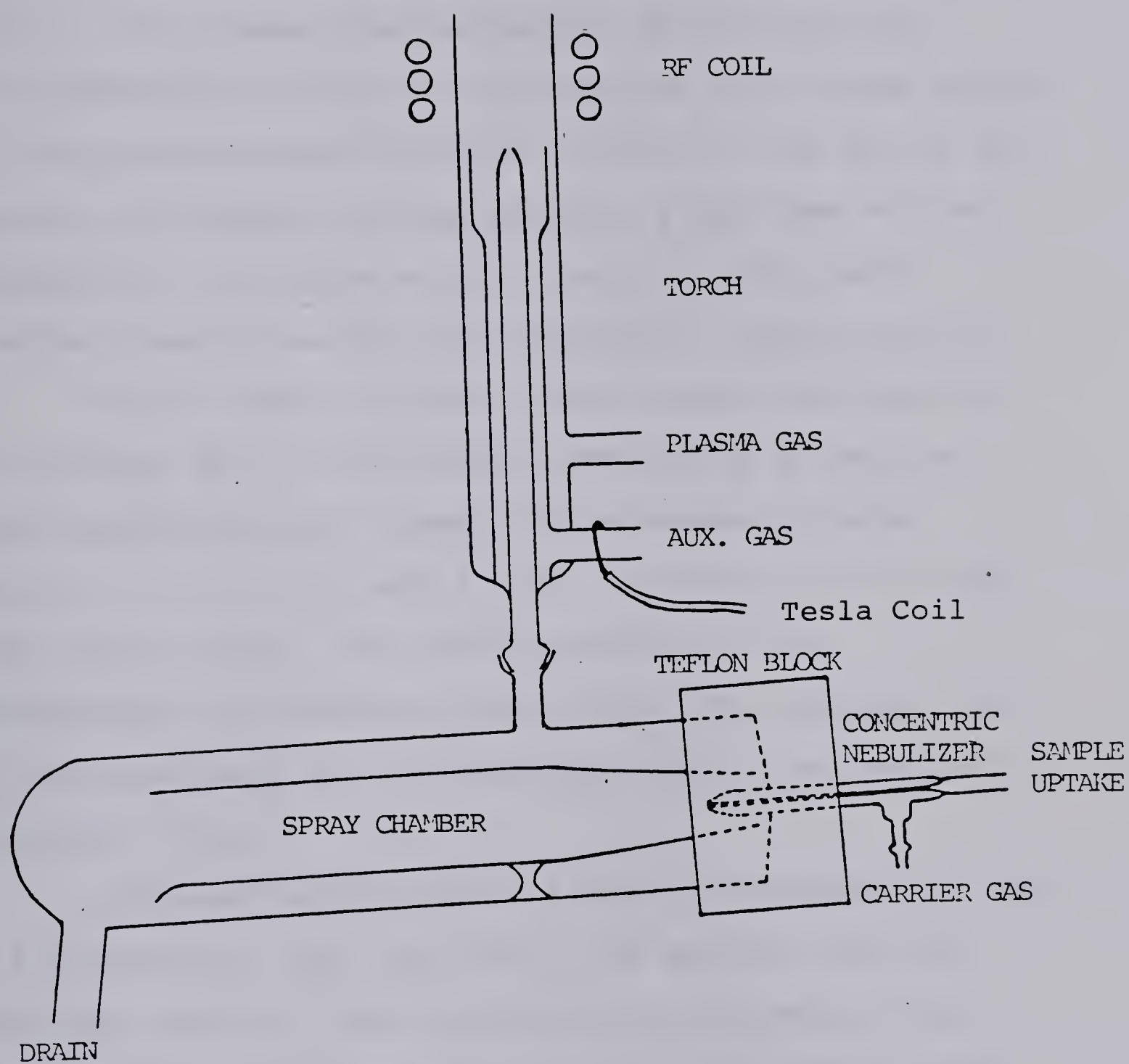


Fig. 4. ICP torch, spray chamber and nebulizer assembly.





## B. The Optical System

A block diagram of the optical system is provided in Figure 5. The plasma source, imaging optical lens and monochromator were mounted on an optical rail system similar to the system designed by Walter (110,111). The use of this optical rail system provided precise, stable and accurate alignment of the plasma source. The rail system also provided flexibility for the experimental configurations.

The 2:1 reduced image of the plasma was formed on the entrance slit of the monochromator by a 10 cm focal length spherical quartz lens. The measurement system employed in this study was a Heath (GCA/MacPherson EU-700) 0.35m monochromator. The specifications of this monochromator are listed in Table II.2. The detectors used in this experiment were 256 and 1024 element self-scanning photodiode arrays.

Alignment of the entire system was achieved by means of a helium-neon laser mounted on the optical rail bed. Since the spherical lens was mounted on the body of the monochromator, different horizontal slices of the plasma could be measured by raising and lowering the monochromator. The position above the load coil could be measured accurately using a precision dial gauge attached to the monochromator (Mitutoyo No. 3052, Japan).



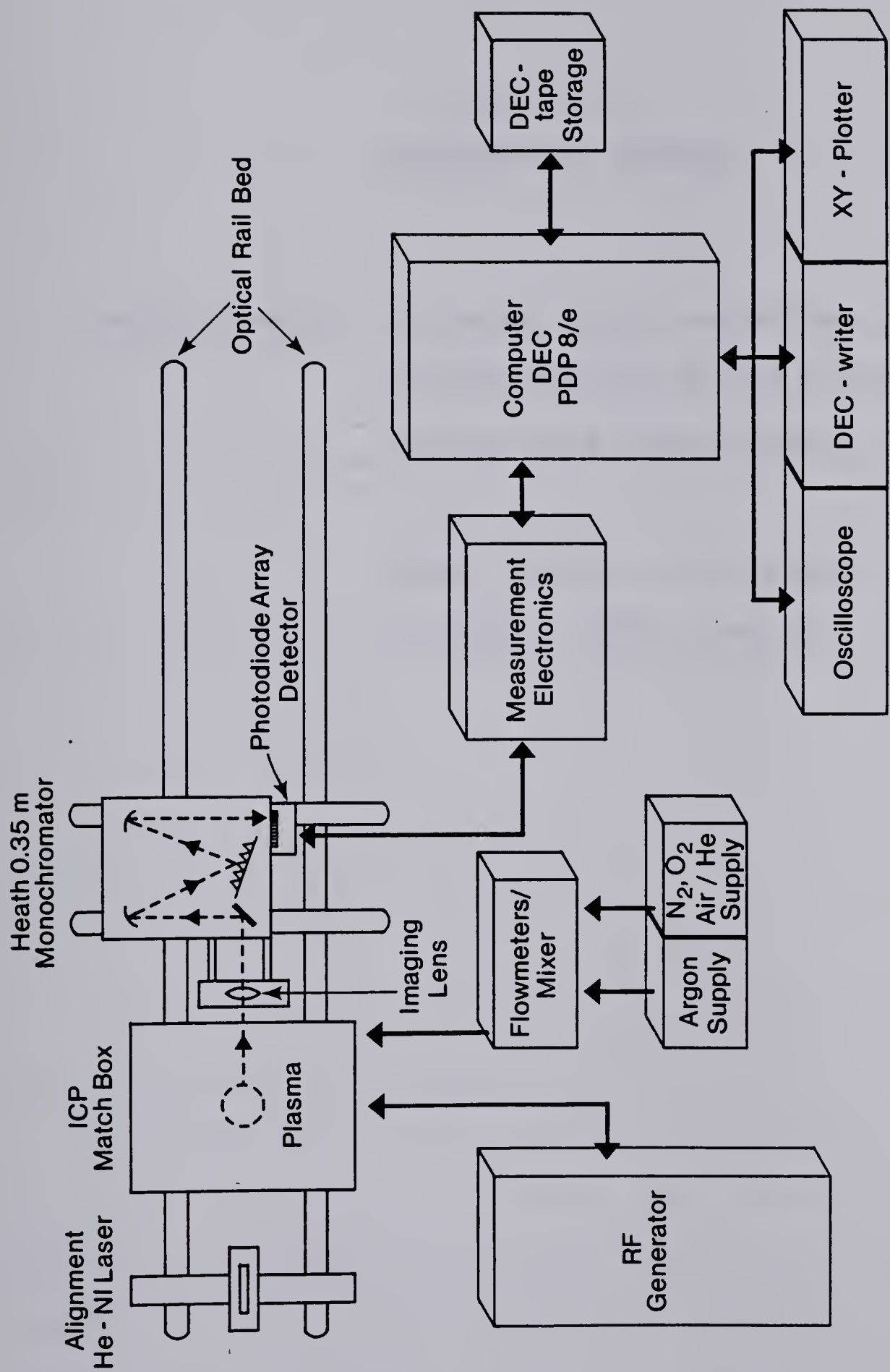


Figure 5. Block diagram of ICP instrumentation.



TABLE II.2  
MEASUREMENT SYSTEM

Monochromator : Scanning Heath monochromator  
(GSA/McPherson EU-700 series) with  
single pass Czerny-Turner mounting

Focal length = 0.35 meter

Grating = 1180 lines/mm





### C. Gas Mixing

Two Rotameters (Matheson, East Rutherford, N.J.) were used to mix argon with other gases ( $N_2$ ,  $O_2$ , Air or He) prior to introducing the coolant or nebulizing gases into the plasma discharge. Matheson Model 605 flowtubes were used to mix the plasma gases for the coolant stream. Matheson Model 603 flowtubes were used for the aerosol flow. The mixed gas plasmas were first initiated using pure argon, then crossed over to the appropriate mixed gas conditions. Further discussion of the experimental observations and running conditions of the mixed gas plasmas will appear in the following chapter.

### D. The Detection Systems

All studies were carried out using electronic image sensors (photodiode arrays). The self-scanning linear silicon photodiode arrays employed in this work were purchased from Reticon Corporation, 910 Benicia Ave., Sunnyvale, CA 94086. Two types of arrays were used for the evaluation of the mixed gas plasmas. The 1024 element photodiode array system was used for spectral characterization and evaluation of the analytical



performance of the mixed gas ICPs. The 256 element photodiode array system was used for spatial profile measurements.

# 1. Detection System for Spectral Characterization and Evaluation of Mixed Gas ICPs

The concept of spectrochemical measurements using a photodiode array has been described and implemented by Horlick and his co-workers (104,112-117). The Czerny-Turner type monochromator coupled to a photodiode array system is illustrated in Figure 6. Total length of this 1024 element photodiode array is 26.01 mm or 1.024" with a detector element height of 0.432 mm or 0.017".

The 0.35m Heath monochromator has dispersion of about 20 Å/mm. An array density of 39.4 diode/mm results in an angstrom/diode unit ratio of 0.5. Thus, the 1024 element photodiode array covers about 50 nm or 500 Å of continuous spectral information when coupled to this monochromator. This photodiode array spectrometer is capable of measuring spectral information anywhere from 200 to 1000 nm regions.



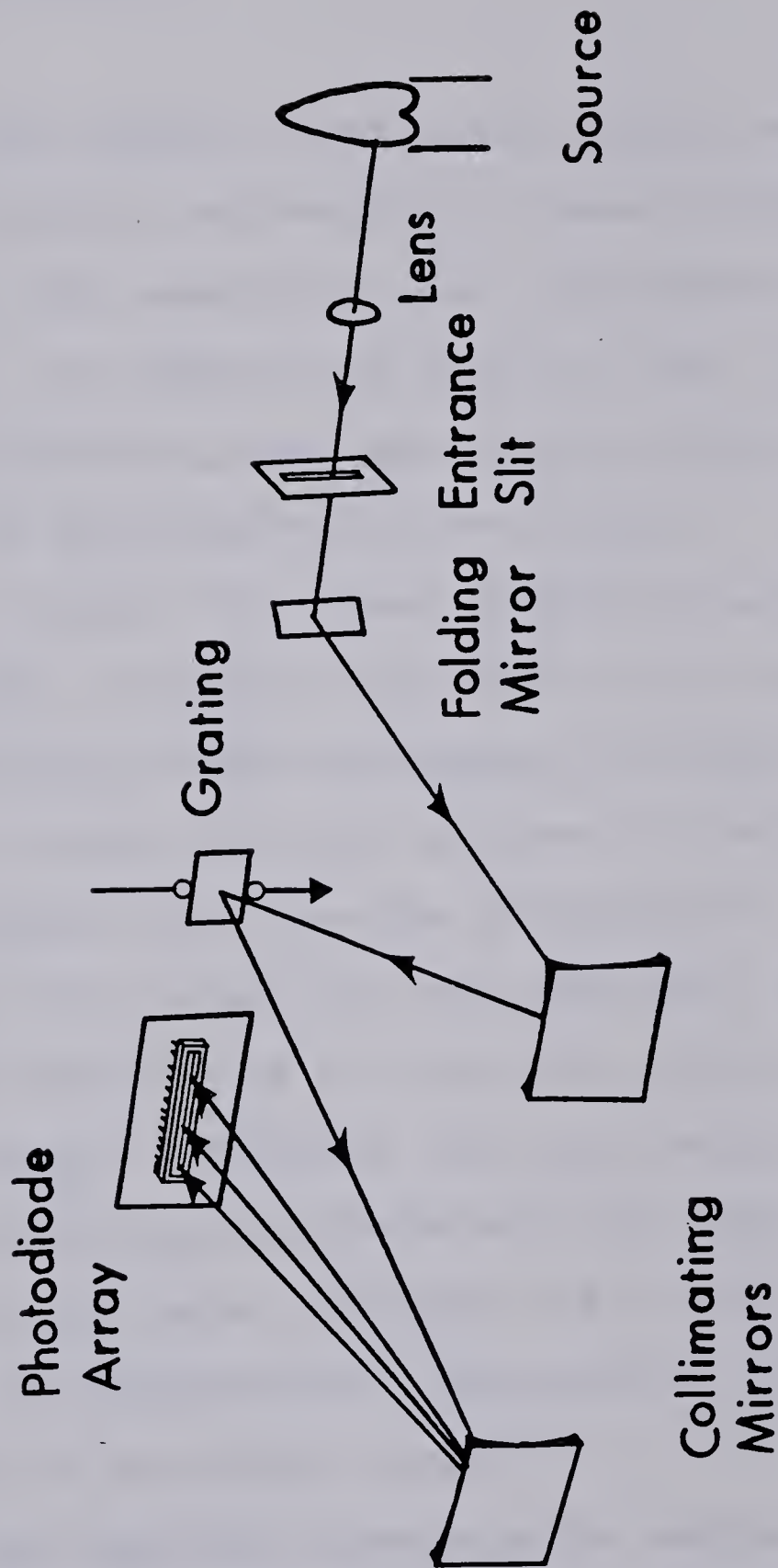


Figure 6. Schematic diagram of Czerny-Turner type monochromator with a photodiode array detector for spectral measurements.





## 2. Detection System for Spatial Profile Measurements

The concept of measuring spatial profiles of analyte emission using a self-scanning linear silicon photodiode array has been demonstrated and implemented by Franklin et al. (105), and Edmonds and Horlick (106). In this study, a spatial profiling array measurement system was set up similar to that reported by the latter.

A linear 256 element photodiode array (Reticon RL-256/128) is mounted vertically in the exit focal plane of a Czerny-Turner type monochromator as shown in Figure 7. The plasma is imaged onto the entrance slit which passes a slice of the plasma image into the monochromator. Thus, the vertical array, when read out, provides a measure of emission intensity as a function of height in the plasma at one particular wavelength. The total height of the plasma image measured by the photodiode array can be altered by adjusting the distance between the source, lens and entrance slit of the monochromator, according to the magnification formulae for bi-convex lenses.

The physical dimensions for each array are 25.4 micron by 25.4 micron. Thus, the 256 element photodiode array behaves like an exit slit of 25.4 micron width and 6.5 mm (0.256") high. In this study, the plasma was imaged onto



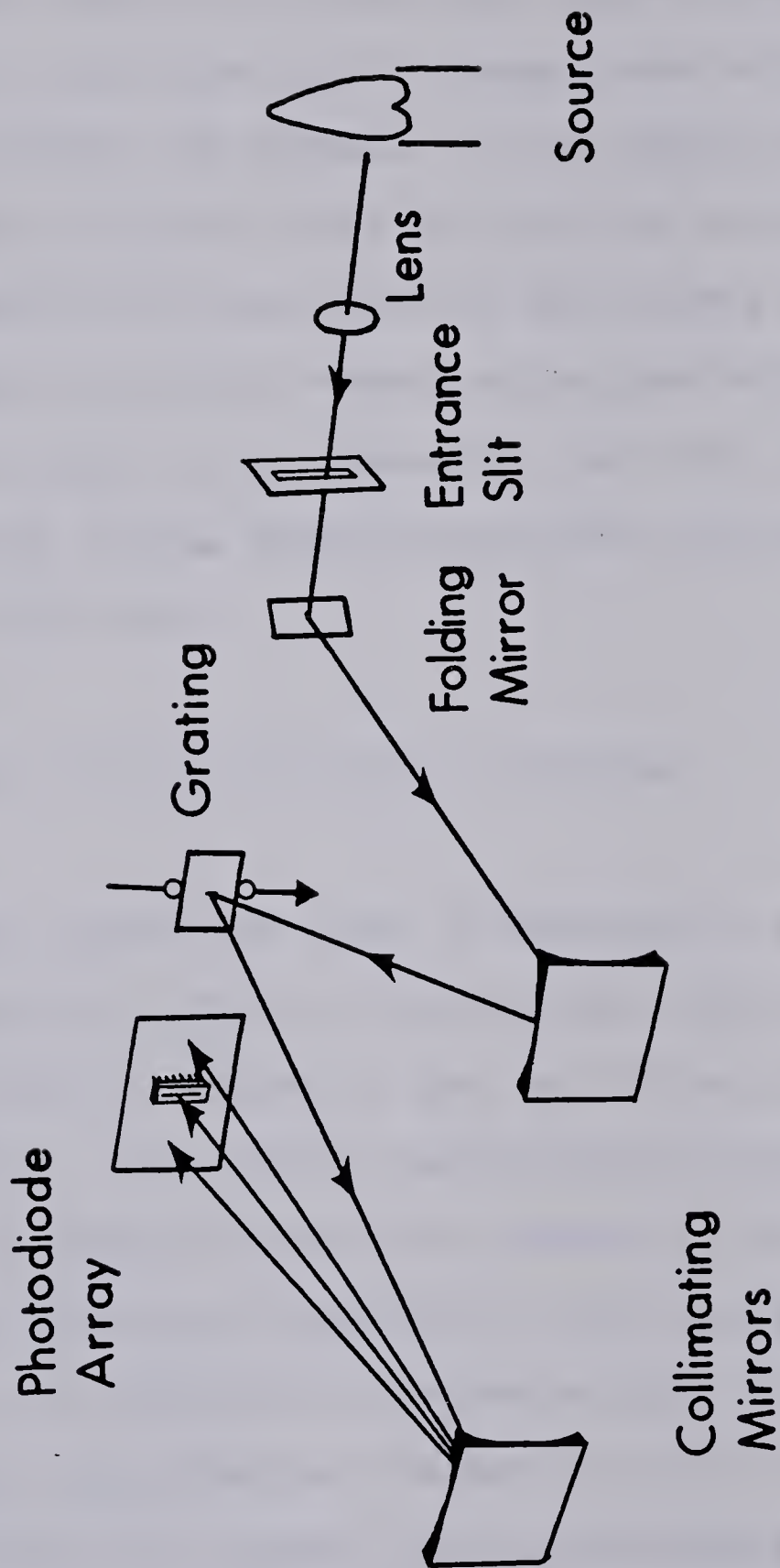


Figure 7. Schematic diagram of Czerny-Turner type monochromator with a photodiode array detector for spatial profile measurements.



the entrance slit of the monochromator using a spherical quartz lens. Since the plasma was imaged down in size by a factor of 3, the total plasma image observed by this array was about 20 mm. The geometry of our system was carefully aligned using a He-Ne laser so that the vertical slice was located exactly in the center of the plasma aerosol channel, and the spatial window viewed by the photodiode array was centered at about 10 mm above the load coil. Therefore, the total spatial window observed extended from about 0 to 20 mm above the load coil.

#### E. Control and Data Acquisition System

The photodiode array is mounted on a driver/amplifier printed circuit board (Reticon RC-408) which in turn is mounted in the exit focal plane of the monochromator. The circuit package also contains the necessary scanning circuit for readout of the array. The photodiode arrays are operated in the charge storage mode and hence are inherently integrating type detectors. First of all, the photodiode is charged up to its full reversed bias potential of 5 volts. This reverse bias charge stored on each diode is then discharged between scans by photon-generated charge carriers (light falling on the diode), as well as by thermally generated charge carrier





(dark current). Thus, the signal level necessary on the subsequent scan to re-establish reverse bias on the photodiode is a measure of the total sum of light intensity and dark current integrated over a time period. The integration time is controlled by the time between start pulses and ranges from 20 ms to about 20 s.

A block diagram of the computer-coupled photodiode array measurement system is illustrated in Figure 8. The start pulse signals the computer that the array has completed its integration. The clock controls the rate at which data is read from the array as well as digitization and storage of the array output signal. The clock rate used in this study was 50 KHz. The array is cooled by a Peltier cooler (approximately -15 to -20 C) in order to minimize the dark current. Nitrogen gas is used to purge the array to prevent frosting over the array.

The measurement system consists of a series of operational amplifiers which serve to amplify, filter and provide a voltage offset for the array signal. A schematic diagram of this circuit is shown in Figure 9.

The analog signal from the array is converted into a digitized signal using a high speed 12 bit analog-to-digital converter (Model 600-SE, ADAC Corporation, Woburn, Mass) interfaced to a PDP-8/e minicomputer and operated under software control. The system used to acquire data was a





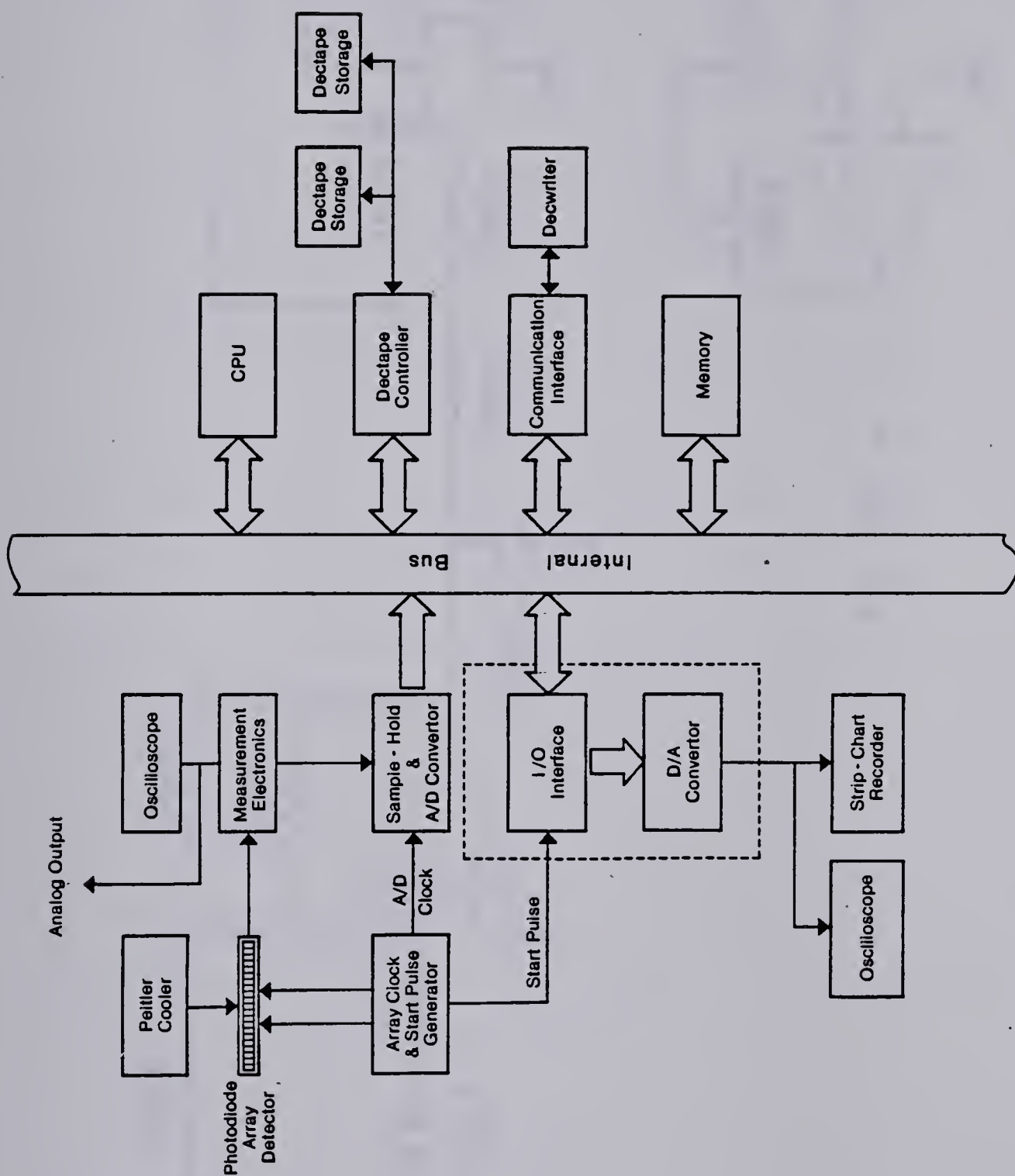


Figure 8. Block diagram of computer controlled photodiode array measurement system.



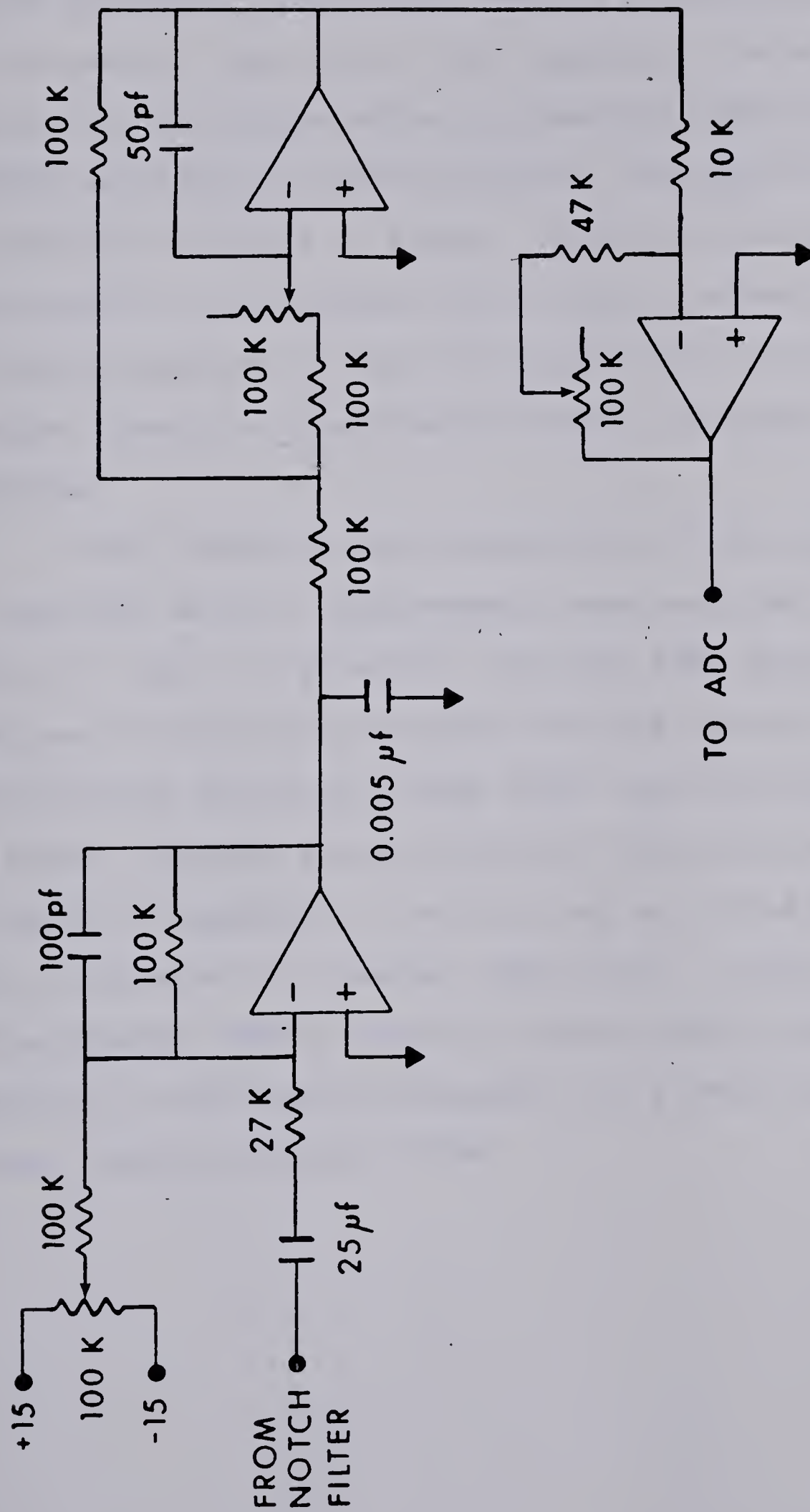


Fig. 9. Signal conditioning electronics for photodiode array.



Digital Equipment Corporation PDP-8/e minicomputer with 16K of core memory, and with an OS/8 operating system. The data acquisition and manipulation programs ran under combined FORTRAN and machine language control. Listings of these programs are provided in Blades' (118) and Carr's (119) dissertations. The acquired data could be stored on DEC-tape, displayed on the oscilloscope, plotted on an X-Y recorder (Hewlett-Packard Model 7045A), or output to a DECwriter.

Abel inversion and manipulation of the acquired data for electron density measurements were performed using an Apple /// (Apple Corporation, CA) with 128K RAM and 4K ROM memories. The operating systems for this computer are the Sophisticated Operating System (SOS) and UCSD-Pascal system. The Pascal language program used for half-width measurements is listed in Appendix A. The data may be stored on floppy disks, displayed on a monitor (NEC Corp.), output to a dot matrix printer (Epson MX-82) or letter quality printer (IBM Selectric II with Escon convertor), or plotted on a digital plotter (Hewlett-Packard 7470A)





## F. Preparation of Chemical Solutions

All solutions were prepared by dissolving the reagent grade salts or pure metals of individual elements in dilute nitric acid.



## CHAPTER III

### EXPERIMENTAL OBSERVATIONS OF MIXED GAS ICPs

#### A. Introduction

Most ICPs currently utilized as excitation sources in analytical atomic spectroscopy are based on argon, although some systems employing combinations of nitrogen (as coolant) and argon (as auxiliary gas and aerosol transport gas) have been used. Although mixed gas ICPs are desirable from an operating cost point of view, there have not been many investigations devoted to the evaluation of the mixed gas plasmas. The intent of this chapter is to illustrate and discuss the experimental observations of the low power mixed gas ICPs.

#### B. Experimental Procedures for Lighting a Mixed Gas ICP

The plasma was first lit under 100% argon environment using operating conditions similar to those for conventional Ar-ICPs (see Table III.1). With the Ar plasma sustained, nitrogen was then slowly introduced to the coolant gas flow of the Ar plasma. The auxiliary argon flow was increased slowly to 1.0 L/min and the argon in the



coolant gas flow was then decreased relatively to the added nitrogen in order to ensure a constant coolant gas flow. A Matheson rotameter-mixer described in Chapter 2 was used in the cross-over operations. Plasma fluctuation was observed during initial introduction of nitrogen into the Ar-ICP. This fluctuation is probably due to the change in impedance of the plasma. Since an automatic servo-driven matching network was attached to the load coil, the change in rf power coupled from the load coil was corrected automatically. Once a stable plasma was obtained, various percentages of nitrogen could be easily introduced to the N<sub>2</sub>-Ar mixed gas ICP. By following this simple procedure, the Ar-ICP can be converted into a 100% nitrogen cooled plasma over an interval of 20 s. Similar procedures were used for the O<sub>2</sub> - Ar, Air - Ar and He - Ar mixed gas ICPs. In the case of O<sub>2</sub> - Ar and He - Ar ICPs, no fluctuations were observed in the initiation step.

### C. Experimental Observations

The plasma volume was reduced considerably when nitrogen was introduced into the argon discharge. The shape changes for 0, 10 and 100% nitrogen cooled plasmas are best illustrated photographically and are shown in Figure 10. The plasma shape is dependent upon the amount of nitrogen



TABLE III.1

## TYPICAL OPERATING CONDITIONS FOR MIXED GAS ICPS

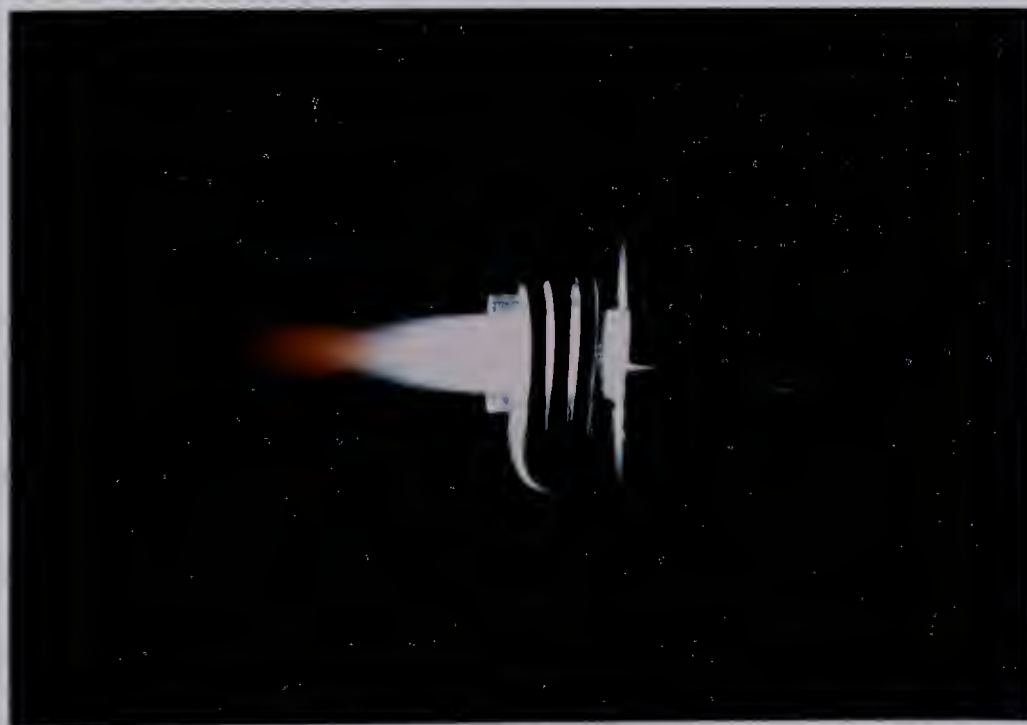
Component	Operating Condition
-----	
Generator	
Power (incident)	0.5 to 2.50 Kw 2.0 Kw (optimum)
Power (reflected)	less than 50 W
Frequency	27.12 MHz
Gas flow rate	
Coolant	15 to 0 L/min (Ar) 0 to 15 L/min (N <sub>2</sub> ) 0 to 15 L/min (O <sub>2</sub> ) 0 to 15 L/min (Air) 0 to 12 L/min (He)
Auxiliary	1.0 L/min (Ar)
Aerosol	0.8 to 1.5 L/min (Ar)
-----	





present in the coolant gas flow of the argon discharge. It is clearly illustrated in Figure 10 that the higher the amount of nitrogen present in the discharge, the smaller is the plasma volume. These observations have been reported elsewhere in the literature (68,74-76,80-84). The reasons for this volume reduction have been described in terms of the thermal pinch effect (62,68,70,126). Since argon and most gases have different thermal conductivities in the plasma, introducing nitrogen or any foreign gas into the Ar-ICPs will drastically alter the thermal characteristics of the plasma. In the environment of 7000 K, nitrogen is 32 times more conductive than argon (68,70). Nitrogen and oxygen are diatomic gases, therefore when they are introduced into the coolant flow of the Ar-ICP they absorb more energy for dissociation into their constituent elements. The purpose of the cooling gas is to prevent the melt down of the external quartz tube, therefore introducing nitrogen into the cooling stream provides an additional cooling effect. Subsequently, the outer surface of the mixed gas plasma becomes cooler and hence less conductive. The mixed gas plasma is then constricted to a smaller volume than that of the Ar-ICP as a consequence of the thermal pinch effect. A reduction of the central aerosol channel as nitrogen replaces argon in the coolant flow is also observed. This reduction, predicted by Fassel et al. (76),





(a)



(b)



(c)

Fig. 10. Photos of (a) Ar-ICP, (b) 10% N<sub>2</sub> cooled ICP, and (c) 100% N<sub>2</sub> cooled ICP, operated at 2.0 Kw power and 1.0 L/min aerosol flow rate.



may increase sample-plasma interaction and serve to reduce solute vaporization interference effects. These predictions will be confirmed in the following chapters.

In contrast to the observations described above, introduction of nitrogen into the aerosol flow of the conventional Ar-ICP increased the size of the central channel and decreased the plasma intensity. This observation further confirmed the validity of the assuming pinch effect.

The present study confirms previously reported observations that the diameter and length of a 100% nitrogen cooled ICPs increased with increasing power (68,74-76,80-84). It was also noted that the plasma intensity increased with increasing power. An inverted 'cone' shaped plasma similar to the one described by Montaser et al. (76) occurred when the coolant flow rate of the 100% nitrogen cooled Ar-ICP increased to 25 L/min. However, when the coolant flow rate was reduced to 5 L/min, an elongated shaped plasma developed.

The plasma volume was also decreased when foreign gases such as air, oxygen or helium were introduced into the coolant stream of the Ar-ICP. The amount of volume reduction depended upon the type and the percentage of foreign gas present in the system. Under similar operating conditions, the volume and the length of the oxygen and air cooled plasmas were observed to be smaller than those of the argon







discharge, but larger than those of the 100% nitrogen cooled plasma. In the case of the helium cooled discharge, the relative size appeared to be just a bit smaller than the argon discharge but the relative plasma intensity decreased significantly. The maximum amount of helium that could be introduced into the system without extinguishing the plasma discharge was determined to be about 70%.

#### D. Conclusions

Several conclusions can be drawn from these initial observations. Obviously, there is no doubt that a low power plasma can be supported by gases such as nitrogen, oxygen, air or helium, and in fact the mixed gas plasmas may be more stable than 100% Ar-ICP. However, these observations do not imply that mixed gas plasmas exhibit better or different analytical performances than the Ar-ICPs.

The remaining objective of this work is to characterize and evaluate the mixed gas plasmas in terms of analytical precision, accuracy, sensitivity, stability, freedom from interference effects, and performance-to-cost ratio. Such characterizations and evaluations have been carried out and will be discussed in the following chapters.



## CHAPTER IV

### VERTICAL SPATIAL PROFILES OF ANALYTE EMISSION FROM A N<sub>2</sub>-AR MIXED GAS PLASMA

#### A. Introduction

Most researchers in this field agree that a major key to a more complete understanding of the ICP is a detailed knowledge of the emission characteristics of an analyte in the plasma as a function of spatial position (28,30,83,106-108,118,120-123). Detailed spatial profiles of analyte emission in an Ar-ICP source have been reported in various studies (106,118,120-123).

Although interest is growing rapidly in the area of mixed gas plasmas, no one has yet published detailed spatial characteristics of analyte emission in mixed gas ICPs. The 256 element photodiode array measurement system previously developed in our laboratory has the capability of measuring analyte intensities as a function of height in the plasma (82-84,106,120-122). This is accomplished by mounting the photodiode array vertically in the exit focal plane of the monochromator (Figure 7). This system has proven to be very effective for measuring spatial profiles of emitting species in the ICP (106,118,120-122). With this detection system,



spatial profiles of the neutral atom and ion lines of a number of elements (Table IV.1) were evaluated as a function of several plasma parameters such as power, aerosol flow rate and percentage of nitrogen present in the coolant stream of the Ar-ICP.

In addition to these spatial profile measurements, an experiment was carried out in which various percentages of nitrogen were introduced into the aerosol flow of the argon or 100% nitrogen cooled plasma, and the spatial profiles of calcium ion line were measured.

## B. Experimental

The Plasma-Therm ICP HFP-2500D 2.5 Kw rf generator, 256 element profiling photodiode array measurement system and electrical measurement system were identical to those described previously in Chapter II. The signal from the photodiode array was amplified and acquired by a PDP-8/e minicomputer. The array was cooled and the signals were signal averaged over 10 scans. All profiles reported in this chapter were background subtracted in order to eliminate plasma spectral background, dark current and array fixed pattern background. Array integration times for each scan varied from 0.5 to 10 seconds depending on the intensity of the emission line being observed. For comparison purposes,





spatial profiles for a given set of operating conditions were measured using similar integration times.

For all profile measurements, the plasma was imaged onto the entrance slit of the monochromator using a spherical quartz lens (focal length = 10 cm, diameter = 2 in). A 3:1 reduced and inverted image of the plasma was focused onto the entrance slit of 100 micron width. The entrance slit passed a thin slice of the plasma image into the monochromator and since the monochromator was stigmatic, the vertically mounted array in the exit focal plane provided a measurement of emission intensity as a function of height in the plasma. The measurement system was carefully aligned using He-Ne laser so that the vertical slice was exactly chosen from the middle of the plasma aerosol channel.

Since each diode has a width of 25.4 microns, the overall length of the 256 element photodiode array is 6.50 mm. The total spatial viewing region in the plasma observed by the vertical array with the 3:1 imaging is 20 mm. Since the array was centered at 10 mm above the induction coil, this measurement system provided spatial information of the emitting species from 0 to 20 mm above the load coil.





### C. Effect of nitrogen on the vertical profiles

Most studies reported in the literature have indicated that a 100% nitrogen cooled plasma is inferior to the conventional Ar-ICP in terms of analytical capabilities when viewed at 10 to 18 mm above the induction coil (74,76). This conclusion was probably reached by comparing analytical performances of various mixed gas plasmas with the plasma observed at the best viewing zone for the pure argon discharge, i.e. at 10-18 mm above the load coil. It is obvious from the observations reported in Chapter III that N<sub>2</sub>-Ar mixed gas plasmas have smaller plasma volumes than those of the conventional Ar-ICP. In the case of the mixed gas plasmas, one would expect that the position of the maximum analyte emission would occur lower in the plasma discharge. But no one has yet reported the spatial shift of the maximum emission position due to the presence of nitrogen in the coolant stream. The main problem, from the author's point of view, has been associated with the lack of complete understanding and appreciation for the power of the spatially resolved data.

On the basis of the above discussion, it can be predicted that the analyte intensity maximum will show a spatial variation with various percentages of nitrogen present in the coolant stream. The validity of this



prediction is confirmed by the spatial profiles provided in Figures 11-15.

The effect of various percentages of nitrogen in the coolant flow on the emission profiles of several elements are shown in Figures 11-15. These profiles were taken for 0, 10, 20, 50 and 100% nitrogen cooled plasmas. All of the data were collected at a constant aerosol flow (1.0 L/min Ar), constant rf power (2.0 Kw) and a constant total volume of the coolant flow (15 L/min). The letters on each figure correspond to: (a) 0%, (b) 10%, (c) 20%, (d) 50%, and (e) 100% nitrogen cooled ICPs. The elements studied are listed in Table IV.1. The ionization potentials and the excitation potentials listed in Table IV.1 were taken from Refs. 124 and 125. For the sake of comparison the spatial profiles with various percentages of nitrogen in the coolant flow have been included for both the neutral atom and ion lines.

It can be seen from these figures that spatial profiles of the studied elements shift towards the induction coil as the percentage of nitrogen introduced to the coolant increases from 0 to 100%. When compared to the conventional argon plasma which has an intensity maximum at 18 mm above the load coil, the position of the profile maximum for 100% nitrogen cooled plasma is found to be at 2 to 4 mm above the load coil. This observation is quite consistent for all elements regardless of whether the line being observed is a



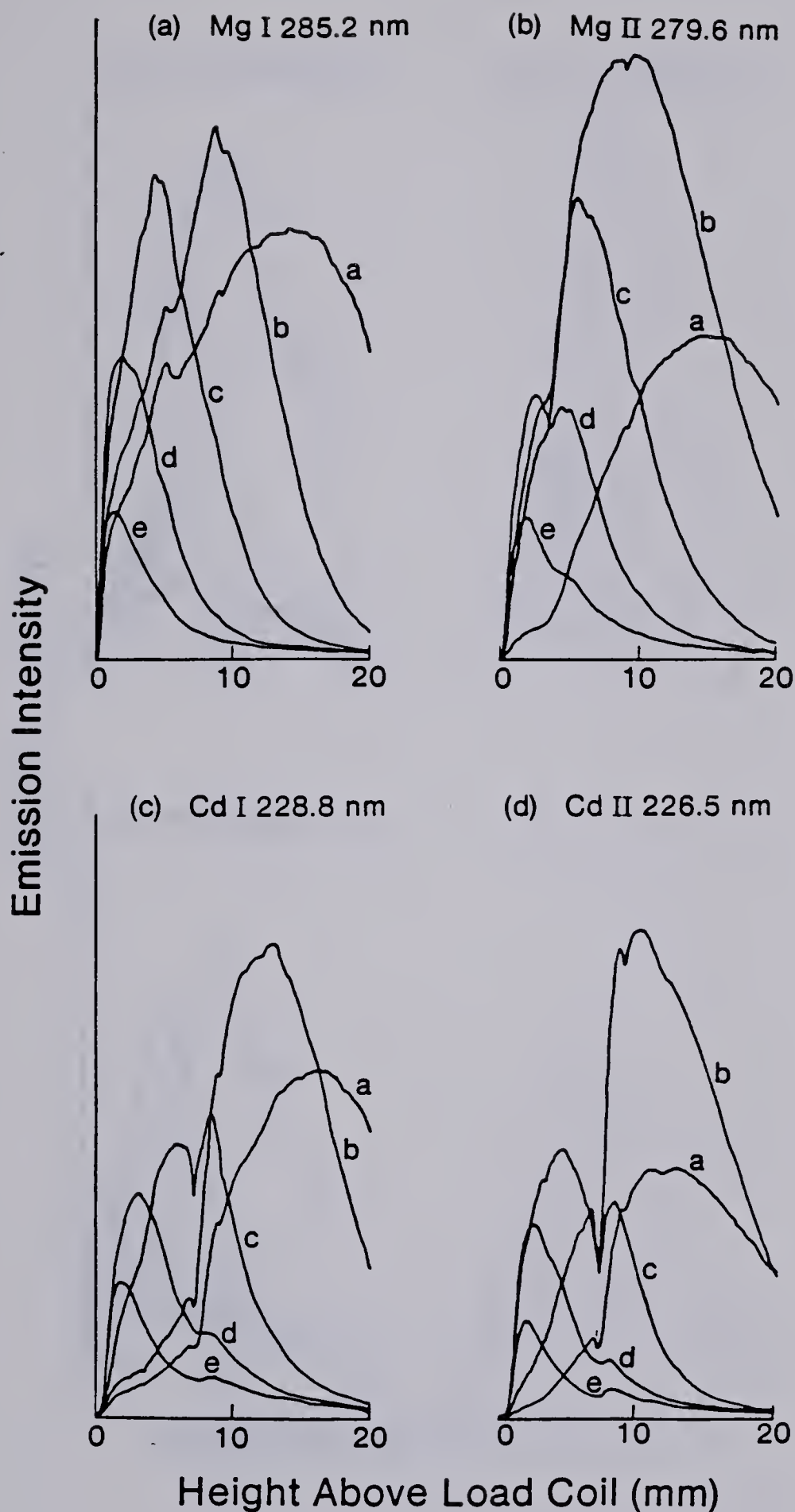


Fig. 11. Spatial profiles of (a) MgI 285.2nm, (b) MgII 279.6nm, (c) CdI 228.8nm, and (d) CdII 226.5nm as a function of  $N_2$ -Ar mixed gas composition. (curve a, 0%; curve b, 10%; curve c, 20%, curve d, 50%; and curve e, 100% nitrogen cooled ICP).







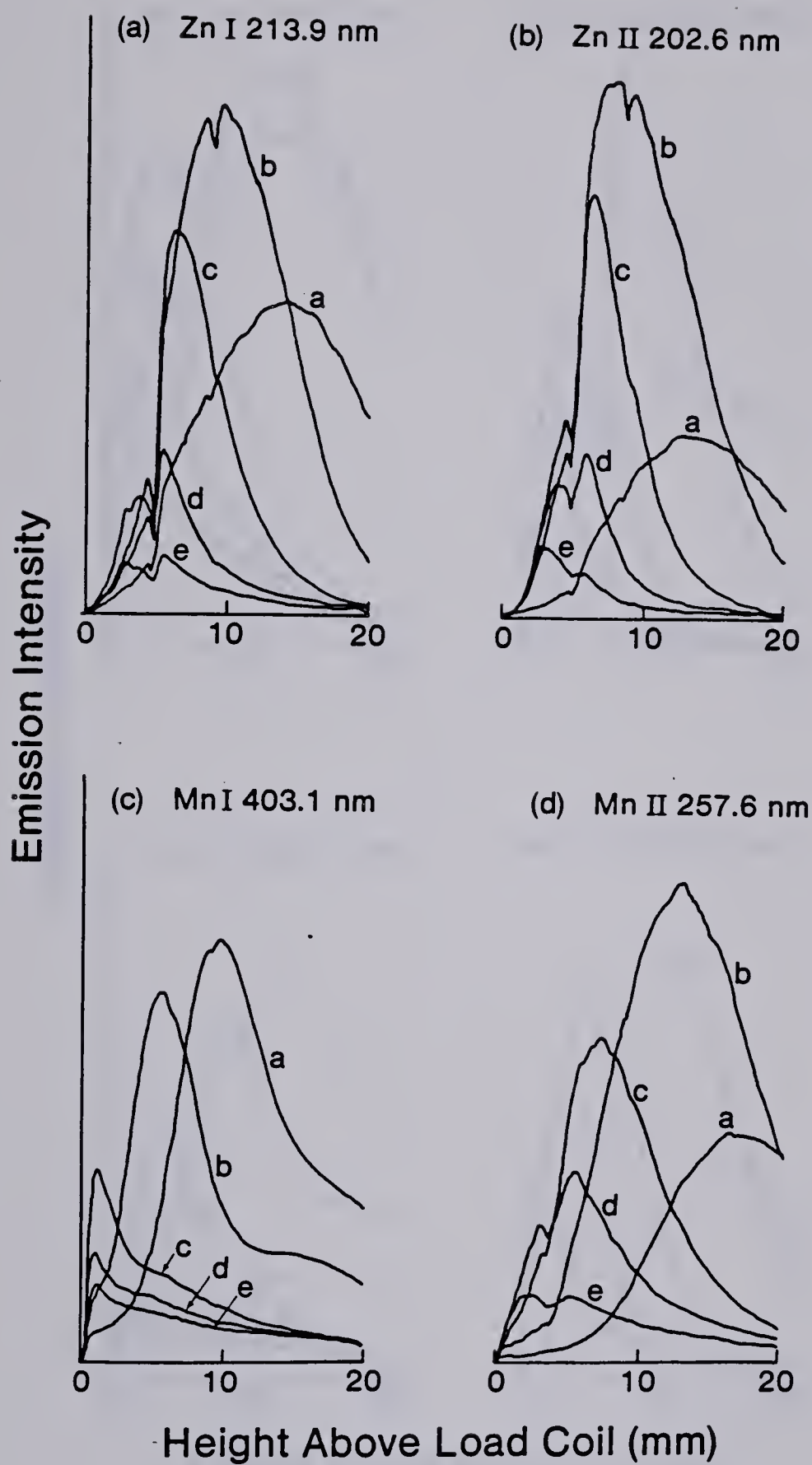


Fig. 12. Spatial profiles of (a) ZnI 213.9nm, (b) ZnII 202.6nm, (c) MnI 403.1nm, and (d) MnII 257.6nm as a function of N<sub>2</sub>-Ar mixed gas composition.



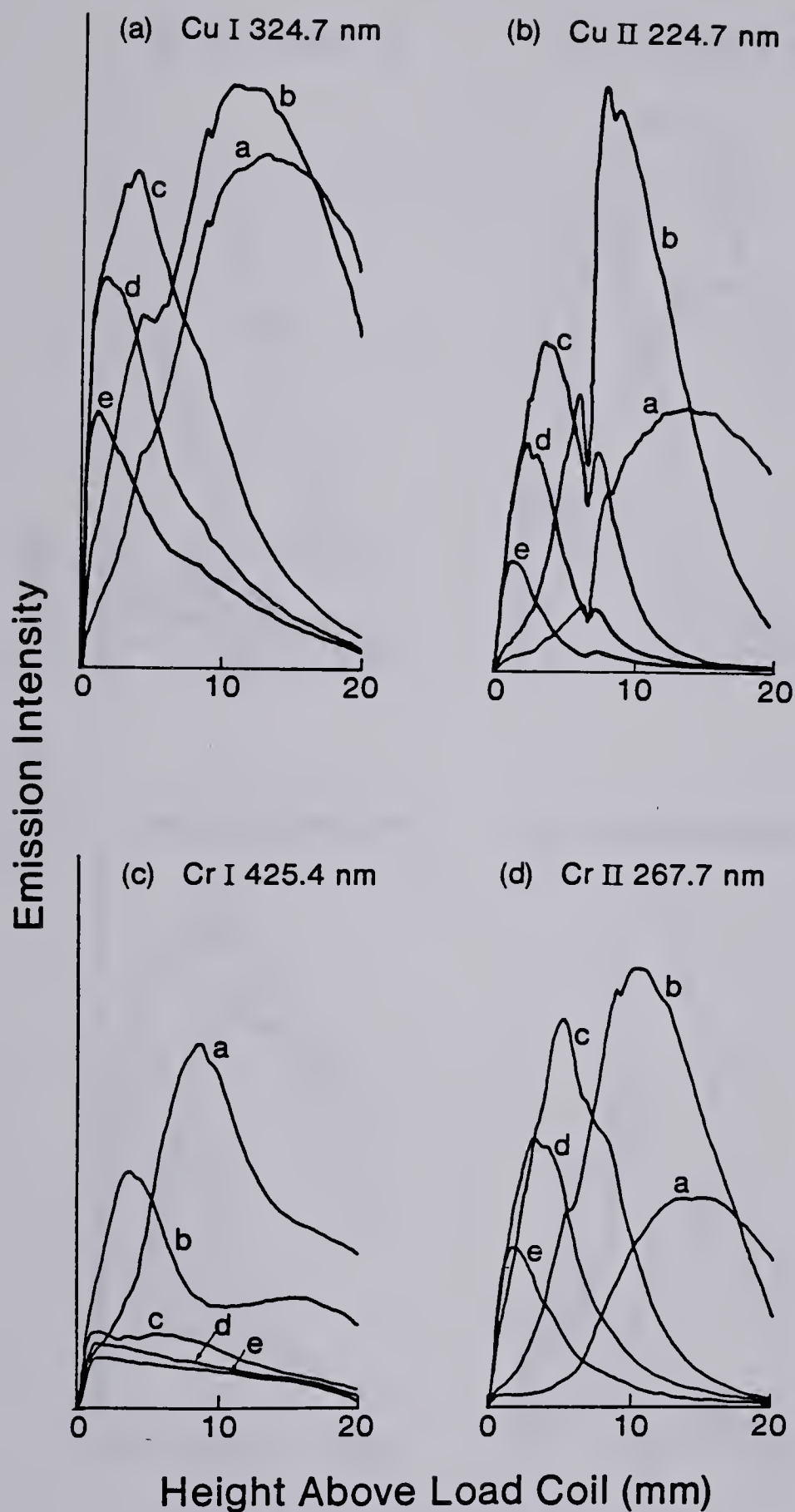


Fig. 13. Spatial profiles of (a) CuI 324.7nm, (b) CuII 224.7nm, (c) CrI 425.4nm, and (d) CrII 267.7nm as a function of N<sub>2</sub>-Ar mixed gas composition.



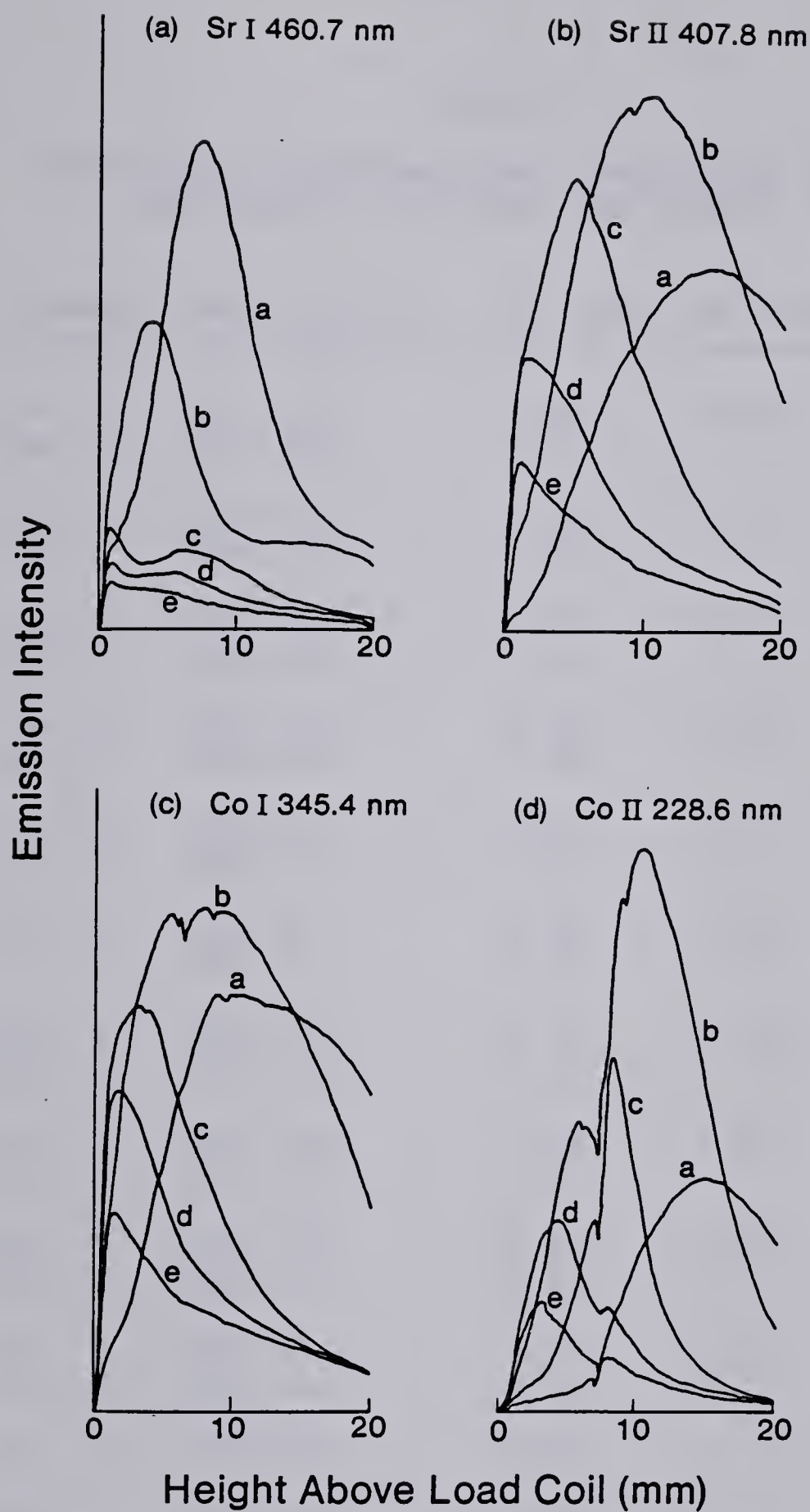


Fig. 14. Spatial profiles of (a) SrI 460.7nm, (b) SrII 407.6nm, (c) CoI 345.4nm, and (d) CoII 228.6nm as a function of N<sub>2</sub>-Ar mixed gas composition.



TABLE IV.1

EXCITATION POTENTIALS AND IONIZATION POTENTIALS  
FOR ANALYTE ATOM AND ION LINES

Element (Wavelength)			EP (eV)	IP (eV)	EP+IP (eV)
-----					
Ba	I	(553.56)	2.24	5.21	
Ba	II	(455.40)	2.72		7.93
Ca	I	(422.67)	2.93	6.11	
Ca	II	(393.37)	3.15		9.26
Cd	I	(228.80)	5.41	8.99	
Cd	II	(226.50)	5.47		14.46
Co	I	(345.35)	4.02	7.86	
Co	II	(228.62)	5.84		13.70
Cr	I	(425.43)	2.91	6.77	
Cr	II	(267.72)	6.18		12.35
Cu	I	(324.7)	3.85	7.72	
Cu	II	(224.7)	8.23		15.95
Mg	I	(285.21)	4.34	7.64	
Mg	II	(279.55)	4.43		12.07
Mn	I	(403.08)	3.08	7.43	
Mn	II	(257.61)	4.81		12.24
Sr	I	(460.73)	2.69	5.69	
Sr	II	(407.77)	3.04		8.73
Zn	I	(213.85)	5.80	9.39	
Zn	II	(202.55)	6.12		15.41
Ar	I	(415.80)	14.53		
Ag	I	(328.07)	3.78		
-----					





neutral atom or ion line. A similar trend hold for elements with different ionization or excitation potentials.

Previous studies have shown that there was a significant increase in the analyte emission intensity when nitrogen was introduced into the Ar-ICP (64-67,80,81,74,75,82,83). The nature of this phenomenon will be discussed and confirmed in terms of the spatially resolved profiles of various elements.

The most striking feature is the large increase in emission intensity for both neutral atom and ion lines caused by the addition of 5 to 20% nitrogen into the conventional Ar-ICP. This effect is clearly illustrated in Figures 11 to 15. In all cases, the intensities peaked when 10 to 20% nitrogen was present in the coolant flow, but the intensities dropped drastically if the amount of the nitrogen in the system was more than 20%. It is perhaps most interesting to note from Figures 11 to 14 that the presence of nitrogen gas affects ion lines of all elements under study more than their corresponding neutral atom lines. For example, when 10 to 20% nitrogen was introduced into the Ar-ICP, spatial intensities of BaII, CaII, CdII, CoII, CrII, CuII, MgII, MnII, SrII and ZnII (ionic) lines increased two to three times more than that obtained with the pure argon discharge; the intensity of their corresponding neutral atom lines showed a relatively small enhancement. For some



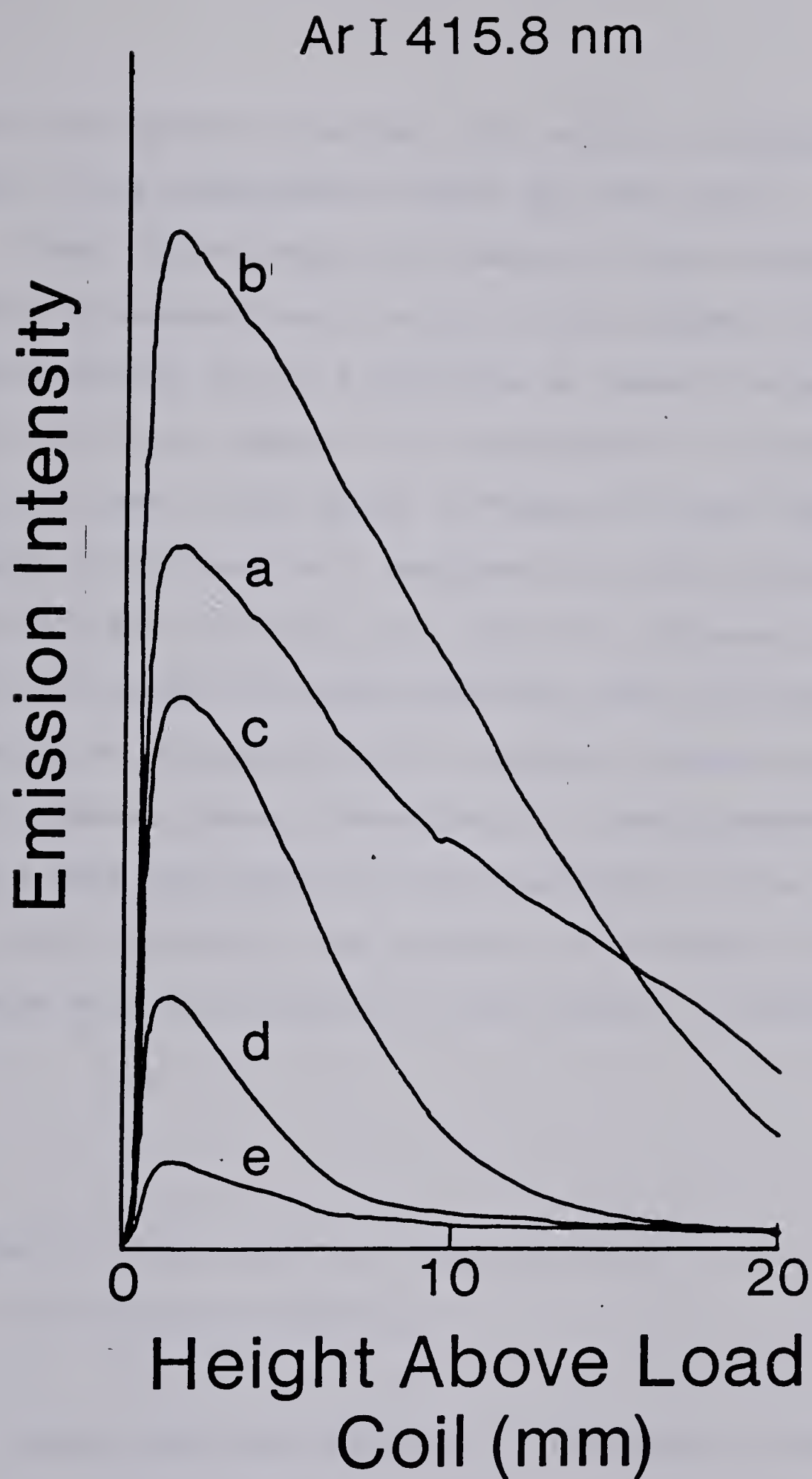


Fig. 15. Spatial profiles of ArI 415.8 nm as a function of  $N_2$ -Ar mixed gas plasmas. Percentages of  $N_2$  in the coolant flow; (a) 0%, (b) 10%, (c) 20%, (d) 50%, and (e) 100%.



neutral atom species like MnI, CrI and SrI (Figures 12c, 13c and 14a), this enhancement effect did not occur.

When 10% nitrogen is present in the coolant stream, the total concentration of argon in the plasma is decreased. One would expect to see a decrease in overall intensity of the ArI 415.8 nm. However, as illustrated in Figure 15, this is not the case. It is shown in Figure 15 that the emission intensity of ArI reaches a maximum for a 10% nitrogen cooled plasma. The ArI intensity for 5 and 10% nitrogen cooled plasmas was higher than that obtained with the pure argon discharge. As discussed before, similar trends were observed for all elements under investigation. These observations indicate that the emission characteristics of the argon plasma were altered by the presence of nitrogen. These phenomena will be discussed in more detail in Chapters VIII and IX.

#### D. Effects of Aerosol Flow Rate and Power on the Vertical Profiles

Apart from the influence of nitrogen on the spatial profiles of analyte emission, there are three major operating parameters which affect the analyte emission in an inductively coupled plasma.





These parameters include :

- (1) rf power coupled to the plasma,
- (2) aerosol flow rate, and
- (3) observation height above the load coil.

These parameters also affect the background continuum and analytical performance of an ICP. These effects will be covered in the following chapters.

Profiles for both neutral atom and ion lines of several elements as a function of plasma power, central aerosol flow rate and coolant flow rate were examined in great detail by Edmonds and Horlick (106). In their paper, they showed that spatial profiles of the emitting species were highly dependent upon the plasma operating parameters.

Although the effects of operating parameters on spatial profiles of various elements of an Ar-ICP were studied by Edmonds and Horlick (106), more recently by Kawaguchi et al. (108) and by Blades and Horlick (118,120), similar experiments were repeated to check the instrumental conditions. However, the intent of this study is to investigate the effects of various operating parameters on the analyte emission profiles of N<sub>2</sub>-Ar mixed gas ICPs, and the collected emission profiles from the N<sub>2</sub>-Ar mixed gas ICPs are compared to those of the conventional argon based



plasma.

A spatial profile study of Sr emission (Figure 16) will be discussed in some detail since most of the spatial data measured in this study are presented in an analogous format. Thirty profiles are presented in Figure 16, each curve representing the Sr emission intensity as a function of height above the load coil. Figure 16 consists of two different sets of spatial profiles: Figure 16a is for ion emission and Figure 16b is for neutral atom emission. The three different frames (I to III) within each figure (16a and 16b) correspond to an aerosol flow rate of 0.8 L/min (Frame I), 1.0 L/min (Frame II) and 1.2 L/min (Frame III). The five different profiles within each frame correspond to different plasma power levels: curve 1 corresponds to power level of 2.25 Kw, curve 2 to 2.00 Kw, curve 3 to 1.75 Kw, curve 4 to 1.50 Kw and curve 5 to 1.25 Kw. These configurations hold for Figures 16 to 27.

In the case of the argon discharge, the effects of rf powers on the SrI and SrII emission profiles were similar to those described by Edmonds and Horlick (106). These effects are illustrated in Figure 16. For the neutral atom emission (SrI 460.7 nm), as the power is increased, the profile maximum shifts towards the load coil. In the case of ion emission (SrII 407.8 nm), the position of the profile maximum is relatively independent of power variations.



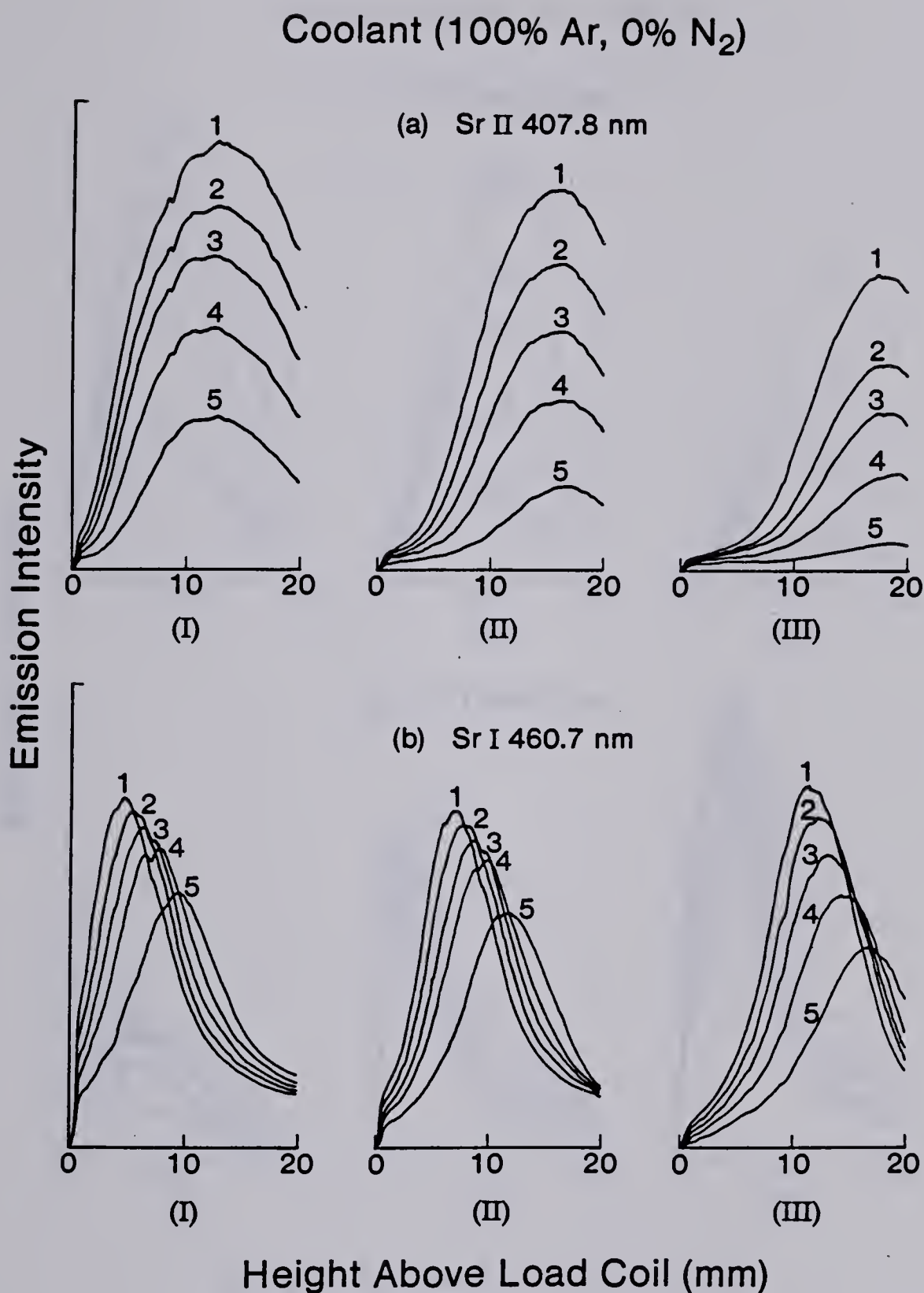


Fig. 16. Vertical spatial profiles for SrII 407.8 nm and SrI 460.7 nm (Ar-ICP). Aerosol flowrates; (I) 0.8 L/min, (II) 1.0 L/min, and (III) 1.2 L/min. RF power; (1) 2.25 Kw, (2) 2.00 Kw, (3) 1.75 Kw, (4) 1.50 Kw, and (5) 1.25 Kw.





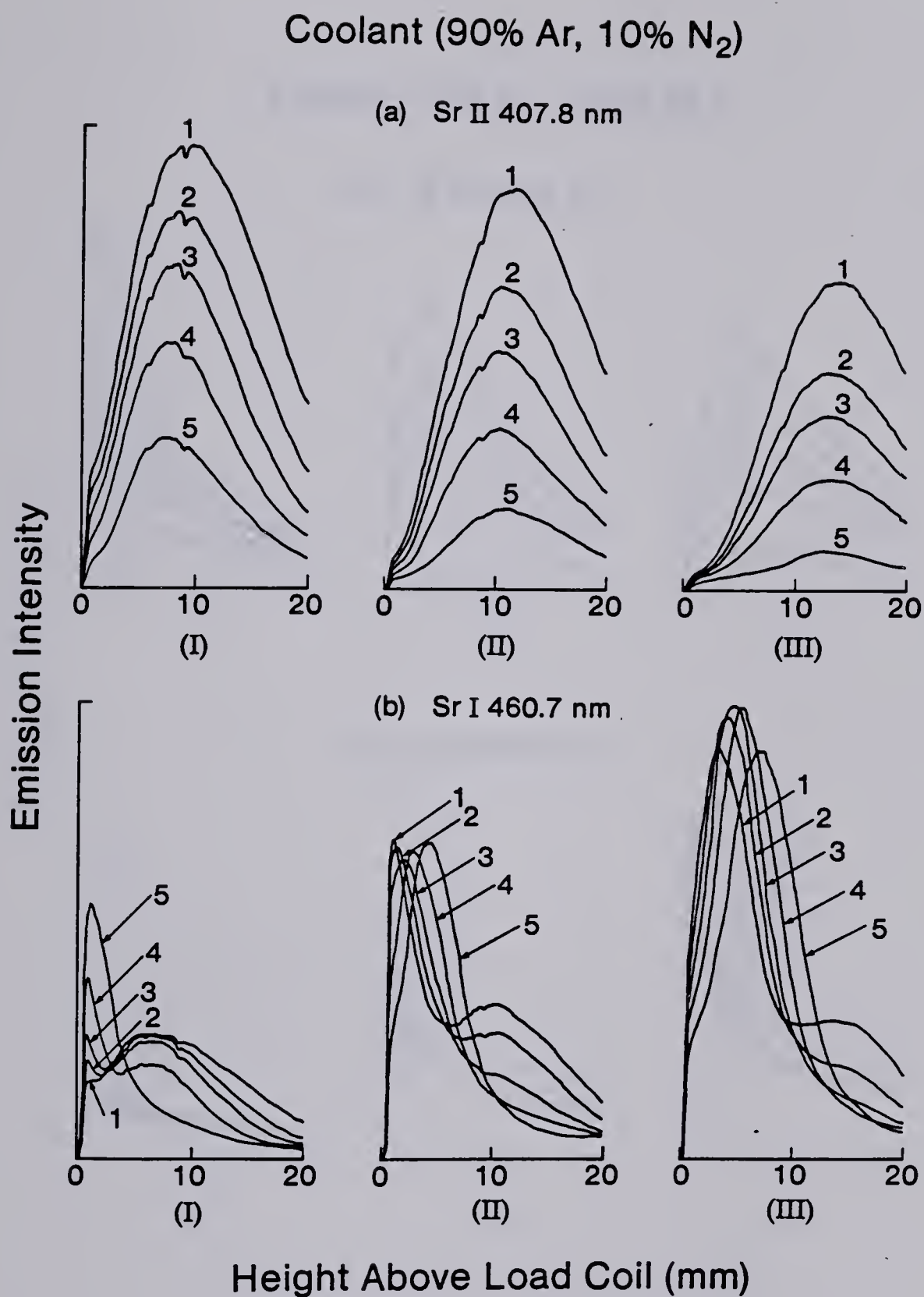


Fig. 17. Vertical spatial profiles for SrII 407.8 nm and SrI 460.7 nm (10% N<sub>2</sub>-cooled ICP). Aerosol flowrates; (I) 0.8 L/min, (II) 1.0 L/min, and (III) 1.2 L/min. RF power; (1) 2.25 Kw, (2) 2.00 Kw, (3) 1.75 Kw, (4) 1.50 Kw, and (5) 1.25 Kw.





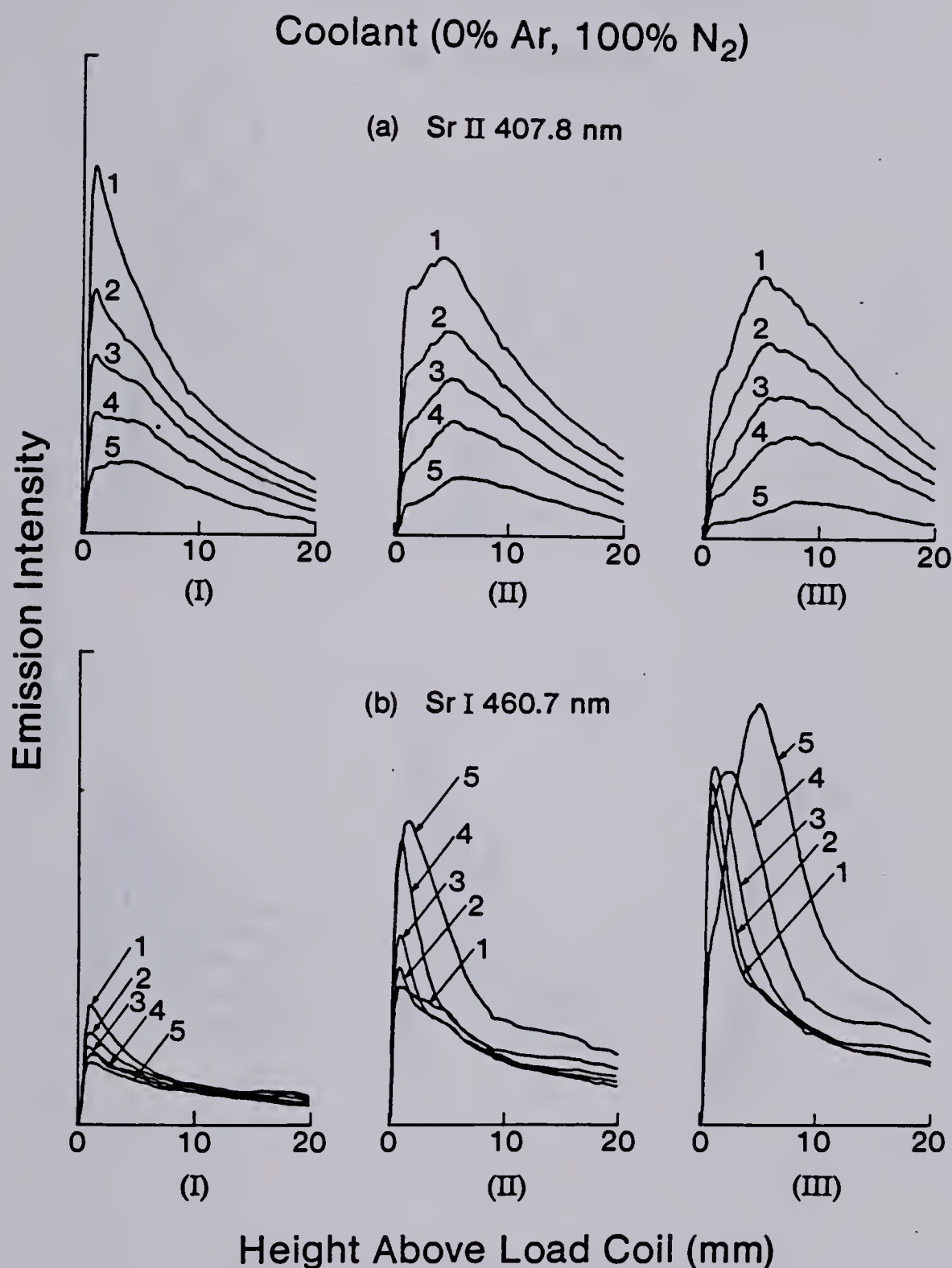


Fig. 18. Vertical spatial profiles for SrII 407.3 nm and SrI 460.7 nm (100% N<sub>2</sub>-cooled ICP). Aerosol flowrates; (I) 0.8L/min, (II) 1.0 L/min, and (III) 1.2 L/min, RF power; (1) 2.25 Kw, (2) 2.00 Kw, (3) 1.75 Kw, (4) 1.50 Kw, and (5) 1.25 Kw.



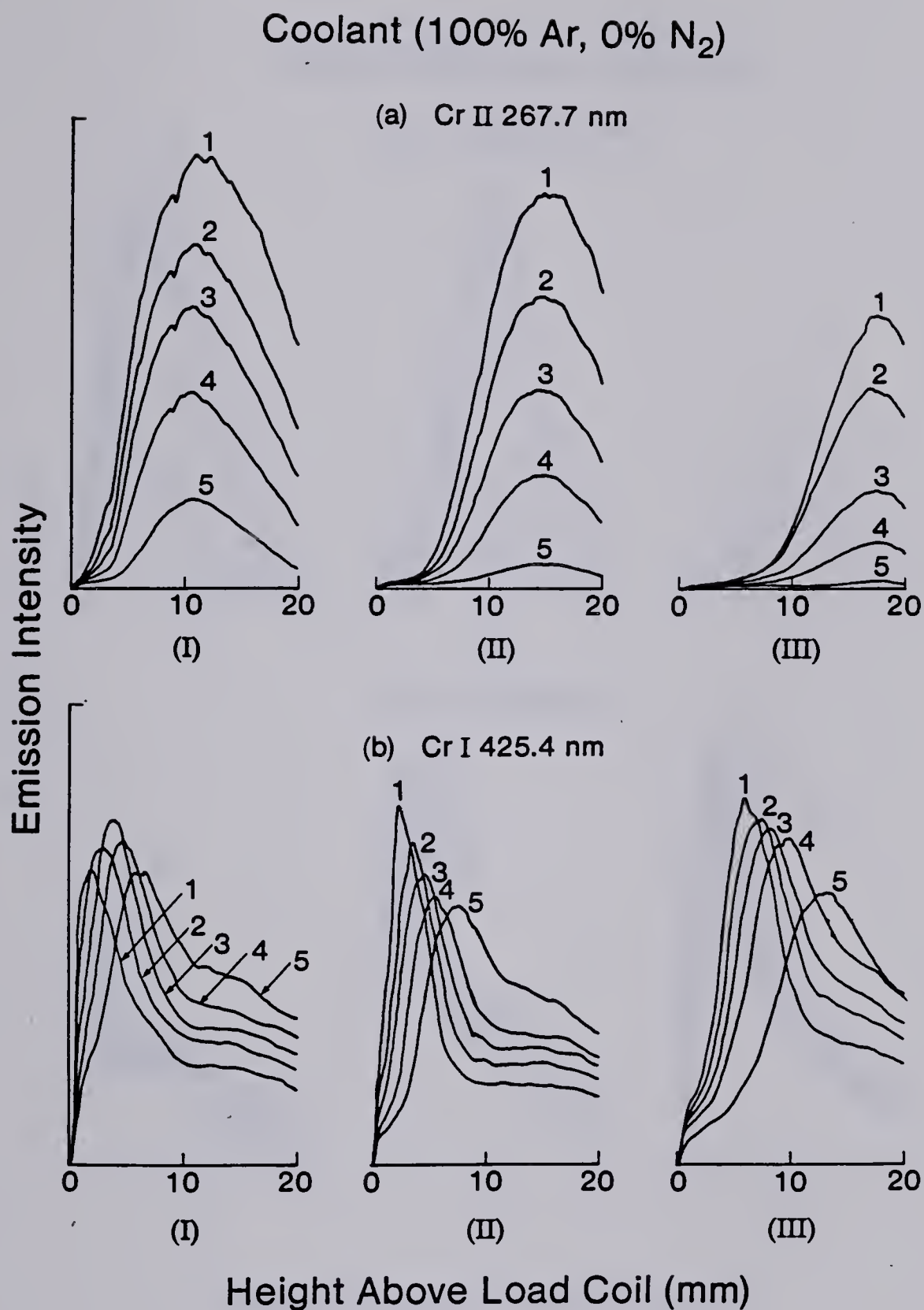


Fig. 19. Vertical spatial profiles for CrII 267.7 nm and CrI 425.4 nm (Ar-ICP). Aerosol flowrates; (I) 0.8 L/min, (II) 1.0 L/min, and (III) 1.2 L/min. RF power; (1) 2.25 Kw, (2) 2.00 Kw, (3) 1.75 Kw, (4) 1.50 Kw, and (5) 1.25 Kw.



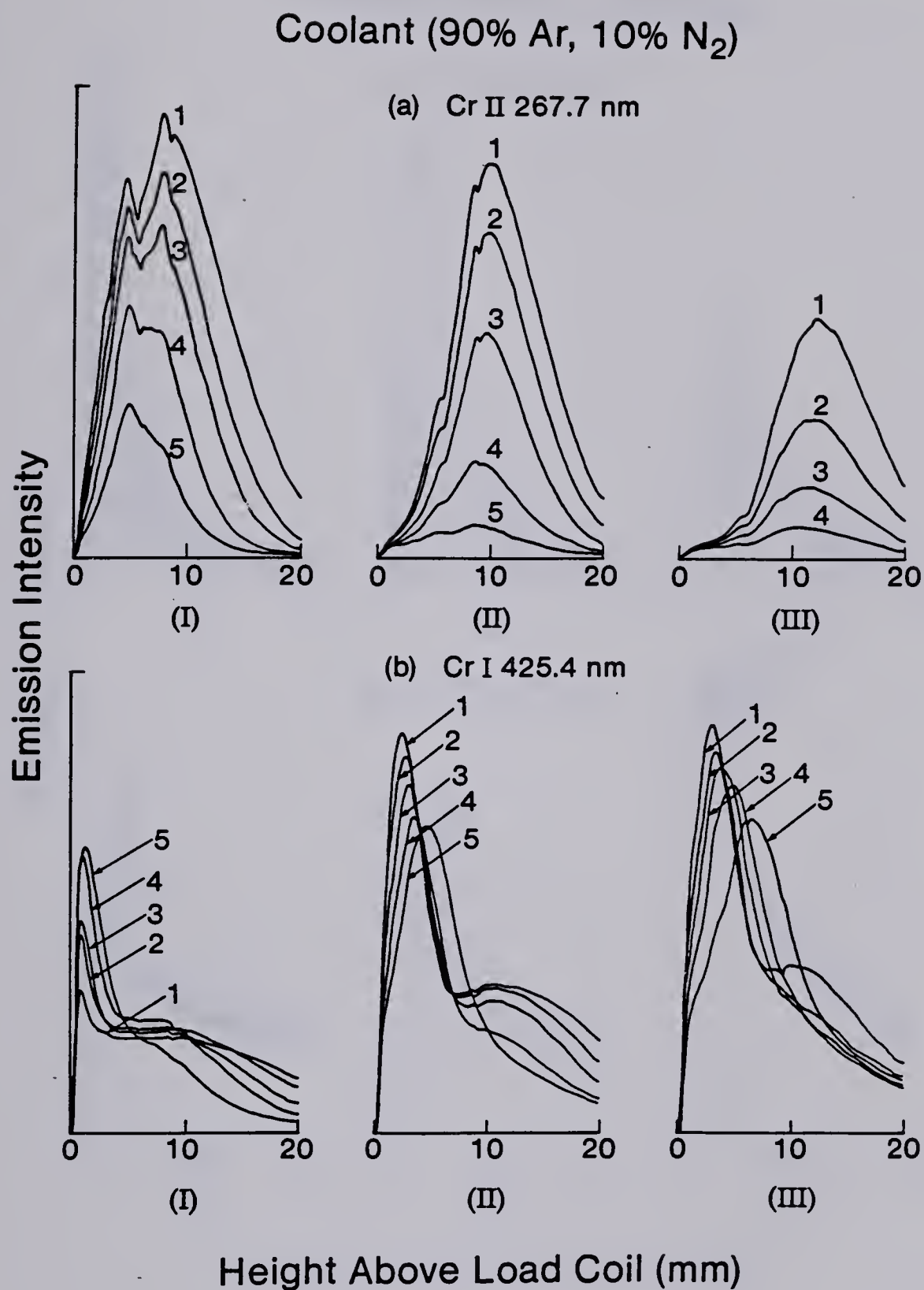


Fig. 20. Vertical spatial profiles for CrII 267.7 nm and CrI 425.4 nm (10% N<sub>2</sub>-cooled ICP). Aerosol flowrates; (I) 0.8 L/min, (II) 1.0 L/min, and (III) 1.2 L/min. RF power; (1) 2.25 Kw, (2) 2.00 Kw, (3) 1.75 Kw, (4) 1.50 Kw, and (5) 1.25 Kw.





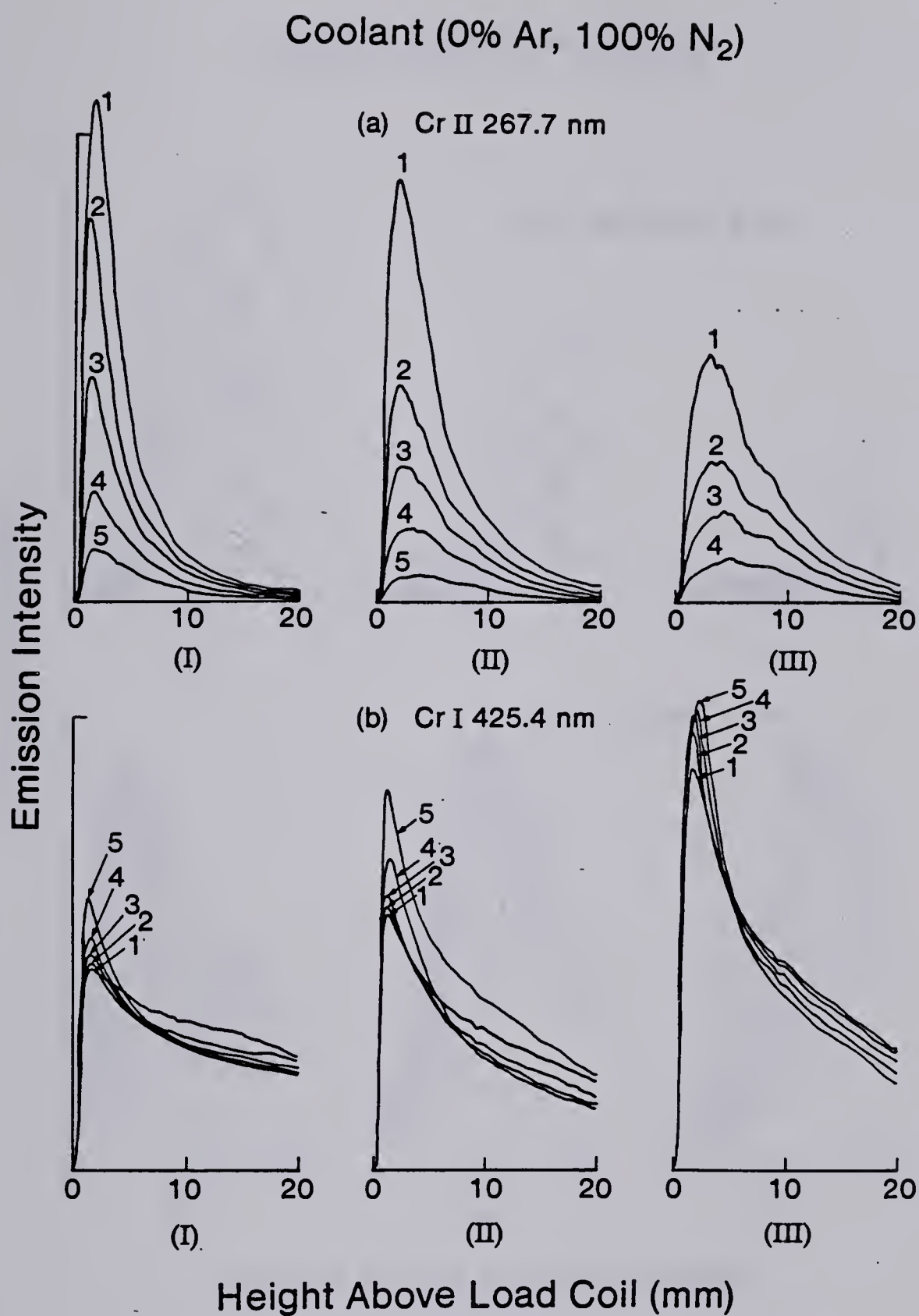


Fig. 21. Vertical spatial profiles for CrII 267.7 nm and CrI 425.4 nm (100% N<sub>2</sub>-cooled ICP). Aerosol flowrates; (I) 0.8 L/min (II) 1.0 L/min, and (III) 1.2 L/min. RF power; (1) 2.25 Kw, (2) 2.00 Kw, (3) 1.75 Kw, (4) 1.50 Kw, and (5) 1.25 Kw.



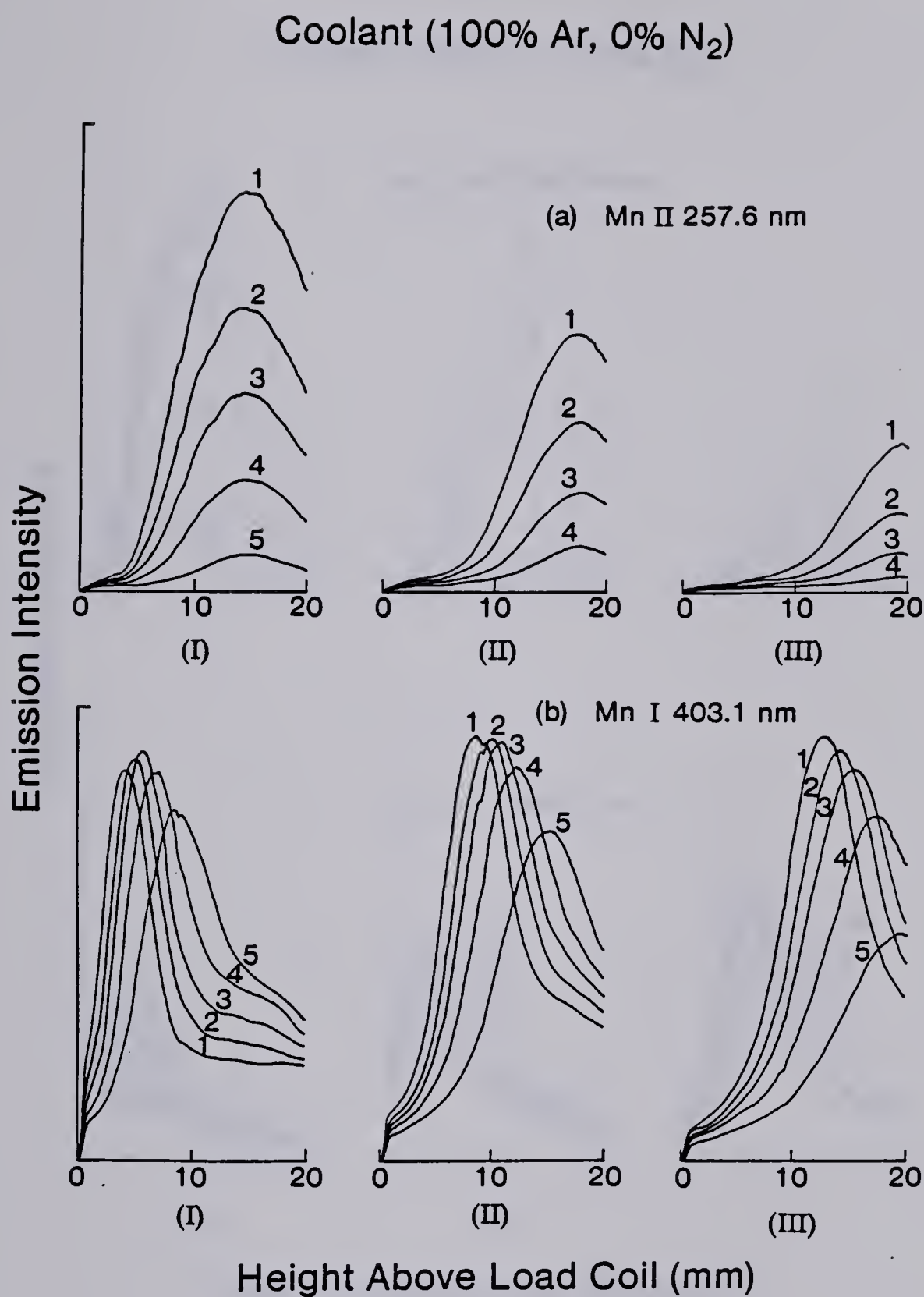


Fig. 22. Vertical spatial profiles for MnII 257.6 nm and MnI 403.1 nm (Ar-ICP). Aerosol flowrates; (I) 0.8 L/min, (II) 1.0 L/min, and (III) 1.2 L/min. RF power; (1) 2.25 Kw, (2) 2.00 Kw, (3) 1.75 Kw, (4) 1.50 Kw, and (5) 1.25 Kw.



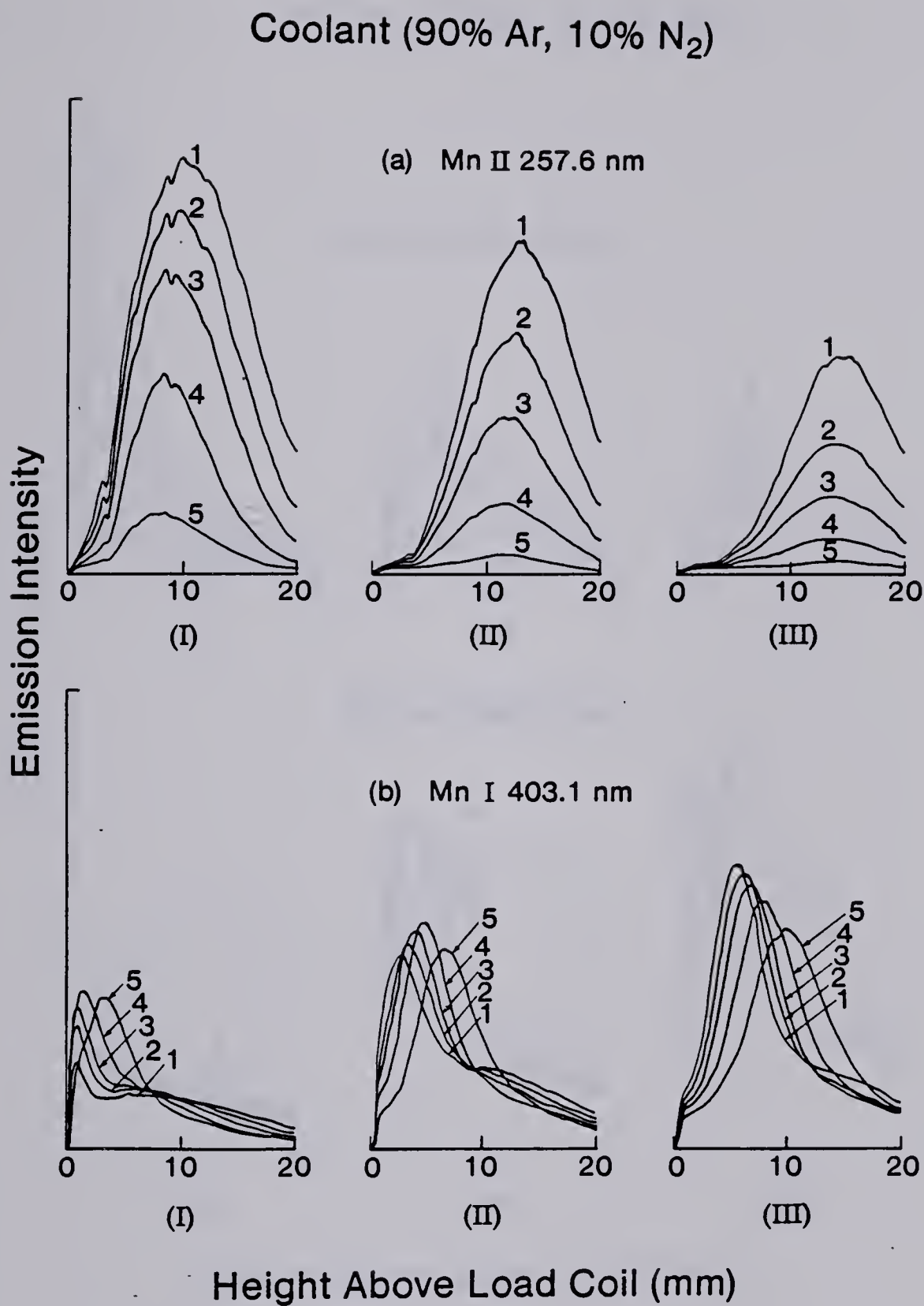


Fig. 23. Vertical spatial profiles for MnII 257.6 nm and MnI 403.1 nm (10% N<sub>2</sub>-cooled ICP). Aerosol flowrates; (I) 0.8 L/min, (II) 1.0 L/min, and (III) 1.2 L/min. RF power; (1) 2.25 Kw, (2) 2.00 Kw, (3) 1.75 Kw, (4) 1.50 Kw, and (5) 1.25 Kw.



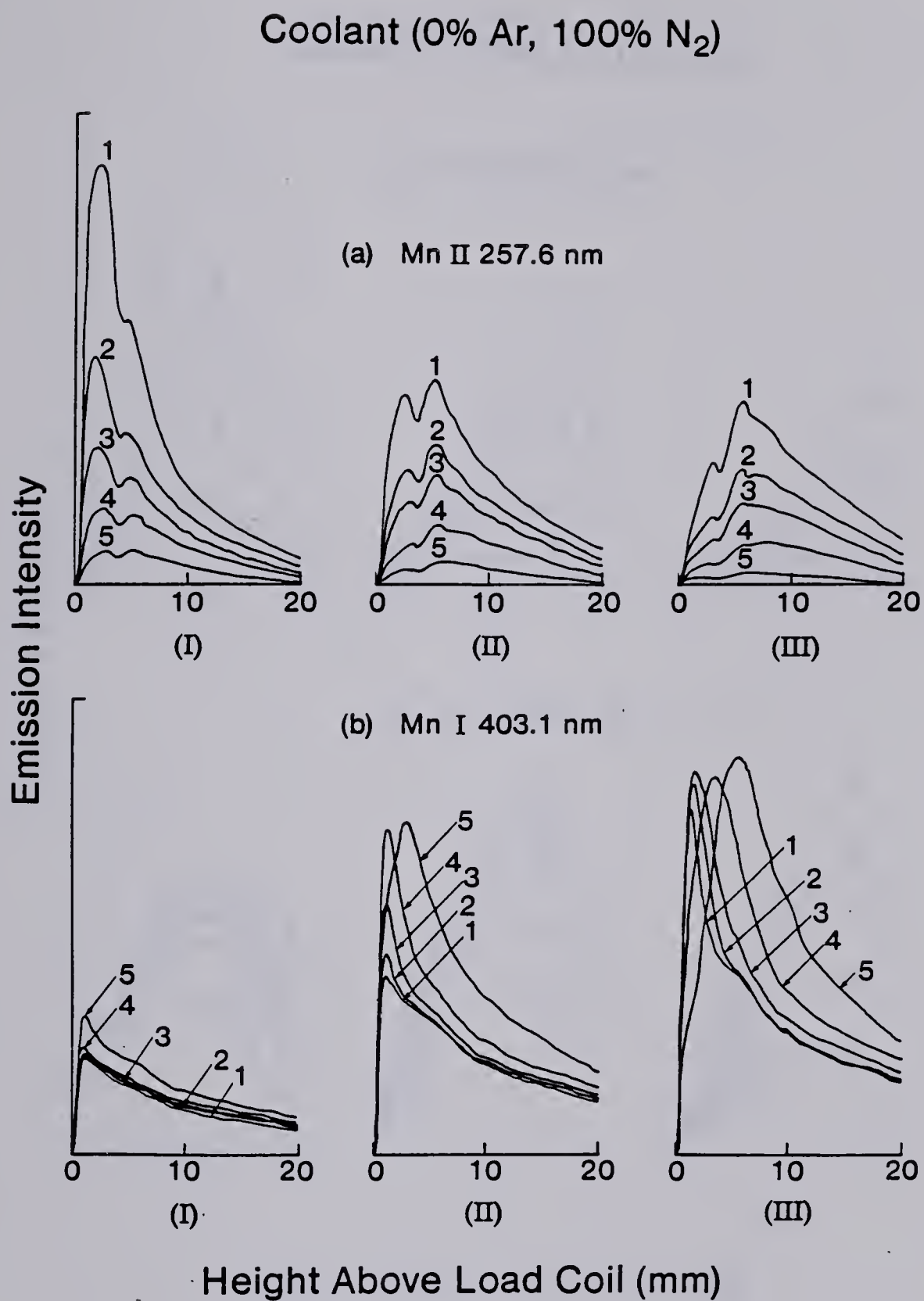


Fig. 24. Vertical spatial profiles for MnII 257.6 nm and MnI 403.1 nm (100% N<sub>2</sub>-cooled ICP). Aerosol flowrates; (I) 0.8 L/min, (II) 1.0 L/min, and (III) 1.2 L/min. RF power; (1) 2.25 Kw, (2) 2.00 Kw, (3) 1.75 Kw, (4) 1.50 Kw, and (5) 1.25 Kw.





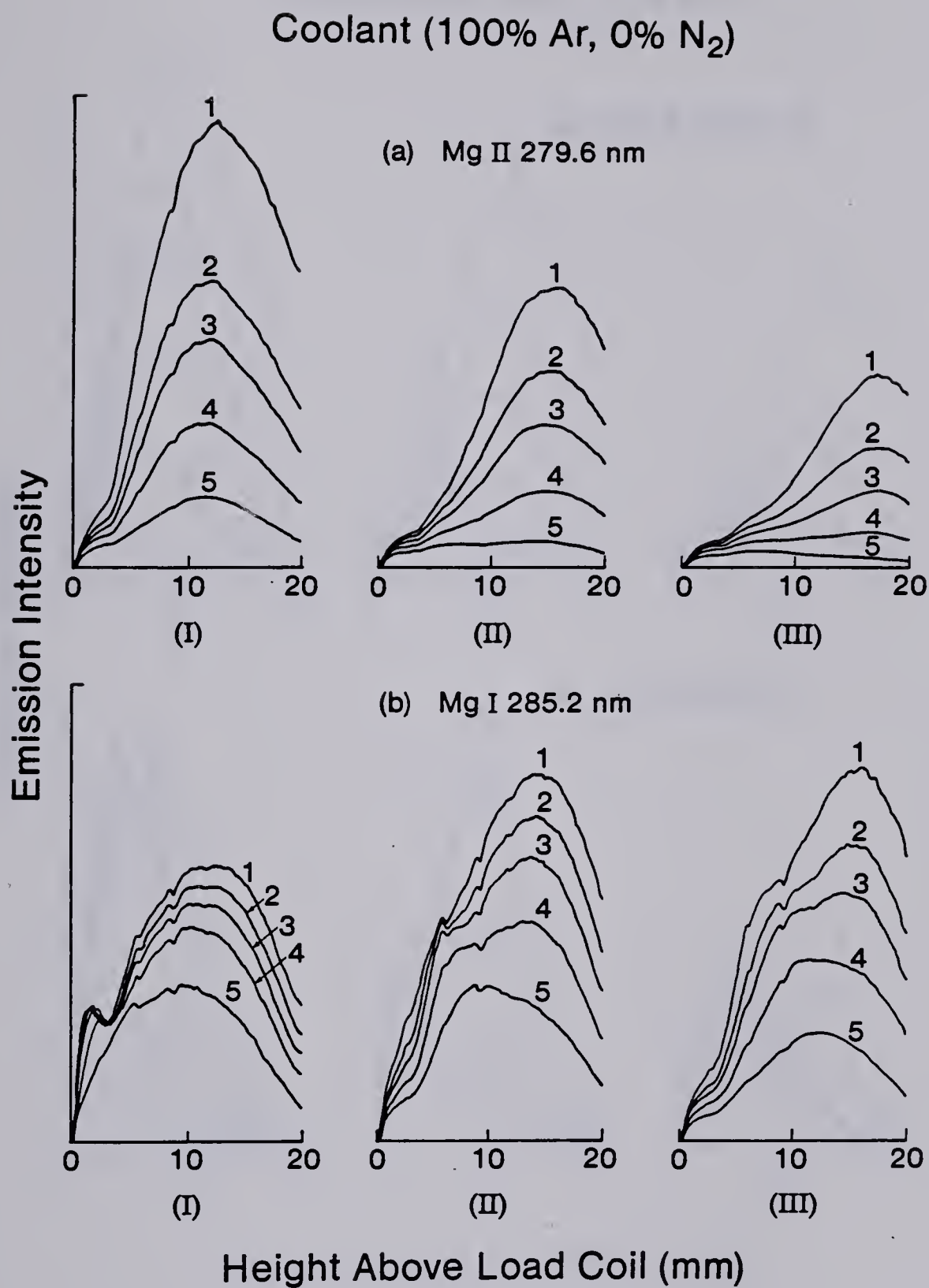


Fig. 25. Vertical spatial profiles for MgII 279.6 nm and MgI 285.2 nm (Ar-ICP). Aerosol flowrates; (I) 0.8 L/min, (II) 1.0 L/min, and (III) 1.2 L/min. RF power; (1) 2.25 Kw, (2) 2.00 Kw, (3) 1.75 Kw, (4) 1.50 Kw, and (5) 1.25 Kw.



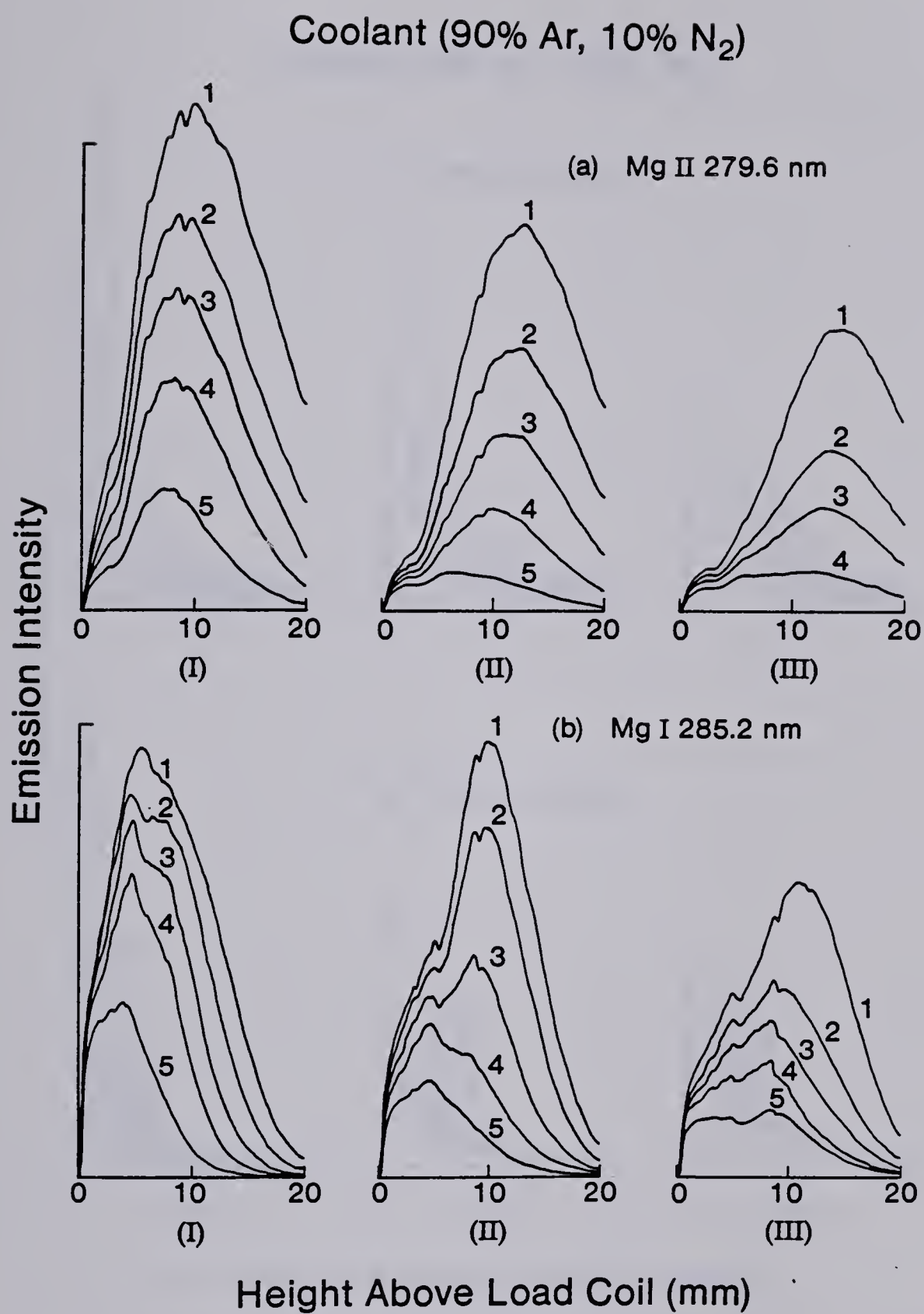


Fig. 26. Vertical spatial profiles for MgII 279.6 nm and MgI 285.2 nm (10% N<sub>2</sub>-cooled ICP). Aerosol flowrates; (I) 0.8 L/min, (II) 1.0 L/min, and (III) 1.2 L/min. RF power; (1) 2.25 Kw, (2) 2.00 Kw, (3) 1.75 Kw, (4) 1.50 Kw, and (5) 1.25 Kw.



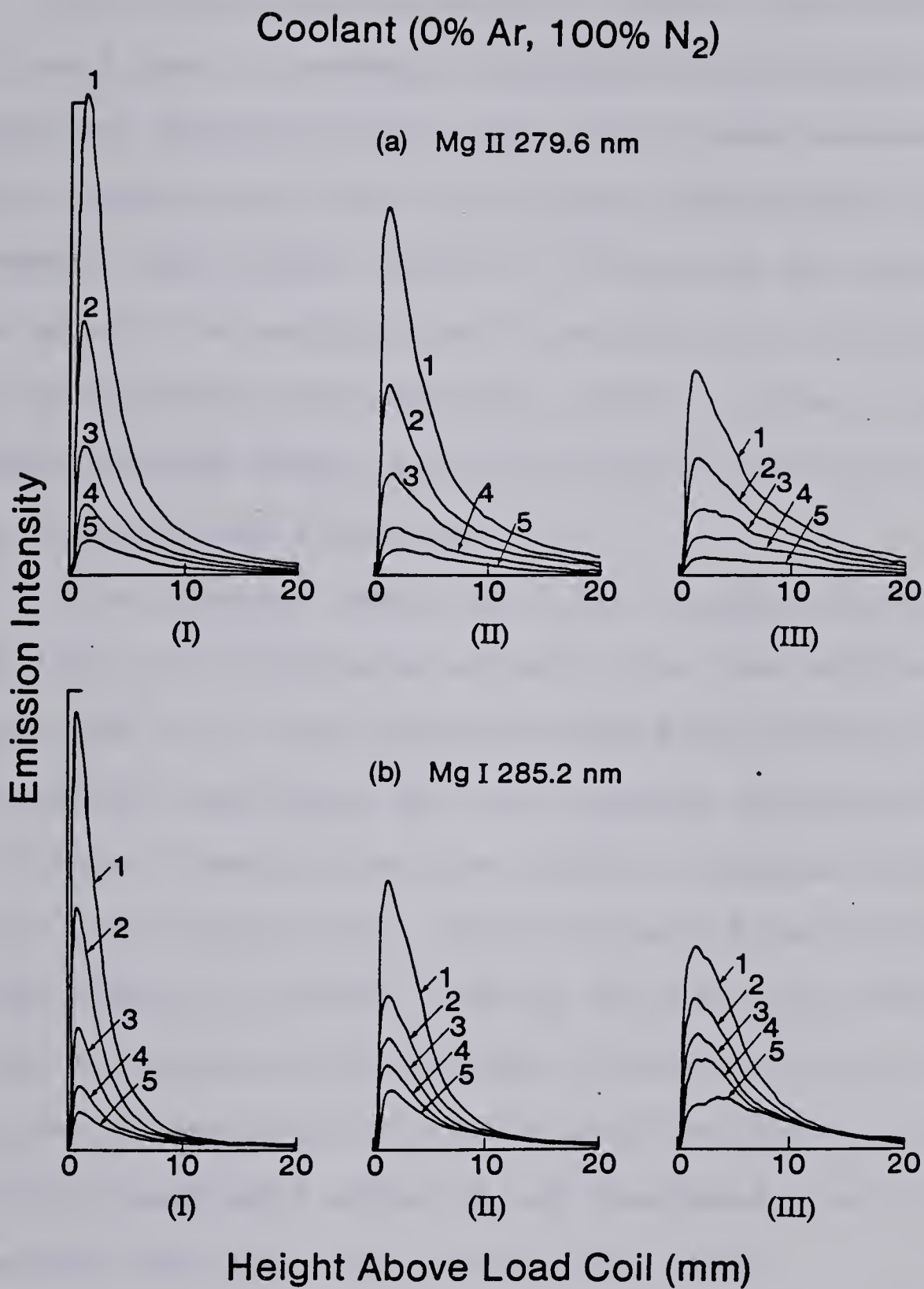


Fig. 27. Vertical spatial profiles for MgII 279.6 nm and MgI 285.2 nm (100% N<sub>2</sub>-cooled ICP). Aerosol flowrates; (I) 0.8 L/min, (II) 1.0 L/min, and (III) 1.2 L/min. RF power; (1) 2.25 Kw, (2) 2.00 Kw, (3) 1.75 Kw, (4) 1.50 Kw, and (5) 1.25 Kw.





The strong dependence of SrI 460.7 nm emission on power could lead to somewhat confusing observations with conventional photomultiplier tube (PMT) based measurement systems, particularly ones with narrow observation windows. For example (see Figure 16b(II)) if one had an observation window about 2 mm centered at 18 mm above the induction coil, the optimum power would be 1.25 Kw (curve 5) as increasing plasma power above this value would result in a reduction in signal intensity.

At a constant power level (for example curve 2 in Figure 16a), an increase in aerosol flow rate shifts the peak maximum to a higher position above the load coil and simultaneously decreases the net emission intensity of the peak. Similar observations also apply to neutral atom emission (see Figure 16b). It can be seen from this figure that the effect of aerosol flow on the ion line emission profiles is considerably different from that of the neutral atom line. In particular, the net profile intensity of the ion line is much more affected and dependent upon the power and aerosol flow than its neutral atom line.

It is important to study the effects of aerosol flow and power on other analyte species in order to see whether these spatial patterns and trends have some generality. The analogous spatial profiles of emission for the major neutral atom lines of Cr, Mn and Mg are shown in Figures 19b, 22b



and 25b, and for their ion lines in Figures 19a, 22a and 25a. From these figures, it is clear that the spatial patterns for the Cr and Mn neutral atom and ion lines are similar to those reported for SrI and SrII lines. However the spatial pattern of the Mg neutral atom line (MgI 285.2 nm, Figure 25b) behaves like its ion line, i.e. peak maxima are independent of the power variations. Another interesting point to note in these figures is that under similar operating conditions all the maximum intensities of the ion lines occurred in the same position above the load coil; whereas, with similar power and aerosol flow the emission profiles of the neutral atom lines peak at different heights above the load coil. For the neutral atom lines, the spatial patterns behave similarly to the trends reported by Edmonds and Horlick, i.e. with similar operating conditions the spatial patterns peak successively higher in the argon plasma in the order of Sr, Cr, Mn and Mg. This sequence correlates roughly with the excitation potential of these lines (Table IV.2).

As mentioned earlier in this chapter, the emission characteristics of the argon plasma are altered by the presence of nitrogen. In the case of the 10% nitrogen cooled plasma, the effects of rf power and aerosol flow on the analyte ion emission (for example SrII 407.8 nm in Figure 17a) are similar to those described for the argon plasma



TABLE IV.2

EXCITATION POTENTIALS AND PEAK POSITIONS  
FOR SOME ANALYTE LINES

Element (Wavelength)	Excitation Potential (eV)	Peak Position*
Sr I (460.73)	2.69	10.5
Cr I (425.43)	2.91	11.4
Mn I (403.08)	3.08	12.6
Mg I (285.21)	4.34	14.1

\* mm above the load coil





(Figure 16a). However, in the case of the  $N_2$ -Ar mixed gas plasma, the effects of power and aerosol flow on the neutral atom emission (Figures 17b, 20b, 23b or 26b) are considerably different from the analyte spatial patterns of the argon plasma (Figures 16b, 19b, 22b or 25b). It can be seen from these figures that the presence of nitrogen pushes the peak intensity towards the load coil. For example, in the case of Sr neutral atom line (see Figure 17b, frame I), as the power is increased from 1.25 to 2.25 Kw the profile maximum appears to be shifting inside the load coil. If the viewing window is held for 0 to 20 mm above the load coil as in the present case, one observes a decrease in emission intensity with increasing power (Figures 17b, 20b, 23b and 26b).

Unlike those observations reported for the argon plasma where neutral atom emission intensity is not strongly affected by aerosol flow variations when compared to the ion line, in the presence of nitrogen the aerosol flow has a significant effect on both the net intensities of neutral atom and ion lines. In contrast to the observations previously mentioned for the argon plasma, with low aerosol flow rate the peak maxima of the neutral atom lines in a 10% nitrogen cooled plasma appears to be independent of power variations. It can be seen from Figure 20b that at a constant aerosol flow (Frame I) the intensity maxima of the





CrI 425.4 nm line peaks at 2 to 4 mm above the load coil regardless of plasma power levels. Similar patterns were also observed for the neutral atom lines of Sr and Mn (Figures 17b and 23b). Because the magnesium neutral atom line behaves spatially like its ion line, the spatial patterns of the MgI 285.2 nm of the 10% nitrogen cooled plasma (Figure 26) are similar to those described for the Ar-ICP (Figure 25b).

Spatially, the 100% nitrogen cooled plasma behaves like the 10% N<sub>2</sub>-Ar mixed gas ICP (Figures 18, 21, 24 and 27). In the case of 100% nitrogen cooled plasma and at a rather low aerosol flow level (Frame I), it is interesting to note that both the neutral atom and ion lines peak at 2 to 4 mm above the load coil. Under these operating conditions, the spatial patterns appear to be independent of the excitation and ionization potentials of the lines being observed, and the emission intensities drop sharply with observation height. Finally, in comparing the 100% nitrogen cooled plasma and argon plasma perhaps the most interesting point to note is that the emission profiles of the ion lines in 100% nitrogen cooled ICP are much narrower than those of the Ar-ICP. The above observations correlate very closely to the plasmas' shapes mentioned and illustrated in Chapter III. It can be seen from Figures 18 to 27 that the spatial behaviour of the analyte ion emission as a function of



central aerosol flow rate is considerably different from that of the neutral atom line. In particular, the intensity of the neutral atom line is significantly increased at higher aerosol flow rate. Whereas, intensities of ion emission profiles optimize at lower aerosol flow rate.

#### E. Effect of Nitrogen in the Aerosol Flow on the Vertical Profiles

For the data presented so far in this chapter, in all cases nitrogen was introduced only to the coolant stream of an Ar-ICP. The effect of introducing various percentages of nitrogen into the aerosol flow (inner channel) on the spatial profiles of calcium ion emission (CaII 393.3 nm) in an Ar-ICP is shown in Figure 28a, in a 100% nitrogen cooled ICP in Figure 28b. The numbers on each figure correspond to : (1) 0%, (2) 20% and (3) 50% nitrogen in the aerosol channel. The experimental operating conditions chosen for the study were 2.0 Kw plasma power, 15 L/min coolant flow and 1.0 L/min aerosol flow. In all cases, the amount of Ar-N<sub>2</sub> mixture in the aerosol flow was adjusted to ensure a constant 1.0 L/min. The visual observations of the effect of nitrogen in the aerosol flow on an Ar-ICP were discussed in Chapter III.



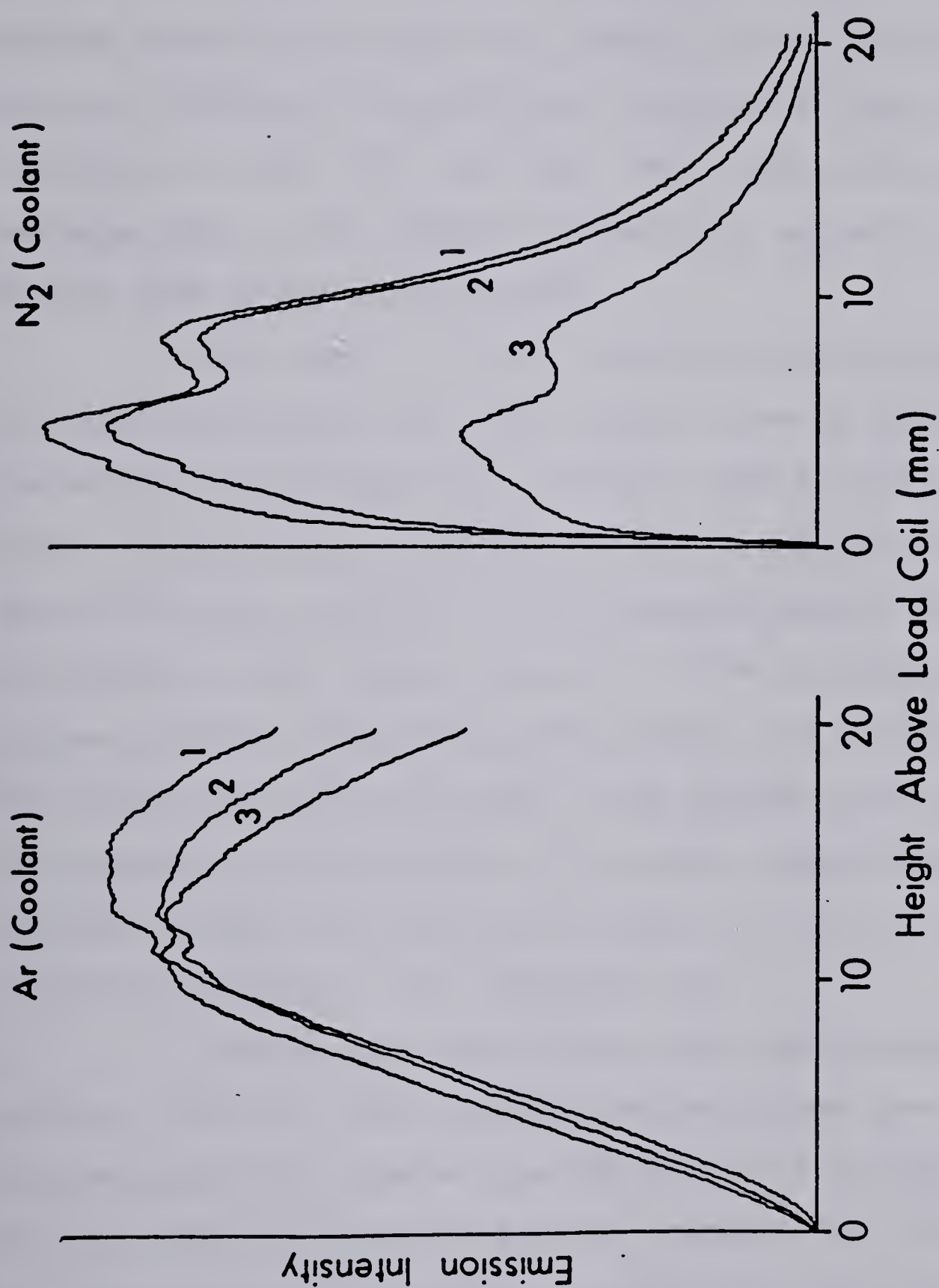


Fig. 28. Vertical spatial profiles for CaII 393.4 nm, (Ar-ICP and 100% N<sub>2</sub> cooled ICP). Percentage of N<sub>2</sub> in the aerosol flow: (1) 0%, (2) 20%, and (3) 50%.







Note that in the case of the Ar-ICP (Figure 28a), as the amount of nitrogen in the aerosol is increased from 0% (curve 1) to 50% (curve 3) the spatial emission maximum shifts towards the load coil. However, this figure (28a) does not indicate a significant reduction in the emission intensity of CaII 393.3 nm line. The plasma with a trace of nitrogen gas in the aerosol channel also appeared to be less stable than conventional Ar-ICP.

In the case of a 100% nitrogen cooled plasma, the addition of nitrogen into the aerosol flow is similar to converting the plasma into a totally 100% N<sub>2</sub>-ICP with all flows being nitrogen. Several attempts were made to convert an Ar-ICP into a N<sub>2</sub>-ICP, but the maximum amount of nitrogen introduced to the aerosol flow of a 100% nitrogen cooled plasma without extinguishing the plasma was limited to 50%. The plasma with 50% nitrogen in the aerosol flow fluctuated and appeared to be unstable. The plasma instability was probably caused by exceeding the limit of the tuning capacity attached to the induction coil.

It can be seen from Figure 28b that nitrogen in the aerosol flow of a 100% nitrogen cooled plasma does not shift the peak maximum. However, as the amount of nitrogen in the aerosol flow is increased from 0% (curve 1) to 50% (curve 3), the emission intensity of calcium ion line decreases drastically. Introducing nitrogen into the aerosol flow



increased the size of the central channel because of the "pinch effect" described in Chapter III. The reduction in emission intensity is attributed to poor sample-plasma interaction. Clearly, the trend indicates that totally 100%  $N_2$ -ICP may not provide any gain in analyte emission intensity over the conventional Ar-ICP or 100% nitrogen cooled plasma.

#### F. Conclusions

Several important conclusions can be drawn from the observations and examples discussed above. It is clear that profiling the emission from an ICP source with a photodiode array provides a unique and detailed picture of analyte emission characteristics. With this profiling technique, the present investigation has unambiguously demonstrated an overall spatial dependence of analyte emission on the amount of nitrogen present in the coolant or aerosol flows of an Ar-ICP. When compared to the conventional Ar-ICP which has a profile maximum for most elements (ion lines) of about 18 mm above the induction coil, the position of the analyte profile maximum in a 100% nitrogen cooled plasma is found to be at 2 to 4 mm above the load coil. The data also indicate that the analyte emission intensities measured from a 10%



nitrogen cooled plasma source were higher than those measured from an argon ICP source. In addition, the 10% nitrogen cooled plasma also appears to affect the emission intensity of ion lines more than that of the neutral atom lines. Also, the data clearly indicate that analyte emission intensities of mixed gas plasmas tend to be optimal at slightly higher aerosol flow rates and powers than the conventional argon discharge. These observations have been very consistent for all elements studied.

On the basis of the observations and discussions presented in Chapters III and IV, we can predict that  $O_2$ -Ar, Air-Ar and He-Ar mixed gas ICPs will show similar spatial characteristics as the  $N_2$ -Ar mixed gas plasmas. The validity of such a prediction will be discussed in the following chapters.

This study also indicates that 100 %  $N_2$ -ICP may not provide better analytical performances than conventional Ar-ICP or  $N_2$ -Ar mixed gas ICPs. Hence, all subsequent experiments are related only to the evaluations and characterizations of the mixed gas plasmas.





## CHAPTER V

### ANALYTICAL AND SPECTRAL CHARACTERISTICS OF N<sub>2</sub>-AR, O<sub>2</sub>-AR, AIR-AR and HE-AR MIXED GAS PLASMAS

#### A. Introduction

The ultimate object of the analytical atomic spectroscopist in studying the plasma is the characterization, evaluation and interpretation of all spectroscopic observations in terms of their spatial and spectral characteristics, analytical capabilities, detection limits and interference effects.

Although the profiling array described in the previous chapter has proven to be very effective for measuring spatial profiles of the emitting species, information about the background intensity, spectral interferences, relative intensities of all emitting species and most importantly the analytical capabilities of various different types of plasmas are not provided. This profiling array system is also limited to the measurement of only one spectral resolution element at a time.

In order to investigate the effects of various percentages of foreign gases (N<sub>2</sub>, O<sub>2</sub>, Air and He) present in





the coolant flow of an Ar-ICP on the emission intensities of the spectral lines of interest, one has to employ a measurement system which is capable of providing simultaneous spectral information over a range of wavelengths. The development and implementation of such a simultaneous multichannel analysis system for spectrochemical measurements has been described in detail by Horlick (104,112-115). The 1024 element photodiode array system previously developed in our laboratory has a capability of simultaneously measuring over 50 nm (500 Å) of continuous spectral information anywhere from 200 to 1000 nm. This is accomplished by mounting the photodiode array horizontally in the exit focal plane of the monochromator (Figure 6). Although the array is not as sensitive a sensor as the photomultiplier tube (PMT), the simultaneous multiwavelength capability of such a system has proven to be an effective means of studying and characterizing various different kinds of plasmas (82-85).

The effects of various percentages of foreign gases present in the coolant stream of a conventional Ar-ICP on the emission spectra containing several emitting species will be discussed. Two different spectral regions will be covered: one includes CaII lines, the other CdI and CdII lines. The background and background subtracted spectra were collected at 2, 5, 10, 15 and 20 mm above the load coil.



In many ICP studies, signal-to-background ratio is used as a figure of merit. Salin and Horlick (127) have shown that this ratio is only significant when the limiting noise present in the system is related to the plasma spectral background. In their paper (127), they have also shown that variation in the rf power level of the ICP could bring about a significant change (a factor of 3 to 4) in the signal-to-background ratios of the CaII and SrII emission lines, but the signal-to-noise ratios of these lines were only decreased to the extent of about 10 to 20%. They have also pointed out that at concentration largely in excess of the detection limit the limiting ICP noise is source flicker. In this case, the precision of the measurement (signal-to-noise ratio) is perhaps more important and meaningful than the signal-to-background ratio in the interpretation of the performance of the ICP source. The concentration levels used in this work were well above the detection limit. Therefore, evaluations and comparisons of the performances for various mixed gas plasmas will be interpreted in terms of signal-to-noise ratios rather than their signal-to-background ratios.

The precisions of the ICP signals were evaluated at different heights and also for various mixed gas combinations using the CaII, CdI and CdII emission signals. In addition, comparisons of precision and background





subtracted spectra containing CdI and CdII species in various mixed gas plasmas will also be presented.

## B. Experimental

The plasma system was identical to the one described in Chapter II. The operating conditions are listed in Table III.1. Foreign gases such as  $N_2$ ,  $O_2$ , Air or He were introduced only to the coolant flow of an argon plasma.

The 1024 element photodiode array measurement system and external measurement electronics were identical to those described in Chapter II (104,112-115) and the signals from the photodiode array were amplified and acquired by a PDP-8 minicomputer.

For all spectral measurements, the plasma was focused onto the entrance slit of the monochromator using a spherical quartz lens (focal length = 10 cm, diameter = 2 in). A 2:1 reduced inverted image of the plasma was focused onto the entrance slit set at 100 microns. The measurement system was carefully aligned using He-Ne laser so that the plasma emission intensity from the middle of the aerosol channel was measured. A He-Ne laser was also used as a reference source for plasma height adjustment. Since the spherical lens was mounted on the body of the monochromator,





different horizontal slices of the plasma could be measured by raising and lowering the monochromator. The position above the load coil could be measured accurately using a precision dial gauge attached to the monochromator (Mitutoyo No. 3052, Japan).

The background signal associated with the array is due to dark current and fixed pattern background (104,112-115). The major source of fixed pattern background is fed through from the clocking signals. The magnitude of this electronic background signal can be minimized with the filter described in Chapter II. Since the electronic background is exactly repeatable from scan to scan, it is removed by subtraction utilizing the computer data acquisition system. The dark current level of the array is significantly reduced by cooling the array. All spectra reported in this work were electronic background subtracted in order to remove the fixed pattern background and residual dark current.

Two types of spectra are reported in this work :

- (1) plasma spectral background containing  
analyte species of interest
- (2) background subtracted spectra with only the  
line emission spectra of analyte species



In the second case, the background signals were obtained by aspirating distilled water.

### C. Characterization of Emission Noise with a Photodiode Array Spectrometer

Noise is unwanted fluctuation and variation in the measured intensity of a signal. The magnitude of the fluctuation is usually expressed in term of r.m.s. noise current or voltage. However, it is often defined as the standard deviation of a number of repeated measurements of the signal. If the number of repeated measurements are large then the standard deviation approximates the r.m.s. noise (128).

In atomic spectroscopy, the signal-to-noise ratio is defined as the ratio of signal intensity ( $S$ ) to the standard deviation ( $\sigma$ ) of the repeated measured intensity.

$$S / N = S / \sigma \quad (11)$$

This quantity is useful in expressing the precision that can be obtained from a given instrument and operating conditions. The reader may refer to R.M.Belchamber's



dissertation for a detailed discussion of the noise characterization of an ICP for atomic emission spectroscopy (129).

All standard deviations and signal-to-noise ratios reported in this work were based on signal integration periods of 10s and 32 repeated measurements. All signals were background subtracted. The background signals were obtained by aspirating distilled water and the mean of 32 repeated measurements were taken. The signal-to-noise ratios were then calculated by dividing the mean of 32 background subtracted signal measurements by their standard deviation.

Using the experimental set-up discussed in Chapter II, the array integration time can be varied from 40ms to over 20s. Since the sensitivity of the array is linearly related to integration time, two apparently equivalent ways of achieving a desired measurement time are possible if one thinks only in terms of the total signal. One is to use an array integration time equal to the desired measurement time (10s) but in most cases array saturations are observed with such long integration times. A second method is to use a short integration time and a signal average of sufficient repetitive scans to achieve the total desired measurement time.

Previous work by Salin and Horlick (127) has illustrated that the standard deviation of the array

The first part of the paper discusses the importance of the study and the objectives of the research. It also outlines the methodology used in the study and the results obtained. The second part of the paper discusses the implications of the study and the conclusions drawn from the research. It also discusses the limitations of the study and the areas for future research. The third part of the paper discusses the significance of the study and the contributions it makes to the field. It also discusses the practical applications of the study and the policy implications of the research. The fourth part of the paper discusses the ethical considerations of the study and the measures taken to ensure the integrity of the research. It also discusses the dissemination of the research findings and the impact of the study on the field. The fifth part of the paper discusses the acknowledgments of the study and the funding sources. It also discusses the references used in the study and the sources of information. The sixth part of the paper discusses the appendices of the study and the additional information provided. It also discusses the index of the study and the location of the information. The seventh part of the paper discusses the glossary of the study and the definitions of the terms used. It also discusses the bibliography of the study and the list of references. The eighth part of the paper discusses the conclusion of the study and the final thoughts of the researcher. It also discusses the future of the study and the potential for further research. The ninth part of the paper discusses the disclaimer of the study and the statement of the researcher. It also discusses the contact information of the researcher and the ways to reach the researcher. The tenth part of the paper discusses the copyright of the study and the permission to use the research findings. It also discusses the terms and conditions of the study and the rules governing the use of the research findings. The eleventh part of the paper discusses the privacy of the study and the protection of the personal information of the participants. It also discusses the confidentiality of the study and the measures taken to ensure the privacy of the participants. The twelfth part of the paper discusses the integrity of the study and the measures taken to ensure the accuracy of the research findings. It also discusses the transparency of the study and the openness of the researcher to criticism and feedback. The thirteenth part of the paper discusses the accountability of the study and the responsibility of the researcher. It also discusses the sustainability of the study and the long-term impact of the research findings. The fourteenth part of the paper discusses the relevance of the study and the applicability of the research findings to the real world. It also discusses the timeliness of the study and the currentness of the research findings. The fifteenth part of the paper discusses the originality of the study and the novelty of the research findings. It also discusses the significance of the study and the importance of the research findings. The sixteenth part of the paper discusses the impact of the study and the influence of the research findings on the field. It also discusses the contribution of the study and the value added by the research findings. The seventeenth part of the paper discusses the legacy of the study and the lasting impact of the research findings. It also discusses the heritage of the study and the cultural significance of the research findings. The eighteenth part of the paper discusses the memory of the study and the recollection of the research findings. It also discusses the history of the study and the evolution of the research findings. The nineteenth part of the paper discusses the future of the study and the potential for further research. It also discusses the prospects of the study and the opportunities for the research findings. The twentieth part of the paper discusses the conclusion of the study and the final thoughts of the researcher. It also discusses the future of the study and the potential for further research.



background signal (limited by electronic readout noise) is independent of integration time. Therefore, the contribution of array background noise to any particular measurement would be similar to using the first approach. They have also indicated that the array background noise became the limiting noise in the system if short integration times with a large number of repeated scans were used. However, when long integration times with a small number of repeated scans were used, the electronic readout noise ceased to be the limiting factor and the noise was then associated only with the ICP analyte signal. Therefore, all spectra for signal-to-noise ratio studies were measured using the longest possible integration time without saturating the array.

A brief study was carried out in order to determine the precision of the signal-to-noise ratios determined by the 1024 element photodiode array measurement system. The experimental operating conditions chosen for the study were 2.0 Kw plasma power, 15 L/min coolant flow and 1.0 L/min aerosol flow. The signal-to-noise ratios of the calcium ion emission line (CaII 393.4 nm) were calculated for five identical experiments under different mixed gas plasmas. For 100% N<sub>2</sub>, 100% O<sub>2</sub>, 100% Air and 70% He cooled plasmas, the observation height was set to observe the calcium emission at 2 mm above the load coil. In the case of the conventional



argon plasma, it was set at 15 mm above the load coil.

A set of signal-to-noise ratios for various types of mixed gas plasmas is given in Table V.1. In addition, for each mixed gas plasma, the determination of signal-to-noise ratios for the calcium emission were repeated five times using similar operating conditions. The mean value and relative standard deviation of signal-to-noise ratios determined for each plasma are also tabulated in Table V.1. Overall, the relative standard deviation varies from 4.8% to 7.9%.

This set of data indicates that during the course of the signal-to-noise ratio experiments, the plasma and photodiode array measurement system remained very stable. The stability of this system allows a meaningful comparison and interpretation of the performances of various types of mixed gas plasmas.

It is seen from Table V.1 that the signal-to-noise ratios obtained for Ar, 100% N<sub>2</sub>, 100% O<sub>2</sub> or 100% Air cooled plasmas are comparable to one another. However, the signal-to-noise ratio increases by a factor of 2 for 70% He cooled plasma. Since these data were measured for Ar, 100% N<sub>2</sub>, 100% O<sub>2</sub>, 100% Air and 70% He cooled plasmas only at one position, these data cannot be taken as a measure of analytical performances of mixed gas plasmas. Studies of the signal-to-noise ratios for various gas combinations observed



TABLE V.1

PRECISION TESTS FOR THE PHOTODIODE ARRAY DETECTION SYSTEM

S/N ratios table, Ca(II) 393.37nm

Type	Run					Mean	Rel Std-Dev
	1	2	3	4	5		
100% Ar	136	146	152	158	144	147	5.7 %
100% N <sub>2</sub>	120	129	108	110	126	118	7.9 %
100% O <sub>2</sub>	131	134	148	152	140	141	6.3 %
100% Air	156	142	144	161	166	154	6.8 %
70 % He	221	225	204	211	228	217	4.6 %

All tests were operated at 2 Kw Power and 1.0 L/min aerosol flow rate.  
 Ar-ICP measured at 15mm above the load coil.  
 100% N<sub>2</sub>, O<sub>2</sub>, Air and He cooled ICPs measured at 2mm above the load coil.





at different positions are required before any definitive conclusions can be drawn on the analytical capabilities and performances of various types of mixed gas plasmas.

D. Spectral Characteristics and Evaluation  
of Mixed Gas Plasmas  
(spectral region centered at 373 nm)

Eight spectra are presented in Figures 29 to 32. Each frame represents the emission spectrum of the mixed gas plasma with a 1.0 ppm solution of calcium nebulizing. The 50 nm spectral window of the photodiode array spectrometer was centered at about 373 nm. The experimental operating conditions were identical to those discussed in the previous section.

1. Nitrogen-Argon Mixed Gas Plasmas

Since most of the spectra measured in this study are presented in an analogous format, the effect of nitrogen on the background emission intensity containing calcium emission lines will be discussed in some detail. In Figure 29, each column consists of four spectra measured at the same observation height i.e. either at 2 mm or at 10 mm



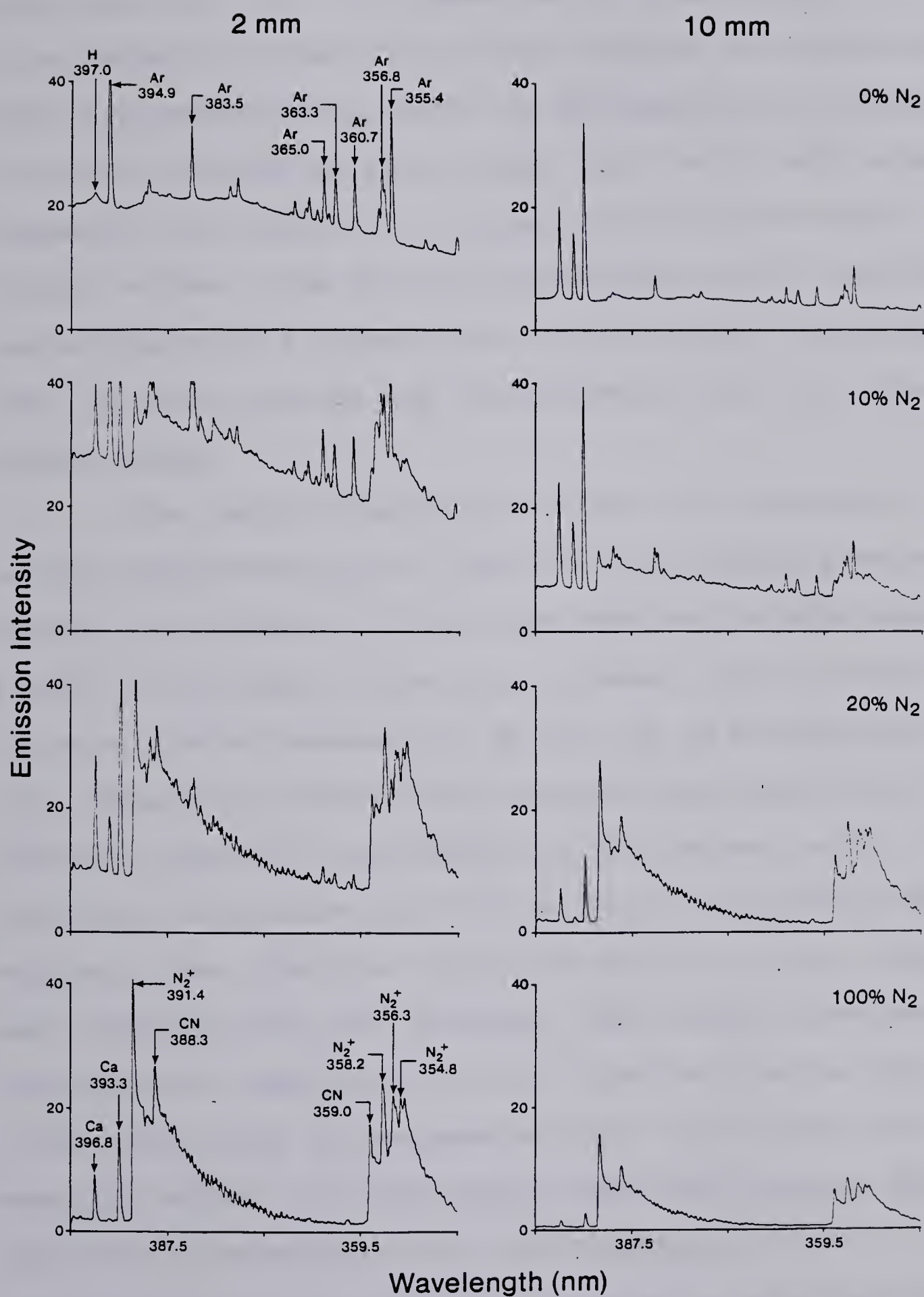


Fig. 29. Background emission spectra for N<sub>2</sub>-Ar mixed gas ICPs at 2 mm and 10 mm above the load coil.



above the load coil. Each spectrum in this column illustrates the effect of nitrogen present in the coolant flow of a conventional Ar-ICP on the background intensity containing calcium emission lines. The row in each column represents the amount of nitrogen introduced into the coolant stream : the top row corresponds to a 0% nitrogen cooled plasma or a conventional argon plasma, the second row 10%, the third row 20% and the bottom row 100% nitrogen cooled plasma.

The spectra presented in Figure 29 illustrate several characteristics of the plasma and analyte emission. Several argon emission lines were observed in this spectral region. In the case of the argon plasma, argon emission lines were more intense at 2 mm than at 10 mm above the load coil. Note that the 397.0 nm hydrogen line represents a potential spectral interference in the determination of calcium if the calcium ion line at 396.8 nm is chosen as the analysis line. When the coolant stream of an argon plasma was converted into 100% nitrogen, the plasma background was somewhat more complicated as two molecular species (CN and  $N_2^+$ ) have relatively strong band emission spectra in this spectral region. In other words, these band spectra would give rise to severe spectral interferences in the determination of other emitting species in this spectral region. Note that in the case of the 100% nitrogen cooled





plasma the calcium 393.3 nm line is 2 nm from the nearest  $N_2^+$  band spectra, therefore the determination of calcium using this analytical line will not be affected.

Another interesting spectral characteristic of the argon and nitrogen cooled plasmas is the broadening of the hydrogen 397.0 nm and 388.9 nm lines as a consequence of the Stark effect. These hydrogen lines appear to be broader than their neighboring argon or calcium emission lines. The Stark effect will be discussed in Chapters VII to IX. It is also interesting to note that the excitation potentials of these hydrogen lines are over 13 eV which gives a strong indication that the ICP discharge has the capability of exciting energetic species.

Continuum emission from the ICP is produced as a consequence of a radiative recombination process (130,131). The non-zero baseline of the spectra shown in Figure 29 is a result of the continuum emission. The continuum emission intensity from an argon or a mixed gas plasma is generally more intense within the load coil and drops rapidly with increasing distance away from the load coil. At 2 mm observation height, the continuum intensity increased when the argon plasma was converted into a 10% nitrogen cooled plasma. However, further increase in the percentage of nitrogen in an argon ICP decreased the continuum intensity. From these observations, it can be generalized that a 10%



nitrogen cooled plasma is a more energetic emission source than the argon or 20 to 100% nitrogen cooled plasmas.

Emission from calcium ions was not observed for the argon plasma at 2 mm above the load coil. In the case of an argon and 10% nitrogen cooled plasma, the best observation height for the calcium ion emission was about 10 mm above the load coil. However, the best viewing zone for the CaII lines was 2 mm above the load coil for 20% to 100% nitrogen cooled plasmas. Since the continuum intensity for the 100% nitrogen cooled plasma at 2 mm was fairly small, a high analyte intensity observed at this height indicated a superior signal-to-background ratio. It can be observed from Figure 29 that the signal-to-background ratio obtained for a 100% nitrogen cooled plasma at 2 mm above the load coil is comparable to that obtained for an argon plasma at 10 mm. The 10% nitrogen cooled plasma appeared to give a higher signal-to-background ratio and thus potentially higher detection power than an argon plasma at 10 mm observation height.

The signal-to-noise ratios for various percentages of nitrogen cooled plasmas measured at different observation heights for the CaII line (393.3 nm, 1.0 ppm) are shown in Table V.2. At lower observation heights (about 2 mm), improvement in signal-to-noise ratio was realized by increasing nitrogen concentration in the coolant flow from 0



TABLE V.2

SIGNAL-TO-NOISE RATIOS FOR N<sub>2</sub>-AR MIXED GAS PLASMAS

Ca(II) 393.4 nm

Height above load coil, (mm)	% N <sub>2</sub> ( Coolant)				
	0%	10%	20%	50%	100%
20	204	130	26	15	6
15	200	284	154	77	10
10	189	462	280	130	51
5	100	300	423	185	87
2	70	112	210	230	176





to 100%. This clearly indicates that the signal-to-noise ratios for 20 to 100% nitrogen cooled plasmas measured in the region of the load coil were higher than that of the argon plasma measured at the same height. At 2 mm above the load coil, the best signal-to-noise ratio was obtained from a 50% nitrogen cooled plasma. As the observation height was increased to 5 mm above the load coil, the 20% nitrogen cooled plasma provided the best signal-to-noise ratio in that particular viewing zone. The 10% nitrogen cooled plasma provided the best signal-to-noise ratio at 10 and 15 mm above the induction coil. However when the observation height was increased to 20 mm above the load coil, the signal-to-noise ratios decreased with increasing nitrogen in the coolant flow.

The overall signal-to-noise ratios were highly dependent on both the concentration of nitrogen in the coolant flow and the observation height. The signal-to-noise ratios obtained from the 10 and 20% nitrogen cooled plasmas were approximately two to three times greater than those obtained from the optimized argon discharge (Table V.2). However the signal-to-noise ratios measured for the 50 and 100% nitrogen cooled plasmas at 2 mm above the load coil were comparable to those measured for the argon discharge above 10 mm observation height. Note that the signal-to-noise ratios for the 100% nitrogen cooled plasmas



dropped drastically with increasing distance away from the induction coil.

These results are consistent with the visual observations of the mixed gas plasmas discussed and illustrated in Chapters III and IV. As the concentration of nitrogen is increased, the plasma shrinks in size and volume, thus peak maximum and the best signal-to-noise ratios for the 100% nitrogen cooled plasma will occur somewhere closer to the induction coil. All these observations implied that the viewing zone for the 100% nitrogen cooled plasma has to be set at 2 to 4 mm above the load coil in order to fully utilize its analytical potentials.

## 2. Oxygen-Argon Mixed Gas Plasmas

Some of the spectral characteristics of the oxygen-argon mixed gas plasmas are illustrated in Figure 30. The experimental operating conditions chosen for this study were identical to those described earlier for the nitrogen cooled plasmas. The background spectra obtained from the oxygen cooled plasmas were somewhat different from those observed in the nitrogen cooled or argon based discharges. In the case of the oxygen cooled plasmas, the argon emission lines were reduced considerably. Since the generation of



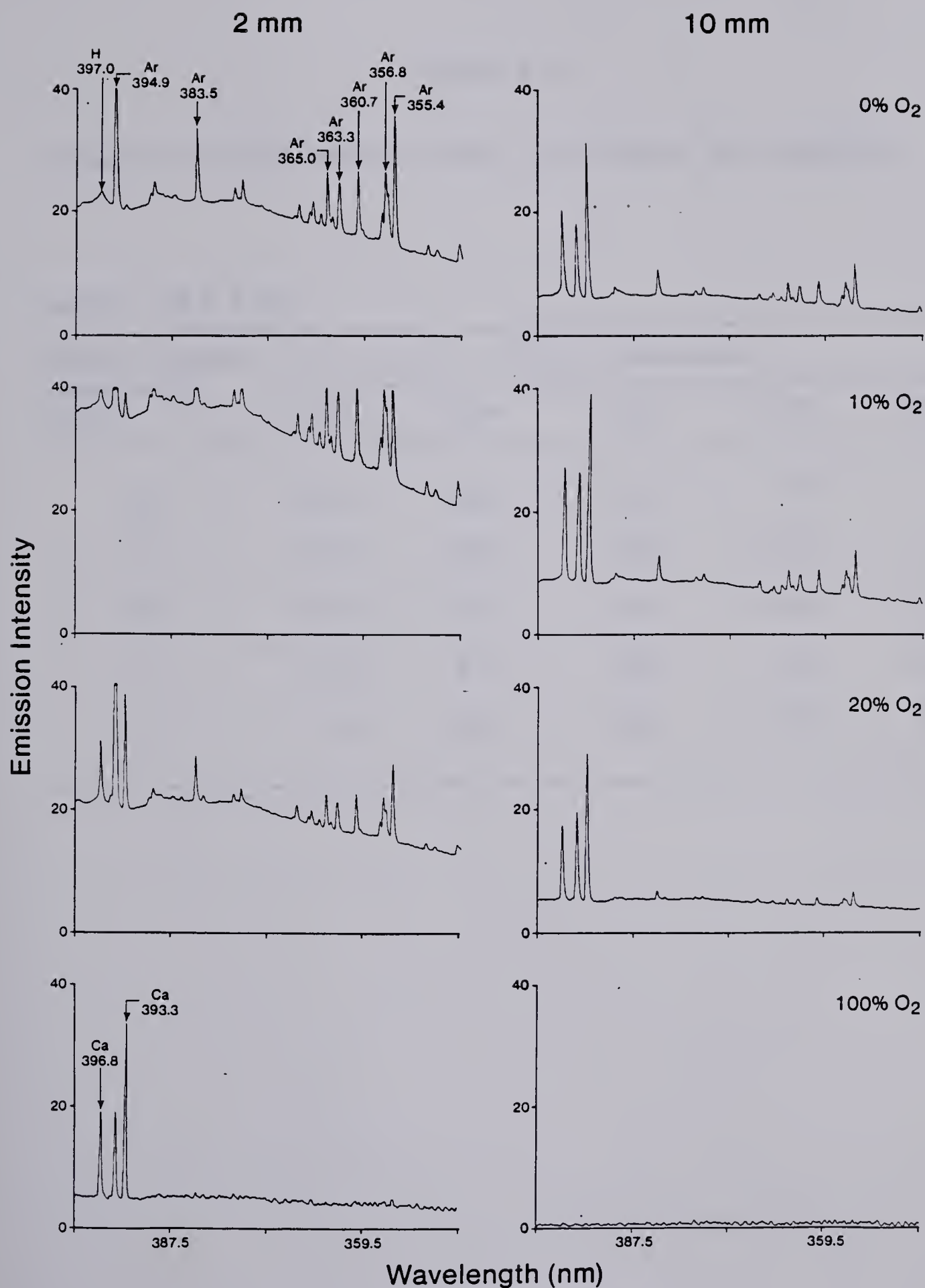


Fig. 30. Background emission spectra for  $O_2$ -Ar mixed gas ICPs at 2 mm and 10 mm above the load coil.





TABLE V.3

SIGNAL-TO-NOISE RATIOS FOR O<sub>2</sub>-AR MIXED GAS PLASMAS

Ca(II) 393.4 nm

Height above load coil, (mm)	% O <sub>2</sub> (Coolant)				
	0%	10%	20%	50%	100%
20	204	144	105	77	4
15	200	220	159	127	31
10	189	384	221	204	50
5	100	275	350	270	204
2	70	164	189	288	265



nitrogen based molecular species (CN or  $N_2^+$ ) depends primarily on the presence of nitrogen in the plasma, the emission intensity of these species should be reduced when oxygen is introduced in place of argon. It is clearly illustrated in Figure 30 that the spectral background of a 100% oxygen cooled plasma observed at 2 mm above the load coil is completely free from the potential spectral interferences caused by the presence of the complicated CN and  $N_2^+$  band emission spectra.

As 10% oxygen was introduced into the coolant flow of an argon ICP, the background continuum was considerably higher than that of the argon or the nitrogen-argon mixed gas plasmas. This observation indicates that a 10% oxygen cooled plasma might be a more energetic source than an argon or a nitrogen cooled discharge. In the case of a 100% oxygen cooled plasma, calcium ion emission lines were not observed at 10 mm above the load coil. It can be seen from Figure 30 that the best signal-to-background ratio for the 100% oxygen cooled ICP occurs at 2 mm above the induction coil. This figure also shows that the signal-to-background ratios for 0 to 100% oxygen cooled plasmas are comparable to one another.

The signal-to-noise ratios for various  $O_2$ -Ar mixed gas ICPs measured at different observation heights for the CaII 393.4 nm line are presented in Table V.3. These data clearly indicate that the precision obtained from a 100%



oxygen cooled plasma is comparable to that of the argon discharge. The greatest enhancement of the signal-to-noise ratio was obtained for 10 and 20% oxygen cooled plasmas observed at 5 to 10 mm above the load coil. Overall, the signal-to-noise ratios measured for the 10% and 20% oxygen cooled ICPs observed at 5 to 10 mm above the load coil were superior to those observed in the optimized conventional argon plasma. In the case of the 50 and 100% oxygen cooled plasmas, the signal-to-noise ratios measured at 2 mm above the load coil were comparable to the best result achieved for the argon ICP.

### 3. Air-Argon Mixed Gas Plasmas

A series of emission spectra for various percentages of air present in the conventional argon plasma are shown in Figure 31. These emission spectra were also measured at 2 and 10 mm above the load coil. The experimental operating conditions were identical to those discussed earlier.

Several generalized observations can be anticipated with respect to the spectra of the air-argon mixed gas plasma. First, if the nitrogen and oxygen cooled plasmas (Figures 29 and 30) are used as a basis for comparison, the intensity of the background continuum obtained from the air cooled plasmas should be somewhat in between the above





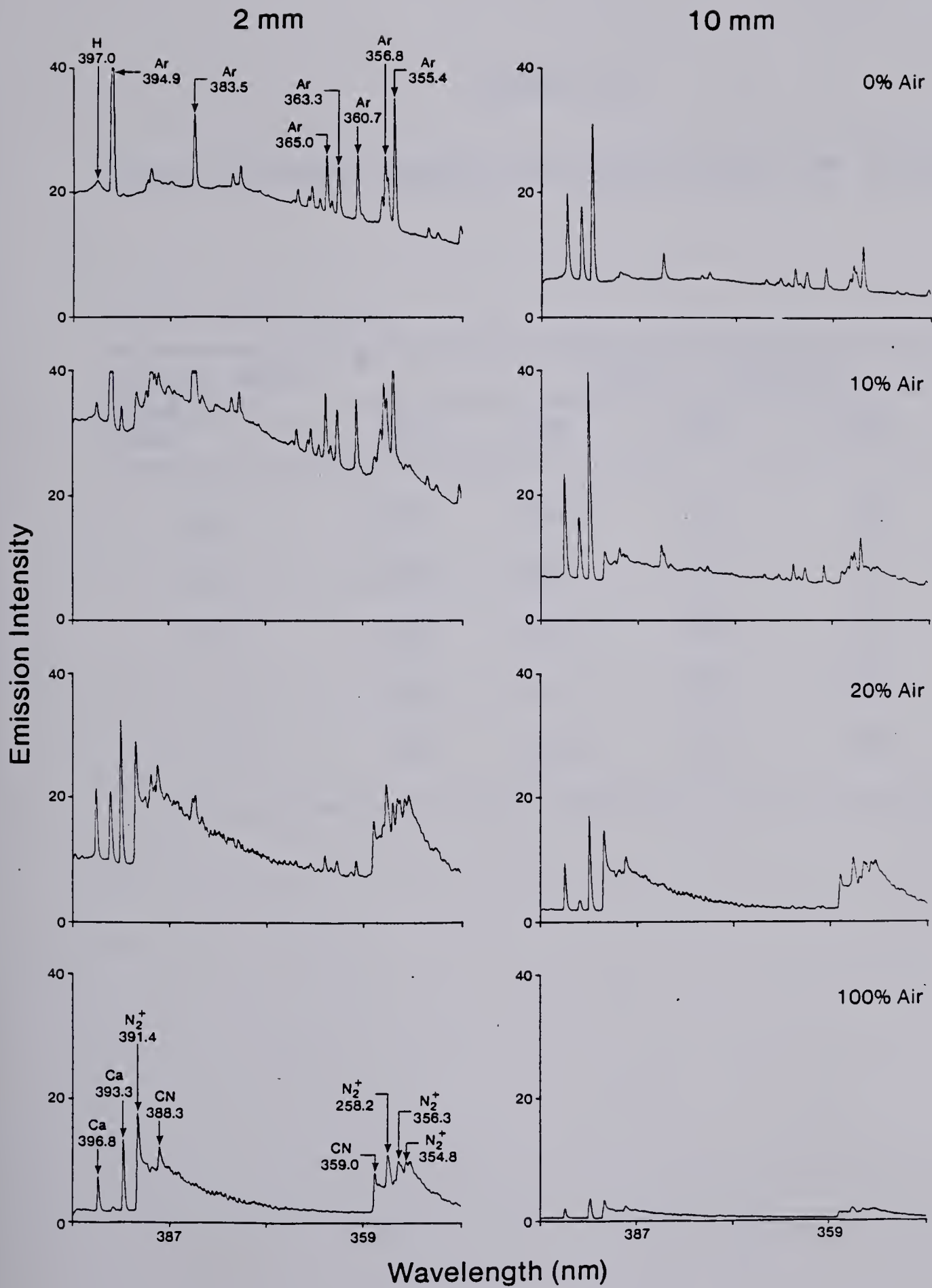


Fig. 31. Background emission spectra for Air-Ar mixed gas ICPs at 2 mm and 10 mm above the load coil.



TABLE V.4

## SIGNAL-TO-NOISE RATIOS FOR AIR-AR MIXED GAS PLASMAS

Ca(II) 393.4 nm

Height above load coil, (mm)	% Air ( Coolant )				
	0%	10%	20%	50%	100%
20	204	184	116	56	8
15	200	207	195	68	22
10	189	442	360	110	56
5	100	215	285	220	132
2	70	121	150	142	151



cases. This is anticipated by nature of the composition of air which consists of 78% nitrogen and 21% oxygen. Second, the intensity of the complex cyanogen (CN) and nitrogen ( $N_2^+$ ) band emission spectra should be less than that observed in the nitrogen cooled plasmas. Third, the net intensity of the calcium ion lines increased by a factor of 1.5 when air was introduced into the coolant flow of the argon plasma.

In the case of the 10% air cooled plasma observed at 10 mm above the load coil, the net enhancement in analyte intensities accompanied with a relatively constant background level implied that 10% air cooled ICP provided a superior signal-to-background ratio over the argon ICP (Figure 31). However, the net analyte emission intensities deteriorated significantly at 10 mm observation height as the percentage of air in the coolant flow of an argon plasma was increased to 100%. As shown in Figure 31, if argon plasma observed at 10 mm above the load coil was used as a basis for comparison, the calcium emission intensities obtained from a 100% air cooled plasma at 2 mm observation height provided a comparable signal-to-background ratio under similar operating conditions.

The signal-to-noise ratios for various types of air cooled plasmas measured at different heights for the CaII line are presented in Table V.4. The signal-to-noise ratios for the air cooled plasmas should show similar in trends to





those of the nitrogen and oxygen cooled ICPs, i.e. (a) the signal-to-noise ratio improved by a factor of 2 to 3 when the argon plasma was converted into a 10% air cooled plasma, (b) the signal-to-noise ratio value obtained for a 100% air cooled plasma at 2 mm above the load coil was comparable to that for the conventional argon ICP, (c) in the case of the 100% air cooled plasma, raising the observation height caused a significant deterioration in the signal-to-noise ratio, and finally (d) the optimized signal-to-noise ratio for a 10% air cooled plasma was measured at 10 mm above the load coil, for 20% at 10 mm, for 50% at 5 mm and for 100% air cooled ICP at 2 mm above the induction coil.

#### 4. Helium-Argon Mixed Gas Plasmas

It is clear from the emission spectra presented in Figure 32 that the addition of helium into the coolant flow of an argon plasma generally reduces the intensities of the analyte, hydrogen and argon emission lines. All the emission bands associated with the cyanogen and nitrogen species were not observed either at higher or lower observation height. Emission from helium neutral atom or ion lines has not been observed in the helium cooled plasmas. The absence of these lines indicates that the ICP discharge does not have the capability of exciting species with excitation potentials



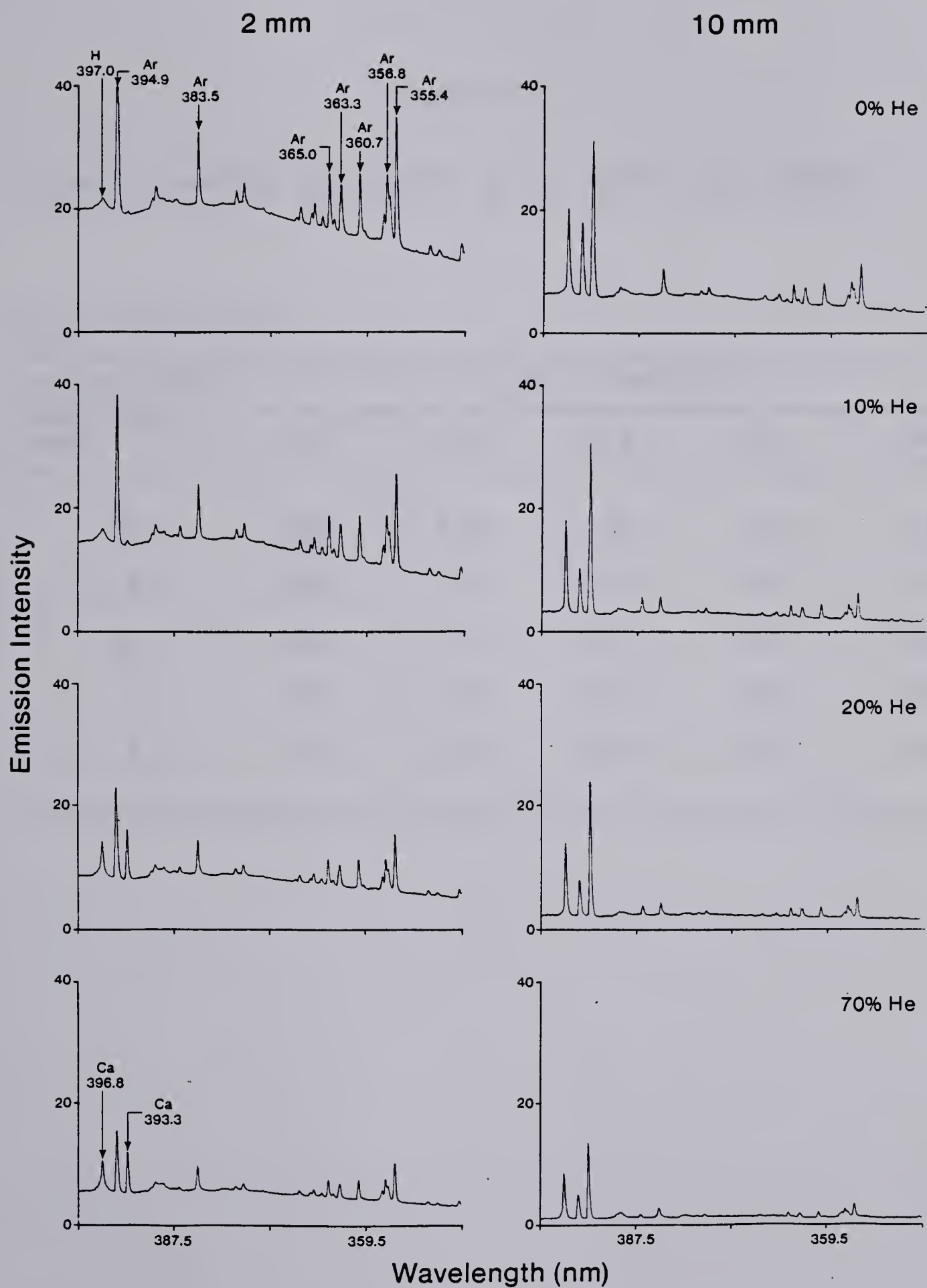


Fig. 32. Background emission spectra for He-Ar mixed gas ICPs at 2 mm and 10 mm above the load coil.



TABLE V.5

## SIGNAL-TO-NOISE RATIOS FOR HE-AR MIXED GAS PLASMAS

Ca(I) 393.4 nm

Height above load coil, (mm)	% He ( Coolant )				
	0%	10%	20%	50%	70%
20	204	148	85	88	15
15	200	177	142	103	76
10	189	275	200	180	100
5	100	200	289	240	180
2	70	102	100	120	225





greater than 25eV. It is also interesting to note that the continuum emission intensity decreases with the presence of helium in an argon ICP. The enhancement of calcium emission lines was not observed for the 10% helium cooled plasma in contrast to most mixed gas plasmas. The net calcium emission intensities observed at 10 mm above the load coil remained relatively constant for 0 to 20% helium cooled plasmas. The intensity of the calcium lines decreased by a factor of 2 when a combination of 70% helium - 30% argon was used as the coolant gas. Several argon emission lines were also present even in a 70% helium cooled ICP, the most prominent one being the 394.8 nm line.

The above trends were generally reflected in the signal-to-noise studies of the helium argon mixed gas plasmas (Table V.5). The best signal-to-noise ratios measured for various types of helium plasmas were either comparable or inferior to those measured for the argon discharge. Under the experimental conditions employed in this study, the results discussed so far do not indicate any significant advantages of using a helium cooled plasma. Furthermore, it should also be noted that the helium cooled plasma is more costly to operate than the conventional argon discharge.



## 5. Final Comparisons of the Mixed Gas Plasmas

(spectral region centered at 373 nm)

A comparison of signal-to-noise ratios for the CaII 393.4 nm line measured at the best observation height for various types of mixed gas plasmas is presented in Table V.6. This signal-to-noise table indicates three distinct patterns as the conventional argon plasma was converted into a mixed gas ICP. First, most of the mixed gas plasmas showed superior signal-to-noise ratios when a combination of 10% foreign gas - 90% argon was used as the coolant gas. Second, the best signal-to-noise ratios were measured at a lower observation height than the conventional argon plasma. Third, most of the mixed gas plasmas except helium cooled plasma improved the signal-to-noise ratios of the CaII line by a factor of two to three.

Clearly, the mixed gas plasma has the potential of significantly expanding the overall analytical capability of the ICP. Analysis of the signal-to-noise ratios suggests that at lower observation heights, about 2 to 5 mm above the load coil, the signal-to-noise ratios obtained for the 100 % N<sub>2</sub>, O<sub>2</sub> or Air cooled plasma are equivalent to that of the conventional argon discharge measured at 15 mm above the induction coil. In addition, it should be noted that the signal-to-noise ratios for the 100 % mixed gas plasmas



TABLE V.6

COMPARISON OF SIGNAL-TO-NOISE RATIOS  
FOR MIXED GAS PLASMAS

Gas (Coolant)				
	Ar	N <sub>2</sub>	O <sub>2</sub>	He
% (Coolant)	100%	10%	10%	20%
Height above load coil, (mm)	20	10	10	5
Ca(II) 393.4 nm S/N ratio	204	462	384	289





decrease significantly with increasing distance away from the load coil. Therefore to draw a generalized conclusion between the comparative analytical performances of the argon and mixed gas plasmas, the investigation of signal-to-noise ratio has to be conducted at different observation heights for both plasmas.

#### E. Spectral Characteristics and Evaluation of Mixed Gas Plasmas (spectral region centered at 228 nm)

Some of the spectral characteristics of the mixed gas plasmas at different observation heights are further illustrated in Figures 33-42. The 50 nm spectral window of the photodiode array spectrometer is now centered at 228 nm. The experimental operating conditions chosen for this study are identical to those described earlier. This spectral region is perhaps more important than the 373 nm range because most of the sensitive analytical lines fall in the 180 to 280 nm region. Cadmium solution was aspirated into the various types of mixed gas plasmas. It is advantageous to evaluate the performances of the mixed gas plasmas using a cadmium solution because CdI 228.8 nm, CdII 226.5 nm and CdII 214.4 nm lines have about equal sensitivity in the



argon plasma source.

### 1. Nitrogen-Argon Mixed Gas Plasmas

Spectra of a nitrogen-argon mixed gas plasma observed at different heights with a 10.0 ppm cadmium solution nebulizing are shown in Figure 33. This figure is identical in format to those described earlier (Figures 29 to 32). The argon emission lines, CN and  $N_2^+$  band emission spectra were not observed in this spectral region. However, the plasma spectral background is complicated as the molecular species (NO) have relatively strong band emission spectra in this spectral region. The NO bandheads lie between the cadmium emission lines. Note that a carbon (CI 247.9 nm) line is present in this region. This is due to the carbon impurity in the water and  $CO_2$  in the main gas supply.

The plasma spectral background containing Cd lines as a function of various percentages of nitrogen present in the coolant flow of an argon discharge is shown in Figure 33. The NO bandheads were not observed in the case of argon plasma. As nitrogen was introduced into the coolant flow, the continuum level increased significantly as the nitrogen reduced the plasma volume. However, the continuum level decreased drastically when more than 20% nitrogen was introduced to the coolant stream. The NO bandheads could be



seen for the 20% to 100% nitrogen cooled plasmas.

It was noted earlier that the photodiode array spectrometer measurement system has background subtracted capability. The cadmium spectra with the background subtracted are shown in Figure 34. The background subtracted spectra for 0 to 100% nitrogen cooled plasmas observed at 2 to 20mm above the induction coil is also illustrated in this figure. It can be clearly seen that the net analyte emission intensities are highly dependent on both the percentage of nitrogen present in the coolant flow and the observation height. It is also clear from this figure that a 10% nitrogen cooled plasma observed at 10 mm above the load coil provides the highest net emission intensities of all the nitrogen cooled plasmas under study. However, the cadmium intensities for the 100% nitrogen cooled ICP at 2 mm observation height was three times smaller than that observed for the argon discharge at 15 mm above the load coil.

It should be noted that the Cd ion emission is more affected by the presence of nitrogen in the coolant flow than its corresponding neutral atom emission. It is seen that the intensity of the neutral atom line increases only about 30% as the argon plasma is converted into a 10% nitrogen cooled plasma, but the intensities of the cadmium ion lines increased by a factor of 3. These trends are generally





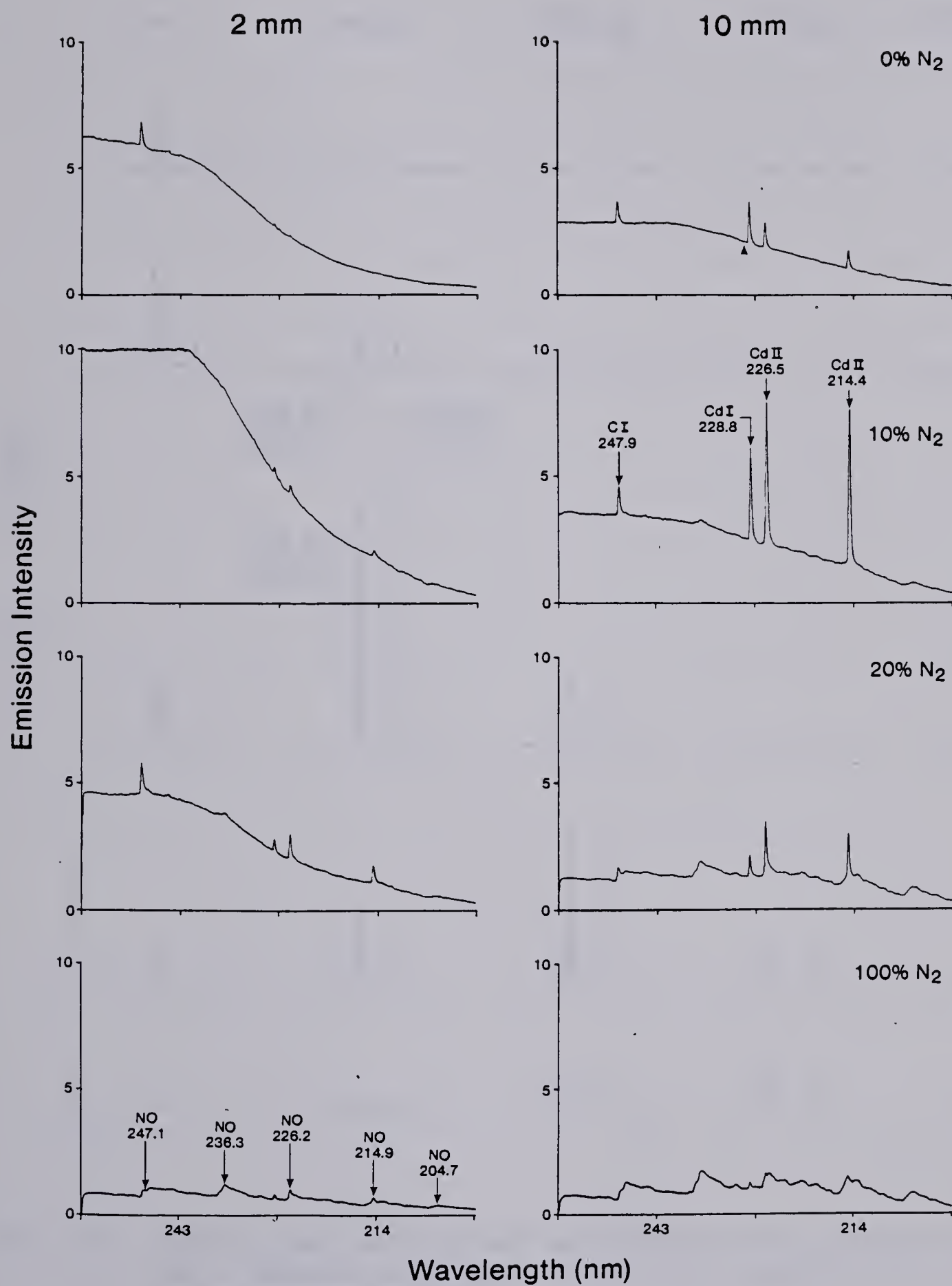


Fig. 33. Background emission spectra for N<sub>2</sub>-Ar mixed gas ICPs at 2 mm and 10 mm above the load coil.



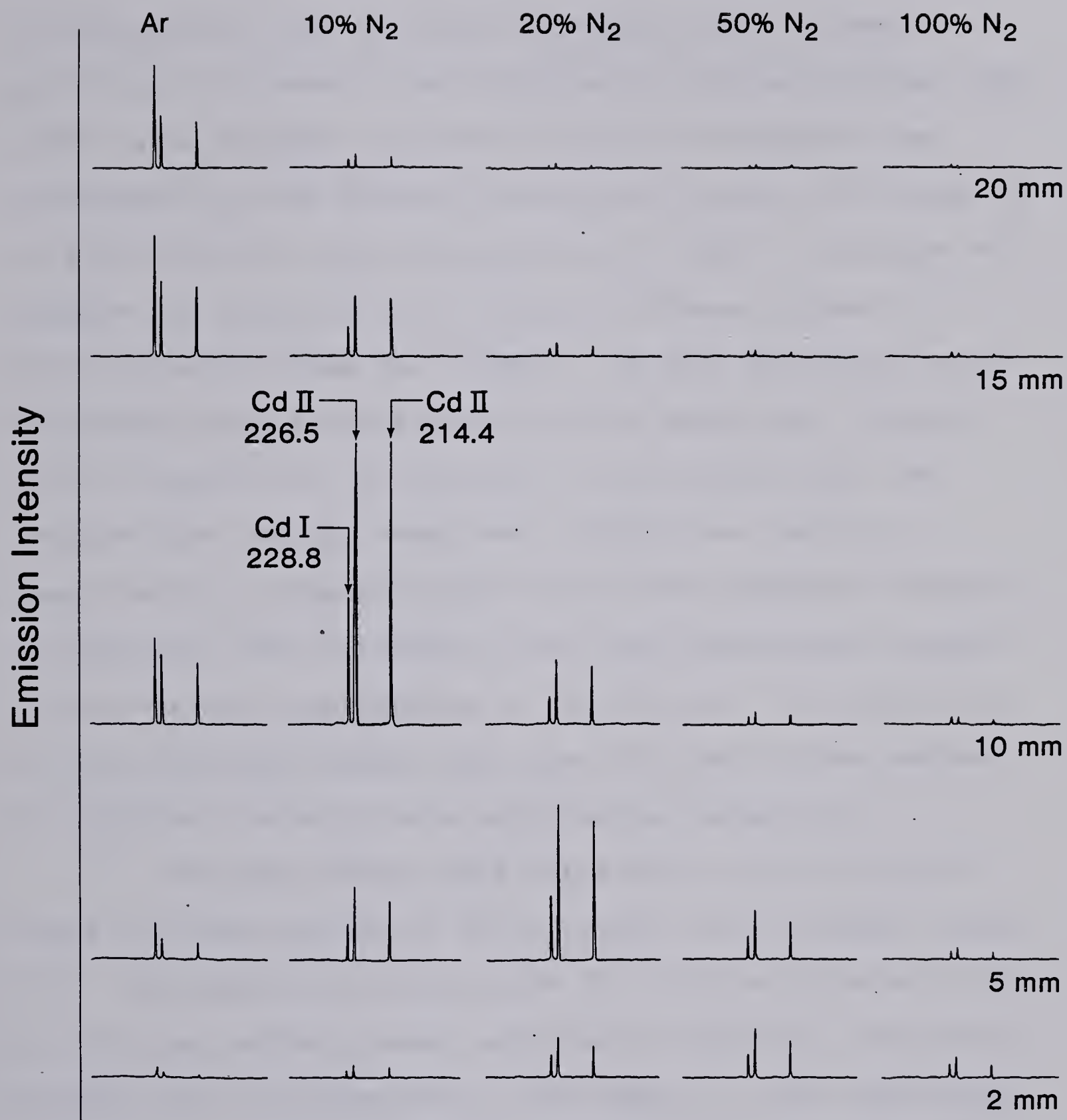


Fig. 34. Background subtracted spectra of CdI and CdII lines as a function of  $N_2$ -Ar mixed gas composition and observation height.



consistent for all the nitrogen cooled plasmas under investigation. Most detection systems currently used in analytical or research laboratories are photomultiplier tube (PMT) based systems; therefore they are limited to the measurement of one spectral resolution element at a time. If only the neutral atom emission line is used to evaluate and compare the sensitivity of various different types of nitrogen-argon mixed gas plasmas, the data collected may be misleading because this spectral line shows only limited gain in sensitivity as nitrogen is introduced into the coolant flow. On the other hand, significant gain in sensitivity is observed when the ion line emission intensity is measured. The photodiode array based measurement system is perhaps more appropriate in carrying out the evaluations of the mixed gas plasmas than the PMT based system because it provides a simultaneous multichannel capability.

The above trends were reflected in the studies of signal-to-noise ratios of the nitrogen cooled plasmas (Table V.7). The signal-to-noise ratios for various different types of nitrogen cooled plasmas measured at different observation heights are also presented in the table. In this experiment, two cadmium lines were used to evaluate the precision of measurement (signal-to-noise ratios) of the mixed gas plasmas, one being the ion line (CdII 214.4 nm) and the other being the neutral atom line (CdI 228.8 nm). In the





TABLE V.7

SIGNAL-TO-NOISE RATIOS FOR N<sub>2</sub>-AR MIXED GAS PLASMAS

(a) Cd(II) 214.4nm

Height above load coil, (mm)	% N <sub>2</sub> ( Coolant )				
	0%	10%	20%	50%	100%
20	25	33	3.0	2.8	1.9
15	31	88	9.2	4.2	3.3
10	30	95	44	5.9	9.3
5	8.7	110	80	29	13
2	3.4	17	22	40	13

(b) Cd(I) 228.8nm

Height above load coil, (mm)	% N <sub>2</sub> ( Coolant )				
	0%	10%	20%	50%	100%
20	58	22	3.4	3.2	4.0
15	64	44	6.4	4.4	5.0
10	43	59	25	6.9	11
5	14	33	45	19	14
2	3.6	6.5	23	29	15



case of the ion line (Table V.7a), a 10% nitrogen cooled plasma measured at 5 mm above the load coil offered a better signal-to-noise ratio than the argon plasma observed at any height and anytime. At 10 mm observation height, the signal-to-noise ratio for the 10% nitrogen cooled plasma was two times greater than that of the argon discharge. In the case of 20% nitrogen cooled plasma, the best signal-to-noise ratio was measured at 5 mm above the load coil. The signal-to-noise ratios increased only about 30% as the argon discharge was converted into a 50% nitrogen cooled ICP. In this case, the best viewing zone was at 2 mm above the induction coil. Introduction of a 100% nitrogen - 0% argon gas combination into the coolant stream deteriorated the signal-to-noise ratio by a factor of 2. However, this disadvantage in signal-to-noise ratio performance is offset by advantages of cheaper operating cost and lower background emission in a 100% nitrogen cooled ICP.

In the case of the cadmium neutral atom line (Table V.7b), the signal-to-noise ratios remained relatively constant for the argon and the 10% nitrogen cooled plasma measured at 15 and 10 mm above the load coil respectively. The signal-to-noise ratio decreases significantly as more than 20% nitrogen - 80% argon gas combination was introduced into the coolant stream. In the case of the 100% nitrogen cooled plasma, the signal-to-noise ratio decreased by a



factor of 4 compared to that of the argon discharge. The overall signal-to-noise ratios for the cadmium neutral atom line measured from the nitrogen-argon mixed gas plasmas were inferior to those measured from the argon discharge.

## 2. Oxygen-Argon Mixed Gas Plasmas

The spectral characteristics of various types of oxygen-argon mixed gas plasmas observed at different heights are illustrated in Figure 35. The background intensity increased considerably when the observation height was lowered from 10 to 2 mm above the load coil. The plasma background also increased significantly when a 10% oxygen - 90% argon mixed gas combination was introduced into the coolant stream, but the background continuum decreased as the percentage of oxygen in the coolant flow was made greater than 20%. The NO bandheads were not observed in this case.

The background subtracted spectra containing cadmium ion and neutral atom lines are shown in Figure 36. These spectra were collected at different observation heights and for various combinations of oxygen and argon in the coolant flow. In contrast to the spectra collected for the nitrogen cooled plasmas where the ion lines were more sensitive than the neutral atom line, both the ion and neutral atom lines





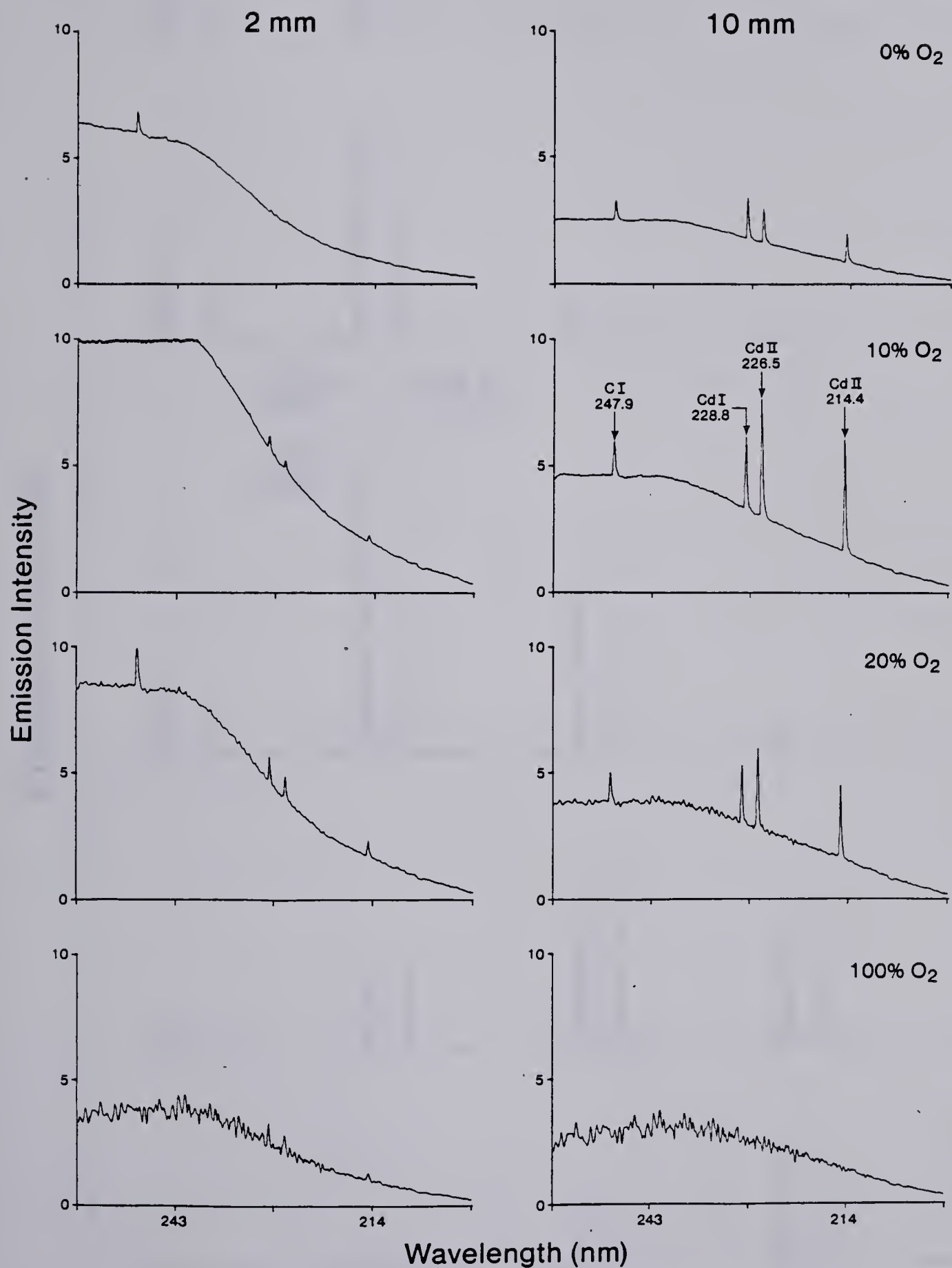


Fig. 35. Background emission spectra for  $O_2$ -Ar mixed gas ICPs at 2 mm and 10 mm above the load coil.



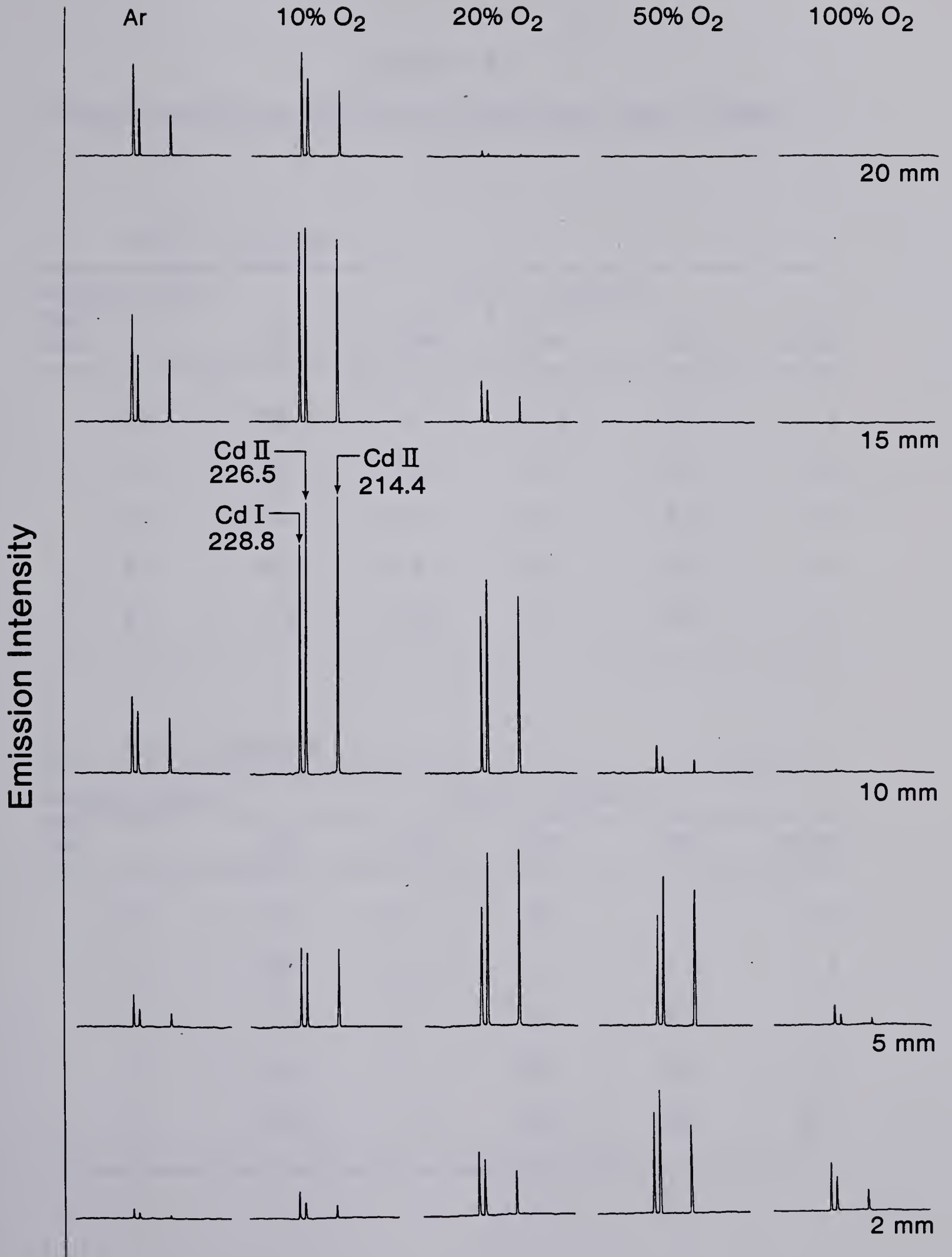


Fig. 36. Background subtracted spectra of CdI and CdII lines as a function of O<sub>2</sub>-Ar mixed gas composition and observation height.



TABLE V.8

SIGNAL-TO-NOISE RATIOS FOR O<sub>2</sub>-AR MIXED GAS PLASMAS

(a) Cd(II) 214.4nm

Height above load coil, (mm)	% O <sub>2</sub> ( Coolant)				
	0%	10%	20%	50%	100%
20	26	38	1.5	0.5	0.4
15	37	59	11	1.4	1.0
10	24	92	32	4.5	1.2
5	5.2	25	62	43	10
2	1.0	5.8	14	29	11

(b) Cd(I) 228.8nm

Height above load coil, (mm)	% O <sub>2</sub> ( Coolant )				
	0%	10%	20%	50%	100%
20	62	35	5.2	0.7	0.5
15	65	52	12	2.0	1.2
10	31	28	20	6.0	1.1
5	10	15	26	20	3.2
2	2.9	4.1	11	16	10





in an oxygen cooled plasma were equally sensitive towards the addition of oxygen into the coolant flow. It is clear from Figure 36 that the net intensities for both the neutral and ion emission lines increased when the conventional argon discharge was converted into 10 to 50% oxygen cooled plasmas.

The signal-to-noise ratios for plasmas with 0 to 100% oxygen in the outer flow measured at different observation heights are presented in Table V.8. For the CdII 214.4 nm line (Table V.8a), the signal-to-noise ratios found in the 10 to 50% oxygen cooled plasmas were two to three times higher than those found in the conventional argon plasma. The best signal-to-noise ratio measured for the 100% oxygen cooled plasma was roughly three times lower than that measured for the argon discharge at 15 mm above the load coil. This was partly due to the presence of the molecular oxygen species in this spectral region. For the CdI 228.8 nm line (Table V.8b), the signal-to-noise ratios obtained from all oxygen cooled plasmas were lower than that from the argon discharge. It is seen from this table that the cadmium neutral atom line is preferred for the analysis of cadmium using the argon discharge. In the case of oxygen cooled plasmas, the cadmium ion lines offered better sensitivities and signal-to-noise ratios than the neutral atom line; therefore the determination of cadmium using the ion



analysis lines would be strongly preferred in this case.

### 3. Air-Argon Mixed Gas Plasmas

The spectral background observed at different heights for air cooled plasmas are shown in Figure 37. The NO bandheads are quite apparent for the 20 to 100% air cooled plasmas. It is also clear from this figure that the presence of the NO bandheads produces serious potential spectral interference for analytical lines that occur in this spectral region. In the case of the 100% air cooled plasma, the three cadmium lines are submerged in the huge NO emission band spectra. The generation of the NO bands is caused primarily by the presence of nitrogen and oxygen in air.

The cadmium spectra with the plasma background subtracted out are shown in Figure 38. Note again that both the cadmium ion and neutral atom lines behave similarly to those of the nitrogen-argon mixed gas plasmas, i.e. (a) ion lines are more sensitive than the neutral atom line towards the addition of air into the coolant flow of an argon ICP, (b) the best observation height for a 10% air cooled plasma was at 10 mm observation height, for 20% at 5 mm and for 50 to 100% air cooled plasmas at 2 mm above the load coil, (c) the net emission intensities for both the cadmium ion and



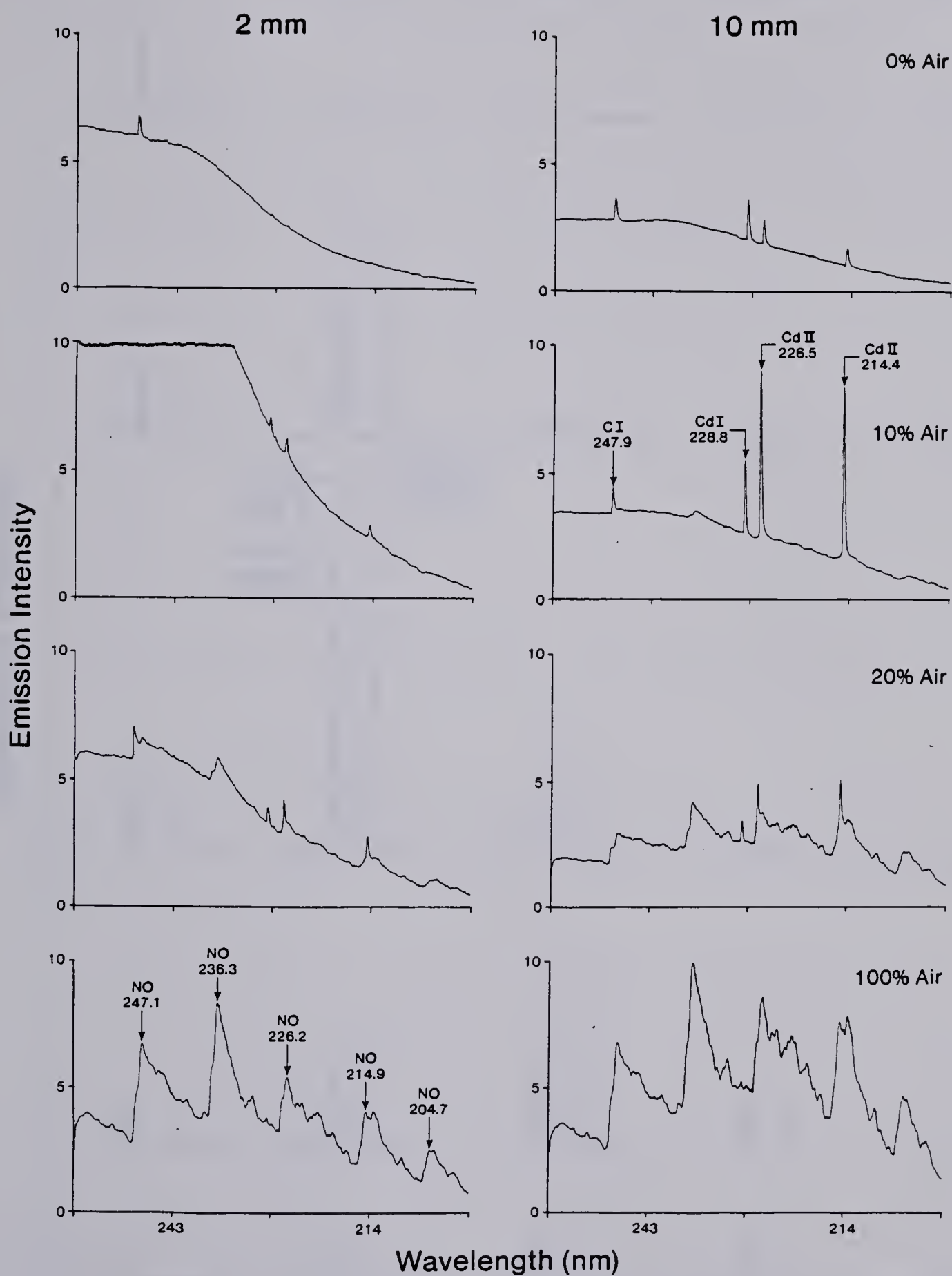


Fig. 37. Background emission spectra for Air-Ar mixed gas ICPs at 2 mm and 10 mm above the load coil.





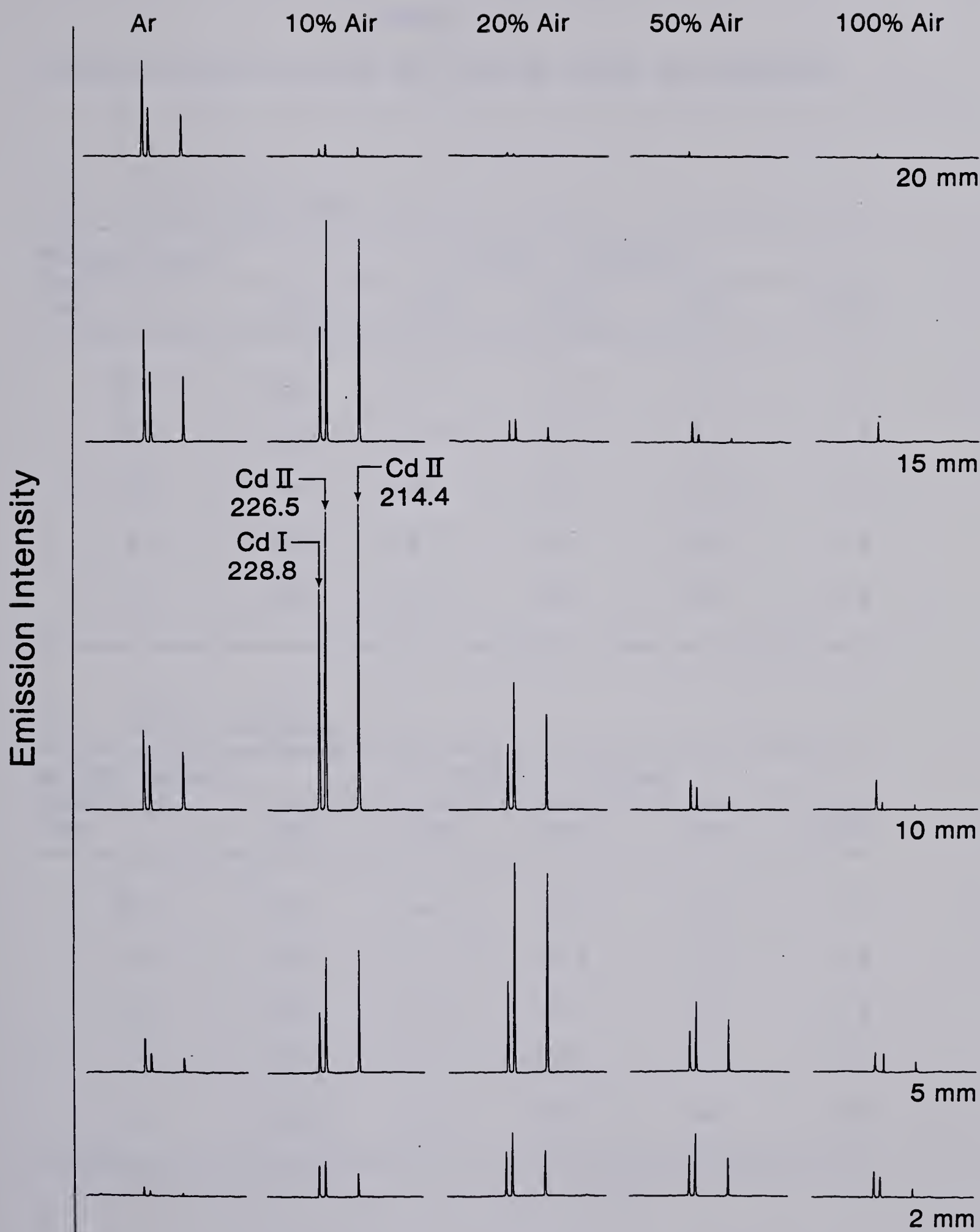


Fig. 38. Background subtracted spectra of CdI and CdII lines as a function of Air-Ar mixed gas composition and observation height.



TABLE V.9

## SIGNAL-TO-NOISE RATIOS FOR AIR-AR MIXED GAS PLASMAS

(a) Cd(II) 214.4nm

Height above load coil, (mm)	% Air ( Coolant )				
	0%	10%	20%	50%	100%
20	31	16	2.3	0.9	0.2
15	33	25	3.9	1.4	0.8
10	20	82	37	4.1	1.3
5	3.4	65	66	21	8.4
2	0.9	13	19	22	1.6

(b) Cd(I) 228.8nm

Height above load coil, (mm)	% Air ( Coolant )				
	0%	10%	20%	50%	100%
20	57	10	4.0	4.0	0.3
15	55	14	9.0	6.1	1.6
10	28	35	23	11	2.1
5	10	14	20	11	10
2	1.5	9.1	11	14	4.9



neutral atom lines increased by a factor of 3 to 4 when the argon discharge was converted into a 10% air cooled ICP, (d) best signals were achieved with a 10% air cooled plasma, the second best being the 20% air cooled discharge, (e) the cadmium intensities obtained from a 100% air cooled plasma at 2 mm observation height were three times less intense than those obtained from the argon plasma observed at 15 mm above the load coil.

The signal-to-noise ratios for all air-argon mixed plasmas observed at different heights are presented in Table V.9. The results follow the general trends shown for the  $N_2$  and  $O_2$  mixed gas plasmas. For the CdII 214.4 nm ion line (Table V.9a), the 10 to 20% air cooled ICPs provided better signal-to-noise ratios than those optimized for the argon discharge. As the amount of air introduced into the coolant flow was increased to values over 50%, the signal-to-noise ratio then deteriorated rapidly. The low signal-to-noise ratios for the 50%-100% air cooled plasmas were probably caused by the NO emission band spectra. For the cadmium neutral atom line (Table V.9b), all signal-to-noise ratios measured for the air cooled plasmas were less than those of the argon discharge. This experiment does not indicate any advantage in using a 50 or 100% air cooled plasma for the elemental analysis in this spectral region.



#### 4. Helium-Argon Mixed Gas Plasmas

The background spectra for helium cooled ICPs for a 10.0 ppm cadmium solution are shown in Figure 39. This figure also illustrates the effect of various percentages of helium in the coolant stream on the emission intensities of background continuum and analyte lines collected at 2 and 10 mm observation heights. In contrast to most of the mixed gas plasmas mentioned so far, the addition of helium into the coolant flow of an argon discharge did not alter the spectral characteristics of the background in this region. The NO bandheads and oxygen molecular emission were not observed in the helium cooled plasmas. A decrease in background continuum was observed when helium was introduced into an argon plasma. It is clear from Figure 39 that the net intensities of the cadmium lines remained relatively constant for 0 to 20% helium cooled ICPs. In the case of the 70% helium cooled plasma, the analyte emission intensities observed at 10 mm were three times greater than those observed at 2 mm above the load coil. At 10 mm observation height, the signal-to-background ratios for the cadmium emission lines obtained from the 70% helium cooled plasma were comparable to those obtained from an argon discharge.

The background subtracted spectra for the helium cooled plasmas presented in Figure 40 do not indicate any





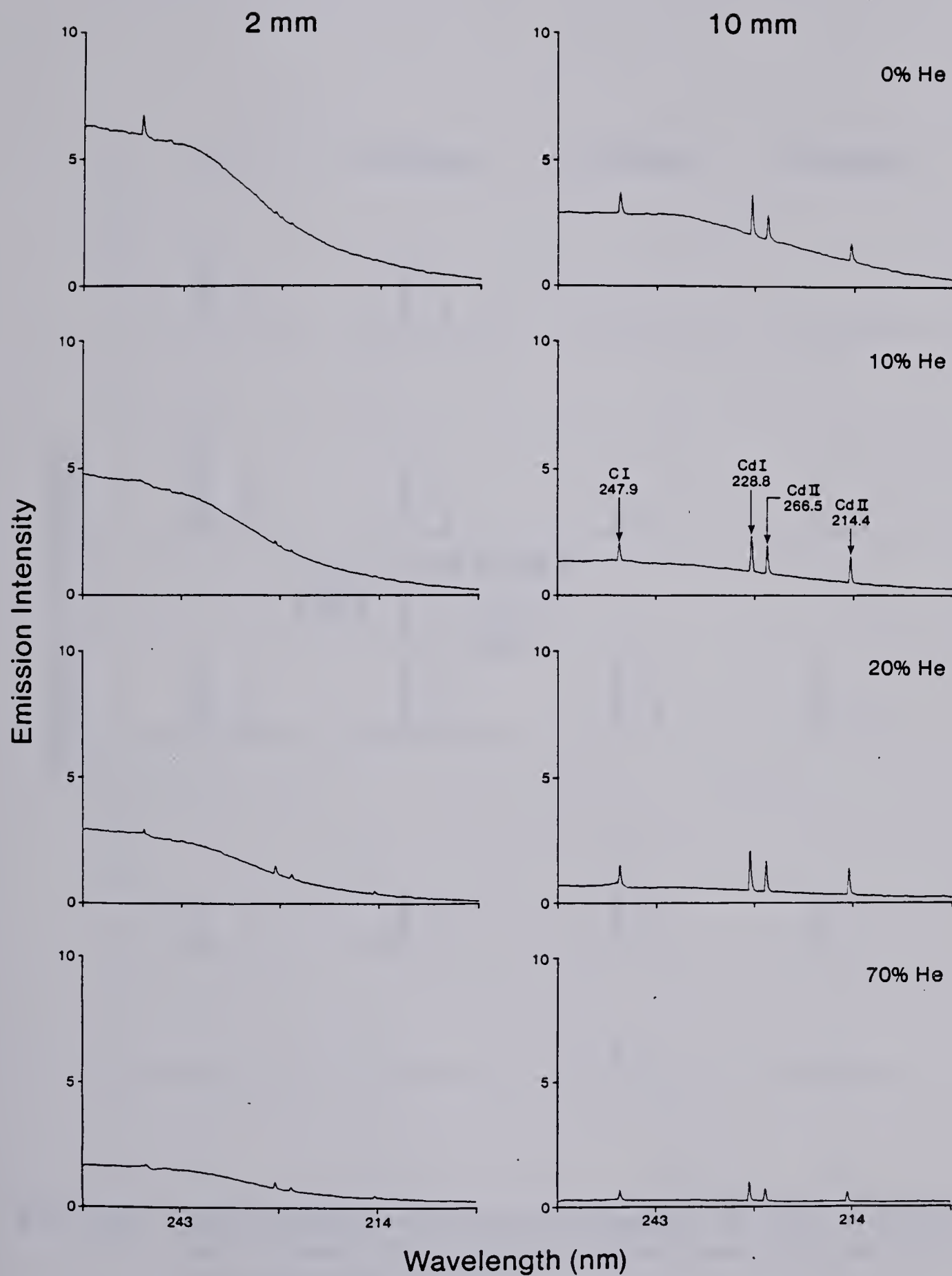


Fig. 39. Background emission spectra for He-Ar mixed gas ICPs at 2 mm and 10 mm above the load coil.



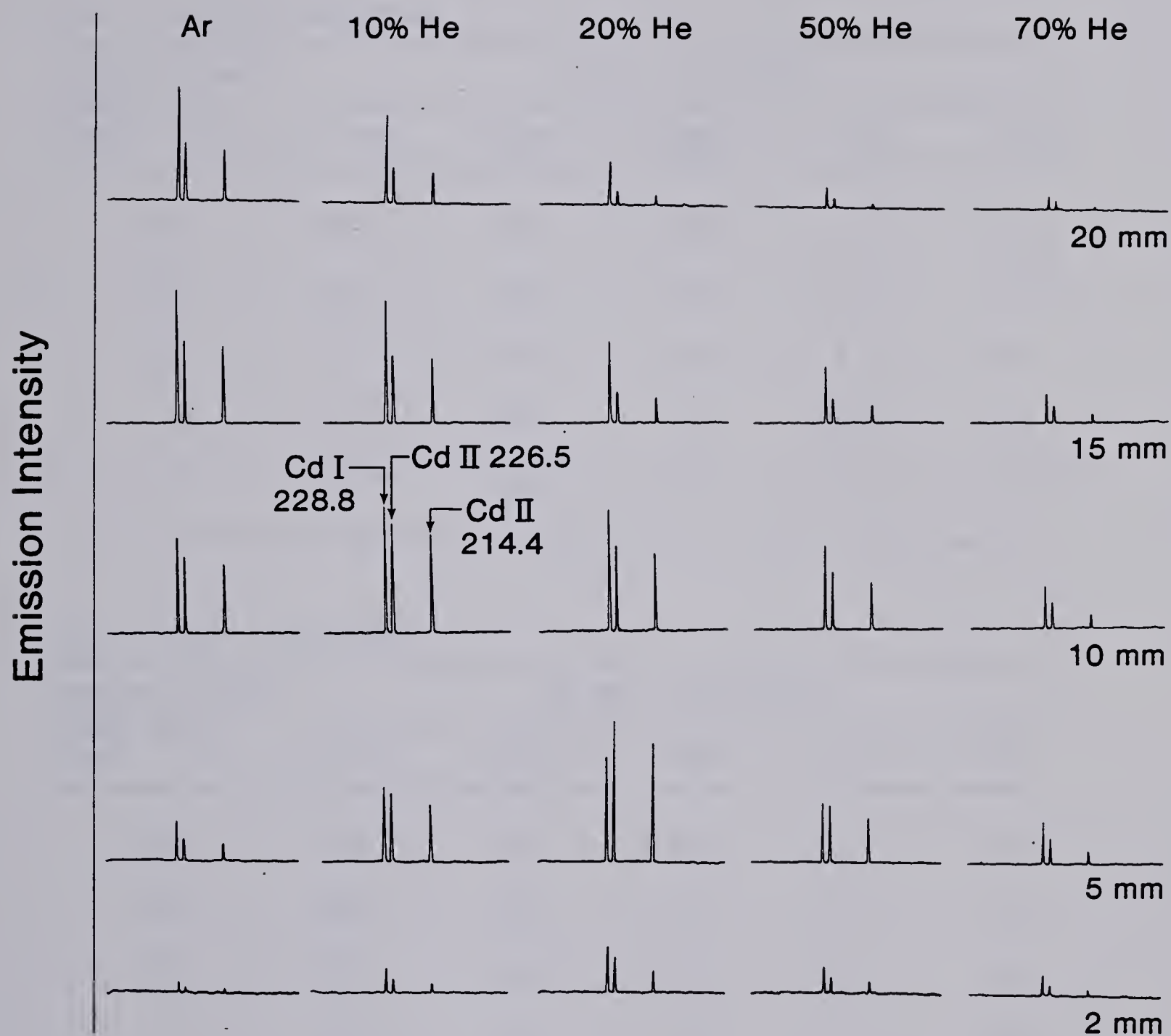


Fig. 40. Background subtracted spectra of CdI and CdII lines as a function of He-Ar mixed gas composition and observation height.



TABLE V.10

## SIGNAL-TO-NOISE RATIOS FOR HE-AR MIXED GAS PLASMAS

(a) Cd(II) 214.4nm

Height above load coil, (mm)	% He ( Coolant )				
	0%	10%	20%	50%	70%
20	25	39	20	4.5	0.8
15	31	48	67	26	3.0
10	30	48	84	47	18
5	8.7	13	76	50	11
2	3.4	4.3	36	22	8.2

(b) Cd(I) 228.8nm

Height above load coil, (mm)	% He ( Coolant )				
	0%	10%	20%	50%	70%
20	58	76	44	20	2.7
15	64	82	97	33	9.7
10	43	39	93	81	39
5	14	11	54	51	30
2	3.6	6.4	36	24	25





significant differences from those of the argon plasma. Note that unlike most of the mixed gas ICPs, both the cadmium neutral atom and ion lines appeared to be relatively insensitive towards the amount of helium present in the argon plasma. Since the addition of helium caused a reduction in the plasma volume, the net analyte intensities of the 50 and 100% helium cooled plasmas collected at the viewing zone higher than 10 mm above the load coil were considerably smaller than those of the argon plasma in the corresponding observation height.

The signal-to-noise ratios for the helium cooled plasmas measured at different heights are presented in Table V.10. For the cadmium ion line (Table V.10a), the signal-to-noise ratios of the 20 to 50% helium cooled plasma increased by a factor of 2 to 3 over that of the argon plasma. The signal-to-noise ratios for the neutral atom line (Table V.10b) also increased as the argon plasma was converted into a helium cooled ICP. As mentioned before the relative emission intensities did not change for 0 to 20% helium cooled plasmas; therefore the increase in signal-to-noise ratios must be due to the suppression of the noise level. In the case of a 70% helium cooled plasma, the signal-to-noise ratios measured for both the neutral atom and ion lines were two to three times smaller than those measured for the argon discharge.



## 5. Final Comparisons of the Mixed Gas Plasmas

(spectral region centered at 228 nm)

The background subtracted spectra of cadmium emission lines for various types of mixed gas plasmas are shown in Figure 41. These spectra were recorded at the optimum operating conditions for each plasma. Several general conclusions could be drawn from this figure. First, similar to spectra at 373 nm region, most of the mixed gas plasmas showed the highest net analyte emission intensities when the combination of 10% foreign gas and 90% argon was introduced into the coolant flow. Second, the optimized signals were measured at a lower observation height than the conventional argon plasma. Third, the net emission signals obtained from the 20% helium cooled plasma were similar to those obtained from the argon discharge. Fourth, the ion line for the 10% nitrogen, 10% oxygen and 10% air cooled plasmas was more sensitive than the neutral atom line towards the addition of these foreign gases into the coolant flow of an argon plasma.

The above trends were generally reflected in the signal-to-noise ratio studies of the mixed gas plasmas (Table V.11). The optimized running conditions are also presented in Table V.11. Overall, the signal-to-noise ratios



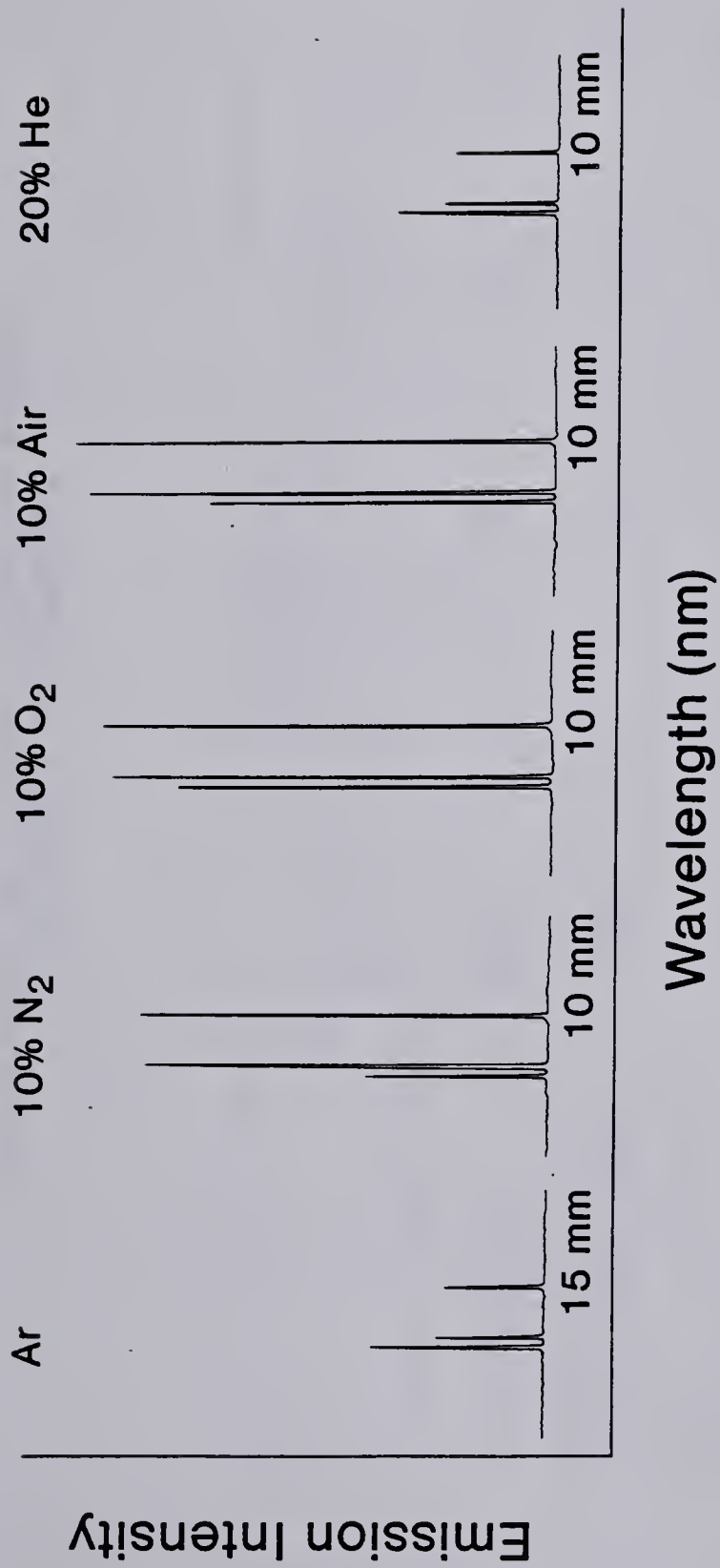


Fig. 41. Comparison of background subtracted spectra of CdI and CdII lines for optimized mixed gas plasmas.



TABLE V.11

COMPARISON OF SIGNAL-TO-NOISE RATIOS  
FOR MIXED GAS PLASMAS

	Gas (Coolant)			
	Ar	N <sub>2</sub>	O <sub>2</sub>	He
% (Coolant)	100%	10%	10%	20%
Height above load coil, (mm)	15	10	10	10
Cd(I) 228.8 nm S/N ratio	64	59	61	97
Cd(II) 226.5 nm S/N ratio	27	96	80	59
Cd(II) 214.4 nm S/N ratio	37	110	92	84





of the ion lines measured for the optimized mixed gas plasmas were three to four times greater than those measured from the conventional argon discharge. However, the signal-to-noise ratios of the neutral atom line were not improved by converting the argon plasma into a mixed gas plasma.

In this particular spectral region, it is most interesting to note that not only the ratio of the neutral atom (CdI 228.8 nm) to the ion lines (CdII 226.5 nm and 214.4 nm) but also the ratio of the two ion lines were affected by the addition of foreign gases into the coolant stream of the conventional argon ICP (Figure 42). It should be noted that the relative intensities of these lines are not the same and vary with observation height. For example, in the case of a 10% oxygen cooled plasma observed at 20 mm above the load coil, the ratio of CdI 228.8 emission to CdII 226.5 emission is 1.3; at 15 mm the ratio is 1.0 and at 10 mm the ratio is 0.8. These observations strongly suggest that mixed gas plasmas may provide different excitation and ionization mechanisms in the ICPs.



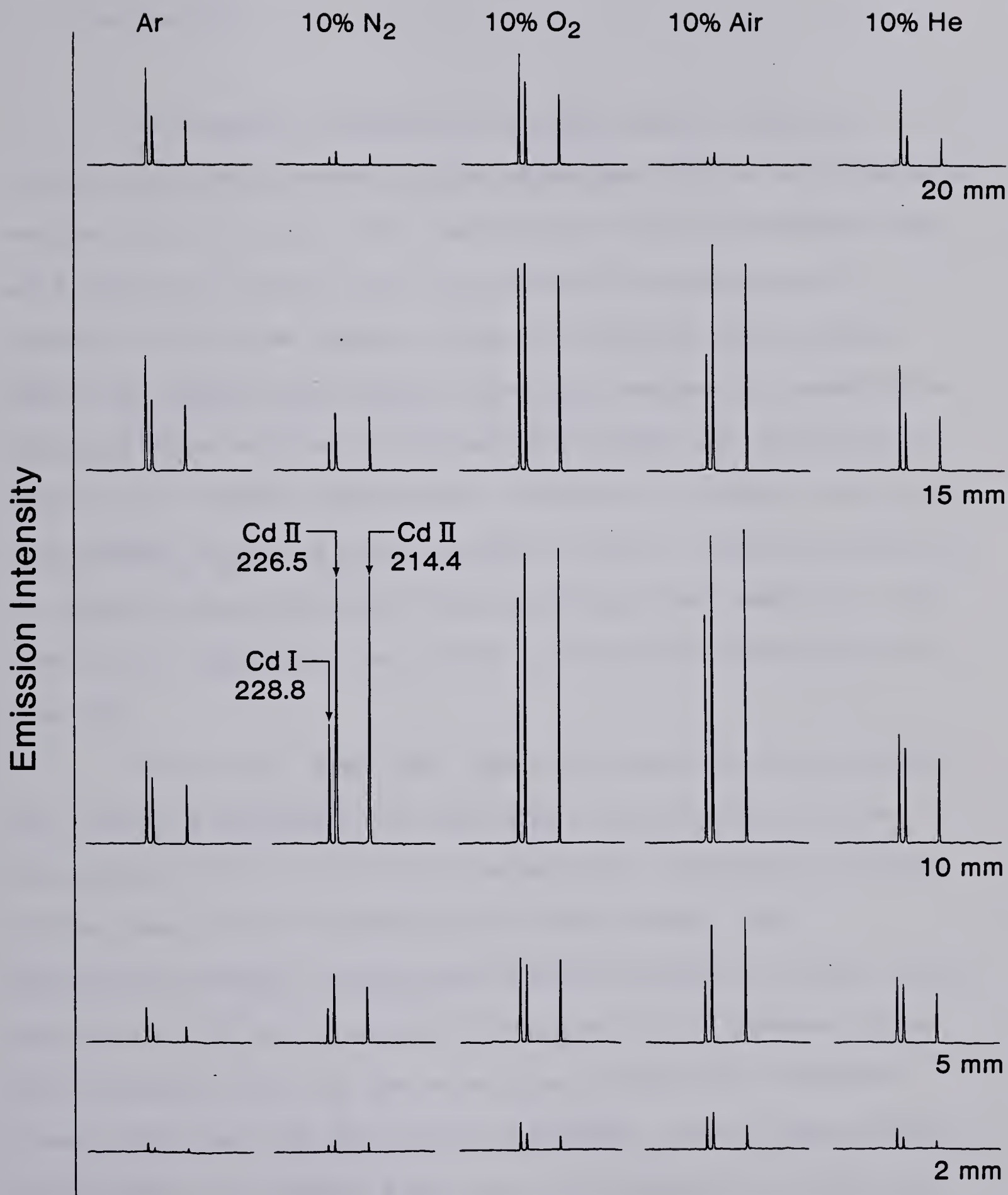


Fig. 42. Comparison of Cd emission spectra for mixed gas plasmas at observation heights of 2mm, 5mm, 10mm, 15mm, and 20mm above the load coil. Coolant gas composition : 100% Ar, 10% N<sub>2</sub>, 10% O<sub>2</sub>, 10% Air, and 10% He.



## F. Conclusions

The results presented in this chapter clearly support the utilization of the mixed gas ICP as an alternate source for the argon ICP. The spectral data correlates very well with the profile data presented in the previous chapter. All these results clearly indicate that analyte emission intensities, signal-to-noise ratios and precisions obtained from a 5 to 20 % mixed gas plasma are superior to that of the conventional argon discharge. Clearly, the mixed gas plasma ( $\text{N}_2\text{-Ar}$ ,  $\text{O}_2\text{-Ar}$ , Air-Ar or He-Ar) has the potential of significantly reducing the operating cost, while at the same time, expanding the overall analytical capability of the ICP.

It is also apparent that the signal-to-noise ratios are strongly dependent on both the concentration of the foreign gas in the coolant flow and the observation height. In the case of the conventional argon plasma, the observation height which gave the best signal-to-noise ratio occurred at 15 to 20 mm above the load coil. However, the best viewing zone for the mixed gas plasmas was somewhat lower than that for the argon discharge. These observations imply that the viewing zone has to be lowered in order to fully realize the analytical capabilities of the mixed gas plasmas.





The intensities of molecular bandhead are strongly dependent on the type of foreign gas added to the conventional argon plasma discharge. For this reason, care should be taken to avoid spectral interferences from molecular bands. In general, these spectral interferences can be avoided by switching to a different set of mixed gas plasma or by using a high aerosol flow to decrease the spectral background (136). Although in certain spectral regions, the mixed gas systems suffer severely from the molecular bandhead interferences, the advantage of high sensitivity of the analyte emission in the mixed gas plasmas warrants further research and development.



## CHAPTER VI

### EVALUATION OF THE ANALYTICAL PERFORMANCE OF MIXED GAS PLASMAS

#### A. Introduction

One of the main objectives of this study is the evaluation of the analytical performance of mixed gas plasmas under various operating conditions. The results presented in Chapter V have shown that the introduction of foreign gases ( $N_2$ ,  $O_2$ , Air or Helium) into the coolant flow of an argon plasma causes considerable changes in analyte emission characteristics. The data presented in Chapter IV demonstrate that analyte emission intensities are also dependent upon plasma power, aerosol flow rate and observation height. It was felt that a knowledge of signal-to-noise ratios as a function of these plasma operating parameters would allow an effective evaluation and comparison of various mixed gas ICPs. Such knowledge can also reveal important characteristics of each plasma source. In this study the signal-to-noise ratio of the CaII 393.4 nm line was measured in order to obtain the comparative data.

In addition to providing acceptable signal-to-noise ratio performance, the ultimate success of a source for



spectrochemical analysis is greatly dependent on the analytical signal being free from interferences. These interferences may be classified into two distinct groups: (i) spectral interferences, and (ii) matrix interferences. Spectral interferences are usually associated with the bandwidth of the spectrometer and the spectral emission characteristics of the analyte and sample matrix. This type of interference is primarily dependent on the characteristics of the spectrometer and are not included in this study.

The second group of interferences, i.e. matrix interferences, can be divided into several subgroups. These include transport, solute vaporization, vapor phase, chemical, and physical interferences (90,137). Matrix interference effects in ICPs have been found to be quite small when compared to the corresponding interferences found in flame emission or in atomic absorption spectrometry. Reviews of matrix interferences in ICPs can be found in the literature (103,121,137). One type of interference that is observed in ICP systems is the effect of easily ionizable elements (EIE's). There are three major confusing reports on the effects of an easily ionizable element (Na, K, or Cs) on analyte emission intensities. Some investigators have observed emission "enhancement", some have observed emission "depression", and some have observed "no effect". In a





recent paper, Blades and Horlick (121) presented data that clarify some of these observations. They demonstrated that the conflicting statements about the effect of the easily ionizable elements on the analyte emission intensities could be explained on the basis of changes in the spatial structure of analyte emission. The experimental results reported by Blades and Horlick (121) suggest that interference studies of an ICP source have to be carried out at different observation heights in order to account for the shift in spatial structure of analyte emission signals that may be caused by the interferant.

In this study the effects of classic matrix interferences on the calcium emission intensity have been measured, namely, (1) the vaporization interference of phosphate, and (2) the ionization interference of potassium. In particular the degree of interference in the mixed gas plasmas was evaluated and described. This study was carried out at three different observation heights above the load coil. At lower observation heights, mixed gas plasmas appear to have decreased vaporization and ionization interferences when compared to a conventional argon plasma discharge. Higher in the aerosol channel, the interfering matrices do not affect the emission intensity of calcium in either the mixed gas ICPs or the conventional argon discharge.

Finally, analytical calibration curves for various





types of mixed gas plasmas measured at their optimum viewing zones will be presented. It will be seen that 10 to 20% O<sub>2</sub> and N<sub>2</sub> cooled plasmas provide better sensitivities than the conventional argon discharge.

## B. Experimental

The Plasma-Therm ICP system discussed in Chapter II was used for all measurements. The operating conditions are listed in Table III.1. Foreign gases such as N<sub>2</sub>, O<sub>2</sub>, Air or He were introduced only to the coolant flow of an argon discharge.

The 1024 element photodiode array measurement system and the external electronics were identical to those described in Chapter II. All signals were background subtracted. The background signals were obtained by aspirating distilled water into the aerosol channel.

Phosphate in the form of H<sub>3</sub>PO<sub>4</sub> was added to the calcium solution. In the study of the effect of EIE on Ca emission, reagent grade potassium chloride was added to the calcium solution. In all cases the concentration of calcium was 1.0 ppm. Solutions containing calcium and the interferent in the ratio of 0, 250, 500, 750 and 1000 were made up using distilled water.



C. Signal-to-Noise Evaluation of Mixed Gas Plasmas  
as a Function of Plasma Power, Aerosol Flow Rate  
and Observation Height

In this experiment, plasma performances were evaluated by comparing signal-to-noise ratios. The object of this study was to evaluate the analytical precision of a mixed gas ICP as a function of plasma rf power, aerosol flow rate and observation height. The calcium 393.4 nm ion line was used to monitor the precision of the ICP source. These measurements were carried out with a photodiode array spectrometer. All signal-to-noise ratios ( $1 / \text{relative standard deviation}$ ) reported here were based on a signal integration period of 10.0 s and 32 replicated measurements. For a given set of plasma conditions, all operating parameters such as gas combination, observation height, aerosol and coolant flows were held constant whilst the signal-to-noise ratios were measured as the power was varied. After completion of the study involving S/N ratios versus power, similar experiments were carried out with all operating parameters being held constant as the aerosol flow was varied.



## 1. Conventional Argon ICP

The results of a precision study for an argon discharge conducted by varying the aerosol flow and plasma power are summarized in Table VI.1. The precision data were based on measurements at 15 mm above the load coil and all measurements were conducted on the same day. The signal-to-noise ratios range from 2 to 204 with the highest value occurring at 1.0 L/min aerosol flow and 1.75 Kw rf power. As mentioned before, the profile peak maximum of the calcium ion emission is greatly affected by the aerosol flow rate. Increasing the aerosol flow rate pushes the emission peak maximum away from the induction coil. If the plasma power and observation height were held constant, one would initially expect to observe an increase in signal-to-noise ratio with increasing aerosol flow rate. However, the precision of the measurements would decrease after a certain aerosol flow rate was reached (1.0 to 1.2 L/min). The precision data presented in Table VI.1 reflect such a correlation of signal-to-noise ratios with aerosol flow rate at all power levels tested.

In the case of a constant low aerosol flow rate (1.0 L/min), it is interesting to note that the value of the signal-to-noise ratio peaks at a particular rf power. One can conclude from the data presented in Table VI.1 that the





## SIGNAL-TO-NOISE RATIOS FOR ARGON PLASMAS

TABLE VI.1

Ca(II) 393.37nm	Observation height = 15mm above load coil					
Power (Kw)	Aerosol flow rate ( L/min )					
	0.6	0.8	1.0	1.2	1.4	1.6
2.25	70	123	119	165	134	103
2.00	99	138	141	134	139	70
1.75	68	141	204	145	137	53
1.50	62	148	185	138	87	42
1.25	58	101	133	138	42	6
1.00	50	87	107	46	5	2

TABLE VI.2

Ca(II) 393.37nm	Observation height = 10mm above load coil					
Power (Kw)	Aerosol flow rate ( L/min )					
	0.6	0.8	1.0	1.2	1.4	1.6
2.25	81	133	110	110	68	34
2.00	95	130	122	140	64	25
1.75	146	152	189	151	53	18
1.50	122	165	164	95	32	8
1.25	136	173	145	43	10	3
1.00	75	123	32	10	1	1



## SIGNAL-TO-NOISE RATIOS FOR ARGON PLASMAS

TABLE VI.3

Ca(II) 393.37nm	Observation height = 5mm above load coil					
Power (Kw)	Aerosol flow rate ( L/min )					
	0.6	0.8	1.0	1.2	1.4	1.6
2.25	64	90	59	24	10	8
2.00	80	105	56	23	13	6
1.75	72	95	69	17	8	8
1.50	86	92	55	11	5	5
1.25	115	111	17	6	3	3
1.00	90	41	3	4	2	2

TABLE VI.4

Ca(II) 393.37nm	Observation height = 2mm above load coil					
Power (Kw)	Aerosol flow rate ( L/min )					
	0.6	0.8	1.0	1.2	1.4	1.6
2.25	31	45	17	11	8	5
2.00	80	56	19	9	7	5
1.75	79	50	19	6	6	5
1.50	72	56	11	5	4	4
1.25	54	30	8	3	3	2
1.00	44	13	5	2	2	3



argon discharge observed at 15 mm above the load coil shows its best analytical performance under moderate plasma power (1.50 to 1.75 KW) and moderate aerosol flow rate (approximately 1.0 L/min).

Analogous precision studies of the conventional argon discharge at different observation heights are tabulated in Tables VI.2 to VI.4. It is clear that the basic precision patterns for the argon plasma measured at 10, 5, and 2 mm above the load coil are similar to those discussed above but that at equivalent power and aerosol flow rate the value of signal-to-noise ratios are much smaller at lower observation heights. These precision data correspond to the spatial information presented in Chapter IV in which the emission intensity of the ion line peaks at 15 to 20 mm above the load coil. Overall, the signal-to-noise ratios measured at different heights reached their maxima when low to moderate plasma power and aerosol flow rate were used.

## 2. Nitrogen - Argon Mixed Gas ICPs

It was pointed out earlier that introducing foreign gases into the coolant flow causes considerable change in analyte emission characteristics. Since there would be an appreciable variation of the signal-to-noise ratio with both the coolant gas combinations and observation height, the





most practical way to study the effect of power and aerosol flow rate on the analytical precision in a mixed gas ICP was to focus on the S/N measurements only at the position of optimum viewing height for each individual mixed gas plasma. The optimized observation height chosen for the various mixed gas ICPs was based on the position of maximum emission presented in Chapter V.

Signal-to-noise ratios obtained from a 10% N<sub>2</sub> cooled plasma while varying the rf power and aerosol flow rate are presented in Table VI.5. These measurements were carried out at an observation height of 10 mm above the load coil. It can be seen from the data presented in Table VI.5 that the optimum aerosol flow rate and rf power for this measurement were 1.4 L/min and 2.25 Kw. These data indicate that a 10% N<sub>2</sub> cooled plasma yields its best signal-to-noise performance under higher power (2.0 to 2.25 KW) and higher aerosol flow (1.2 to 1.6 L/min) than the conventional argon discharge. In addition, under similar operating conditions, the signal-to-noise ratios obtained from a 10% N<sub>2</sub> cooled plasma were generally higher than those obtained from the conventional argon discharge (Tables VI.1 to VI.4).

The analogous precision studies of the 20 and 100% N<sub>2</sub> cooled plasmas measured at 5 and 2 mm respectively are presented in Tables VI.6 and VI.7. These studies indicate trends which are in agreement with Greenfield's early work





SIGNAL-TO-NOISE RATIOS FOR N<sub>2</sub>-AR MIXED GAS PLASMAS

TABLE VI.5

Ca(II) 393.37nm 10% N<sub>2</sub> cooled plasma at 10mm above load coil

Power (Kw)	Aerosol flow rate ( L/min )					
	0.6	0.8	1.0	1.2	1.4	1.6
2.25	54	71	150	233	369	278
2.00	93	111	196	244	312	202
1.75	98	186	213	222	215	124
1.50	95	143	198	212	181	110
1.25	76	128	187	195	81	44
1.00	57	101	111	86	30	14

TABLE VI.6

Ca(II) 393.37nm, 20% N<sub>2</sub> cooled plasma at 5mm above load coil

Power (Kw)	Aerosol flow rate ( L/min )					
	0.6	0.8	1.0	1.2	1.4	1.6
2.25	94	142	234	307	291	173
2.00	112	199	301	423	295	128
1.75	137	185	228	213	191	141
1.50	106	176	170	145	138	106
1.25	92	88	135	73	59	35
1.00	48	50	63	17	12	7



SIGNAL-TO-NOISE RATIOS FOR N<sub>2</sub>-AR MIXED GAS PLASMAS

TABLE VI.7

Ca(II) 393.37nm, 100 % N<sub>2</sub> cooled plasma at 2mm above load coil

Power (Kw)	Aerosol flow rate ( L/min )					
	0.6	0.8	1.0	1.2	1.4	1.6
2.25	52	73	142	130	143	107
2.00	74	123	127	162	129	61
1.75	93	107	138	182	105	83
1.50	65	86	84	105	65	31
1.25	38	59	60	62	27	8
1.00	23	26	36	24	5	2



(64-71). In general, the trends indicate that  $N_2$ -Ar mixed gas plasmas require higher aerosol flow rates and rf powers than a conventional argon ICP in order to achieve best signal-to-noise ratios. Note that under optimized operating conditions, signal-to-noise ratios achieved by a 10 to 20%  $N_2$  cooled ICP are two to three times better than that achieved by the conventional argon ICP. Also the data presented in Table VI.7 clearly indicate that the signal-to-noise ratio data measured for a 100%  $N_2$  cooled plasma are reasonably comparable to those of the argon ICP. It is an advantage to use the 100%  $N_2$  cooled plasma because of the lower operating cost.

### 3. Oxygen - Argon Mixed Gas ICPs

The precision investigations of 10, 20, and 100%  $O_2$  cooled plasmas operated at different powers and aerosol flow rates are presented in Tables VI.8 to VI.10. In many ways, oxygen cooled plasmas behaved like nitrogen - argon mixed gas plasmas : (1) the signal-to-noise ratios found in the 10 to 20%  $O_2$  cooled plasmas were roughly two times better than those of the conventional argon discharge, (2) signal-to-noise ratios achieved by a 100%  $O_2$  cooled ICP was roughly equivalent to those of the Ar-ICP, and (3) in order to optimize the signal-to-noise ratio, the oxygen cooled





SIGNAL-TO-NOISE RATIOS FOR O<sub>2</sub>-AR MIXED GAS PLASMAS

TABLE VI.8

Ca(II) 393.37nm, 10 % O<sub>2</sub> cooled plasma at 10mm above load coil

Power (Kw)	Aerosol flow rate ( L/min )					
	0.6	0.8	1.0	1.2	1.4	1.6
2.25	45	139	165	270	276	139
2.00	115	144	242	384	291	161
1.75	122	150	234	265	194	86
1.50	97	156	216	187	208	55
1.25	88	148	166	109	61	22
1.00	80	131	172	83	29	4

TABLE VI.9

Ca(II) 393.37nm, 20% O<sub>2</sub> cooled plasma at 5 mm above load coil

Power (Kw)	Aerosol flow rate ( L/min )					
	0.6	0.8	1.0	1.2	1.4	1.6
2.25	65	91	118	291	221	59
2.00	47	147	229	350	157	51
1.75	79	163	220	239	115	33
1.50	113	185	218	189	57	13
1.25	141	196	217	107	20	7
1.00	92	173	126	13	2	2



SIGNAL-TO-NOISE RATIOS FOR O<sub>2</sub>-AR MIXED GAS PLASMAS

TABLE VI.10

Ca(II) 393.37nm, 100% O<sub>2</sub> cooled plasma at 2 mm above load coil

Power (Kw)	Aerosol flow rate ( L/min )					
	0.6	0.8	1.0	1.2	1.4	1.6
2.25	87	121	288	365	80	25
2.00	83	239	240	148	57	14
1.75	80	178	171	90	33	12
1.50	82	124	131	23	9	4
1.25	74	113	42	7	3	2
1.00	43	15	5	1	2	1



ICPs required higher power and aerosol flow rate than the argon ICP.

#### 4. Air - Argon Mixed Gas ICPs

Changes in signal-to-noise ratios for the 10, 20, and 100% air cooled ICPs as a function of rf power and aerosol flow rate are shown in Tables VI.11 to VI.13. The maximum signal-to-noise ratios were obtained with an aerosol flow rate of 1.2 L/min and the rf power level of 2.0 to 2.25 Kw. From this set of data, we see that the best precision was achieved by a 10% air cooled plasma observed at 10 mm above the load coil. In most respects, the data presented in these tables clearly indicate that air cooled plasmas behave quite similarly to the nitrogen and oxygen cooled ICPs just discussed.

#### 5. Helium - Argon Mixed Gas ICPs

The precision measurements for 10, 20, and 70% helium cooled plasmas as a function of aerosol flow rate and rf power are presented in Tables VI.14 to VI.16. Because of high fluctuation and low stability, the signal-to-noise ratios for the 70% helium cooled ICP operated with powers less than 1.75 Kw were not measured. The helium cooled



## SIGNAL-TO-NOISE RATIOS FOR AIR-AR MIXED GAS PLASMAS

TABLE VI.11

Ca(II) 393.37nm, 10% Air cooled plasma at 10mm above load coil

Power (Kw)	Aerosol flow rate ( L/min )					
	0.6	0.8	1.0	1.2	1.4	1.6
2.25	59	126	207	215	319	153
2.00	125	132	203	442	373	126
1.75	120	161	263	328	298	95
1.50	111	186	229	172	172	55
1.25	87	153	121	162	108	50
1.00	68	98	110	65	56	7

TABLE VI.12

Ca(II) 393.37nm, 20% Air cooled plasma at 5 mm above load coil

Power (Kw)	Aerosol flow rate ( L/min )					
	0.6	0.8	1.0	1.2	1.4	1.6
2.25	128	149	277	285	211	50
2.00	192	209	283	235	207	65
1.75	116	167	212	168	165	38
1.50	103	139	187	143	111	21
1.25	97	81	195	100	38	11
1.00	51	64	66	25	6	3





## SIGNAL-TO-NOISE RATIOS FOR AIR-AR MIXED GAS PLASMAS

TABLE VI.13

Ca(II) 393.37nm, 100% Air cooled plasma at 2 mm above load coil

Power (Kw)	Aerosol flow rate ( L/min )					
	0.6	0.8	1.0	1.2	1.4	1.6
2.25	83	129	114	173	127	90
2.00	76	138	151	144	144	85
1.75	53	97	123	120	90	58
1.50	53	90	94	98	46	22
1.25	51	71	86	40	26	8
1.00	30	47	37	8	2	2



## SIGNAL-TO-NOISE RATIOS FOR HE-AR MIXED GAS PLASMAS

TABLE VI.14

Ca(II) 393.37nm, 10 % He cooled plasma at 10mm above load coil

Power (Kw)	Aerosol flow rate ( L/min )					
	0.6	0.8	1.0	1.2	1.4	1.6
2.25	50	71	208	215	160	66
2.00	64	119	246	251	137	54
1.75	72	116	182	237	114	38
1.50	113	117	176	185	92	34
1.25	152	145	172	134	26	7
1.00	97	161	56	25	4	2

TABLE VI.15

Ca(II) 393.37nm, 20 % He cooled plasma at 5 mm above load coil

Power (Kw)	Aerosol flow rate ( L/min )					
	0.6	0.8	1.0	1.2	1.4	1.6
2.25	90	131	174	237	281	168
2.00	100	167	235	212	211	137
1.75	101	183	248	224	124	97
1.50	126	163	143	222	154	80
1.25	94	163	196	159	83	45
1.00	75	138	105	77	17	5



## SIGNAL-TO-NOISE RATIOS FOR HE-AR MIXED GAS PLASMAS

TABLE VI.16

Ca(II) 393.37nm, 70 % He cooled plasma at 2 mm above load coil

Power (Kw)	Aerosol flow rate ( L/min )					
	0.6	0.8	1.0	1.2	1.4	1.6
2.25	117	184	135	96	46	21
2.00	132	225	143	26	23	15
1.75	216	151	60	13	12	9
1.50	N/D	N/D	N/D	N/D	N/D	N/D
1.25	N/D	N/D	N/D	N/D	N/D	N/D
1.00	N/D	N/D	N/D	N/D	N/D	N/D

N/D = not determined





plasma seems to behave like a conventional argon discharge where maximum signal-to-noise ratios were best achieved with moderate power and aerosol flow rate.

These observations suggest two distinct patterns:

(1) argon and helium cooled ICPs in which precision data is maximized with moderate power (less than 2.00 Kw) and moderate aerosol flow rate (less than 1.2 L/min). (2) nitrogen, oxygen and air cooled ICPs in which the maximum signal-to-noise ratios were achieved with higher rf power and aerosol flow rate. These studies also indicate that air cooled plasmas generally behave like nitrogen cooled ICPs, and that the helium cooled plasmas behave like argon discharges. Hence, all subsequent experiments are focused only on the evaluation and characterization of the argon, nitrogen and oxygen cooled ICPs.

#### D. Interference Studies of the Mixed Gas ICPs

##### 1. Phosphate on Calcium Emission, Solute Vaporization Interference

The interference of phosphate on calcium was evaluated under our current normal experimental operating conditions (2.0 Kw and 1.0 L/min aerosol flow rate). The



experiments were repeated for different mixed gas plasmas measured at different observation heights. In the case of an Ar-ICP source, solute vaporization interferences, such as phosphate on calcium, have been extensively studied by various workers (90,137). In the case of mixed gas ICPs, a study of this interference effect has not been reported in the literature. The solute vaporization interference has been attributed to the formation of a refractory compound, for example  $\text{Ca}_2\text{P}_2\text{O}_7$  or  $\text{Ca}_3(\text{PO}_4)_2$  whose thermal stability leads to a low efficiency for free atom formation. Much of the data on the vaporization interference that has appeared in the literature has not been consistent, with some investigators reporting signal "enhancement", some observing "depression", while some reporting "no effect". These conflicting observations were later discovered to be caused by a shift in spatial structure of the analyte emission. In order to clarify some of these observations, a spatial study of the vaporization interference effect has been undertaken.

The results obtained for the interference of phosphate on calcium for  $\text{N}_2$ -Ar mixed gas plasmas are shown in Figure 43. Interference of phosphate on calcium was studied up to 1000 fold excess. In addition, this study was conducted at 2, 10, and 18 mm above the load coil. The letters on the figure correspond to various percentages of nitrogen introduced into the coolant flow of an argon



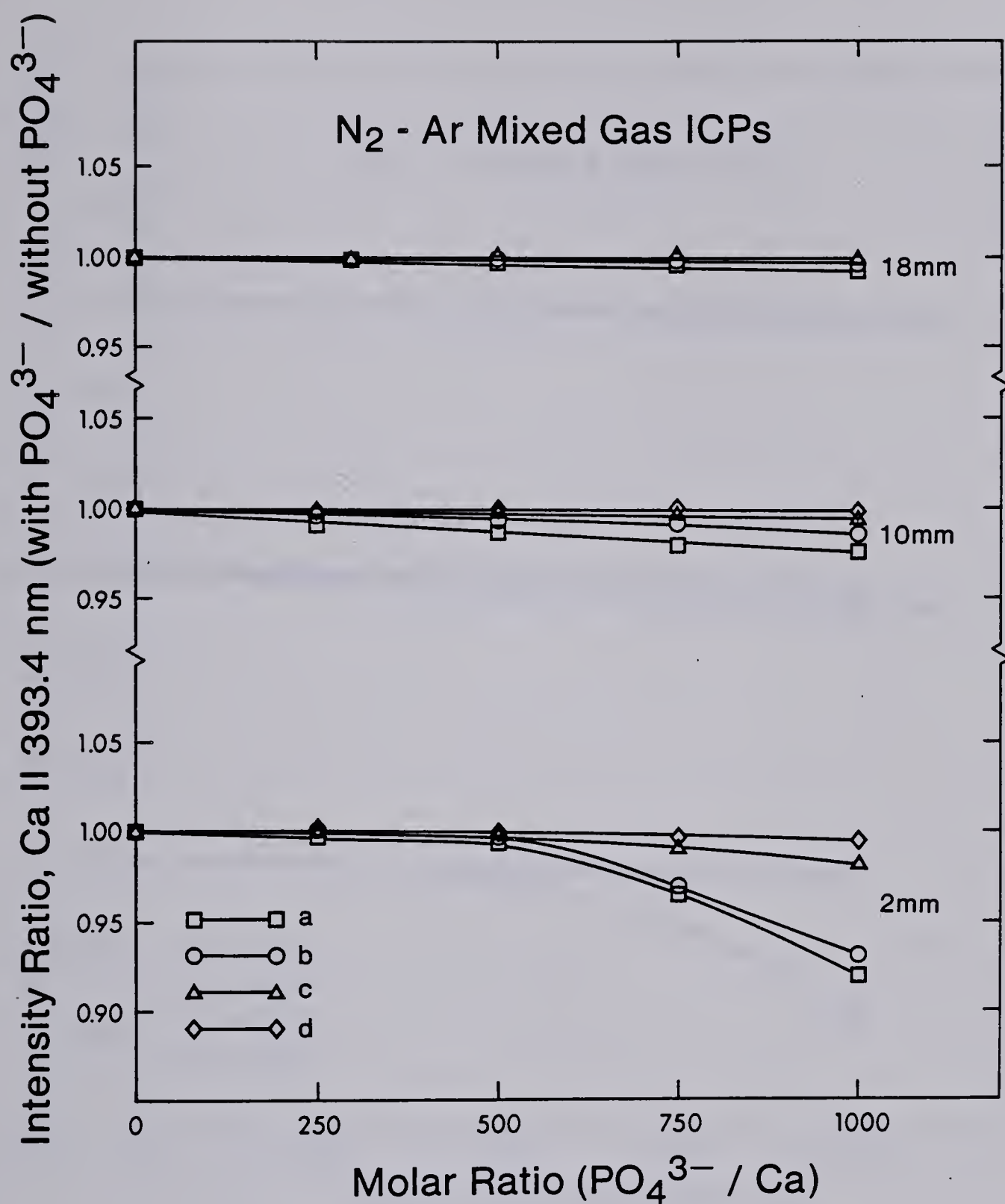


Fig. 43. Effect of PO<sub>4</sub><sup>3-</sup> interference on CaII 393.4 nm emission in N<sub>2</sub>-Ar mixed gas ICPs, at observation heights of 2mm, 10mm, and 18mm above the load coil. Percentage of N<sub>2</sub> in the coolant flow; (a) 0%, (b) 10%, (c) 20%, and (d) 100%.





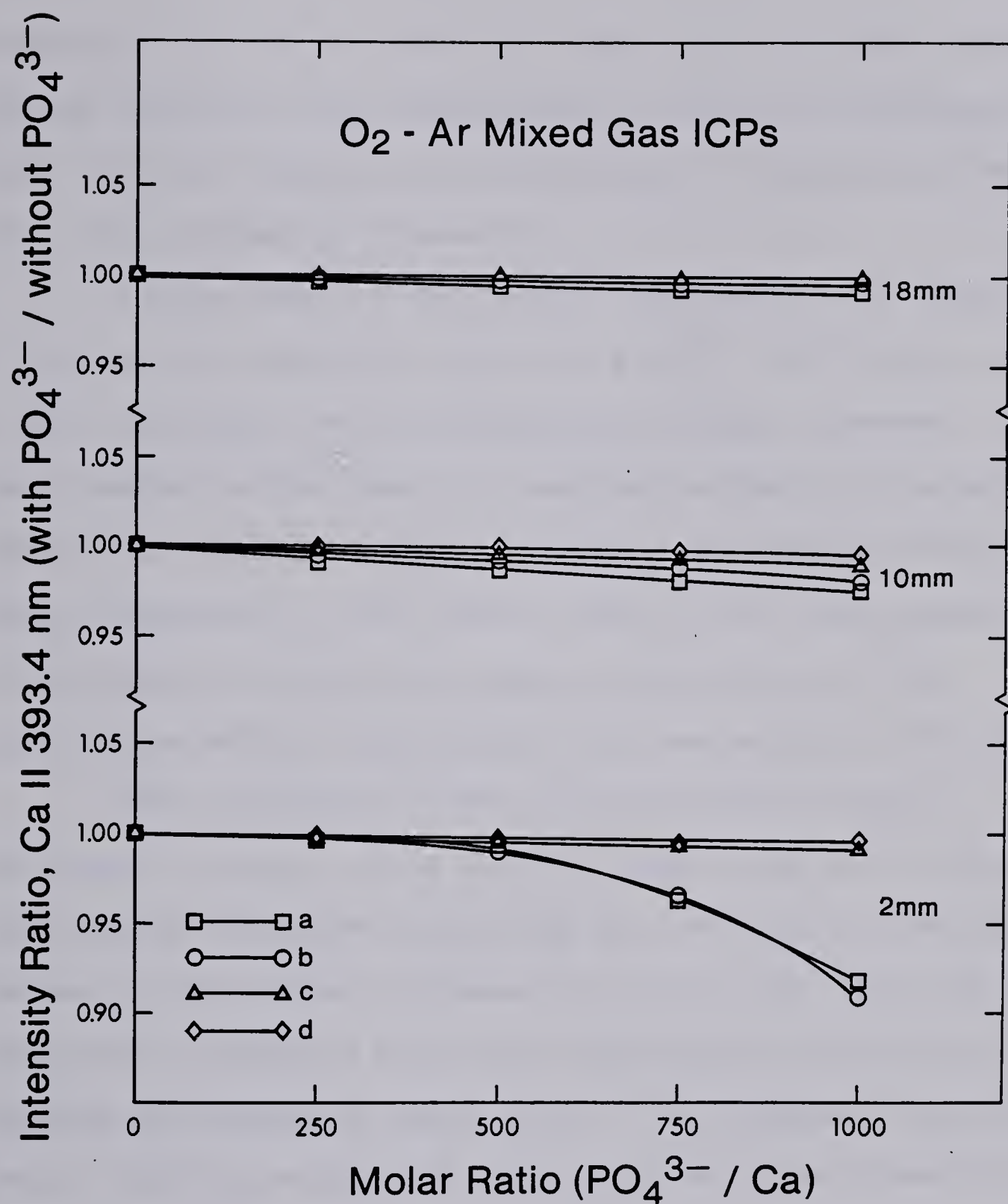


Fig. 44. Effect of PO<sub>4</sub><sup>3-</sup> interference on CaII 393.4 nm emission in O<sub>2</sub>-Ar mixed gas ICPs, at observation heights of 2mm, 10mm, and 18mm above the load coil. Percentage of O<sub>2</sub> in the coolant flow; (a) 0%, (b) 10%, (c) 20%, and (d) 100%.





discharge: (a) 0%, (b) 10%, (c) 20%, and (d) 100%. Ratios of calcium emission with interferant to without interferant for each individual operating condition as a function of molar ratio are plotted in Figure 43.

In the case of the Ar-ICP, suppression of about 10% in the calcium emission signal at a  $\text{PO}_4^{3-} / \text{Ca}^{2+}$  molar ratio of 1000 occurred low in the aerosol channel. However, this "suppression" effect was not observed higher in the aerosol channel. It should be noted that the suppression effect is highly dependent on the viewing zone, hence the present investigation confirms the spatial dependency of the interference effect reported by various workers (137,138).

The interesting point to note from the data presented in Figure 43 is that the magnitude of the signal "suppression" depends critically on the amount of nitrogen present in the coolant stream. It can be seen from the data presented in Figure 43 that the suppression of calcium emission by phosphate interferant is considerably smaller for the 100%  $\text{N}_2$  cooled ICP than it is for the conventional Ar-ICP. At 2 mm above the induction coil, as one goes from Figure 43a to 43d, i.e., increasing the nitrogen concentration from 0 to 100%, the magnitude of the vaporization interference becomes smaller. The same holds true for higher observation heights.

The analogous set of data for  $\text{O}_2$ -Ar mixed gas ICPs



is shown in Figure 44. It can be seen from the data presented in the figure that introducing oxygen into the coolant stream minimizes the vaporization interferences. From the data presented in Figures 43 and 44, it appears that introducing foreign gases into the coolant flow is a convenient way for reducing the solute vaporization interference effects. High in the plasma aerosol channel the solute vaporization interference is at its minimum. This trend is true for both the  $O_2$ -Ar and  $N_2$ -Ar mixed gas plasmas.

## 2. Potassium on Calcium Emission, Effect of an Easily Ionizable Element

The effect of EIEs in analytical ICP emission spectrometry has been investigated extensively by several workers (121,138-141). For discussions of the interference effects produced by the EIE in the ICP source the reader is referred to Larson et al. (138), Blades and Horlick (121), and Roederer et al. (142). The addition of an EIE increases the electron density in flames such that the equilibrium shifts towards the neutral atom species causing enhancement of neutral atom line emission (139,143). This situation is not well defined in the plasma source. In fact, significantly different results have been reported by



various investigators for these interference effects. Kirkbright et al. (144,145) reported that the addition of excess EIE into the ICP source did not affect the emission intensity of several species. Watson and Steele (146) reported that the emission intensities from several elements showed enhancement at 10 mm above the load coil, and depression at 15 mm above the induction coil. Recent work by Blades and Horlick (121), and Roederer et al. (142) have shown that enhancement and depression of the emission by EIE could be explained in terms of the spatial structure of analyte emission.

The results for the present study on the effect of an EIE in the  $N_2$ -Ar mixed gas plasma source are illustrated in Figure 45. Experimental data were obtained at 2, 10, and 18 mm above the load coil and the effect of potassium on calcium was studied up to 1000 fold excess. This figure is similar in format to those studies of the vaporization interference just discussed.

It can be seen from the data presented in Figure 45 that the interference effects are highly dependent on the viewing height. The enhancement of the emission intensity of the calcium ion line is quite significant at 2 mm above the load coil. Increasing the observation height from 2 mm to 10 mm above the load coil significantly reduced the "enhancement" effect to "no" effect. In increasing the







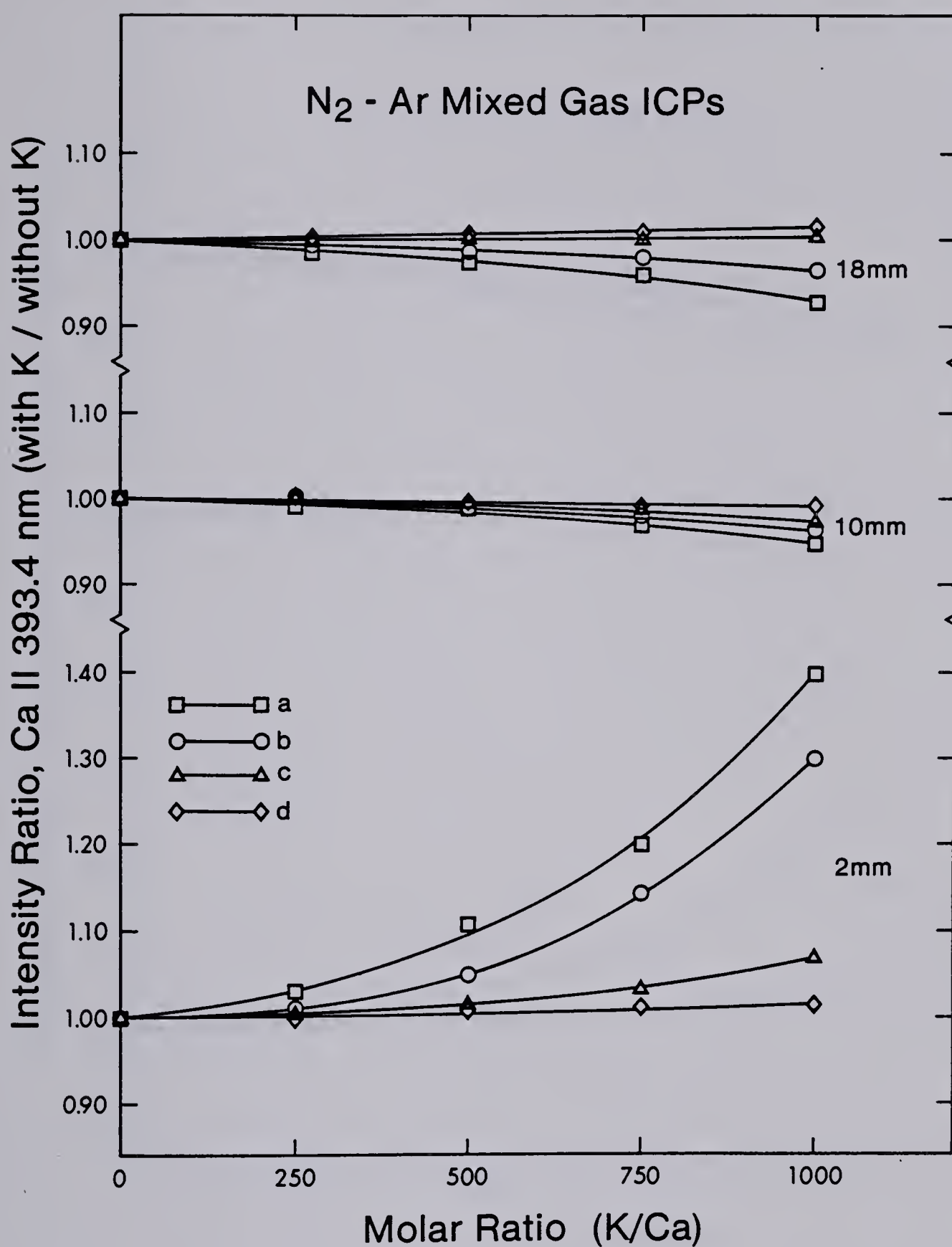


Fig. 45. Effect of K interference on CaII 393.4 nm emission in  $N_2$ -Ar mixed gas ICPs, at observation heights of 2mm, 10mm, and 18mm above the load coil. Percentage of  $N_2$  in the coolant flow; (a) 0%, (b) 10%, (c) 20%, and (d) 100%.



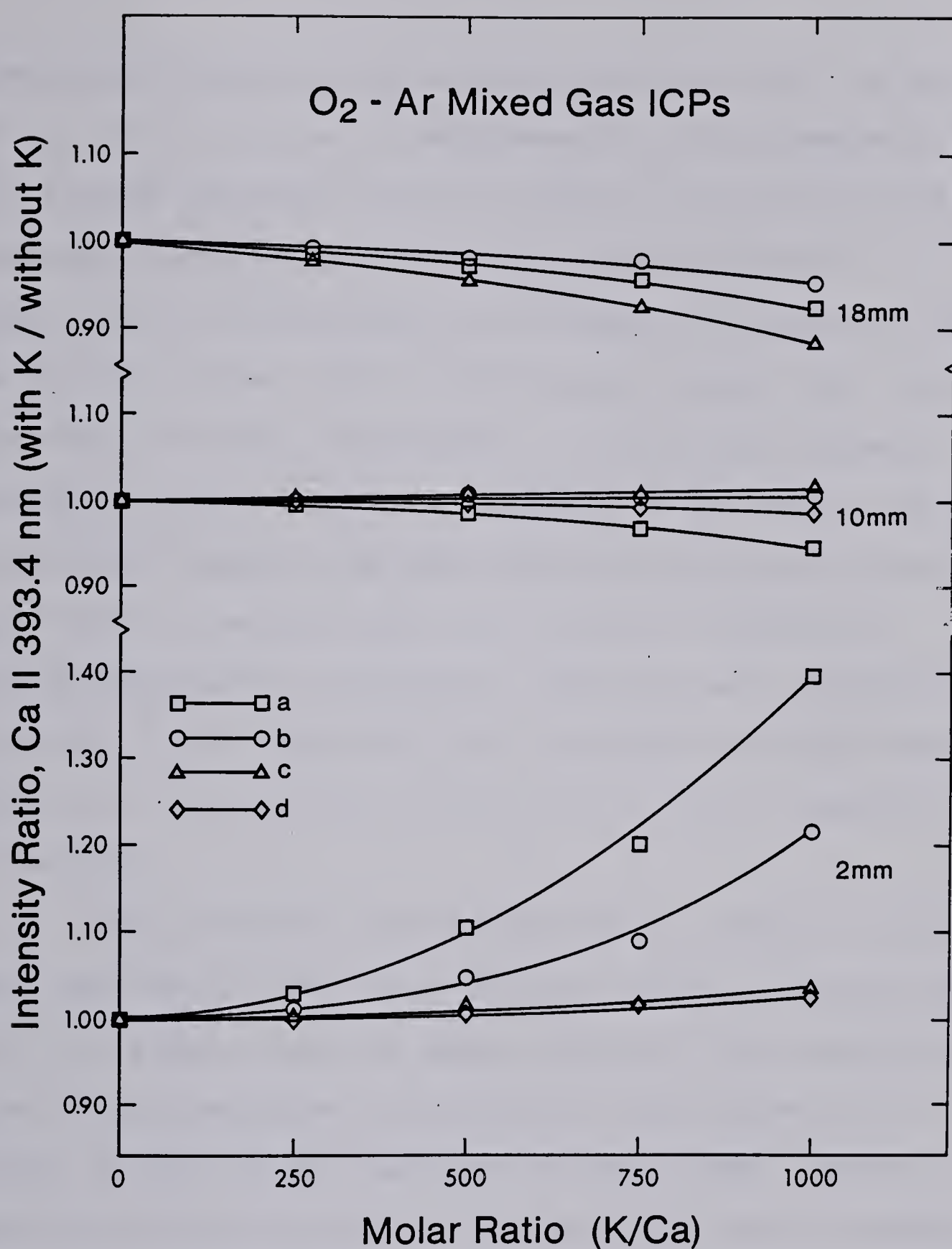


Fig. 46. Effect of K interference on CaII 393.4 nm emission in O<sub>2</sub>-Ar mixed gas ICPs, at observation heights of 2mm, 10mm, and 18mm above the load coil. Percentage of O<sub>2</sub> in the coolant flow; (a) 0%, (b) 10%, (c) 20%, and (d) 100%.



observation height to 18 mm above the load coil, we see that the ion line emission is suppressed by the presence of the EIE. Another important point to note in this figure is the remarkable similarity between the ionization and vaporization interferences as nitrogen is introduced into the coolant stream. Both interference studies show that the magnitude of signal suppression or enhancement depends critically on the amount of nitrogen in the coolant flow of an argon ICP source. The magnitude of this interference is significantly reduced when more and more nitrogen is introduced into the ICP source. From the data presented in Figure 45, it is clear that the nitrogen cooled ICP has the tendency to minimize the effect of K on the Ca emission ionization.

The analogous set of data for the oxygen - argon mixed gas ICP is shown in Figure 46. First, it can be seen from this figure that the basic nature of the ionization interference patterns for the Ca ion line emission is similar to that of the nitrogen cooled plasma. Second, introducing the foreign gas into an Ar-ICP source seems to be a convenient way of minimizing this matrix effect.



### E. Analytical Calibration Curves

The effect of various nitrogen or oxygen cooled plasmas on the analytical calibration curves of calcium and manganese are shown in Figures 47 to 49. The calibration curves were measured using 0, 10, 20, and 100% mixed gas plasmas. The numbers on each figure correspond to the following manner: (1) 0%, (2) 10%, (3) 20%, and (4) 100% N<sub>2</sub> or O<sub>2</sub> cooled plasmas. For the sake of comparison, the calibration curves were determined at the optimum observation height for each plasma, for example, Ar-ICP at 18 mm whereas 100% N<sub>2</sub> cooled ICP at 2 mm above the load coil.

It can be seen from these figures that calibration curves for all ICPs are linear over the concentration range between 0.1 ppm to 1000 ppm. For both calcium and manganese, slopes of the intensity versus concentration plots are all near unity and show reasonable reproducibility. It is important to note that the sensitivity of the calibration curve improved when the conventional argon discharge was converted into a 10 or 20% mixed gas ICP. However, the sensitivity decreased when more than 20% foreign gas was introduced into the coolant flow of the argon discharge.





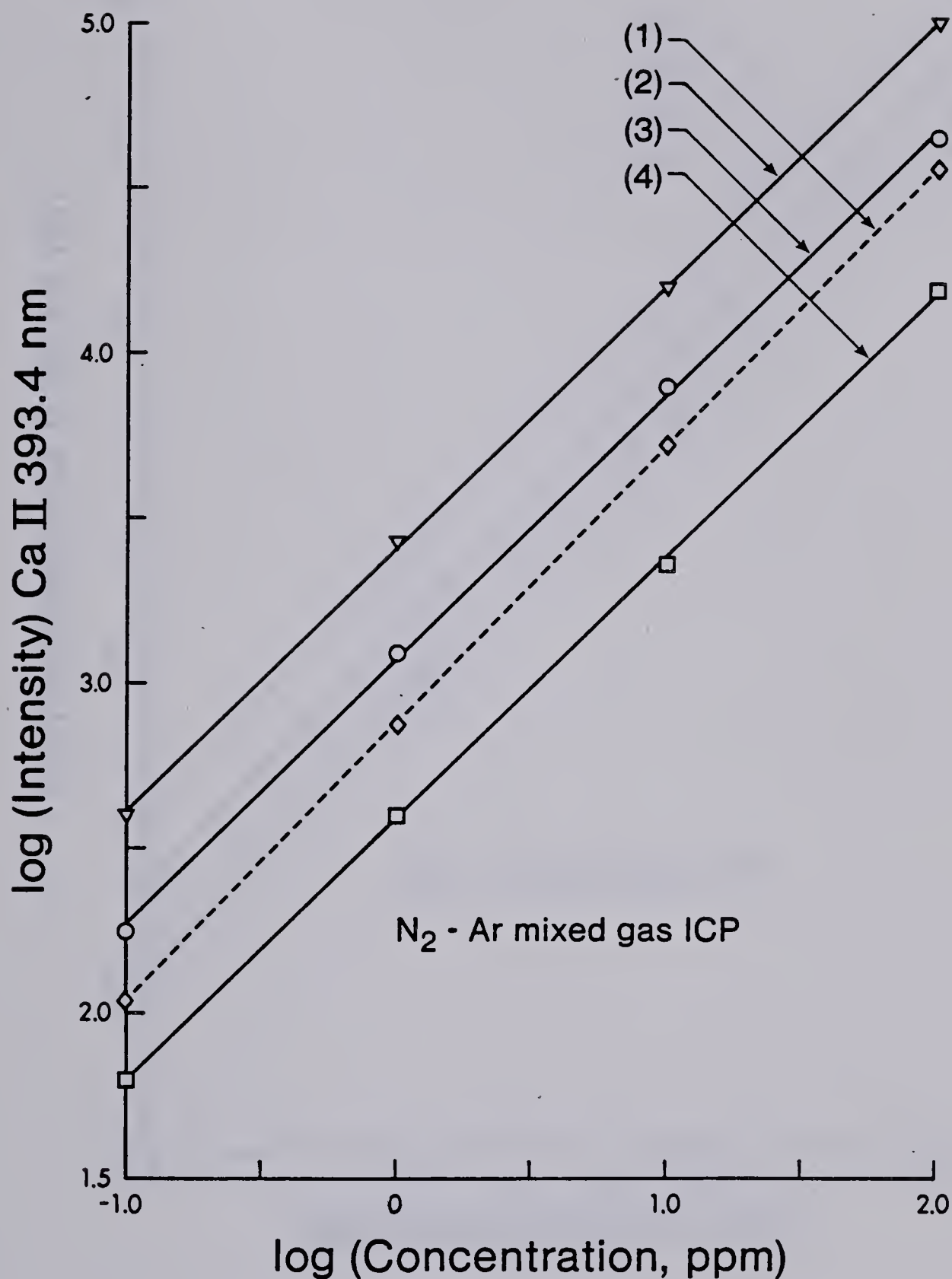


Fig. 47. Effect of N<sub>2</sub>-Ar mixed gas ICPs on the analytical calibration curves for CaII 393.4 nm line. Coolant gas composition and observation height above the load coil; (1) 100% Ar at 18mm, (2) 10% N<sub>2</sub>- 90% Ar at 10mm, (3) 20% N<sub>2</sub>- 80% Ar at 5mm, and (4) 100% N<sub>2</sub> at 2mm.



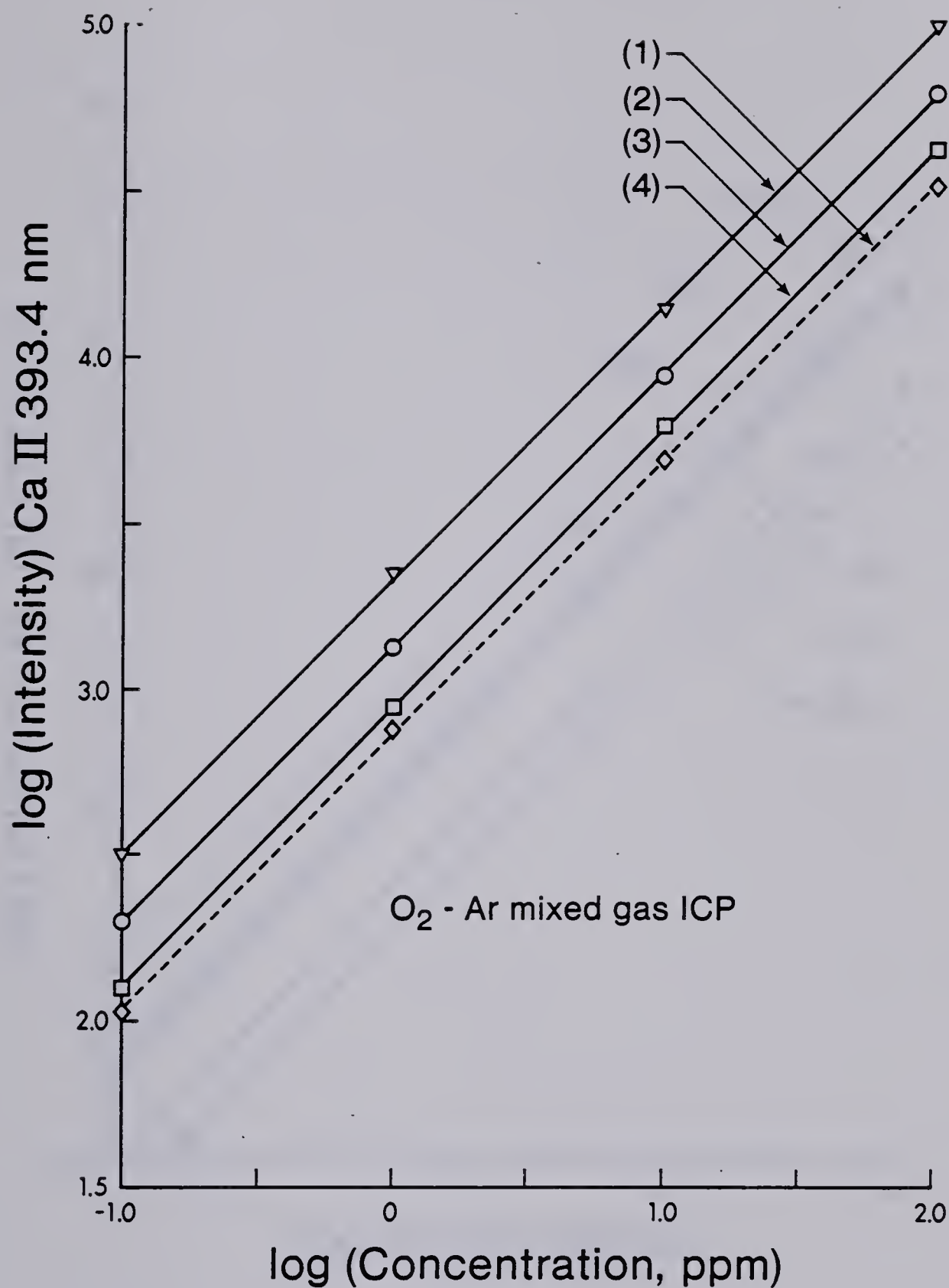


Fig. 48. Effect of O<sub>2</sub>-Ar mixed gas ICPs on the analytical calibration curves for CaII 393.4 nm line. Coolant gas composition and observation height above the load coil; (1) 100% Ar at 18mm, (2) 10% O<sub>2</sub>- 90% Ar at 10mm, (3) 20% O<sub>2</sub>- 80% Ar at 5mm, and (4) 100% O<sub>2</sub> at 2mm.



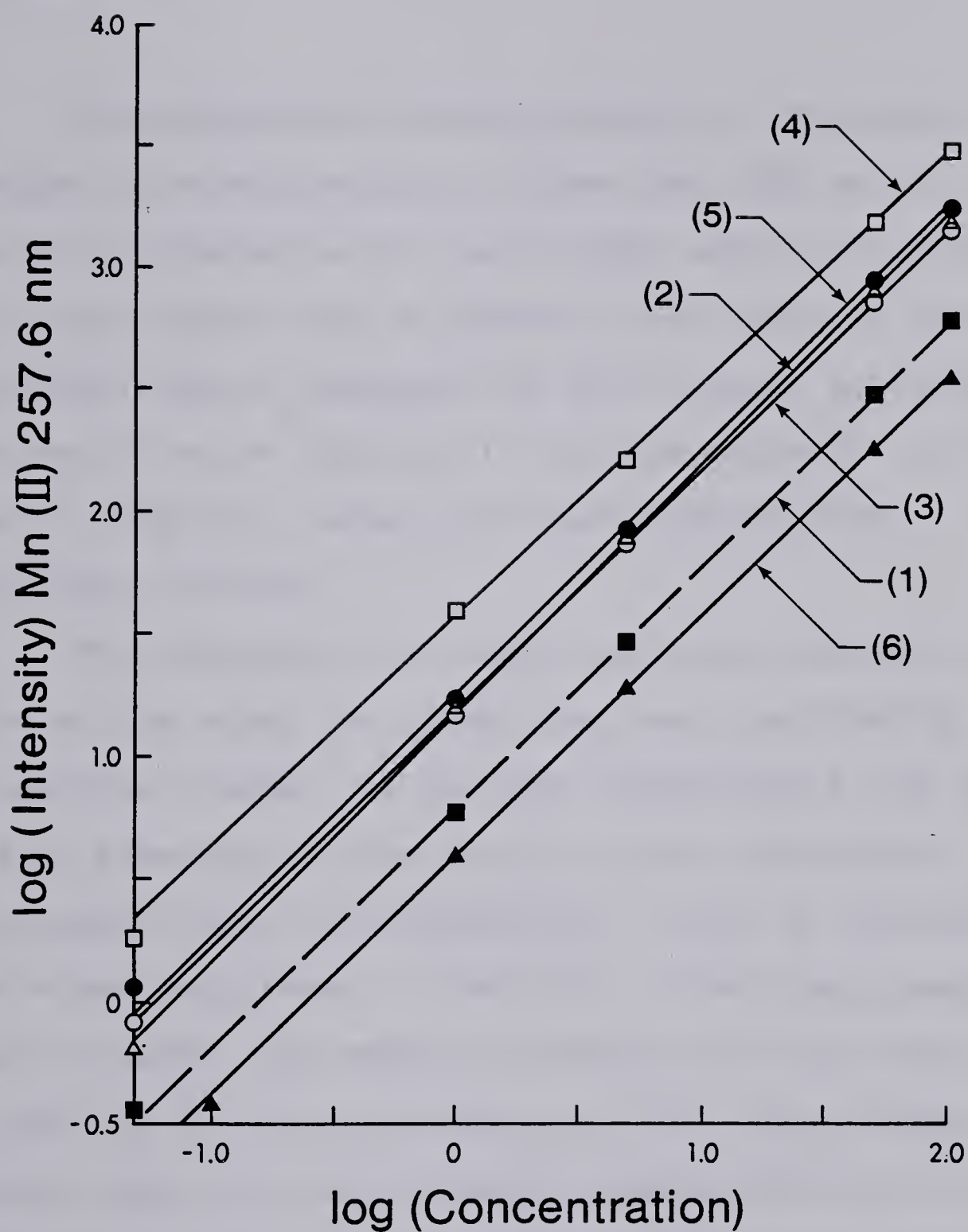


Fig. 49. Effect of N<sub>2</sub>-Ar mixed gas ICPs on the analytical calibration curves for MnII 257.6 nm line. Coolant gas composition and observation height above the load coil; (1) 100% Ar at 18mm, (2) 10% N<sub>2</sub>- 90% Ar at 10mm, (3) 20% N<sub>2</sub>- 80% Ar at 5mm, and (4) 100% N<sub>2</sub> at 2mm.





## F. Conclusions

The experimental data presented in Chapters III to VI support the utilization of mixed gas ICPs as an alternative discharge for the ICP-AES especially when 5 to 20% of the foreign gas is present in the coolant flow. The particular results presented in this chapter indicate that mixed gas ICPs are superior to the conventional Ar-ICP in terms of stability, sensitivity and freedom from interference effects.

The dependence of analyte emission intensity on the nature of the mixed gas plasma has been clarified by spatial and spectral studies. It has been demonstrated that the emission intensity of the analyte signal increased significantly when the conventional Ar-ICP is converted into a 10% mixed gas plasma. In addition, mixed gas plasmas appear to affect the emission intensity of ion lines more than that of the neutral atom lines. All these results strongly imply that the emission characteristics of the Ar-ICP source have been altered considerably by introducing the foreign gas into the source. Obviously more work remains to be done in order to unveil the excitation phenomena associated with the mixed gas ICPs.

Since there are quite a number of electrons present in the ICP source, it is apparent that the majority of



solute-plasma interactions has to originate through the collisions of the analyte with energetic electron. Hence, understanding of the mechanisms for excitation and ionization processes definitely requires the measurements of electron number density in the plasma source. Such measurements have been carried out and will be presented in Chapter VII.



## CHAPTER VII

### ELECTRON DENSITY MEASUREMENTS IN ICPs USING A PHOTODIODE ARRAY DETECTION SYSTEM

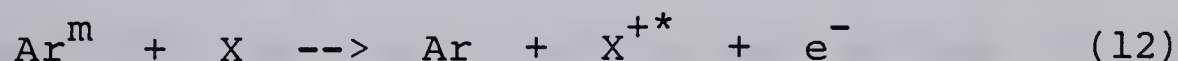
#### A. Introduction

The preceding chapters focused on the empirical evaluation and characterization of mixed gas plasmas in terms of their spectral characteristics and analytical performance. Despite the proven success of the ICP as an excitation source, the development of ICP techniques is still hindered by a lack of understanding, at a fundamental level, of excitation and ionization processes in the plasma discharge. Because the analyte intensities are greatly influenced by ICP operating parameters such as plasma power, aerosol flow rate, and plasma gas composition, a change in any of these variables will definitely alter the excitation and ionization characteristics in the plasma and thus the magnitude of plasma temperature. Therefore, a close interplay between theory and experiment is mandatory in order to ensure a more complete understanding of the excitation processes in the ICP.



## B. Excitation and Ionization Mechanisms in Mixed Gas ICPs

Parallel to plasma diagnostic investigations, theoretical models of the ICPs are beginning to emerge (86-88,93,120,122). Although the excitation and ionization processes in the plasma have been investigated by a number of workers, there have been quite a number of conflicting reports concerning the mechanism of excitation and ionization of the analyte in the plasma source. At present, several mechanisms have been proposed by different authors to explain the observed emission intensities in the plasma discharge (122,101,103). The most prominent excitation model, originally proposed by Mermet (101), is based on energy transfer from argon metastable atoms to the analytes known as Penning ionization.



This energy transfer is possible because radiative decay of excited argon metastables is quantum mechanically forbidden. Therefore the excess energy carried by excited metastable states may often be transferred to other species. Boumans and de Boer (79) published an in-depth study of the possible nonthermal mechanisms in the plasma discharge involving





argon metastable interactions.

Recently, Boumans and de Boer (79) set up a simple mathematical model in which the argon metastable atoms act as both an ionizer of analyte species through the Penning process and as ionizant (an easily ionizable constituent) to account for nonthermal overpopulation of the ion levels. In their hypothesis, the metastable levels were considered to be easily ionizable with an ionization potential of only 4.21 eV. Since transitions between the excited metastable levels and the ground state are forbidden, the argon metastable states have considerably longer lifetimes than the radiative decay. Because of this long lifetime, these metastable states would act as a very effective energy buffer for the analyte species and thus influence the excitation characteristics in the ICP. Since the metastable states are about 11.5 eV above ground state, they are capable of ionizing and exciting a large fraction of analyte introduced into the plasma. Boumans and de Boer (79) also emphasized that the model must be substantiated by a large number density of argon metastable atoms, in the order of  $10^{14} \text{ cm}^{-3}$ , before the model can be considered valid. Recently, Mermet and Trassy (147) have reported the metastable concentration in the center of a 2.1 Kw discharge to be in the order of  $10^{12} \text{ cm}^{-3}$ . With this concentration, the model proposed by Boumans and de Boer offers a reasonable



prediction on the ionization and excitation mechanisms in the plasma.

At first, these explanations seem intuitively reasonable. However, there are several physical considerations which lead one to question the validity of this proposed Penning process in the ICP. Although the excited argon metastable states have sufficient energies to excite many analyte atoms, it is important to point out that several emission lines with ionization and excitation potentials (IP + EP) above 11.5 eV, such as CdII (226 and 214 nm), ZnII (202.5 nm), MnII (257.6 nm), CrII (267.7 nm) and CuII (224.7 nm), have always been observed in the plasmas. This means that ionization and excitation processes resulting from argon metastable collisions are not energetic enough and therefore alternative explanations must be proposed for the excitation of these energetic species.

The validity of the argon metastable collision theory is further challenged by the conclusions of several authors that comparatively fewer argon metastable atoms exist in the atmospheric and high temperature discharges than might first be thought. The metastable state densities for ArI in a low pressure plasma (0.05 to 0.1 torr) were investigated by Jolly and Touzeau (148) using self-absorption measurements. They reported a drastic decrease in argon metastable concentrations as pressure or





the discharge current was increased. With the pressure of 0.1 torr and the discharge current of 500 A, an argon metastable concentration of  $5 \times 10^{10} \text{ cm}^{-3}$  was measured in their experiment, which is considerably lower than the value reported for the atmospheric discharge by Mermet and Trassy (147). Since the rate of decay of metastable levels increased with pressure and temperature, Vacquie et al. (149) described the metastable destruction due to collisional deactivation, which led either to excitation to a higher level or to deexcitation during a superelastic collision. The latter process, which is potentially important with slower electrons, leads to a very large energy transfer in the discharge and thereby a favourable deactivation process.

In a recent paper, Williams and Coleman (150) calculated the frequencies for the argon-argon and argon-electron collisions from the macroscopic parameters of the atmospheric pressure plasma. The frequency of  $2 \times 10^8 \text{ s}^{-1}$  was calculated for the argon-argon collision rate, and an even higher frequency of  $2 \times 10^{11} \text{ s}^{-1}$  was calculated for argon-electron collisions. The higher rate is probably due to the low mass and high mobility of the electrons. From these calculations, the tendency of metastable atoms towards collisional decay in a high temperature atmospheric discharge, such as ICP, is extremely high. Because of the





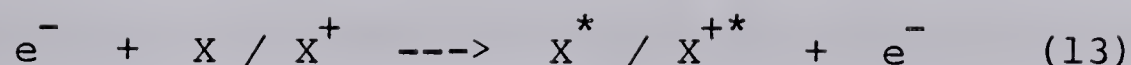
high collision rate in high temperature plasma even very short lived radiative states are strongly quenched. Based on the collision frequency of argon-electron and the relatively small population of argon metastable atoms in the atmospheric discharge, it would seem unlikely that excitation and ionization processes in this discharge are caused by collisions with energetic argon metastable atoms.

Furuta and Horlick (122) have recently suggested different mechanisms of excitation for neutral atom and ionic species. In their paper, they reported that neutral line emission low in the plasma is likely a result of electron collision and that of the ionic species generation and excitation result from collision with energetic argon species. Based on the arguments presented so far, it is doubtful that, in the case of atmospheric pressure plasma, the excited argon species are concentrated enough to excite and ionize a large fraction of analyte introduced into the plasma.

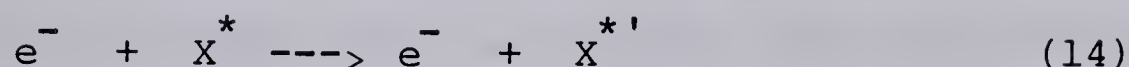
Most recently, Alder et al. (96) have proposed that analyte excitation and ionization in the ICP are primarily dominated by electron impact. In fact, many reactions may occur by electron collisions (87), namely,

- (1) excitation from the ground state



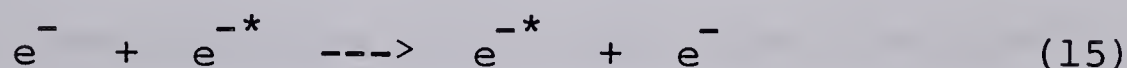


(2) excitation from another excited state



(3) by superelastic collisions and ionization to  $X^{+}$  and  $X^{2+}$ .

(4) by energy transfer within the electrons



Electron number density measurements in the Ar-ICP have been made by several workers over a wide range of operating conditions (88,93,94,96,98,103). Experimental results available from these measurements indicate that electron number density in an argon ICP is in the range of  $10^{13}$  to  $10^{16} \text{ cm}^{-3}$ . Because of the high number density of electrons in the plasma, it is logical to assume that electrons are one of the major physical parameters that govern the excitation and ionization processes in the plasmas. Various authors have already measured the electron number density in a high rf argon plasma (88,93,94,96,98,103) in order to predict the excitation



mechanisms in that excitation source. Most workers believe that the spatial distribution of the excitation temperature and the electron density is an important parameter to be investigated in order to understand the excitation mechanisms in the plasma source. However, few measurements of the spatial distribution of electron density in the ICP, particularly mixed gas plasmas, have been made (88,94,98) and no correlation has been made between the spatial resolution of the electron density and that of the analyte emission intensity.

In contrast to the argon metastable atoms, energy acquired by free electrons is not quantized. The electrons can therefore acquire or transfer any amount of energy from/to neighboring particles. Electrons can pick up widely differing amounts of energy from collisions of the second kind and also from the oscillating rf field. Therefore, in a plasma with a high density of electrons, there is a high probability of atoms colliding with energetic electrons. When an atom collides with an energetic electron, the energy of the electron is easily transferred to the atom; therefore the excitation mechanism in the ICP involves collisions of a second kind in which the energy of an electron is converted into excitation energy of an atom.

The efficiency with which energy transfer between atom-atom, atom-electron or electron-electron collisions





occurs depends on the collision frequency for each process. Because of the low mass and high mobility of electrons, electron-atom collisions will occur at a higher rate than the atom-atom collisions. Collision frequencies for these processes have been calculated by Williams and Coleman (150). Comparison of these collision rates ( $10^8 \text{ s}^{-1}$  for atom-atom and  $10^{11} \text{ s}^{-1}$  for atom-electron) indicates that the greater part of the ground state atoms will be excited or ionized in collisions with energetic electrons, whereas only a small fraction of the ground state atoms involved is likely to acquire excitation or ionization energy by colliding with the excited argon atoms, analyte atoms or argon metastables. The predominance of atom-electron collisions in producing and destroying the excited analyte states implies that metastable levels may be of little importance in the ICP, and therefore the excitation or ionization energy transfer has to be accomplished by the analyte atoms and energetic electrons. Since electron may take on a continuum of energies they are capable of exciting and ionizing a wide range of analytes.

The recombination between ions and electrons often occurs in the presence of a third body (three body collision). The third body can be an electron, an atom or an ion either excited or in the ground state. The energy liberated in the recombination process is shared by the





three bodies and reappears as kinetic or excited energy. The background continuum observed in the plasma is primarily a result of radiative recombination of ions and electrons. In the vicinity of the induction coil the background continuum emission is fairly high which indicates a high electron density near the load coil.

The observed high sensitivity of ion lines in mixed gas plasmas may be explained by large effective cross-sections of charged particles for elastic collisions with electrons. Due to coulombic interactions, effective cross-sections of ions for electron encounters are large; therefore, there is a great likelihood that the frequency of ion-electron collisions is higher than that of the atom-electron collisions. Numerical data and theoretical treatments for the effective cross-sections of neutral and charged particles for elastic collisions with electrons are discussed in detail by Boumans (91).

It is unlikely that any of these proposed mechanisms dominates the excitation and ionization mechanisms in the plasma discharge. Among them, the energy transfer from energetic electron to the analyte seems to provide a reasonable prediction of the excitation and ionization processes in the plasma source, but the role of excited argon metastables or other excited species cannot be neglected. In addition, several of the mechanisms may be



acting simultaneously to produce excited or ionized states.

A study of spatially resolved analyte emission and electron density will certainly provide an important set of data to distinguish which of these mechanisms can be considered most probable excitation and ionization mechanisms in analytical ICP spectroscopy. The intent of this work is to study the nature of interactions between the analytes and electrons. This chapter will also briefly discuss various methods of electron density measurement. The mapping of electron density in the ICP as a function of various operating conditions will be discussed in the following chapters. Mixed gas ICPs ( $\text{Ar-O}_2$ ,  $\text{Ar-N}_2$ ) will also be used as probes for the study of electronic excitation in the plasma. The effects of the introduction of various percentages of nitrogen and oxygen on the electron density of the argon ICP will also be discussed in the following chapters. The correlation of the electron density with the emission intensity of cadmium atom and ion lines will be discussed in Chapter IX.

The present model is strictly based upon the experimentally characterized discharge in spectrochemical analysis; however, the theoretical model will not be presented in this work. The experimental facts presented in these chapters establish the foundation for describing the fundamental processes occurring within the discharge and the



most probable interaction of plasma with analyte.

### C. Electron Density Measurements

Although the electron density is an important parameter in the plasma discharge, the measurement of electron density is usually associated with large uncertainties. Depending on the methods and operating conditions used, the results of electron density measurements may differ by several orders of magnitude. The electron density in the ICP measured by various workers varies from  $10^{13}$  to  $10^{16}$   $\text{cm}^{-3}$ . In general, the electron density in the plasma discharge can be measured by several methods, namely

1. Microwave probe
2. Optical interferometry
3. Background continuum
4. Intensity ratio of an ion-atom line pair  
of an element
5. Line merging method
6. Measurement of line profile







## 1. Microwave Probe

Extensive use of electromagnetic radiation as a probe for the study of electron concentration, particularly in the microwave region, has been made (151). Unfortunately, microwave probes are limited in applicability by the plasma frequency cutoff, and also limited to the study of plasmas with electron densities below  $10^{13} \text{ cm}^{-3}$ . Since the majority of research in analytical atomic emission spectroscopy involve plasmas with electron densities well above  $10^{13} \text{ cm}^{-3}$ , measurement of electron densities using microwave probes are not suitable.

## 2. Optical Interferometry

Several techniques have appeared in recent years that take over where microwave diagnostics are no longer applicable. The theory of this optical interferometric method is based on the contributions of electronic and non-electronic parameters to the refractive properties of ionized gases in the plasma discharge. Several workers in the field of high temperature plasma physics (151) have demonstrated the applicability of interferometry to the study of electron density in plasma sources. Although interferometry has been successfully applied to a wide



variety of plasma experiments, application of this technique to electron density measurements in analytical plasma spectroscopy is unrealistic due to the high complexity of the experiment.

### 3. Background Continuum Method

The third method, based on the measurement of absolute continuum intensity (88,98), provides an electron density measurement which has a weak dependence upon the assumed electron temperature. Provided the electrons have a Maxwellian velocity distribution, the electron densities may be determined from a measurement of the continuum intensity (refer to Chapter I, Equation 6).

For the proper interpretation of a measured continuum intensity in terms of electron densities, the plasma dimensions, electron temperature and the compositions of the plasma must be known. Using this method, Kornblum et al. (98) reported the values of electron density for an atmospheric pressure Ar-ICP between  $5 \times 10^{14}$  and  $2 \times 10^{15} \text{ cm}^{-3}$ . The basic assumption of this method is the plasma be in LTE state where  $T_e = T_{ion}$ . In addition, the value of  $T_{ion}$  was derived from Saha's equation. Errors in the experimental temperature determinations in the ICP are large, therefore this method of electron density measurement is not very



accurate. Furthermore, small impurity concentrations of foreign gases or charged particles in the argon plasma will make significant contributions to the continuum intensity, mainly because of the recombination processes. The molecular bandheads that arise in the mixed gas plasmas further complicate the electron density measurement by this continuum method.

#### 4. Intensity Ratios

The electron density can be measured by the intensity ratio of an atom-ion pair of the same element. It is the most convenient method for electron density measurements in the plasma discharge. This intensity ratio method is based on the Saha-Eggert equation (refer to Chapter I, Equation 7).

When the Saha-Eggart equation is used to calculate  $N_e$ ,  $T_{ion}$  is assumed to be  $T_{exc}$ , and  $T_{exc}$  is derived from argon lines. Results obtained by Mermet (93), Boumans et al. (99), and Kalnicky et al. (94) were  $2 \times 10^{13}$ ,  $2 \times 10^{14}$  and  $10^{15} \text{ cm}^{-3}$  respectively. The value of  $N_e$  obtained by this method show a range of values due to the differences in the 'assumed'  $T_{ion}$ . Experimentally, such a method is more attractive than optical interferometry because the experiment can be set up easily and the method is readily applicable. In order to





ensure that the intensity ratio of the two lines observed be sensitive and accurate, it is important that the two lines under study must be in the same spectral region. To make an accurate determination of the intensity ratio, the monochromator has to be calibrated against a standard tungsten filament lamp. It is also important to select a suitable set of lines because the precision of the intensity ratio method depends on the difference between the energies of the lines used. Although this method fits the majority of analytical spectrochemical conditions very well, it has the serious drawback of being indirect, as it requires not only the known accurate transition probabilities but also requires computation of the electron density from the Saha-Eggert equation (Equation 7). Since experimental results available from measurements with the argon plasma over a wide range of operating parameters (79,88,93-97) indicate that local thermal equilibrium (LTE) does not prevail in this plasma source, the major drawback of this line ratio method is the requirement that the plasma be in LTE.

## 5. Line Merging Method

Another method for the electron density measurement is based on observation of the merging of atomic emission





lines at the series limit. This line merging method has been extensively investigated both theoretically and experimentally by various workers (152-155). Application of this technique to electron concentration measurements in analytical plasma spectroscopy was first reported by Montaser et al. (155). This method is based on the Inglis-Teller theory which states that as the principal quantum number of the lines in the series increases, the halfwidth due to Stark broadening also increases. As the principal quantum number increases, the wings of the Stark broadened lines overlap and form a continuum as the series limit is approached. The principal quantum number at which the merging occurs depends on the electron number density. The validity of the Inglis-Teller formula has recently been questioned by several workers (152-154). The major drawback of this method is that when the series limit is approached, the emission intensity of the lines under investigation falls rapidly. Therefore, the series limit where the line merging occurred is not well defined and is also subjected to many approximations. This method of electron density measurement can only be considered as an estimation because of the imprecise nature of the method. Also, spectra of most elements at their higher quantum series are subjected to severe background or spectral interferences; hence, an expensive high resolution spectrometer is required.



## 6. Measurement of Line Profile

A direct method for determining the electron density based on the measurement of line profiles (Stark width) has gained in popularity in analytical atomic spectroscopy (13,88,93,98,100). Unlike other methods, this technique is nearly independent of the plasma temperature. Therefore, electron density can be calculated from the measured line profiles even if the temperature is only approximately known. This technique provides a more precise and accurate electron density determination than the Saha-Eggert method (line ratio method) where errors in temperature measurement contribute to large uncertainty in the resulting values of electron density. This method can also be employed directly even if the system is not in LTE. Over the past few years, this method has been considerably improved (92) and the Stark profile method is now fundamentally quite accurate with theoretical considerations giving rise to less than 10% uncertainty in the values obtained. Errors in this technique are largely determined by the experimental measurements of line emission, and also by the application of the Abel inversion technique to the data where such post processing is required.

Although this technique is accurate and precise, it





is not without disadvantages. First, the intensity of the line of interest must be measured over the large body of the plasma if spatial profiles are required for Abel transformations (92,151). Second, a knowledge of accurate Stark parameters is essential for calculation (92). Third, the experimental line profiles must be deconvoluted to account for instrumental and Doppler broadening (92,151). Finally and most importantly, measuring the line profiles is an extremely tedious process, which can take excessive amount of time and effort.

This last problem is partially solved by implementing Abel inversion and measuring the electron density from Stark broadening using a photodiode array measurement system. The measurement of radial emission intensities from the ICP via the Abel inversion process will be discussed later in this chapter.

#### D. Line Broadening

The line profile is actually the convolution of the physical and instrumental profiles. The former is the shape of the line which is due to the physical conditions of the plasma source. In general, the physical shape of a line is controlled by three major factors, (92,151).





a. Natural broadening,

which has its origin in the finite lifetime of an excited state. Its contribution to the halfwidth is normally only in the order of 0.001 Å and therefore it is usually ignored in comparison with other contributions.

b. Doppler broadening,

which is due to the random motion of the emitting atoms relative to the observer (detector).

c. Collisional or pressure broadening (Stark Effect),

which results from the perturbation of energy levels by collision (Lorentz broadening) and by the pressure of an electric field of surrounding charges (Stark broadening).

Since the contributions to the line profiles by natural and instrumental broadening processes amount to less than 1%, they are negligible. The following discussion will be limited to the two dominant causes of the line broadening in the plasma discharge, i.e., thermal Doppler effect and interatomic collisional effect (Stark effect).



## 1. Doppler Effect

The motion of a radiating particle towards or away from an observer leads to a wavelength shift of the emitted line, the so-called Doppler shift. In an excitation source, the random motions of the radiating particles cause Doppler broadening of the lines. In the case of Maxwellian distributions, such lines have Gaussian profiles which are governed by the following equation:

$$\Delta\lambda_{\frac{1}{2}}^D = \lambda \left( \frac{2kT}{mc^2} \right)^{\frac{1}{2}} = 7.16 \times 10^{-7} \lambda \left( \frac{T}{m} \right)^{\frac{1}{2}} \quad (16)$$

where  $\lambda$  = the wavelength of the line

$kT$  = the thermal energy of the emitting atoms  
or ions

$m$  = mass of atom or ion

$c$  = speed of light

Inspection of this relationship shows that thermal Doppler broadening is most pronounced for the lines of light elements at high temperature.

It is possible to calculate the plasma temperature using the Doppler effect on the line profile. However, before a measured line width is used, it is necessary to



make sure that the thermal Doppler effect is really the most prominent and important line broadening mechanism. In addition, before calculating the extent of thermal Doppler broadening in the line profile, the other cause of line broadening in the plasma, such as the Stark effect, has to be considered.

## 2. Stark Effect

The atom and ion emission line profiles of species which are embedded in a dense gas or plasma, will be determined by the extent of interactions of the emitters with the surrounding charged or neutral particles. This type of line broadening is generally known as pressure broadening. From the practical point of view, the pressure broadening can be further subdivided into:

- a. Resonance broadening
- b. Van de Waal's broadening
- c. Stark broadening

depending on whether the broadening is caused by interactions with (a) atoms of the same kind, (b) atoms or molecules of different kinds or (c) charged particles. Since ions and electrons (charged species) are present in the inductively coupled plasma in sufficiently high concentration, the long range coulombic forces are dominant,





and therefore the dominant broadening process for line profiles will be the Stark effect. Because of its importance in plasma diagnostics, the following discussion will be limited only to Stark broadening.

The evaluation of electron densities from Stark broadening, which is based on a comparison of the measured and calculated line widths, shows a consistency within 6 to 10% for hydrogen beta and alpha lines (92,151,156). Because of its accuracy, the measurement of Stark half-widths has emerged as one of the most reliable and convenient methods for the determination of electron densities in plasma discharges. In the Stark broadening calculations, only electrons and singly positively charged ions are normally considered; therefore, hydrogen line profiles should be used for the most reliable electron density measurements. Calculations for higher ionizations are of little practical interest because Doppler broadening tends to dominate in highly ionized plasma (92).

The Stark broadened profiles of the hydrogen Balmer lines have been measured by several workers (13,88,93,94,98,100). Under comparable operating conditions, they are the most strongly broadened lines of all elements and are therefore of great practical importance. The Stark method is generally recognized as the most accurate technique for measuring electron densities in plasma





discharges.

Halfwidths of these hydrogen lines exhibit a Stark effect in which the halfwidth is proportional to the two-thirds power of the electron density.

$$\Delta\lambda_{\frac{1}{2}}^S = C(N_e, T) N_e^{2/3} \quad (17)$$

where  $\Delta\lambda_{\frac{1}{2}}^S$  is the full Stark width, and  $C(N_e, T)$  is a coefficient that is only a weak function of the electron density. In addition, it has a slight temperature dependence through the ion-ion correlation of Debye-shielding correction and the velocity dependence of the impact broadening (92).

Values of the coefficient  $C(N_e, T)$  for the theoretical profile of the  $H_\beta$  line can be found in the book by Griem (92). The value of the theoretical or reduced halfwidth,  $\alpha_{\frac{1}{2}}$ , must be retrieved from the theoretical profile first. The theoretical or reduced  $H_\beta$  line profile is presented as a function of  $S(\alpha)$  (reduced Stark profile) versus  $\alpha$  (reduced wavelength distance). The hydrogen-beta line shows only a small asymmetry, which has been discussed in detail by Griem (92). Data for the reduced hydrogen-beta Stark profile presented in Figure 50 were quoted from Griem (92).

One half of the symmetrical reduced Stark profile



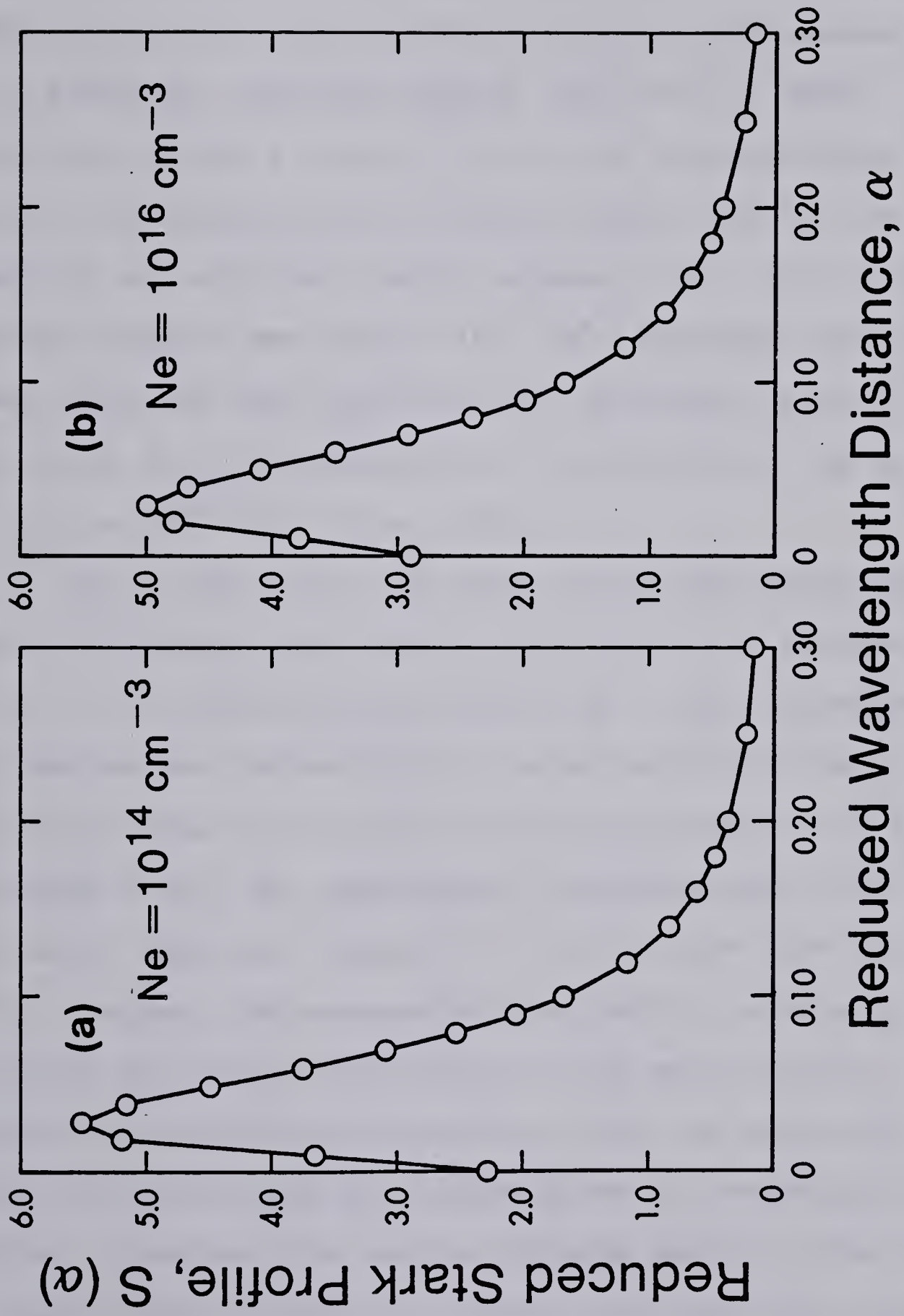


Fig. 50. Theoretical profiles for  $H\beta$  486.1 nm. Electron density; (a)  $10^{14} \text{ cm}^{-3}$  and (b)  $10^{16} \text{ cm}^{-3}$ . (The data are found in H.R. Griem's "Plasma Spectroscopy", McGraw Hill, 1964).



for a discharge with a 5000 K temperature and  $10^{14}$  electrons per  $\text{cm}^3$  is represented in Figure 50a. Figure 50b corresponds to the calculated Stark profile with same temperature but with a different electron density ( $10^{16} \text{ cm}^{-3}$ ). Both calculations yield a central dip in the hydrogen-beta line profile. The characteristic central dip is due to the absence of an unshifted Stark component (92). Calculation of the Stark profile for  $N(e) = 10^{14} \text{ cm}^{-3}$  produced central maxima about 58% down from the peak intensity (Figure 50a), in contrast to a calculated dip of only 40% for the plasma with  $N(e) = 10^{16} \text{ cm}^{-3}$  (Figure 50b).

The  $H_\beta$  486.1 nm line profile obtained experimentally using a photodiode array measurement system is presented in Figure 51. It should be noted that the x-axis corresponds to the diode number instead of the usual wavelength axis. The distance between two adjacent diodes represents 0.48 Å in wavelength units. The experimental hydrogen-beta line observed in this lab (Figure 51) did not give rise to a central minimum. The absence of the central minimum is attributed to the low resolution of the monochromator. Also, the electron density and temperature for the analytical plasma are higher than the values given to the calculated profiles, therefore the central minimum would be smaller than that of the calculated reduced Stark profiles presented in Figure 50.







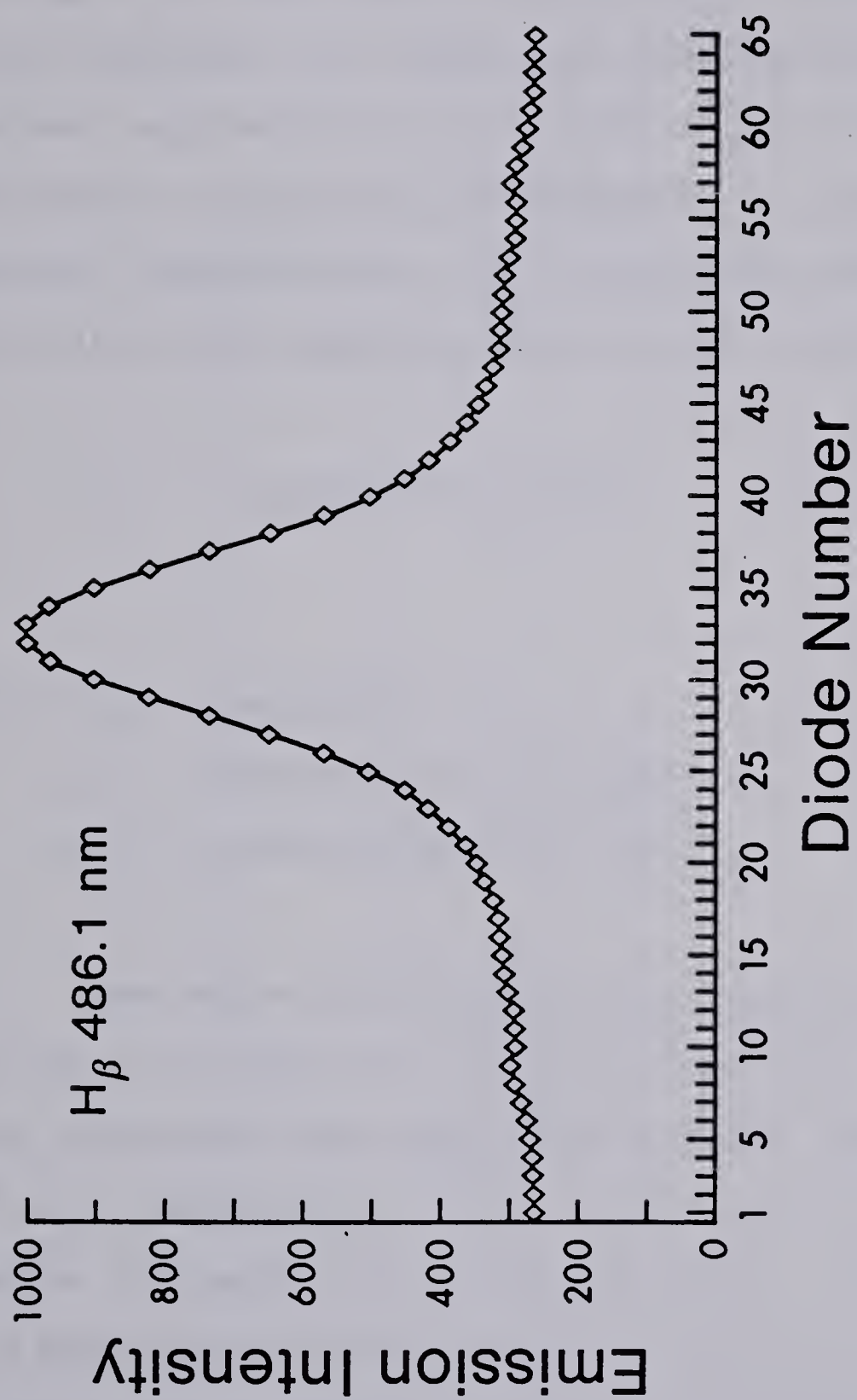


Figure 51. Experimental profile for  $H_\beta$  line emission as measured by a photodiode array detector.



One point regarding the expression in Equation 17 deserves mention at this time. The temperature contribution to  $C(N_e, T)$  is negligible in comparison to the contribution by  $N_e$ , therefore the temperature term may be dropped. The resultant expression for the Stark width is then considerably temperature independent. In general, for most diagnostic applications, the relationship between half-widths and electron density can be expressed as,

$$\Delta\lambda_{\frac{1}{2}} = 2.50 \times 10^{-9} \alpha_{\frac{1}{2}} N_e^{2/3} \quad (18)$$

where  $\Delta\lambda_{\frac{1}{2}}$  = halfwidth, Å,  
 $\alpha_{\frac{1}{2}}$  = theoretical halfwidth,  
 $N_e$  = electron density,  $\text{cm}^{-3}$ .

The value of the theoretical halfwidth, i.e. the value of  $\alpha$  at which  $s(\alpha)$  is at one-half of its maximum value, retrieved from Figure 50 is 0.077. Substituting  $N_e = 10^{14} \text{ cm}^{-3}$ , Temperature = 5000 K and  $\alpha_{\frac{1}{2}} = 0.077$  into Equation 18 yields a halfwidth of 0.42 Å. For  $N_e = 10^{16} \text{ cm}^{-3}$ , the halfwidth of hydrogen-beta line due to the Stark effect was calculated to be 9.63 Å. The calculated Stark halfwidths of the  $H_\beta$  (486.1 nm) line for some typical temperatures and electron densities are presented in Table



TABLE VII.1  
CALCULATED DOPPLER AND STARK HALF-WIDTHS OF H $\beta$  LINE  
FOR SOME TYPICAL TEMPERATURES AND ELECTRON DENSITIES

Hydrogen line (486.1 nm)		
	Temp = 5000 K	Temp = 10000 K
	N <sub>e</sub> = 10 <sup>14</sup> cm <sup>-3</sup>	N <sub>e</sub> = 10 <sup>16</sup> cm <sup>-3</sup>
Stark width	0.42	9.63
Doppler width	0.25	0.35



VII.1. Note that the contribution of the temperature variable on the Stark width calculation (Table VII.1) amounts to less than 1%. It is clearly presented in Table VII.1 that the calculated Stark halfwidths of the hydrogen line, for a given electron density, is almost independent of plasma temperature. Under identical temperatures, the calculated halfwidth increases significantly with electron density.

The Doppler contribution to the halfwidth broadening can be calculated from Equation 16. The calculated Doppler halfwidths for some given temperatures and electron densities are also presented in Table VII.1. It should be noted from Equation 16 that thermal Doppler broadening is most profound for lines of light elements and at high temperatures. The temperature dependency of the Doppler effect is clearly illustrated in Table VII.1. The calculated Doppler halfwidth increases 40% when the plasma temperature increases from 5000 to 10000 K. It can also be seen that for a given temperature, variation in electron density has no effect on the Doppler halfwidth.

Deviations from the Stark effect on the  $H_{\beta}$  line occur when electron number density is low. The results of  $\log(N_e)$  versus  $\log(\text{halfwidth})$  for the plasma temperatures of 5000, 10000 and 20000 K are shown in Figure 52 and the temperature dependency of line width measurements is clearly





illustrated. It also indicates that deviations from linearity are more significant for a plasma with low electron number density and high temperature. With the electron density greater than  $10^{14} \text{ cm}^{-3}$ , variations in plasma temperature have a negligible influence on the measurement of electron density as a function of halfwidth. For a plasma with high electron density, the halfwidths of the  $H_\beta$  line exhibit a linear Stark effect (Figure 52) which also obeys the two thirds power law (Equation 17). In general, at low electron density ( $N_e < 10^{14} \text{ cm}^{-3}$ ) and at high temperature ( $T > 10000 \text{ K}$ ), line broadening due to the Stark effect becomes insignificant, and the line shapes will be increasingly dominated by Doppler broadening effects. Therefore, for a low electron density and high temperature plasma source, the line profile must be deconvoluted to account for thermal Doppler broadening. It is most fortunate that the electron densities in the ICP source determined from the measurement of the  $H_\beta$  line are in the range of  $10^{14}$  to  $10^{16} \text{ cm}^{-3}$ . Therefore, Doppler broadening can be ignored for the measurements of the  $H_\beta$  halfwidths under our current plasma operating conditions.



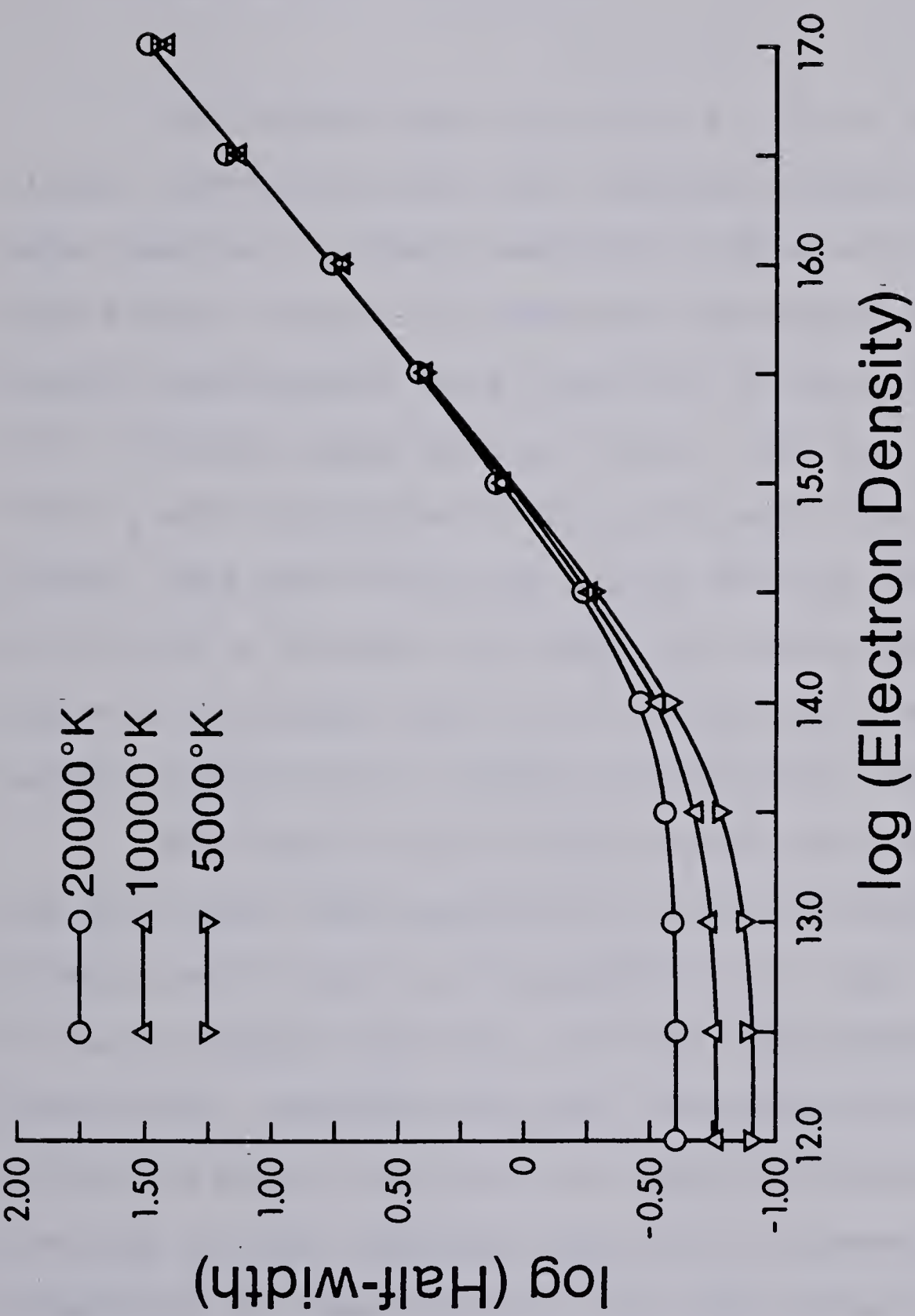


Figure 52. Calculated log(half-width) of the H $\beta$  emission as a function of log(electron density) for the temperature range from 5000 K to 20000 K.



## E. Experimental

### 1. Experimental Conditions

The Plasma-Therm ICP-2500D 2.5 Kw rf generator, 1024 element photodiode array and electronic measurement systems were identical to those described in Chapter II. Unless specifically noted, all operating conditions for electron density measurements were identical to those listed in Table III.1. Foreign gases such as 10% N<sub>2</sub>, 100% N<sub>2</sub>, 10% O<sub>2</sub>, and 100% O<sub>2</sub> were introduced into the coolant flow of an argon plasma. Data were collected in the vertical axis at 2, 5, 10, 15 and 20 mm above the load coil, while the horizontal data was collected from 0.0 to 8.5 mm away from the center aerosol channel with a lateral displacement step of 0.5 mm.

The signal from the photodiode array was amplified and this signal was acquired by a PDP-8 minicomputer. Diode intensities for the H $\beta$  line profile were input to an Apple /// microcomputer with 128 K of RAM. The background subtraction, smoothing and Abel Inversion programs were written in Pascal and ran on an Apple /// microcomputer. Listings of these combined programs are presented in Appendix A. The Abel inverted data was stored on Apple ///'s floppy disks, displayed on a monitor screen, plotted on a digital plotter (Hewlett-Packard Model 7470A) or output to a







parallel (Centronic 739) or serial (IBM selectric II) printer. The halfwidth measurements of the  $H_\beta$  line were evaluated from the overall Abel inverted radial intensities over a span of 64 diodes (approximately 30.7 Å in the wavelength scale).

For all spectral measurements, the plasma was focused onto the entrance slit of the Heath 0.35 meter monochromator using a spherical quartz lens (focal length = 10 cm, diameter = 2 in). A 2:1 reduced and inverted image of the plasma was focused onto the entrance slit set at 10 microns. Such a small entrance slit was used in order to reduce the contribution of instrumental broadening to the  $H_\beta$  line profile. The measurement system was carefully aligned using a He-Ne laser so that the diode measured the plasma emission intensity from the middle of the central channel. The He-Ne laser was also used as a reference source for plasma height adjustments. Since the spherical lens was mounted on the body of the monochromator, different horizontal slices of the plasma could be measured by raising or lowering the monochromator. The positions above the load coil (vertical measurements) could be measured accurately with a precision dial gauge attached to the base of the monochromator (Mitutoyo No. 3052, Japan). A second similar precision dial gauge attached to the side of the monochromator was used to indicate the positions of



displacement away from the middle of the center aerosol channel, i.e. the horizontal profile measurements.

All spectra reported in this work were electronic or spectral background subtracted in order to remove fixed pattern background or spectral background. Background subtraction for the species that is part of the background, such as hydrogen lines, will be discussed in the following section.

## 2. Background Subtraction, "Slope" Method

One of the key features of the electronic image sensors, such as the photodiode array, is the capability of subtracting out the electronic or spectral background. The removal of spectral background by subtraction utilizing the computer data acquisition system (112-115) provides "background free" spectral information of the analytes over a wide range of wavelengths. The background spectrum containing Cd lines emitted from a 10% N<sub>2</sub> - 90% Ar cooled ICP source is shown in Figure 53a. The background spectrum without cadmium being aspirated and collected under similar operating conditions is shown in Figure 53b. The background subtracted cadmium spectrum in Figure 53c clearly illustrates a cleaner cadmium emission line spectrum with the background nitric oxide bands and carbon line removed.



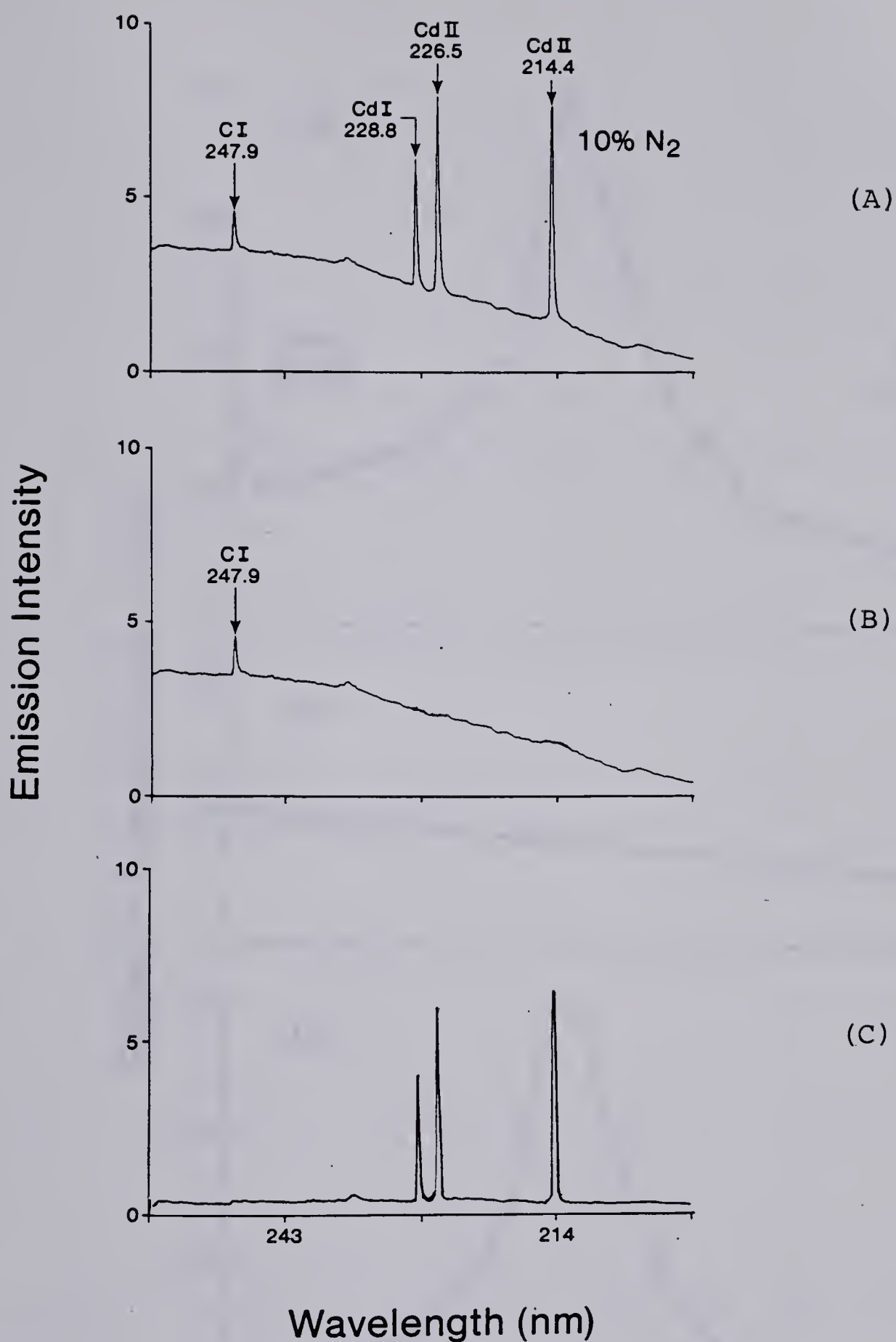


Fig. 53. Spectra illustrating the power of electronic background subtraction; (A) original emission spectrum, (B) background emission spectrum, and (C) electronic background subtracted spectrum.





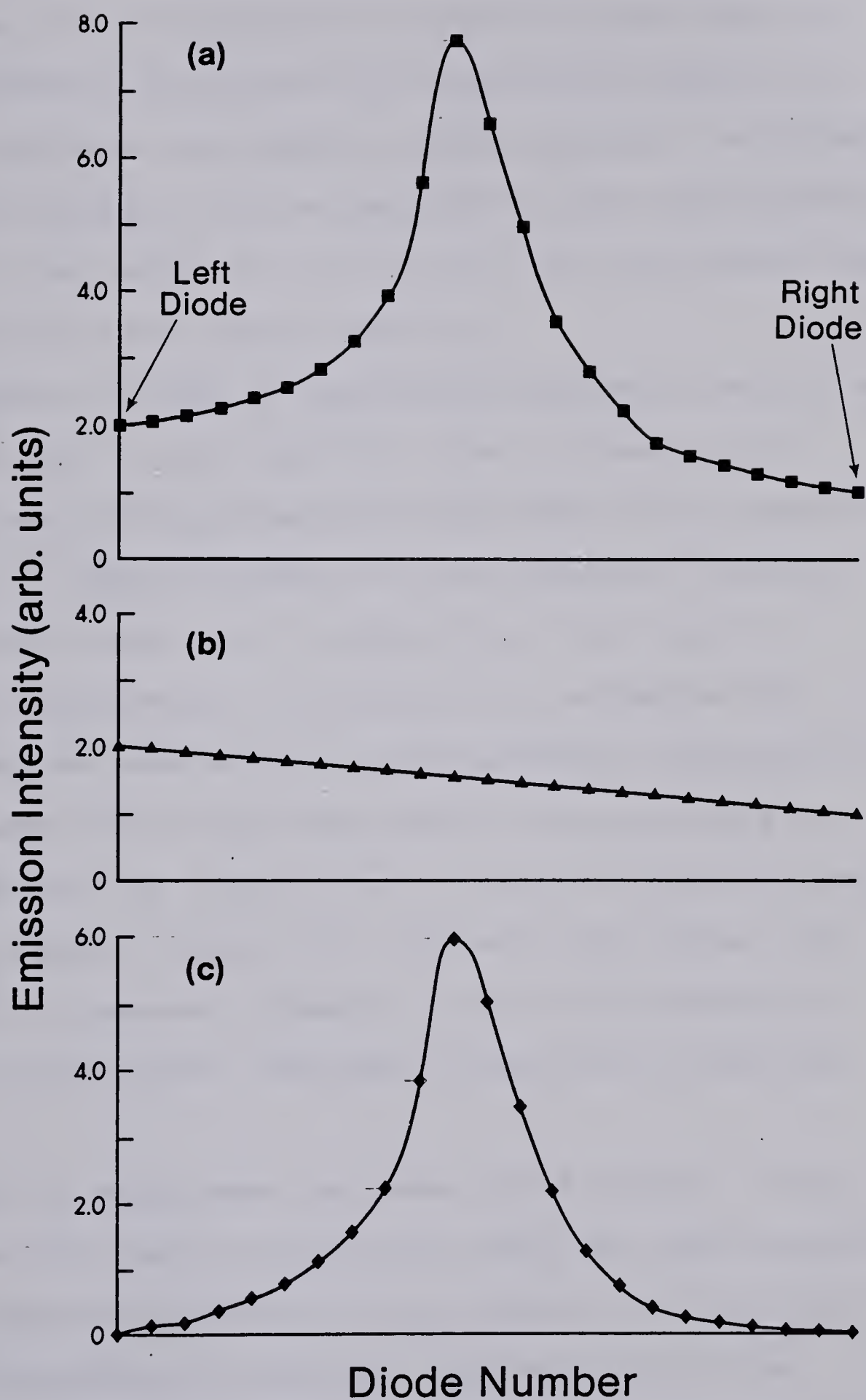


Fig. 54. Schematic representation of the background subtraction using "slope" method.





The presence of the electronic or spectral background can sometimes severely interfere with the analyte signals of interest, therefore the computer aided electronic background subtraction capability of the photodiode array spectrometer is clearly a key factor in facilitating the measurement and interpretation of the analyte spectra.

However, if such a background subtraction method is performed on the  $H_{\beta}$  line profiles, the  $H_{\beta}$  lines will be subtracted because they themselves are part of the spectral background. In order to measure the  $H_{\beta}$  emission intensity, an alternative method must be devised so that the d.c. background continuum due to electron-ion recombination processes can be subtracted. The multichannel capability of the photodiode array based measurement system provides an ideal system for the acquisition of spectral intensity data of the  $H_{\beta}$  intensity (Figure 54). Without this system, the measurement of spectral intensity data at an increment of 0.48 Å by a conventional PMT based system would indeed be tedious.

The d.c background continuum level beneath the  $H_{\beta}$  line (Figure 54b) can be subtracted using the slope method. Since the measured photodiode array signals are digitized, it is only necessary to determine the magnitude of the background intensity for each diode. The acquired array signal as a function of array diode number is shown



schematically in Figure 54a. The "slope" program requires the operator to input the signal intensity for the left and right diodes at the wings of the  $H_{\beta}$  line profile. The value of the slope can be calculated using the following equation

$$M(\text{gradient}) = \frac{I(x)_r - I(x)_l}{\text{Right diode \#} - \text{Left diode \#}} \quad (19)$$

where  $I(x)_r$  = digitized intensity at right diode,  
 $I(x)_l$  = digitized intensity at left diode.

The calculated gradient (M) is then be used to determine the magnitude of background intensity for each diode (Figure 54b),

$$IB(x) = M * x + C \quad (20)$$

where  $IB(x)$  = digitized intensity of the background  
 at diode x,

C = a constant which is equal to the  
 intensity at the left wing diode,  
 i.e.  $I(\text{Left diode})$

Since the measured analyte emission intensity for each diode consists of analyte and background components,



the analyte signal for diode  $x$  shown in Figure 54c,  $S(x)$ , is simply the difference between measured intensity,  $I(x)$ , and calculated background intensity,  $IB(x)$ ,

$$S(x) = I(x) - IB(x) \quad (21)$$

### 3. Transformation of Lateral Intensity into Radial Intensity by Abel Inversion

If the plasma is thin and flat such as the d.c. plasma (14-19), it is possible to calculate the electron density directly from the measured emission intensity of the H line (150). Since the ICP is a circular toroidal type of plasma, the emission intensity observed from the side of the plasma is the result of contributions from all layers within the source. In the case of ICP, it is important to obtain spatially resolved intensity information along the radial axis, so that the local emission intensity profile from a certain depth within the source can be used to calculate electron density without contributions from other depths along the optical path. From the fundamental point of view, it would be most interesting to calculate and map the electron density along the radial optical axis, and to





correlate the electron densities with the analyte emission intensities from various depths and heights within the plasma source.

Two methods for solving this problem have been reported in the literature, one a graphical method (91) and the other a numerical method (157-162). The graphical method is tedious and not accurate, and also requires a tremendous amount of manual work. The numerical method that converts the spatially integrated lateral information into spatially resolved radial information is known as Abel transformation or Abel Inversion. The application of this technique to spectroscopic data is extensively documented in the literature (159,160). Radial spatial distributions of emission intensity in the ICP were measured by Kornblum and de Galan (88,98) in order to calculate the temperature, and electron densities as well as to study the matrix effect in the plasma source. Kalnicky et al. (94), Jarosz et al. (95), Alder et al. (86), Blades and Horlick (120,121), and Furuta and Horlick(122) have all used the Abel inversion technique to obtain radial profiles for the purpose of calculating distribution of plasma temperature and analyte emission, and electron densities. The application of this technique to the ICP source has been discussed in detail by several workers (159,160,162); therefore, it will not be repeated in this thesis. However, a short discussion on the calculations of



radial intensity data from the corresponding lateral intensity data is warranted.

The relationship between the measured lateral intensity,  $I(x)$ , and the desired radial intensity,  $i(r)$ , is shown in Figure 55. If a cylindrical plasma is assumed, the inversion of a measured lateral intensity into a radial distribution of emittance is governed by the following equation:

$$i(r) = - \frac{1}{\pi} \int_r^{r_0} \frac{I(x)}{(x - r)} dx \quad (22)$$

where  $x$  = the lateral coordinate

$r$  = the radial coordinate

For practical purposes, Equation 22 is probably best represented in terms of a least square fit polynomial expression. This method tends to fit the entire lateral intensity distribution with a polynomial which is then used to solved Equation 22. Analytically, if the number of slices,  $N$ , is large, then the whole integral expression of Equation 22 can be approximated using a summation expression

$$i_k(r) = \frac{1}{r_0} \sum_{n=k}^N a_{k,n} I_n(x) \quad (23)$$



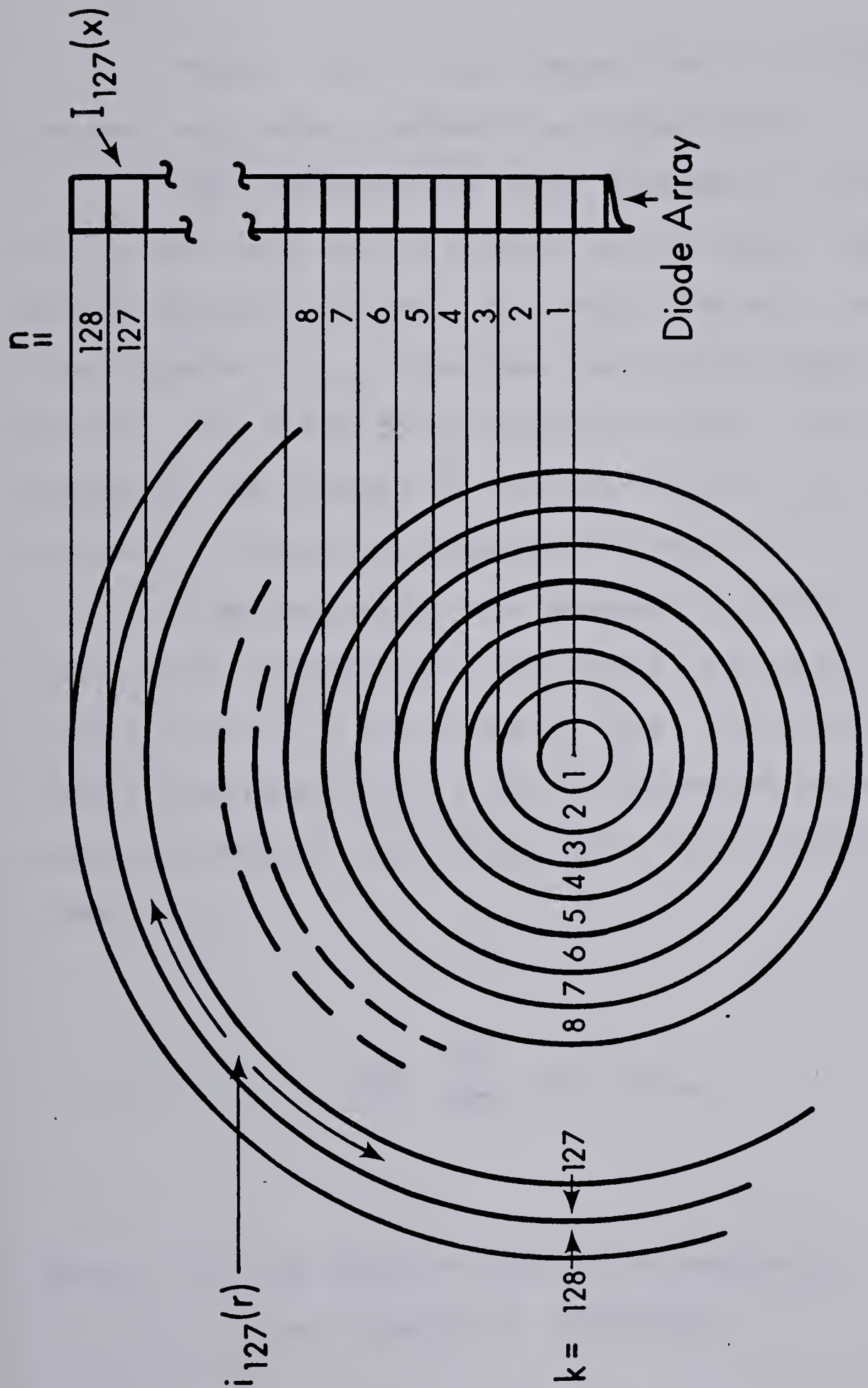


Figure 55. Schematic representation of the lateral and radial variables involved with Abel inversion.





where  $n$  and  $k$  are integer position indices for the lateral and radial intensities respectively.

This approach was first proposed by Bockasten (161) and later redefined by Cremers and Birkebak (158). Using the second degree polynomial for each interval, the coefficients,  $a_{k,n}$ , have been calculated from Equation 23 for  $N = 10, 20$  and  $40$  by Bockasten (161). For checking purposes, the results of the calculated  $i_k(r)$  from  $I_n(x)$  at various  $r$  values are tabulated in Table VII.2.

A second method was proposed by Nestor and Olsen (163) which assumed that the lateral intensity is a linear function of  $x^2$  in each lateral step. Using this method, the radial intensity,  $i_k(r)$ , may be expressed in terms of the measured lateral intensity,  $I_n(x)$ , by the following summation

$$i_k(r) = - \frac{2}{\pi a} \sum_{n=k}^N I_n(x) B_{k,n} \quad (24)$$

where  $a$  = the width of the slice sampled by two consecutive intervals.

The coefficients,  $B_{k,n}$ , can be evaluated by using the





following expressions

$$\text{and } B_{k,n} = -A_{k,k} \quad \text{for } n = k \quad (25)$$

$$B_{k,n} = A_{k,n-1} - A_{k,n} \quad \text{for } n \geq k + 1 \quad (26)$$

where

$$A_{k,n} = \frac{(n^2 - (k-1)^2)^{\frac{1}{2}} - ((n-1)^2 - (k-1)^2)^{\frac{1}{2}}}{2n - 1} \quad (27)$$

To test the accuracy of this method, the radial data was generated from the lateral intensity data provided in Table VII.2. The radial data was calculated using expressions shown in Equations 25 to 27. Lateral data were obtained from Reference 161. The comparisons of the radial intensities generated by the Bockasten's method (161) and by the Nester and Olson's method (163) are presented in Table VII.2 which clearly indicates that the radial intensity data provided by both methods are virtually identical. Since the Nestor and Olson method is easier to program on a microcomputer than the polynomial method, the Nestor and Olson approach for radial intensity calculations is utilized in this work. The Abel inversion program is listed in Appendix A. This program is written in Pascal and runs on an Apple /// microcomputer with 128 K RAM and can be easily altered to be implimented into other microcomputers.



TABLE VII.2

TRANSFORMATION OF LATERAL DATA INTO RADIAL DATA BY  
(A) BOCKASTEN'S, AND BY (B) NESTOR AND OLSON'S METHOD

Segments x	Lateral N(x)	Radial* R(x)	Radial** R(x)
0.00	1600	1018.592	1018.58
0.25	1599	1018.273	1018.28
0.50	1596	1017.318	1017.31
0.75	1591	1015.723	1015.72
1.00	1584	1013.486	1013.48
1.25	1575	1010.603	1010.60
1.50	1564	1007.067	1007.07
1.75	1551	1002.873	1002.87
2.00	1536	998.012	998.01
2.25	1519	992.474	992.47
2.50	1500	986.247	986.25
2.75	1479	979.319	979.32
3.00	1456	971.674	971.67
3.25	1431	963.296	963.29
3.50	1404	954.165	954.17
3.75	1375	944.260	944.26
4.00	1344	933.555	933.55
4.25	1311	922.022	922.02
4.50	1276	909.631	909.63
4.75	1239	896.346	896.34
5.00	1200	882.126	882.13
5.25	1159	866.926	866.92
5.50	1116	850.692	850.69
5.75	1071	833.364	833.36
6.00	1024	814.873	814.87
6.25	975	795.138	795.14
6.50	924	774.063	774.06
6.75	871	751.535	751.53
7.00	816	727.420	727.42
7.25	759	701.554	701.55
7.50	700	673.735	673.73
7.75	639	643.710	643.71
8.00	576	611.155	611.15
8.25	511	575.639	575.64
8.50	444	536.576	536.58
8.75	375	493.124	493.12
9.00	304	443.994	443.99
9.25	231	387.031	387.03
9.50	156	318.055	318.06
9.75	79	226.336	226.34
10.00	0	0.000	0.00

\* Radial data calculated by Bockasten's method.

\*\* Radial data calculated by Nestor and Olson's method.



There are several requirements imposed on the Abel inversion calculations in order to generate meaningful radial data from the corresponding lateral data. These requirements have been discussed previously (98,159,160). The first requirement is the symmetry of the lateral profile along the horizontal axis of the plasma source. The exact location of the central point along the horizontal lateral profile, where  $x = r = 0$ , is important for the Abel inversion calculation. Incorrect assignment of this point will lead to large errors in the radial emittance near the center of the discharge; sometimes, it will also lead to negative emittance (98). With this requirement in mind, the central point, where  $x = r = 0$ , was determined from the midpoint between the two maxima of the lateral intensity profile.

The second problem is associated with the number of successive measurements over the entire horizontal width of the plasma. The greater the number of acquired lateral data points, the more accurate the generated radial data will be (159). Finally, a further refinement on the radial distributions can be obtained by smoothing the acquired lateral profiles.

All these requirements have been easily met in the study of Blades and Horlick (159) by using a 256 element photodiode array based measurement system. The acquisition







of 256 separate lateral intensities across the plasma diameter (18 mm) resulted in very high quality input lateral data for the Abel inversion.

Although their proposed method is excellent for intensity profile measurements, there are several physical limitations which inhibit the use of such an array based detection system for the  $H_\beta$  spectral line profile measurements. First, the profiling array system described by Blades and Horlick (159) is limited to the measurement of only one spectral resolution element at a time; therefore, such a system is poorly suited for the halfwidth measurements of the  $H_\beta$  line profile. Second, the 256 element photodiode array used in their measurements is relatively insensitive compared to the 1024 element photodiode array system that can be used for direct measurements of  $H_\beta$  line profiles as indicated below.

In order to study the effects of various operating parameters on electron densities via hydrogen line profile measurements, one should employ a measurement system which is capable of providing a measurement of the complete  $H_\beta$  line profile. The 1024-element photodiode array system described previously in Chapter II to IV (see Figure 6) is an ideal detector for this study. Without such a system, the tedious process of measuring line intensity as a function of wavelength at each spatial point would take excessive amount



of time and effort. Another advantage is the capability of the array based system for continuum background measurement and subtraction.

The lateral spectral data were measured at successive steps of 0.5 mm over the entire horizontal width of the plasma. Since more data points are warranted for refining the calculated radial intensities, the number of sampled data points were doubled by reconstructing the midpoints using the formula presented by Wilson and Edwards (164). Because the sampled points have a constant separation, the original spectrum,  $X(t)$ , becomes a convolution of the data with the series

$$(\dots, \frac{2}{5\pi}, -\frac{2}{3\pi}, \frac{2}{\pi}, \frac{2}{\pi}, -\frac{2}{3\pi}, \frac{2}{5\pi}, \dots) \quad (28)$$

which are the values of the sinc function for the integer value of  $n$ .

The midpoint reconstruction is obtainable from the following equation (164):

$$\begin{aligned} X(t) = & 0.6366( X(t_i) + X(t_i+\Delta) \\ & -0.2122( X(t_i-\Delta) + X(t_i+2\Delta) ) \\ & +0.1273( X(t_i-2\Delta) + X(t_i+3\Delta) ) \\ & + \dots \end{aligned} \quad (29)$$



where  $t = t_i + 0.5$  ,

$X(t_i)$  = sample value

$X(t)$  = constructed midpoint

The midpoint reconstruction program is listed in Appendix A. In order to minimize error for the midpoint reconstruction, a 20-point convolution was used in this work.

A further refinement of the reconstructed lateral intensity data was obtained through the quadratic smoothing routine as described by Savitsky and Golay (165), where a set of seven points is moved over the entire array of the constructed lateral data points. An example using the Savitzky-Golay filtering for the lateral intensity profile of  $H_\beta$  486.1 nm line is shown in Figure 56. The  $H_\beta$  (486.1 nm) horizontal lateral profile was measured at 10 mm above the load coil and is shown in Figure 56b. The calculated radial profile from a non-smoothed lateral data set is presented in Figure 56c. The radial intensity distribution calculated from a smoothed lateral data set using the Savitzky-Golay filtering is shown in Figure 56a. Figure 56 clearly illustrates the importance of lateral data smoothing prior to the radial intensity calculations. It should be noted that with smoothed lateral data points, a smoothed radial profile is obtained (Figure 56a). Besides overall fluctuations due to noise, Figure 56c also indicates that





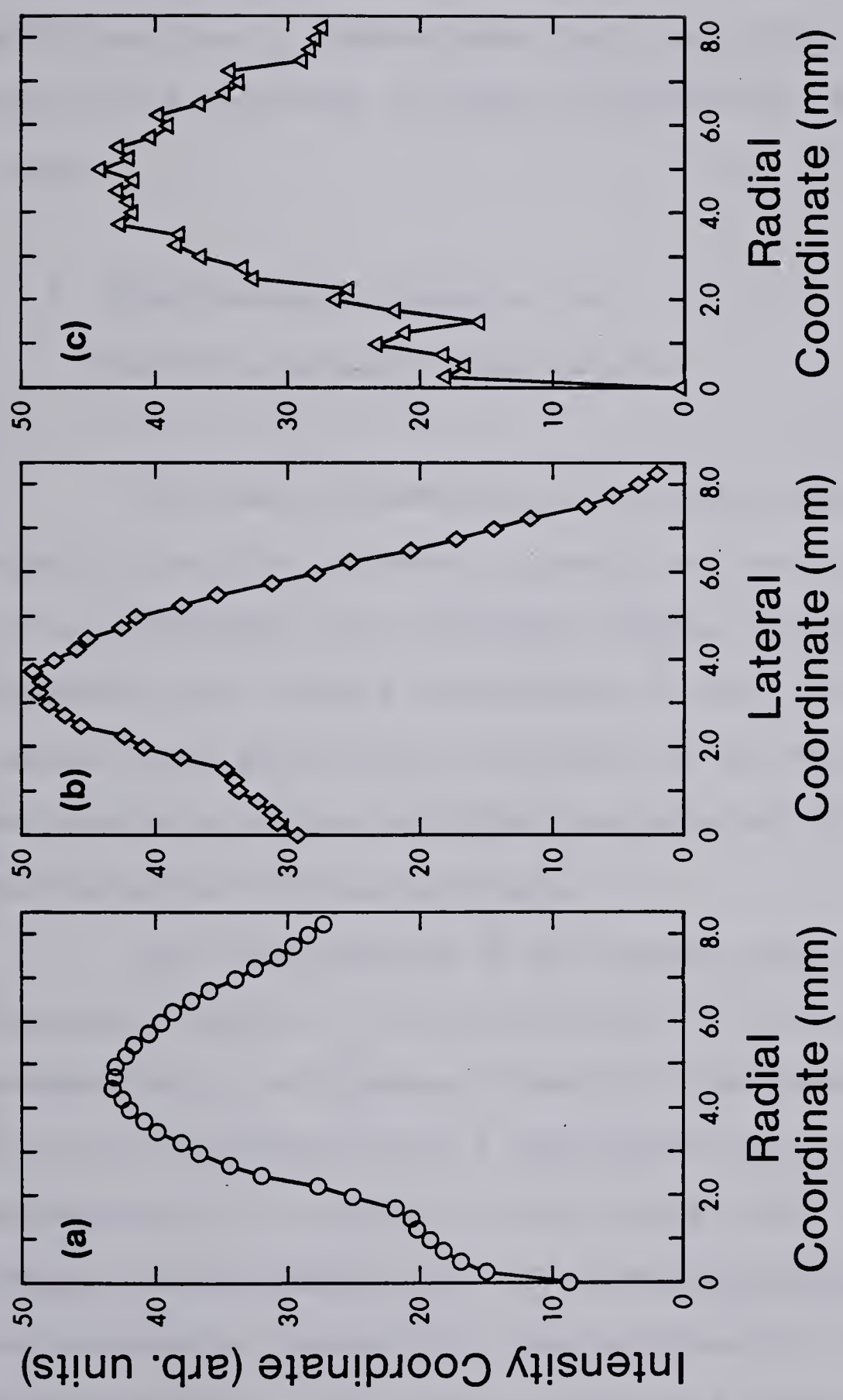


Figure 56. (a) Radial intensities calculated from lateral test data with smoothing.  
(b) Lateral test data.  
(c) Radial intensities calculated from lateral test data without smoothing.





fluctuations are more severe near the aerosol channel ( $r = 0$  mm) than at the profile maximum ( $r = 4$  mm). These radial profiles clearly demonstrate that smoothing of the lateral profile is required in order to eliminate the unwanted noise.

#### 4. Experimental Procedure for Electron Density Measurements

In order to measure the radially resolved hydrogen spectral profile, lateral intensities for a given diode, i.e., wavelength, at different lateral positions were converted into radial intensities by Abel inversion. The lateral data points were acquired by the PDP-8 minicomputer and the data points were then transferred into the Apple /// microcomputer for calculations.

The construction of half-width data,  $\Delta\lambda_{\frac{1}{2}}$ , from the measured lateral  $H_{\beta}$  line intensity,  $L(\lambda_i)$ , are shown schematically in Figures 57 and 58. The lateral  $H_{\beta}$  line profile as measured with a photodiode array system is shown schematically in Figure 57. The diode index is  $i$  and the lateral displacement index is  $x$ . The displacement between two successive lateral  $H_{\beta}$  line profiles is 0.5 mm. An array of 64 photodiodes was used to define a single  $H_{\beta}$  line profile. Thus, the intensity of the  $H_{\beta}$  line,  $L(\lambda_i)$ ,



measured with the  $i^{\text{th}}$  photodiode array corresponds to the hydrogen intensity at a particular spectral wavelength of (Figure 57). A total of 18 lateral  $H\beta$  line profiles were measured for each observation height. Lateral data were measured at 2, 5, 10, 15, and 20 mm above the induction coil.

The relationship between the measured lateral intensities,  $L_n(\lambda_i)$ , as measured with a photodiode array and the desired radial intensities,  $R_n(\lambda_i)$ , calculated by the Abel inversion is shown schematically in Figure 58. Since more data points are warranted for refining the calculated radial intensities (Figure 58c), the number of sampled data points in the lateral axis (Figure 58a) were doubled by reconstructing the midpoints (Figure 58b) using the formula presented by Wilson and Edwards (164). A further refinement of the constructed lateral data were obtained through Savitsky and Golay's smoothing routine(165). This step was found to be necessary because the Abel inversion is very sensitive to non-smoothed lateral data points (see Figure 56). The radial intensity data (Figure 58c) were then calculated from the constructed lateral (Figure 58b) data by Abel inversion. Finally, the half-width,  $\Delta\lambda_{\frac{1}{2}}$ , was measured using the radial intensity data along the wavelength axis (Figure 58d).

The program for Abel inversion was written so that



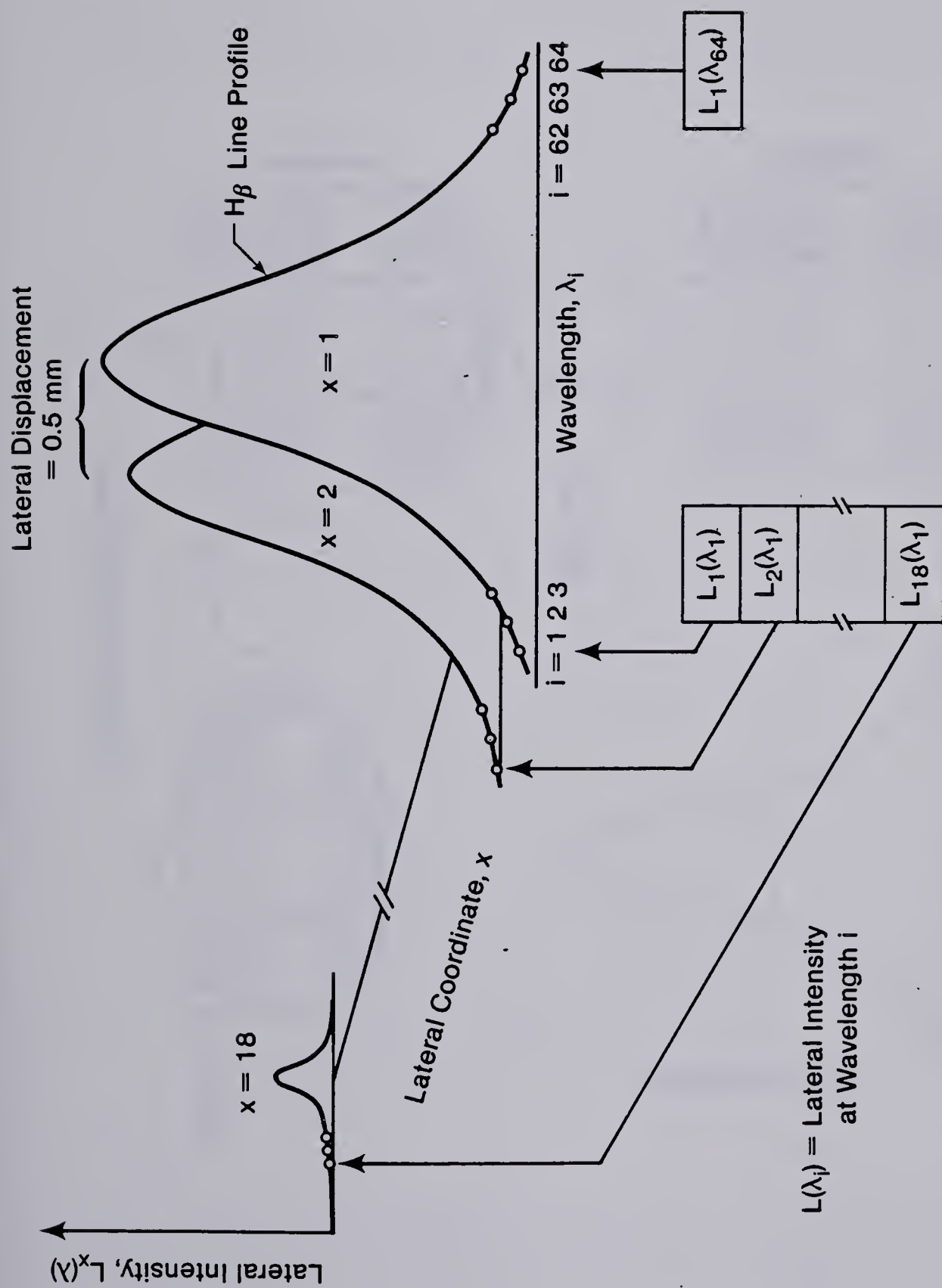


Figure 57. Schematic diagram of lateral  $H_\beta$  line emission profiles measured with a photodiode array system.





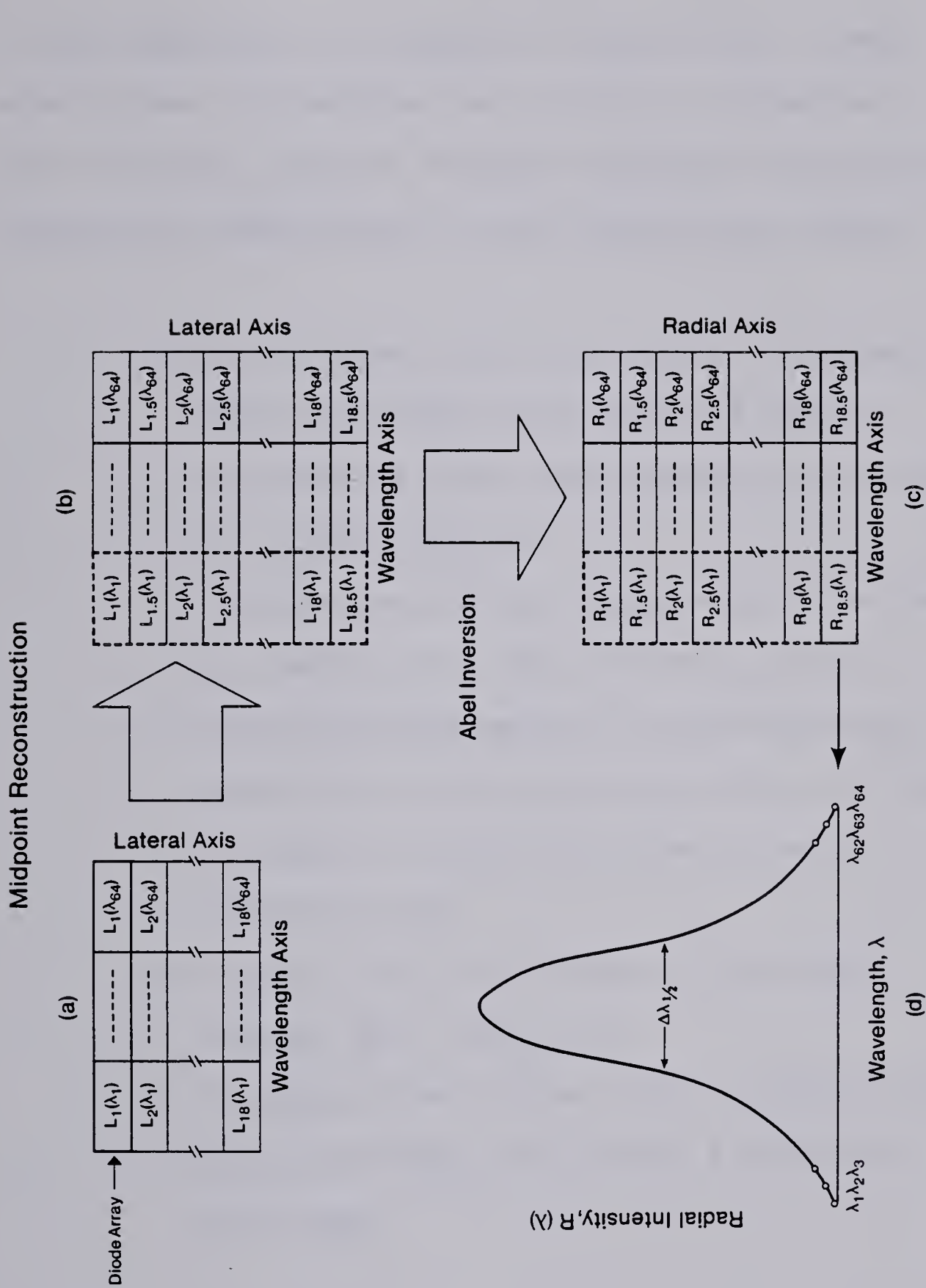


Fig. 58. Schematic representation of the lateral and radial variables involved with electron density measurements from line emission profiles; (a) measured lateral data, (b) expanded lateral data, (c) calculated radial data via Abel inversion, and (d) calculated half-width for electron density measurements.



it was executed in a series of subroutines. These subroutines (procedures) are listed in Appendix A, along with the main program. Program execution is accomplished by linking the subroutines in the appropriate order:

- a. The program reads the lateral information from the floppy disk into the memory
- b. It performs background subtraction using the "Slope" method
- c. Midpoint reconstruction procedure is used to double the number of data points
- d. Savitzky-Golay method for smoothing by a simplified least square procedure is used to smooth the reconstructed lateral intensity data
- e. Lateral data is converted into radial data by Abel Inversion
- f. The calculated radial data is stored back onto the floppy disk under a different file name.

Finally, the electron densities were calculated from the halfwidths of the  $H_{\beta}$  line (radial intensity as a function of diode number).



## F. Results and Discussion

The horizontal lateral intensity profile for the  $H_\beta$  (486.1 nm) line is shown in Figure 59. Note that the line profile for the  $H_\beta$  line shows a high symmetry along the center aerosol axis, which complies well with the circular symmetry of the plasma shape. The symmetrical nature of this profile minimizes errors in the Abel inversion calculations (98,159,160). This emission profile was measured using the experimental conditions listed in Table III.1, and measured at 2 mm above the load coil. It is interesting to note that the region of the most intense emission for the  $H_\beta$  line occurs at 3 mm off axis, which extends well into the main body of the plasma discharge. Also, the  $H_\beta$  profile dips significantly at the center of the plasma aerosol channel. The lateral profiles observed corresponded closely to those reported by Furuta and Horlick (122).

The halfwidths of the  $H_\beta$  line were measured using the procedures described earlier. First of all, data pairs shown in Table VII.3, i.e. half-width versus electron density, were input to the linear regression program. After the regression coefficients had been calculated, values of electron concentration may be made based on the curve fit by key in the value of the measured halfwidth. A plot of  $\log(\text{half-width})$  versus  $\log(\text{electron density})$  for the data



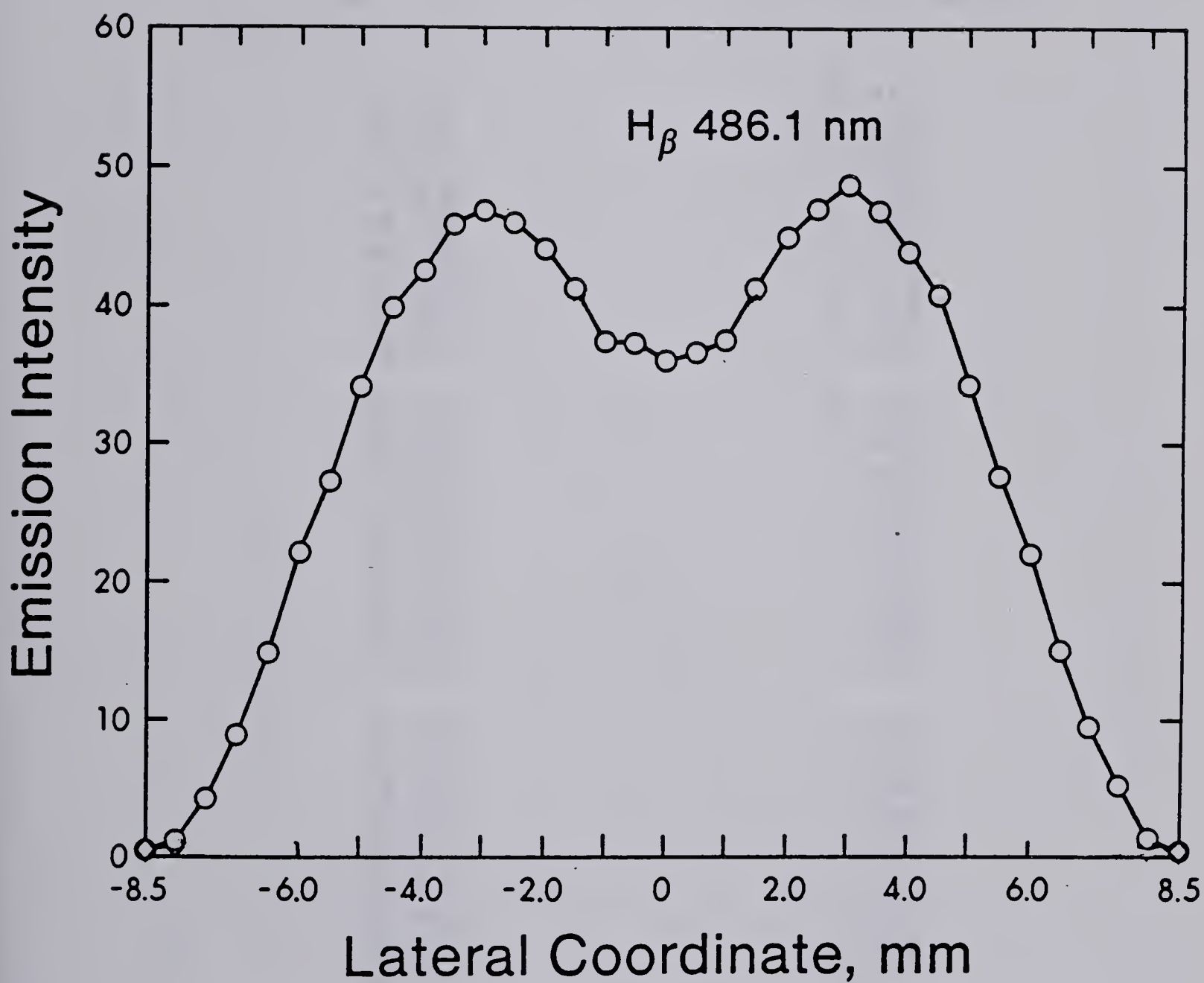


Figure 59. Radial emission profile for H $\beta$  486.1 nm at 2 mm above the load coil.





TABLE VII.3

DATA PAIRS FOR HALF-WIDTH OF  $H_{\beta}$  LINE  
VERSUS ELECTRON DENSITY MEASUREMENTS

$\log ( N_e )$	$\log ( \text{half-width} )$
-----	
14.00	-0.40
14.30	-0.194
14.48	-0.076
14.60	0.009
14.70	0.072
14.78	0.124
14.85	0.170
14.90	0.210
14.95	0.243
15.00	0.286
15.30	0.486
15.48	0.602
15.60	0.686
15.70	0.751
15.78	0.803
15.85	0.848
15.90	0.886
15.95	0.921
16.00	0.979
16.30	1.179
16.48	1.296
16.60	1.380
16.70	1.444
16.78	1.497
16.85	1.542
16.90	1.580
16.95	1.615
-----	



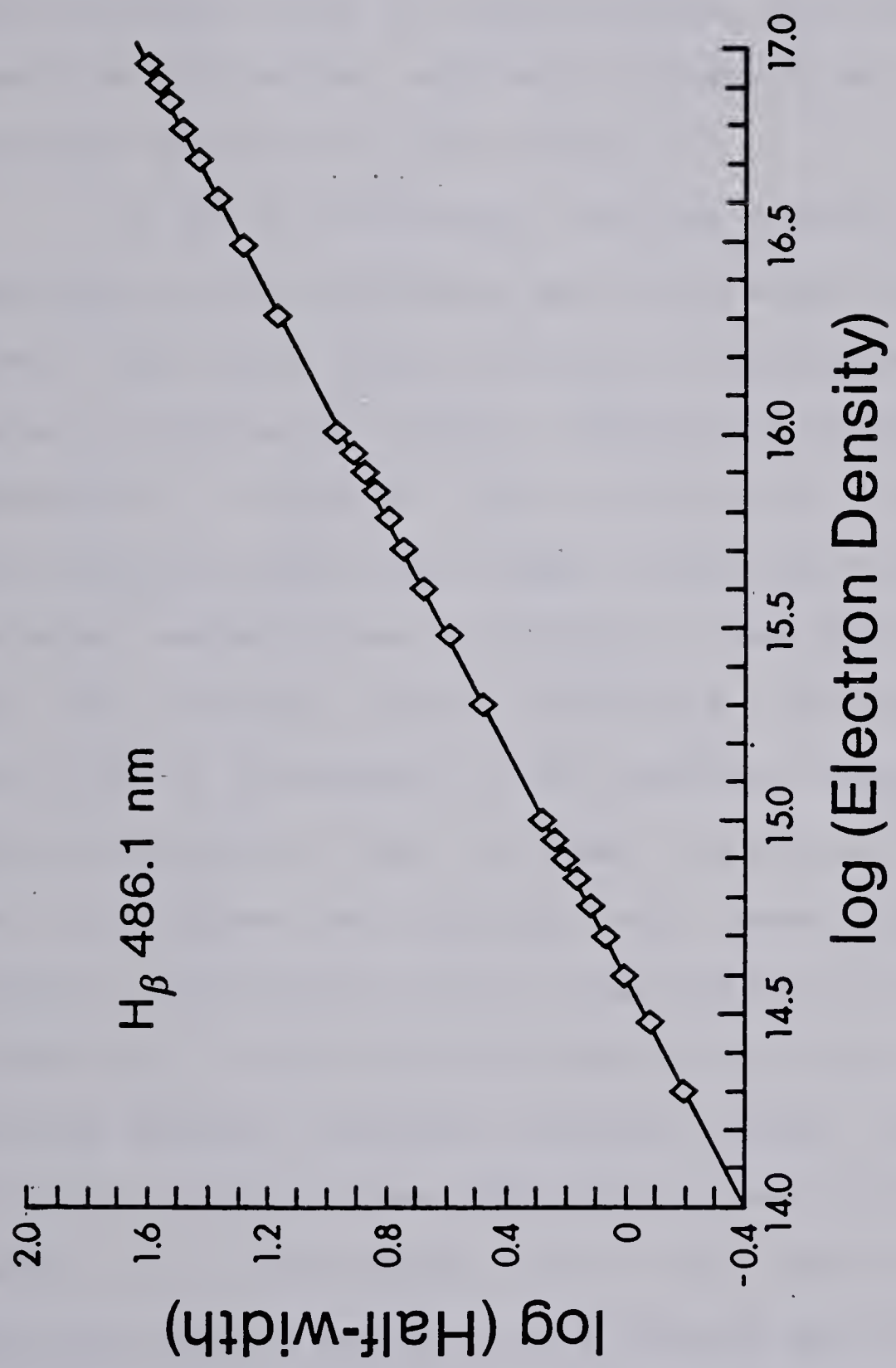


Figure 60. Plot of log(half-width) versus log(electron density).



pairs presented in Table VII.3 is shown in Figure 60. Because of the symmetrical nature of the intensity distributions along the central axis, only one-sided profiles for lateral and radial intensities, and also for electron density will be studied.

A set of horizontal electron density profiles were measured at five different positions above the load coil (2mm, 5 mm, 10mm, 15mm and 20 mm). The complete electron density profiles at various observation heights are presented in Figure 61. These profiles were obtained for a 100% conventional argon plasma. They were collected at a constant aerosol flow (1.0 L/min), constant rf power (2.0 Kw) and a constant coolant flow rate (15 L/min). The letters on Figure 61 correspond to the electron density profile collected at (a) 2 mm, (b) 5 mm, (c) 10 mm, (d) 15 mm and (e) 20 mm above the induction coil. These profiles show several interesting spatial characteristics of the argon discharge. All the electron density profiles observed at various heights exhibited off-axis maxima, indicating a toroidal shaped plasma. With an increase in observation height, i.e. from Figures 61a to 61e, the position of the off-axis density maximum moves towards the plasma center. In contrast to the analyte emission which peaks at higher observation heights, the overall magnitude of the electron density profile decreases significantly with increasing





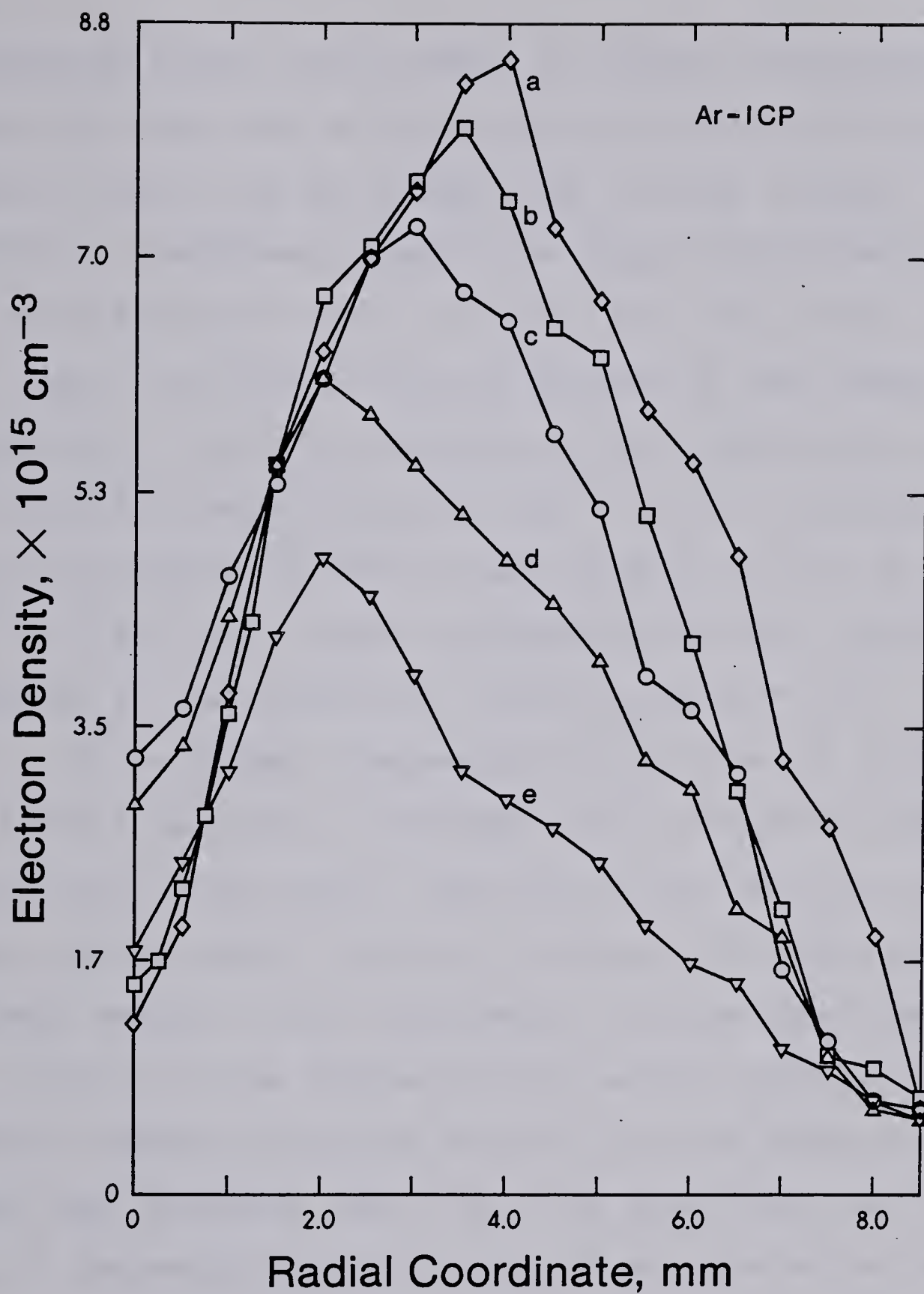


Fig. 61. Radial electron density profiles of an Ar-ICP as a function of observation height; (a) 2 mm, (b) 5 mm, (c) 10 mm, (d) 15 mm, and (e) 20 mm above the load coil.



observation height. This effect is clearly illustrated in Figure 61, which can be interpreted as resulting from the dynamic flow of the hot plasma gas. At high viewing positions, the plasma temperature drops significantly when the hot plasma gas comes in contact with the cooler outer gas. Since the electron density depends on the plasma temperature, a drop in temperature will undoubtedly result in a drop in electron density. The values of electron density at various heights ranged from  $0.6 \times 10^{15}$  to  $8.0 \times 10^{15} \text{ cm}^{-3}$  and are in close agreement with those reported elsewhere in the literature (refer to Table VII.4).

It is rather interesting to note that in contrast to the overall decrease in the magnitude of electron density distribution with height, the value of the electron density in the center aerosol axis as a function of height exhibits a "hump" shape. In this experiment, we have found that in the vicinity of the plasma central aerosol channel, the net electron density increased initially as the observation height was increased from 2 to 10 mm above the load coil, then it decreased gradually after 10 mm observation height. This observation is illustrated in Figure 62. The vertical electron density profile has striking resemblance to the 'hump' shapes of the analyte vertical emission profiles presented in Chapter IV, i.e.,

"as one observes the analyte emission intensity up the



TABLE VII.4

## SURVEY OF ELECTRON DENSITY IN AN AR-ICP

	Range of electron density, $\text{cm}^{-3}$	
Kornblum et al. (98)	$0.5 \times 10^{15}$	to $2.0 \times 10^{15}$
Kalnicky et al. (94)	$10^{15}$	
Mermet (93)	$3.0 \times 10^{15}$	to $2.7 \times 10^{16}$
Montaser et al. (155)	$0.4 \times 10^{15}$	to $3.0 \times 10^{15}$
Choot and Horlick	$0.5 \times 10^{15}$	to $7.5 \times 10^{15}$





analyte channel, it initially increases, reaches a maximum and then decreases forming an emission intensity peak or maximum" (118).

The position of this electron density maximum was found to be in close proximity with those of the analyte emission peak maxima which are around 10 to 15 mm above the load coil. This observation suggests that the analyte emission intensity and the electron density have a similar vertically spatial pattern in the analyte channel. However, one must be cautioned with the fact that this is also the region of greatest uncertainty in the Abel inversion data. Finally, in comparing Figures 61 and 62, perhaps the most interesting to note is that the electron density distributions in the vicinity of the center aerosol channel peak higher in the plasma, whereas at 4 mm off the center axis the electron distributions clearly peak lower in the plasma. This observation is illustrated in Figure 63. Vertical electron density profiles for (a) 0 mm, (b) 2.0 mm, and (c) 4.0 mm off the central aerosol channel are shown in the figure.

For a perspective on the distribution of the electrons in the ICP, a typical contour plot of the discharge is outlined in Figure 64. The maximum electron density ( $7.0 \times 10^{15} \text{ cm}^{-3}$ ) occurs near the load coil and 3 mm off the center axis. It can be seen that the maximum electron concentration decreases as the observation height





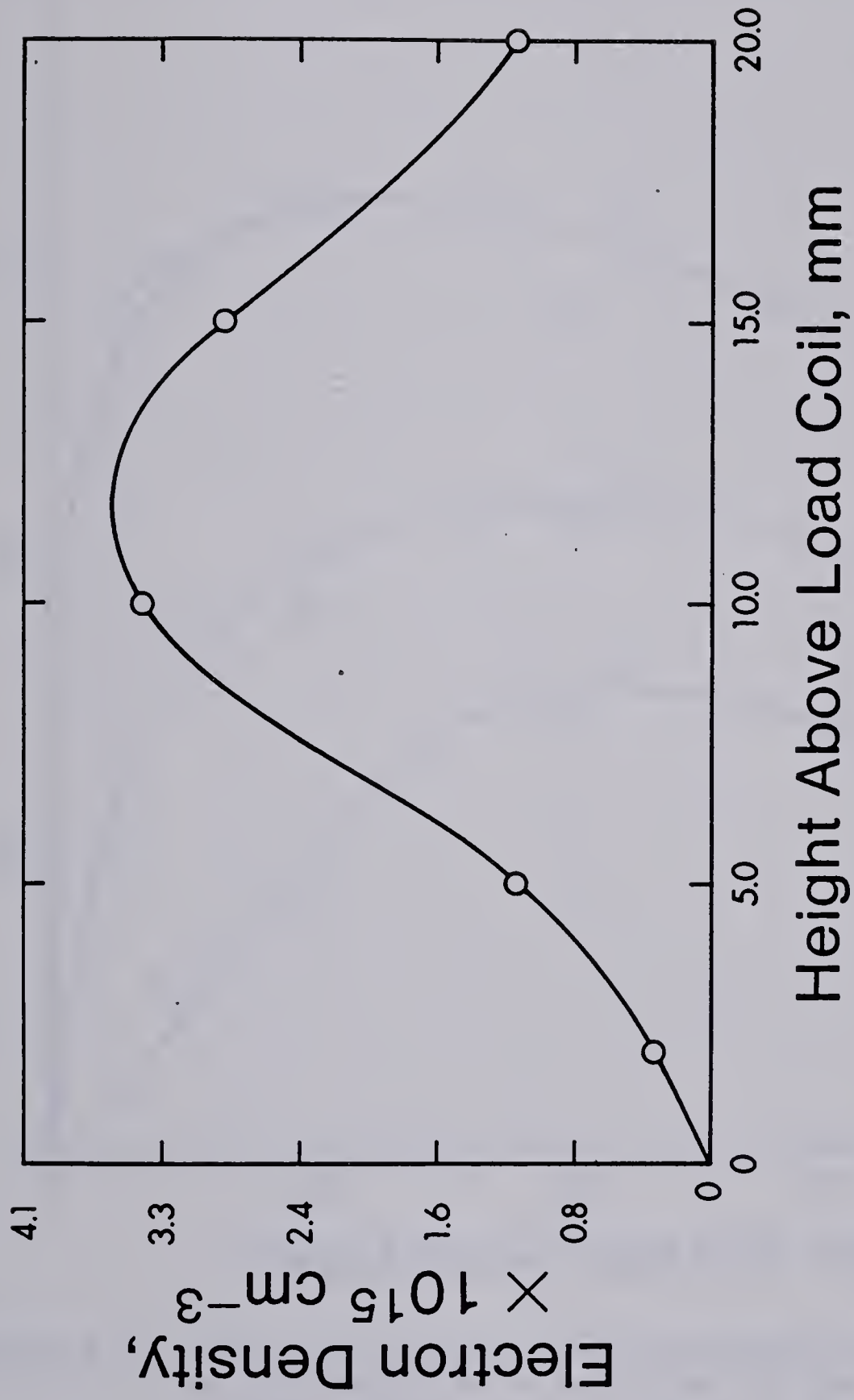


Figure 62. Vertical spatial electron density profile for an Ar-ICP.



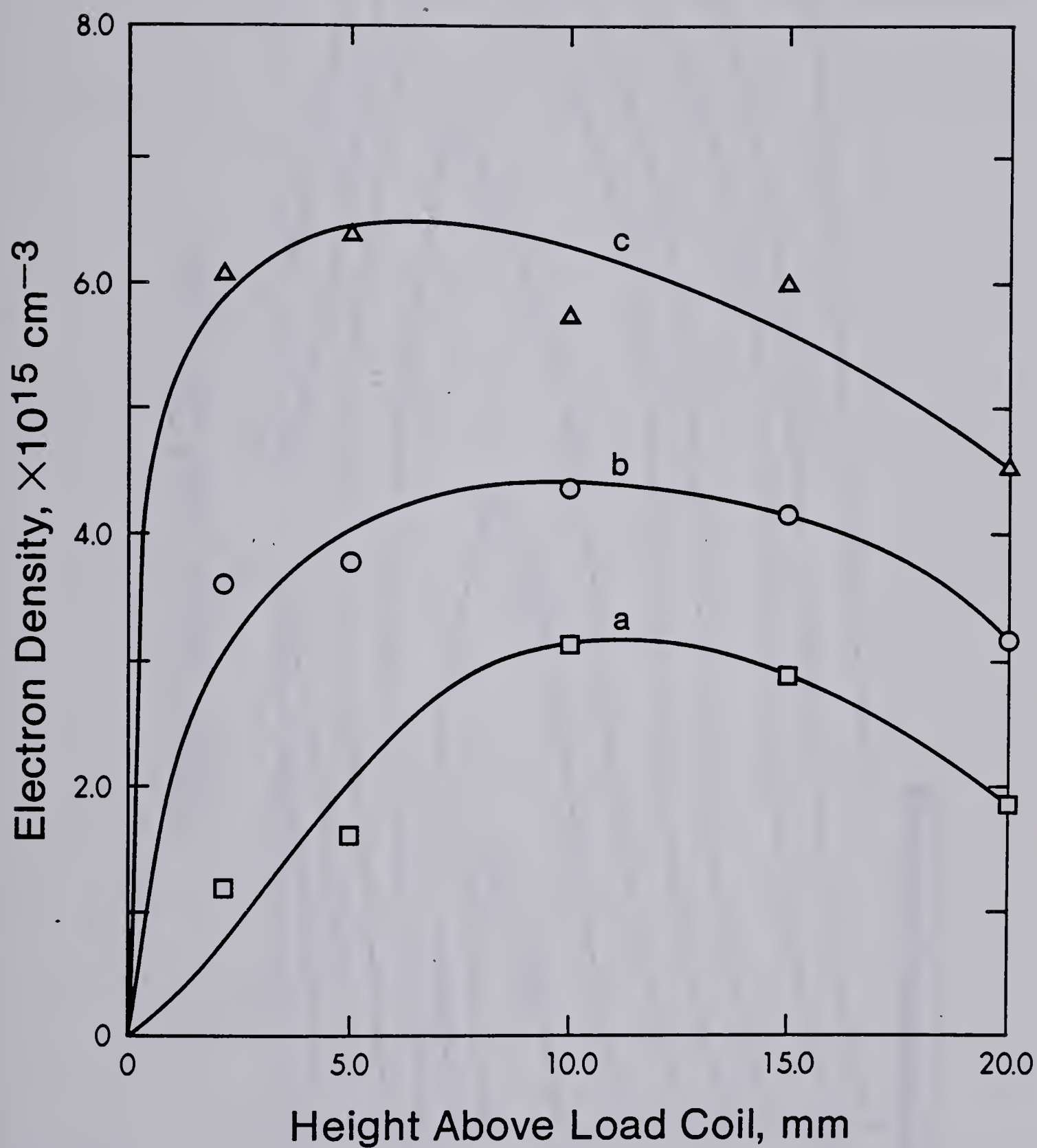


Figure 63. Vertical spatial electron density profile of an Ar-ICP as a function of distance off plasma central axis; (a) 0.0 mm, (b) 2.0 mm, and (c) 4.0 mm off central aerosol channel.



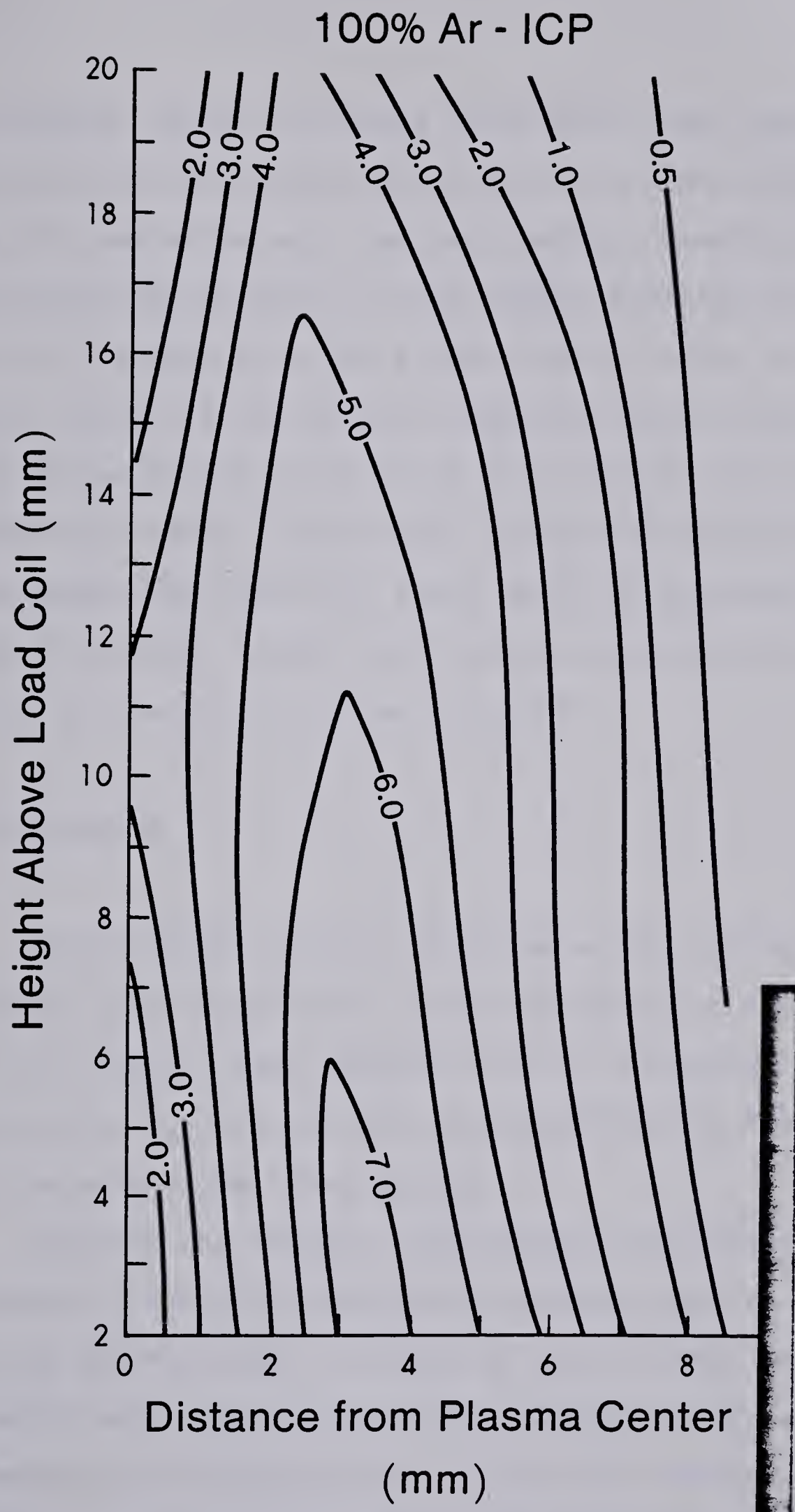


Fig. 64. Electron density map of an Ar-ICP (solid line marks torch edge).





is increased. Along the radial horizontal axis, the electron density is significantly reduced in the plasma center,  $r = 0.0$  mm. As one moves out, the net electron density increases rapidly and then plateaus as the radial distance varies from 0.0 to 3.5 mm away from the plasma center. After 4.0 mm away from the center of the aerosol channel, the net electron density drops rapidly from  $7.5 \times 10^{15} \text{ cm}^{-3}$  to  $0.5 \times 10^{15} \text{ cm}^{-3}$ . A generally similar horizontal pattern is observed at all heights above the load coil but a shift of electron density towards the plasma center with increasing observation height can also be clearly seen from Figure 64.

#### G. Conclusions

This chapter clearly illustrates the ability of the photodiode array system for the measurements of the electron density in the ICP. The tedious task of collecting and measuring the  $H_{\beta}$  line emission is significantly facilitated using the photodiode array system.

Because the analyte intensities are greatly influenced by the ICP operating parameters such as plasma power and aerosol flow, a change in any of these variables will definitely alter the electron distributions, excitation and ionization characteristics of the ICP. Before drawing any definitive conclusions about the excitation and



ionization mechanisms in the plasma, it is important to study the effect of operating parameters on the electron and emission distributions in the plasma in order to see whether these spatial patterns have some generality. Such characterizations have been carried out and will be discussed in the following chapters. Chapter VIII will also discuss the effects of alien gases in the coolant flow of an Ar-ICP on the spatial patterns of the electrons.



## CHAPTER VIII

### SPATIAL DISTRIBUTION OF ELECTRON DENSITIES IN ARGON, NITROGEN-ARGON, AND OXYGEN-ARGON MIXED GAS PLASMAS

#### A. Introduction

Up to this point the discussion of electron distribution in the ICP has been limited to observations of a conventional argon discharge operated at 2.0 Kw and 1.0 L/min aerosol flow rate. It is known that variations in rf power and nebulizer flow rate can cause significant changes in the analyte emission intensities and their spatial behaviour (83,106,120,122). In addition, this work has demonstrated that the analyte emission signals are also highly dependent on the amount of foreign gas present in the coolant stream of an argon discharge. From a fundamental point of view it would be useful to measure the spatial distribution of the electron concentration in the plasma source as a function of different operating parameters. Knowledge of electron distribution in the plasma source may provide a rational prediction of the excitation and ionization mechanisms in the ICP. Finally, the electron distribution in the plasma can reveal important physical





properties of the ICP which may indirectly affect the analytical performances of the plasma source.

The object of this investigation is to provide spatially resolved electron densities for a plasma operated at different aerosol flow rates and rf power. The discussions will also include comparisons of electron distribution in Ar, 10% and 100% N<sub>2</sub>, and 10% and 100% O<sub>2</sub> cooled plasmas.

The results presented in Chapters III to VI showed an increase in analyte emission intensities when 10% nitrogen or oxygen was introduced into the coolant stream of a conventional argon discharge. In this chapter, it will be seen that electron densities are also very much affected by the presence of foreign gases in the ICP source. The mixed gas plasmas also reveal changes in spatial structure of the electron density distribution.

For the present work, the values of electron density were measured from the Stark broadening discussed in Chapter VII. The addition of hydrogen to the plasma source, via coolant or aerosol flow, could cause significant changes in spatial and intensity characteristics of the analyte emission signals; therefore, hydrogen gas was not introduced into the plasma source. The hydrogen emission signals for the Stark broadening calculations were obtained from the dissociation of water molecules.





## B. Experimental

The plasma system was the Plasma-Therm ICP system discussed in Chapter II. Unless specifically noted, all operating conditions are as listed in Table III.1. The measurement systems were identical to those described in Chapter VII. Foreign gases such as nitrogen and oxygen were introduced only to the coolant flow of a conventional Ar-ICP.

The electron density was determined using the Stark effect on the  $H_{\beta}$  line. After Abel transformation, the radial distribution of electron density was calculated using the procedures presented in Chapter VII.



### C. Spatial Distribution of Electron Density in an ICP Source

The electron density distribution for the conventional argon discharge operated at 2.0 Kw rf power were measured and are presented in Figure 65. The nebulizer flow rate was set at 1.0 L/min. Measurements were made at 2, 5, 10, 15, and 20 mm above the load coil. In addition, measurements of electron density from the hydrogen Stark broadening were collected for 0.0 to 8.5 mm away from the central plasma axis with a displacement step of 0.5 mm. Because of the symmetrical nature of intensity distribution (refer to Figure 59), only one-sided profiles of electron density are shown in Figure 65.

The spatial profile study of electron density (Figure 65) will be discussed in some detail as most of the spatial data measured in this study are presented in an analogous format. Five profiles are presented in Figure 65, each curve represents the radial electron density profile measured at different observation heights, i.e. curve a corresponds to 2 mm above the load coil, curve b to 5 mm, curve c to 10 mm, curve d to 15 mm and curve e to 20 mm above the induction coil. These configurations hold for Figures 65, 67, 69, 71, 73, 75 and 77.

The electron density distribution in the



conventional argon discharge while distilled water was aspirated in the aerosol channel is presented in Figure 65. These profiles show several interesting spatial characteristics of the argon discharge. All the electron density profiles measured at various heights exhibit off-axis maxima. It should be noted that with an increase in observation height, i.e. from curve a to e, the position of the off-axis density maximum moves towards the plasma center axis. All these distributions reflect the toroidal shaped plasma discharge. The introduction of the cooler aerosol gas into the central axis causes a considerable temperature drop in the middle of the discharge. This may result in the central dip of the electron number density, and subsequently give rise to a "doughnut" shaped plasma. The central dip is less profound in the upper viewing height than in the region near the load coil. In contrast to the analyte emission signal which peaks higher in the aerosol channel, the overall magnitude of electron density profiles decreases significantly with increasing observation height. This may be attributed to the dynamic flow of the hot plasma gas. At higher viewing heights, the current density is smaller, therefore the plasma temperature drops significantly when hot plasma gas comes in contact with the cooler outer gas. Since the electron density is highly dependent on the plasma temperature, a drop in temperature will undoubtedly result





in a drop in electron density. The values of electron density measurements shown in Figure 65 vary from  $0.6 \times 10^{15} \text{ cm}^{-3}$  to  $8.0 \times 10^{15} \text{ cm}^{-3}$ , which are in close agreement with those reported in the literature (93,94,96-99).

Another interesting point to note in Figure 65 is the remarkable similarity between the vertical electron density profile along the aerosol channel and the vertical emission profiles of the analyte signals presented in Chapter IV. It is clearly illustrated in Figure 65 that in the vicinity of the plasma central aerosol channel, the net electron density increases as the observation height is raised from 2 to 10 mm above the induction coil, then it decreases gradually after the 10 mm observation height. The vertical electron density profile has a striking resemblance to the "hump" shape of the analyte emission profiles presented in Chapter IV. Correlations of electron density profiles to the analyte emission profiles have been carried out and will be discussed in the following chapter.

A contour map of the electron density distribution in a conventional argon discharge is shown in Figure 66. The plasma was operated at 2.0 Kw and with an aerosol flow rate of 1.0 L/min. The numbers on the lines represent the electron density in the order of  $\times 10^{15} \text{ cm}^{-3}$ . This figure shows several interesting characteristics of the conventional argon plasma. The electron density is greatest



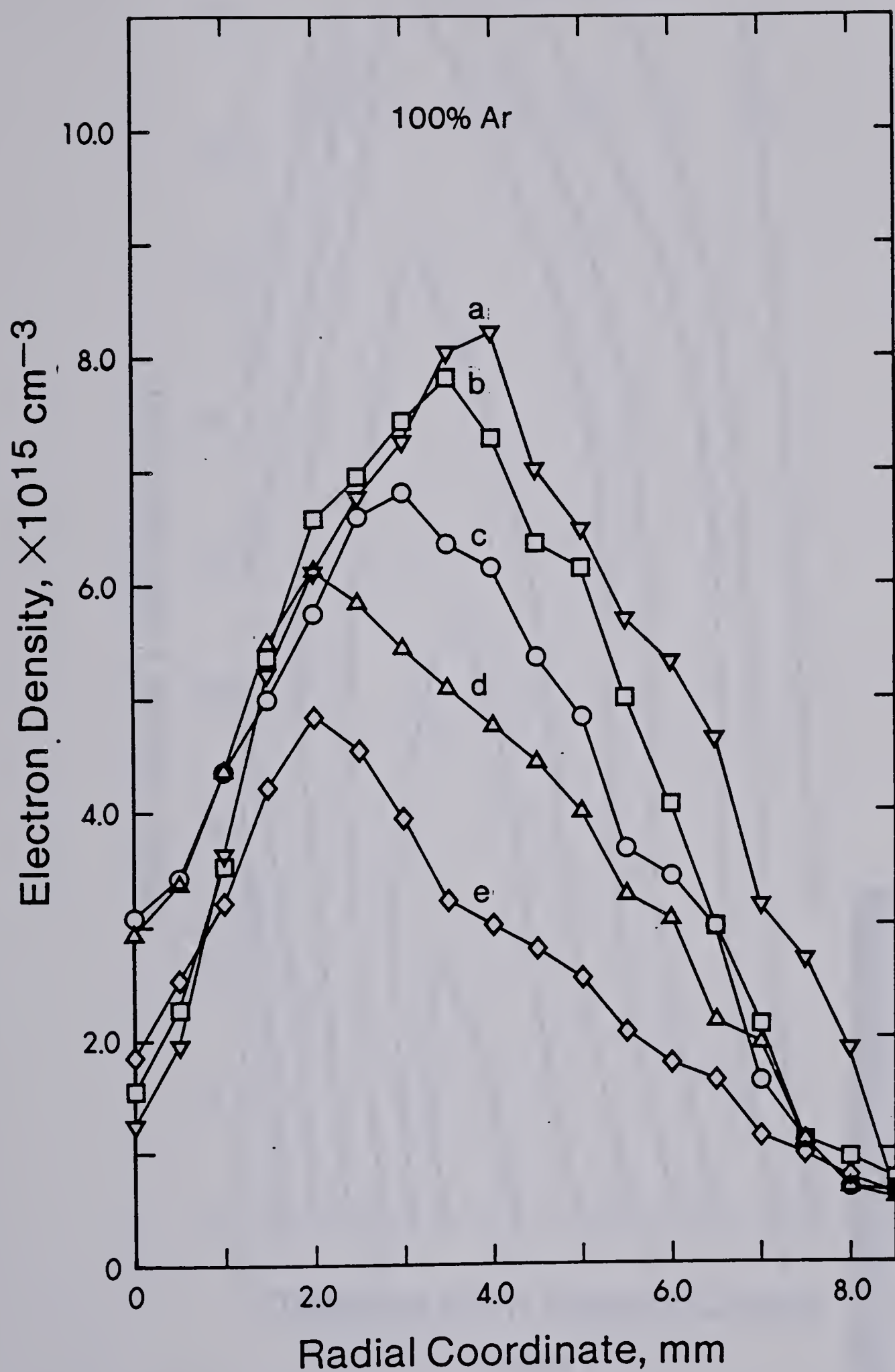


Fig. 65. Radial electron density profiles of an Ar-ICP as a function of observation height; (a) 2 mm, (b) 5 mm, (c) 10 mm, (d) 15 mm, and (e) 20 mm above the load coil, operated at 2.0 Kw power and 1.0 L/min aerosol flow rate.



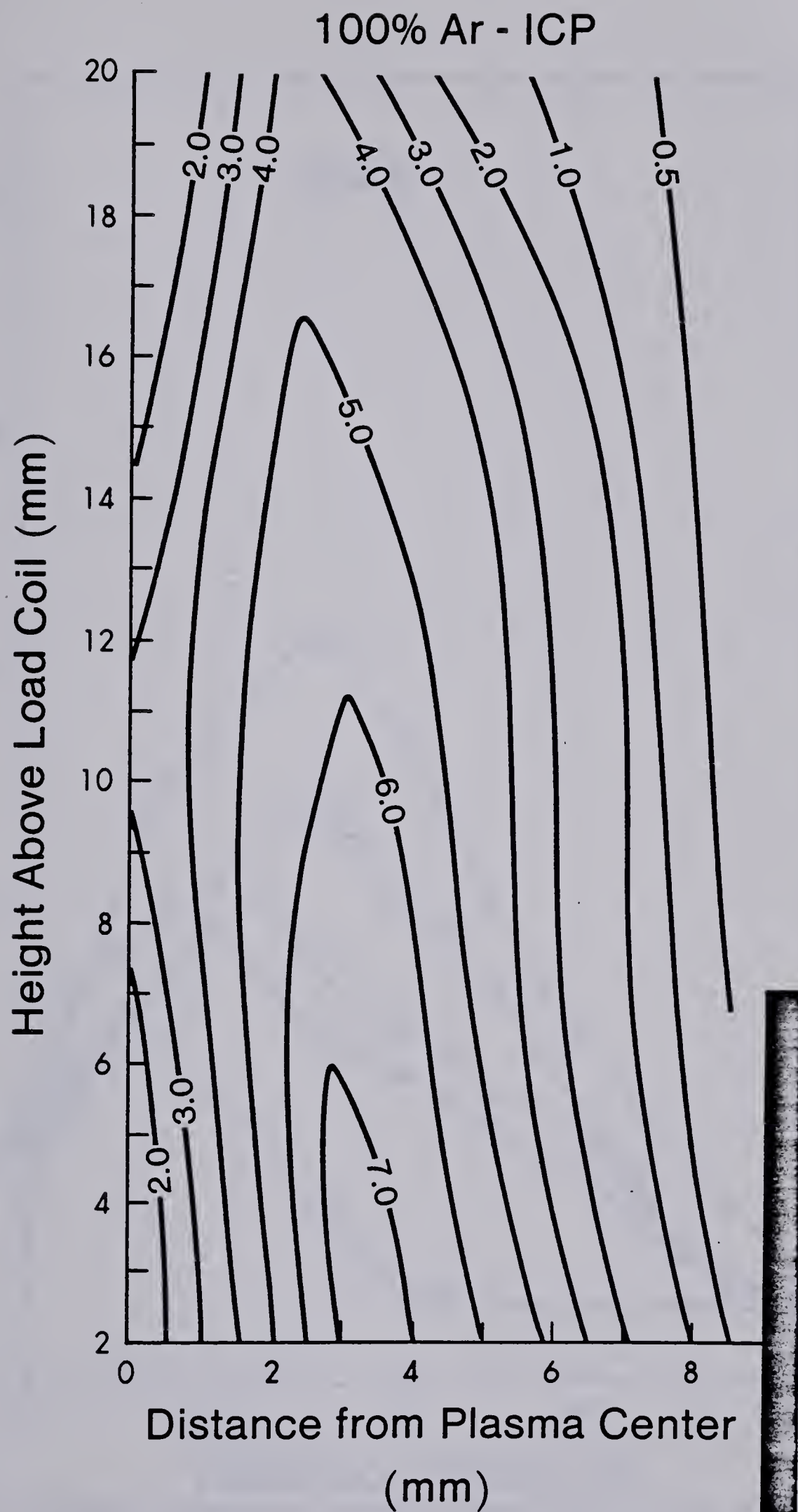


Fig. 66. Electron density map for an Ar-ICP (solid line marks torch edge), operated at 2.0 Kw power and 1.0 L/min aerosol flow rate.





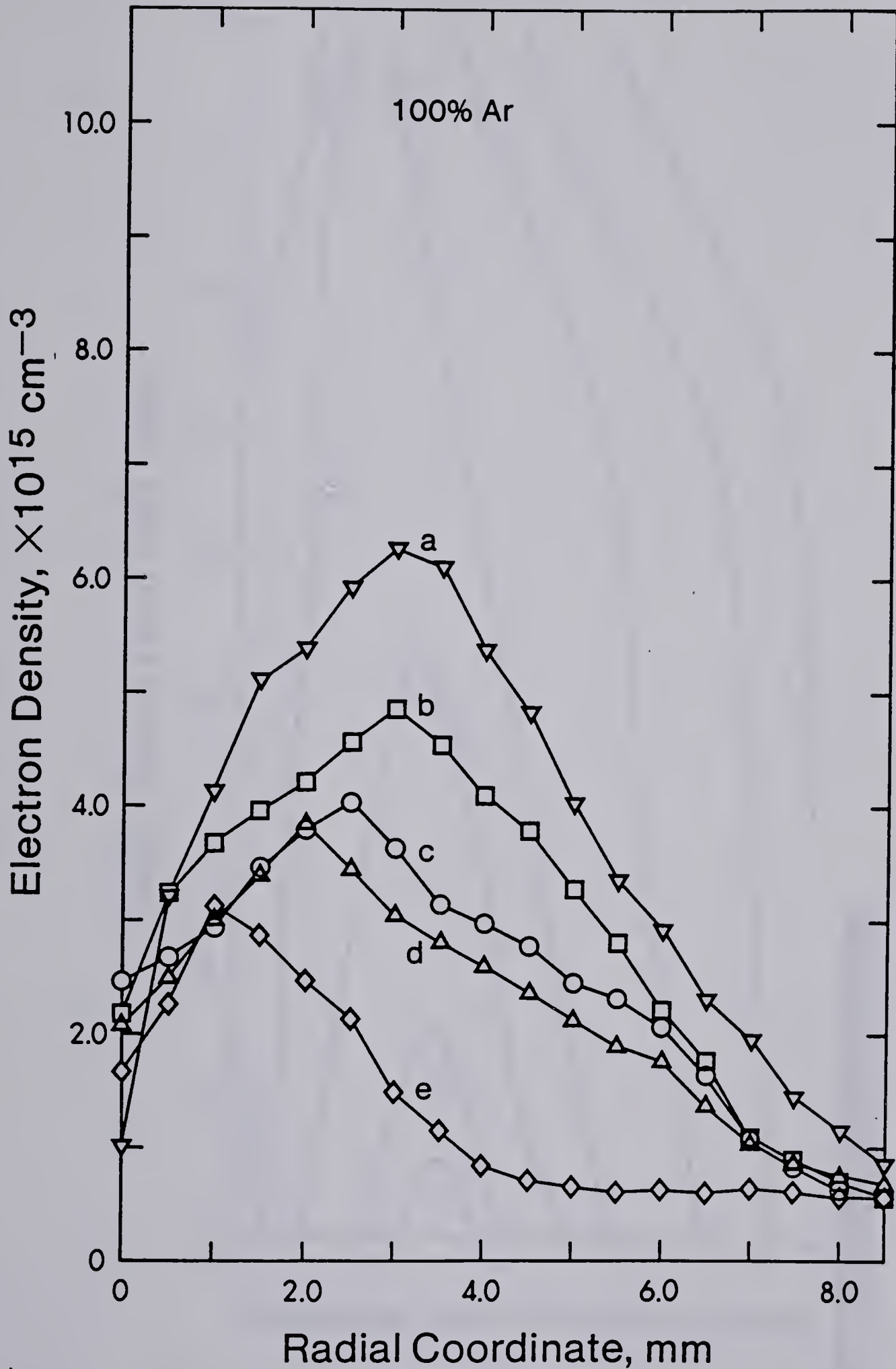


Fig. 67. Radial electron density profiles of an Ar-ICP as a function of observation height; (a) 2 mm, (b) 5 mm, (c) 10 mm, (d) 15 mm, and (e) 20 mm above the load coil, operated at 1.5 Kw power and 1.0 L/min aerosol flow rate.





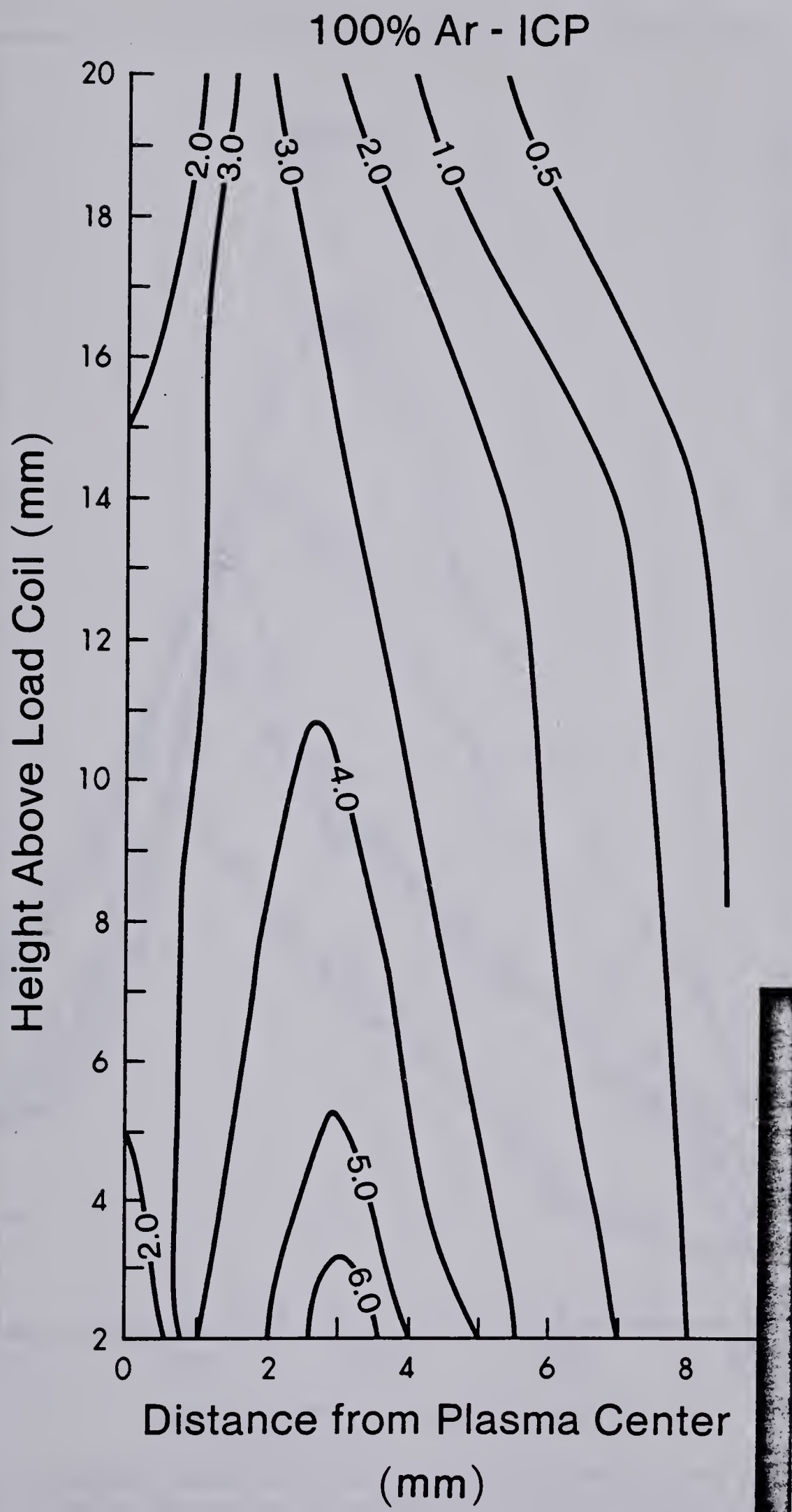


Fig. 68. Electron density map for an Ar-ICP, operated at 1.5 Kw power and 1.0 L/min aerosol flow rate.



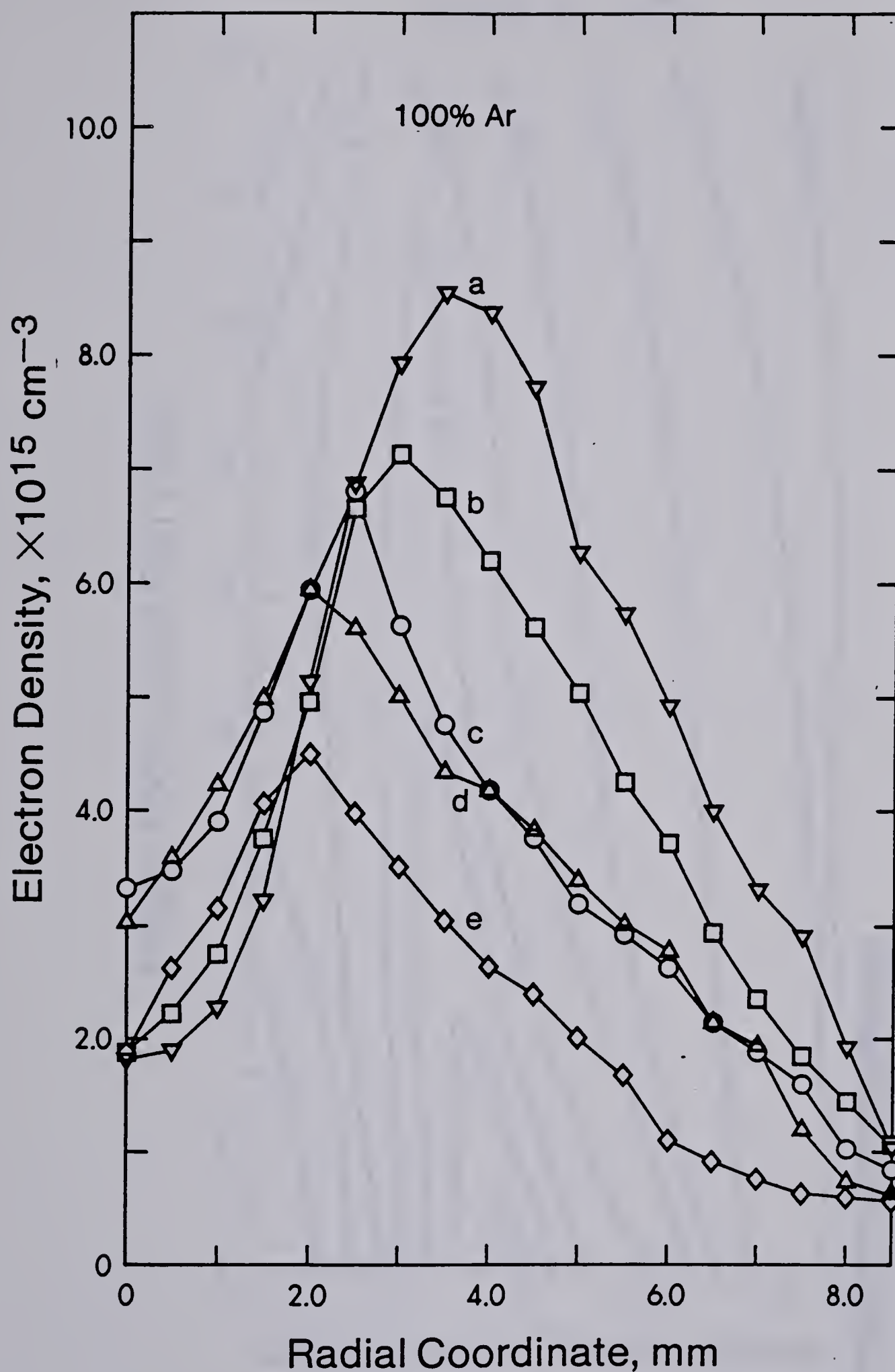


Fig. 69. Radial electron density profiles of an Ar-ICP as a function of observation height; (a) 2 mm, (b) 5 mm, (c) 10 mm, (d) 15 mm, and (e) 20 mm above the load coil, operated at 2.0 Kw power and 1.5 L/min aerosol flow rate.



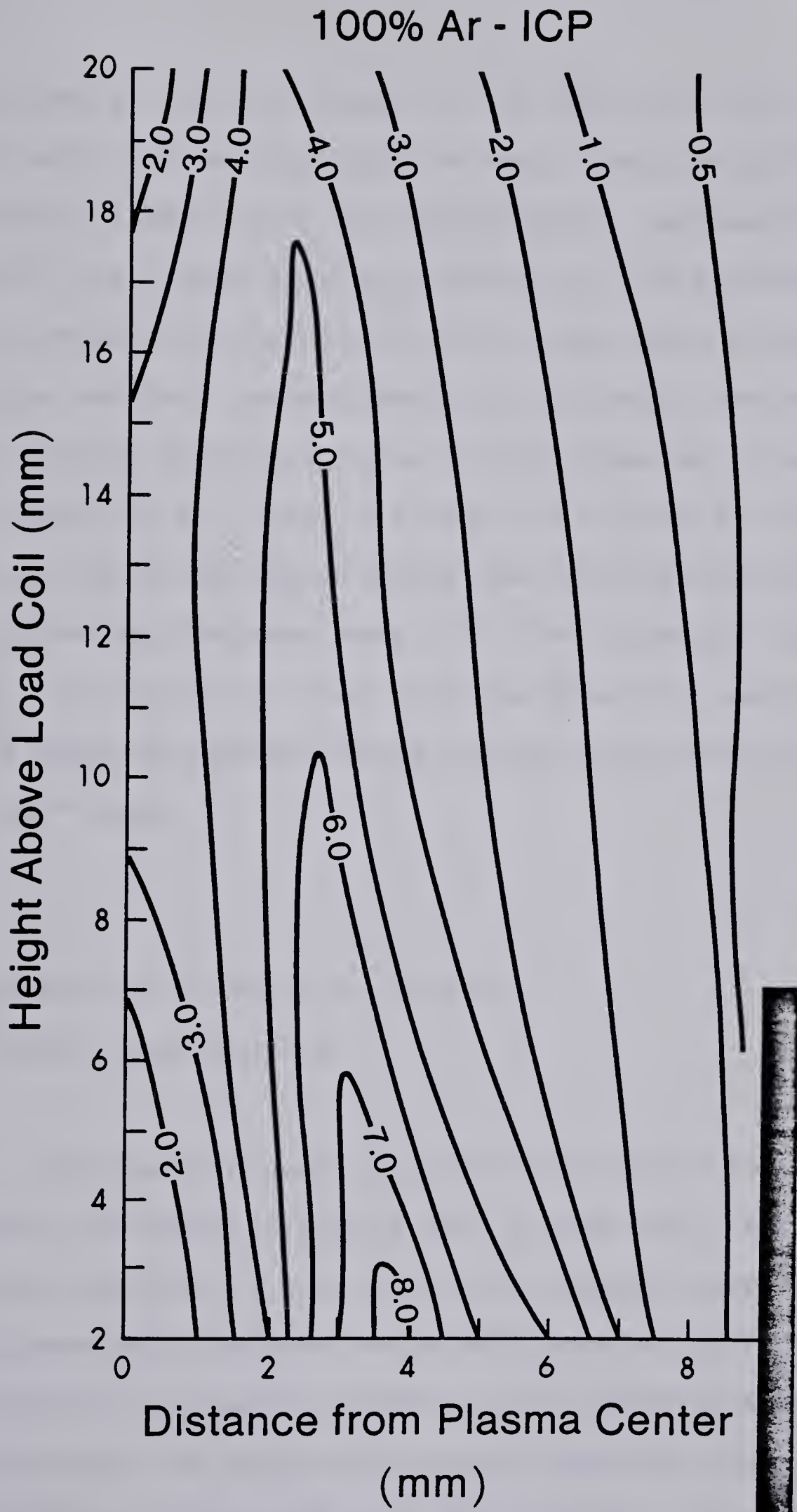


Fig. 70. Electron density map for an Ar-ICP, operated at 2.0 Kw power and 1.5 L/min aerosol flow rate.





in the spatial regions closer to the load coil and drops quickly with increasing distance away from the load coil. The density distribution is significantly reduced in the center of the plasma axis as a result of the aerosol channel. Note that the distribution zone tends to elongate along the vertical axis, especially following the contours of the current density stream. Off-axis maxima at all spatial heights are clearly visible in Figure 66. In addition, the zones move towards the central aerosol axis with increasing distance away from the induction coil. Finally, it should be noted that the electron density profile along the central axis exhibits characteristics of the "hump" shape.

#### 1. Effects of rf Power on Electron Density Distribution

The electron density profiles obtained for the 1.50 Kw Ar-ICP are shown in Figure 67. In this case, the aerosol flow rate was kept at 1.0 L/min. For comparison purposes, the ordinate and abscissa scale as presented in Figure 67 are identical to that of Figure 65. Preliminary measurements indicated that the magnitude and the distribution of the electron density depended upon the rf power. The density



profiles obtained from a 1.50 Kw Ar-ICP (Figure 67) are similar only in shape to the previous 2.0 Kw Ar-ICP's density profiles (Figure 65). Apparently, both plasmas exhibit a drop in electron density in the central axis. Dramatic differences in the electron density values are observed for the plasmas operated at different powers. In general, the overall magnitude of the electron density for the 1.50 Kw plasma at various observation heights is lower than that of the 2.0 Kw plasma. It is important to note that the profile maxima for the 1.50 Kw plasma (Figure 67) shifted towards the central aerosol channel. Note that an optimum density profile is obtained at 2 mm above the load coil.

A contour plot of electron density is presented in Figure 68. In the central aerosol channel, the optimum electron density zone occurs somewhere in between 5 mm to 15 mm above the load coil. This again indicates a "hump" shaped vertical density profile. The major difference between the contour plots of 1.50 Kw and 2.0 Kw plasmas is the magnitude of the electron density. This can be rationalized by considering that the current coupled to the plasma from the induction coil decreases by changing the rf power from 2.0 Kw to 1.50 Kw. It is also interesting to note that the volume bounded by the stream remains unchanged by decreasing the rf power.



## 2. Effects of Aerosol Flow rate on Electron Density Distribution

Edmonds and Horlick (106) demonstrated that the emission spatial patterns are highly dependent not only on the power but also the aerosol flow rate parameters of the plasma. In order to clarify the nature of spatial structure of electron density, a similar study was conducted on the electron density in the plasma as a function of aerosol flow rate. The spatial electron density profiles in the region of 2 to 20 mm above the load coil are provided in Figure 69, which has the same axis scales as presented in Figures 65 and 67. The conditions chosen for this study were 2.0 Kw rf power and 1.0 to 1.5 L/min aerosol flow rate. The electron density profiles with 1.0 L/min aerosol flow rate are shown in Figure 65 and that of 1.50 L/min aerosol flow rate are provided in Figure 69.

As the central aerosol flow rate is increased, the electron density in the central axis is expected to decrease because of the higher influx of cooler aerosol gas. However, it is demonstrated in Figure 69 that this is not the case. In addition, the net electron concentration and vertical density profiles in the middle axis are roughly identical in





both cases.

At a fixed power, an increase in aerosol flow rate (from 1.0 to 1.5 L/min) does not shift the peak electron density maxima away from the central axis. It is evident that changing the aerosol flow does not affect the overall magnitude of the electron density profiles (Figure 69). Also, the overall shape of the electron distributions for different aerosol flow rates (Figures 65 and 69) is almost identical in both cases.

The effect of changing aerosol flow rate on the electron density contour map of an argon plasma is demonstrated in Figure 66 for 1.0 L/min and Figure 70 for 1.5 L/min. In the latter case, the optimum electron distribution still occurred near the induction coil. It can be seen that the contour plot of electron density is independent of the plasma aerosol flow rates. It is somewhat unclear as to why these unexpected results occurred.

### 3. Effects of Foreign Gases in the Coolant Stream on the Electron Density Distribution

It was well established in Chapters IV to VI that nitrogen or oxygen introduced into the coolant flow of a conventional argon plasma can have a marked effect on the





emission intensities and the spatial characteristics of analyte signals. In all cases, the analyte emission signals were at their maxima when 10% nitrogen or oxygen was introduced into the coolant flow.

One of our major goals in studying a mixed gas plasma is to optimize the system and also to understand the mechanisms involved in optimization. From this point of view, a fundamental study of the electron density distribution was carried out in the ICP when nitrogen or oxygen was introduced into the coolant flow. Since the emission characteristics of the argon discharge are altered by the presence of the nitrogen or oxygen, it is important to study the effects of various amounts of nitrogen or oxygen in the argon discharge on electron density distribution.

#### a. 10% Nitrogen Cooled ICP

The effects of 10% nitrogen on the spatial profiles and absolute magnitude of electron concentration are shown in Figure 71. The curves shown in the figure are plots of radial electron density profile as a function of observation height above the load coil. These plots are analogous to those presented in Figure 65. The mixed gas plasma was operated at 2.0 Kw power and 1.0 L/min aerosol flow rate. As



10% nitrogen was introduced into the coolant flow of an argon plasma, the electron concentration at the lower region of the plasma (2 to 10 mm above the load coil) was higher than that of the argon discharge (Figure 65). This observation has undoubtedly indicated that a 10% N<sub>2</sub> cooled plasma is a more energetic source than the conventional Ar-ICP. It can be seen that higher in the plasma (10 to 20 mm above the load coil) the electron density fell below that of the argon plasma. The lowering of the electron density was due to the smaller plasma volume of the 10% N<sub>2</sub> cooled discharge. This effect is clearly illustrated in the contour plot for the electron density of a 10% N<sub>2</sub> cooled discharge in Figure 72.

It is interesting to note that lower in the plasma, the electron concentration shifted away from the central axis as the argon plasma was converted into a 10% N<sub>2</sub> cooled ICP. At 2 mm above the load coil, the radial position for the maximum electron density occurred at 4.25 mm away from the central axis. However, the density maximum shifted towards the central aerosol channel at higher observation heights. For example, at 20 mm above the induction coil the profile maximum occurred at 2 mm from the aerosol channel.

A comparison of the data shown in Figures 65 and 71 also indicates that in the central aerosol channel, electron density increases significantly when Ar-ICP is converted



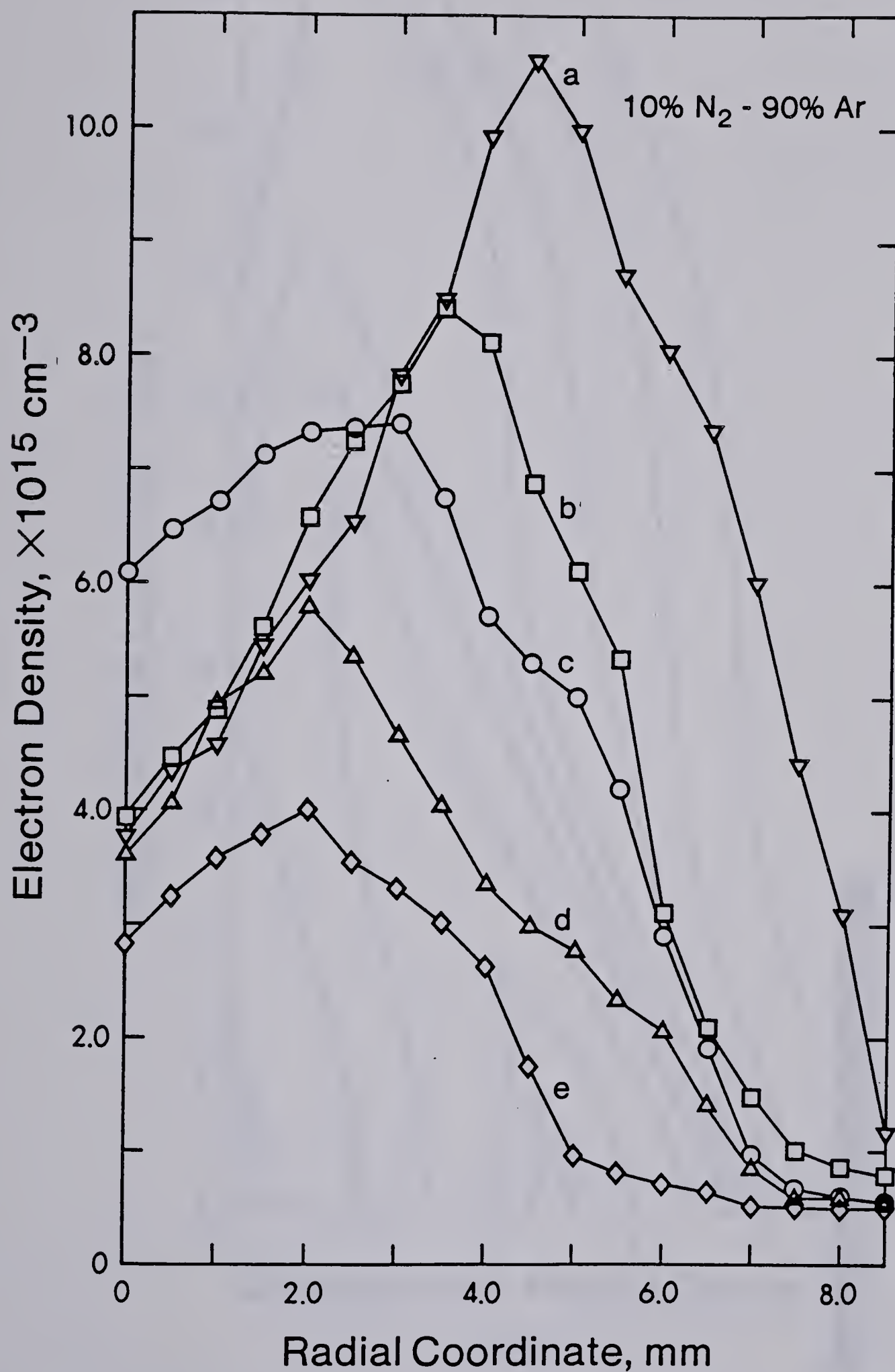


Fig. 71. Radial electron density profiles of a 10% N<sub>2</sub> cooled ICP as a function of observation height; (a) 2 mm, (b) 5 mm, (c) 10 mm, (d) 15 mm, and (e) 20 mm above the load coil, operated at 2.0 Kw power and 1.0 L/min aerosol flow rate.







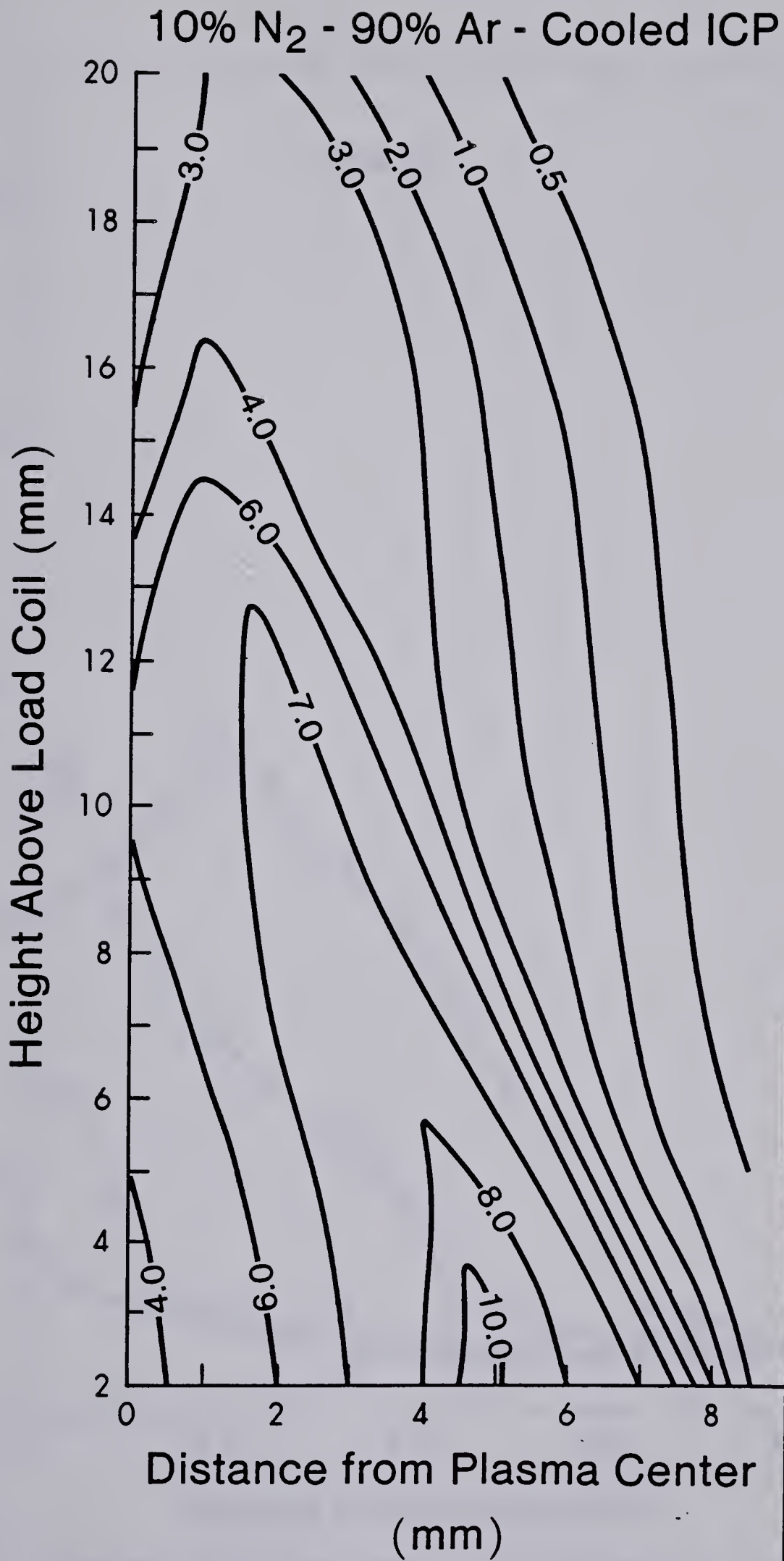


Fig. 72. Electron density map for a 10% N<sub>2</sub> cooled ICP, operated at 2.0 Kw power and 1.0 L/min aerosol flow rate.



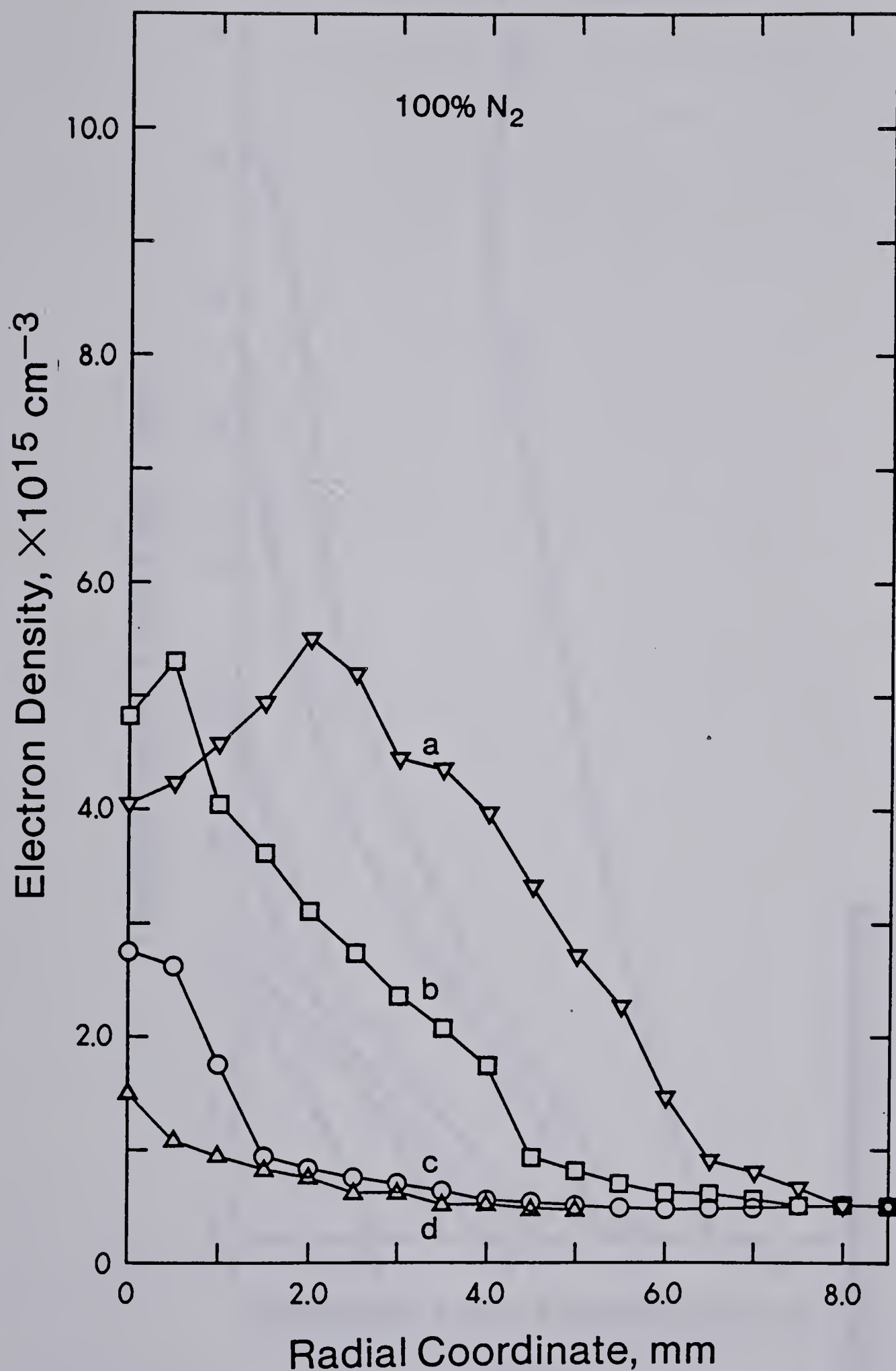


Fig. 73. Radial electron density profiles of a 100% N<sub>2</sub> cooled ICP as a function of observation height; (a) 2 mm, (b) 5 mm, (c) 10 mm, (d) 15 mm, and (e) 20 mm above the load coil, operated at 2.0 Kw power and 1.0 L/min aerosol flow rate.



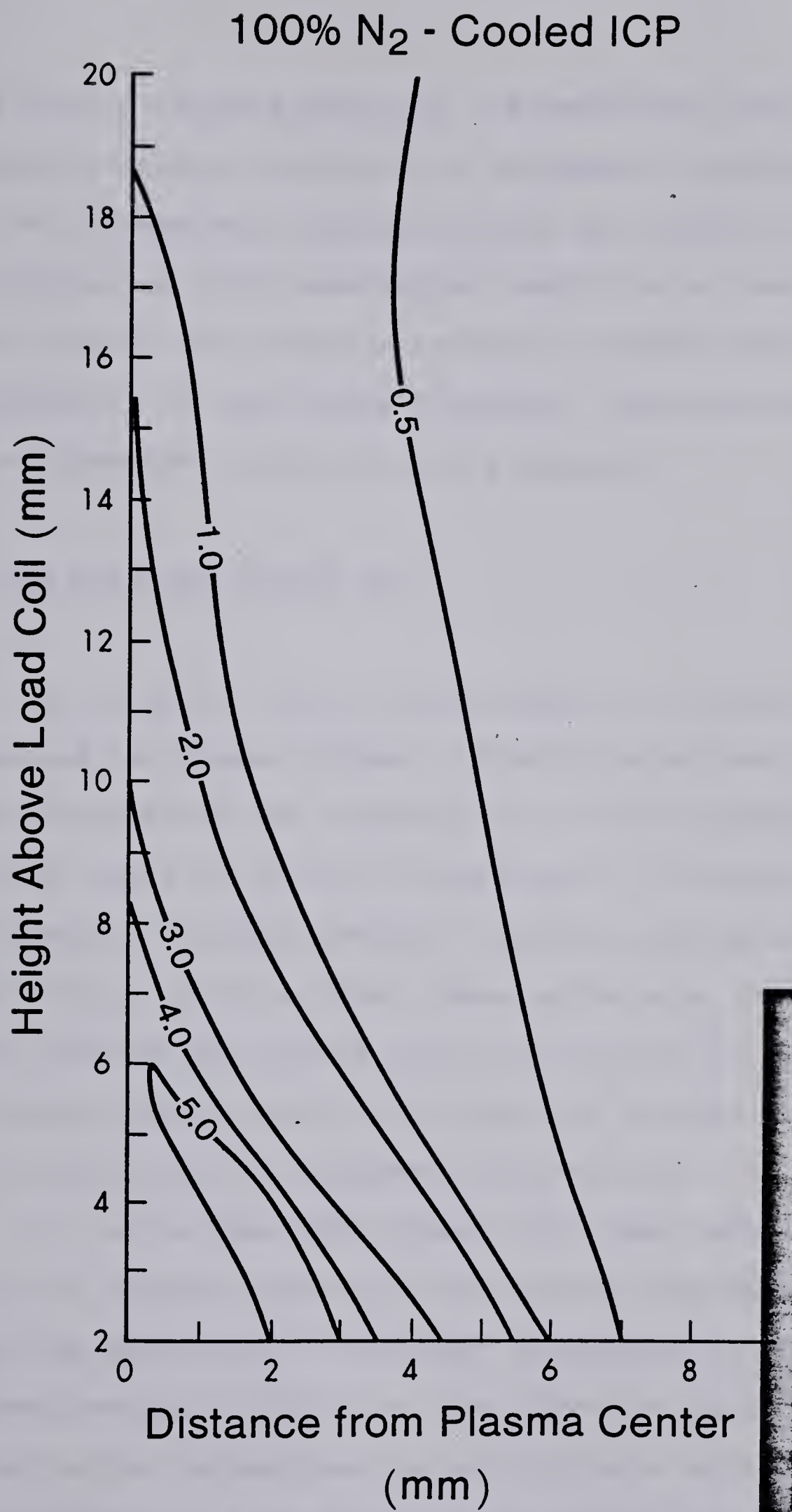


Fig. 74. Electron density map for a 100% N<sub>2</sub> cooled ICP, operated at 2.0 Kw power and 1.0 L/min aerosol flow rate.





into a 10% N<sub>2</sub> cooled plasma. As was mentioned previously, the analyte emission intensities increased significantly when 10% nitrogen was introduced into the coolant flow of an argon discharge. This observation leads one to conclude that electron density and emission intensity exhibit some degree of correlation in the plasma discharge. This correlation will be discussed in the following chapter.

#### b. 100% Nitrogen Cooled ICP

In order to verify the correlation of peak density maximum and the plasma volume, a similar experiment to the one mentioned above was repeated for a 100% N<sub>2</sub> cooled ICP. The curves shown in Figure 73 are plots of electron density as a function of radial position from the central axis for a 2.0 Kw 100% N<sub>2</sub> cooled plasma. These plots were collected at various observation heights above the load coil. Photodiode array insensitivity made it difficult to measure the electron profile at 20 mm above the load coil.

It can be seen from these plots that radial spatial profiles of electron density shift towards the induction coil as the percentage of nitrogen introduced to the coolant increases from 0% to 100%. At 2 mm above the load coil, as compared to the conventional argon discharge which has a density maximum at 4 mm away from the central axis, the





position of the density maximum for the 100%  $N_2$  cooled discharge is found to be at 2 mm away from the central aerosol channel. The above discussion is further substantiated by the contour plot provided in Figure 74. In this figure, it can be seen that the electron density zone is constricted to a smaller volume than that of the argon discharge. Previous studies have indicated that a  $N_2$ -Ar mixed gas plasma was constricted to a smaller volume when argon discharge was converted into a totally 100%  $N_2$  cooled ICP. Under similar operating conditions, the electron maximum was shifted towards the central plasma axis as a result of the reduction in plasma volume.

Increasing the coolant nitrogen concentration from 0% to 100% (Figures 65 and 73) significantly decreases the magnitude of the electron density. The results presented in Figures 73 and 74 clearly indicate that spatial position and intensity of the density maximum is undoubtedly related to the plasma volume. In Figure 74, the most interesting point to note is perhaps the contour plot of electron density for a 100%  $N_2$  cooled ICP which follows closely to the size and shape of the plasma discharge discussed in Chapter III.

#### c. 10% Oxygen Cooled ICP

Before drawing any definitive conclusions about the



correlation of electron density profiles and plasma volume, perhaps it is important to study other mixed gas plasmas in order to see whether these spatial patterns and trends have some generality. The analogous spatial profiles of electron density for the 10% O<sub>2</sub> cooled plasma are shown in Figure 75. The experimental operating conditions chosen for this study were identical to those described earlier for the N<sub>2</sub> cooled plasmas.

Several important conclusions can be drawn based on the spatial radial electron density profiles of the 10% O<sub>2</sub> - 90% Ar mixed gas ICP. First, if the argon plasma (Figures 65 and 66) is used as a basis for comparison, the overall magnitude of the electron density obtained from the 10% O<sub>2</sub> cooled plasma is somewhat higher than that of the argon discharge. This clearly indicates that a 10% O<sub>2</sub> cooled plasma is a more energetic source than the conventional Ar-ICP. Second, for a given observation height the intensity of density maximum is pushed towards the middle plasma axis as the argon discharge is converted into a 10% O<sub>2</sub> cooled ICP. Third, at viewing zones higher than 10 mm, the magnitude of electron density for the 10% O<sub>2</sub> cooled ICP is smaller than that of the Ar-ICP. This effect is again substantiated by the contour plot provided in Figure 76. A comparison of Figures 66 and 76 clearly illustrates that a pinch effect occurred in the plasma due to the introduction



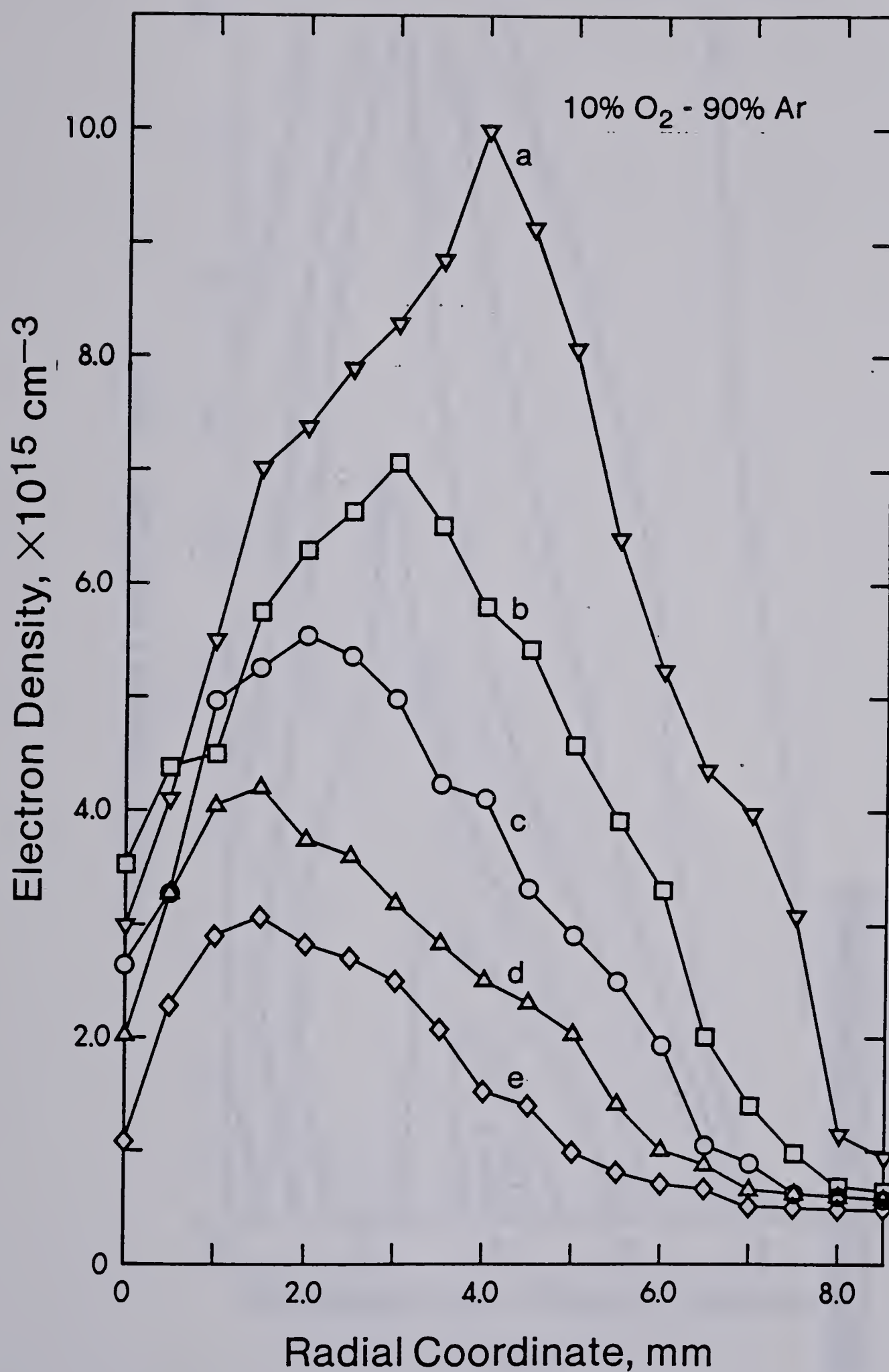


Fig. 75. Radial electron density profiles of a 10% O<sub>2</sub> cooled ICP as a function of observation height; (a) 2 mm, (b) 5 mm, (c) 10 mm, (d) 15 mm, and (e) 20 mm above the load coil, operated at 2.0 Kw power and 1.0 L/min aerosol flow rate.







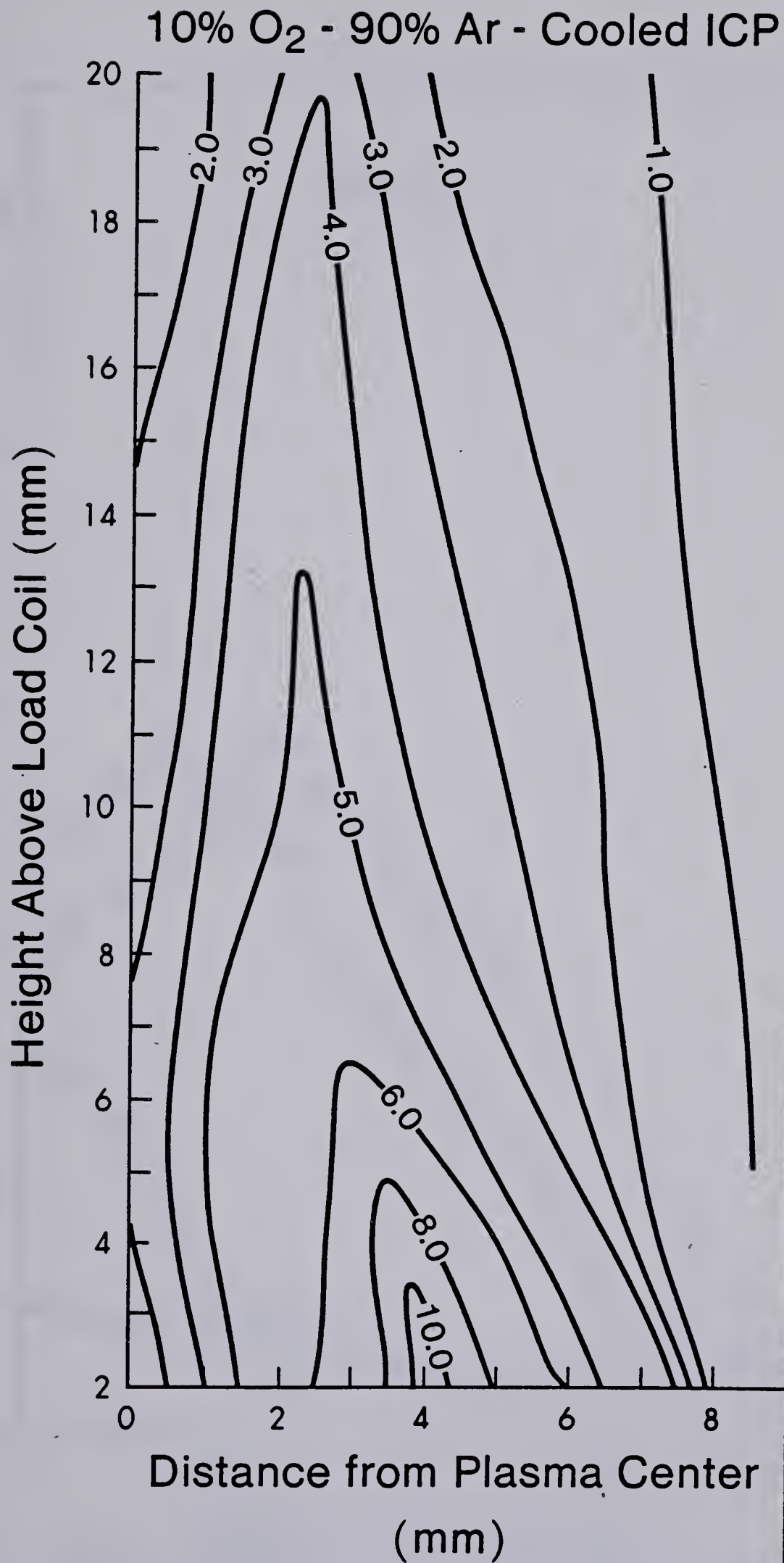


Fig. 76. Electron density map for a 10% O<sub>2</sub> cooled ICP, operated at 2.0 Kw power and 1.0 L/min aerosol flow rate.



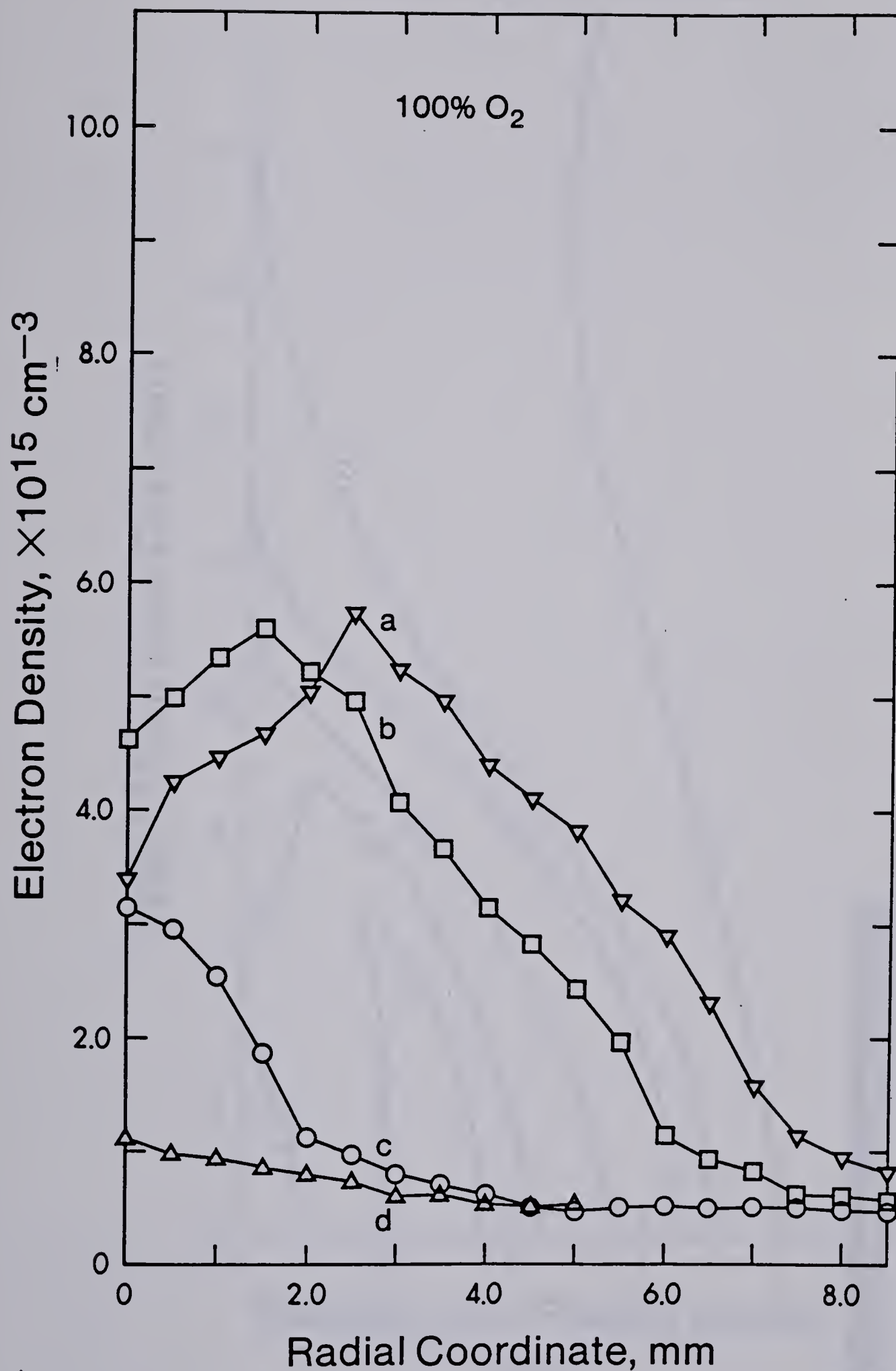


Fig. 77. Radial electron density profiles of a 100% O<sub>2</sub> cooled ICP as a function of observation height; (a) 2 mm, (b) 5 mm, (c) 10 mm, (d) 15 mm, and (e) 20 mm above the load coil, operated at 2.0 Kw power and 1.0 L/min aerosol flow rate.



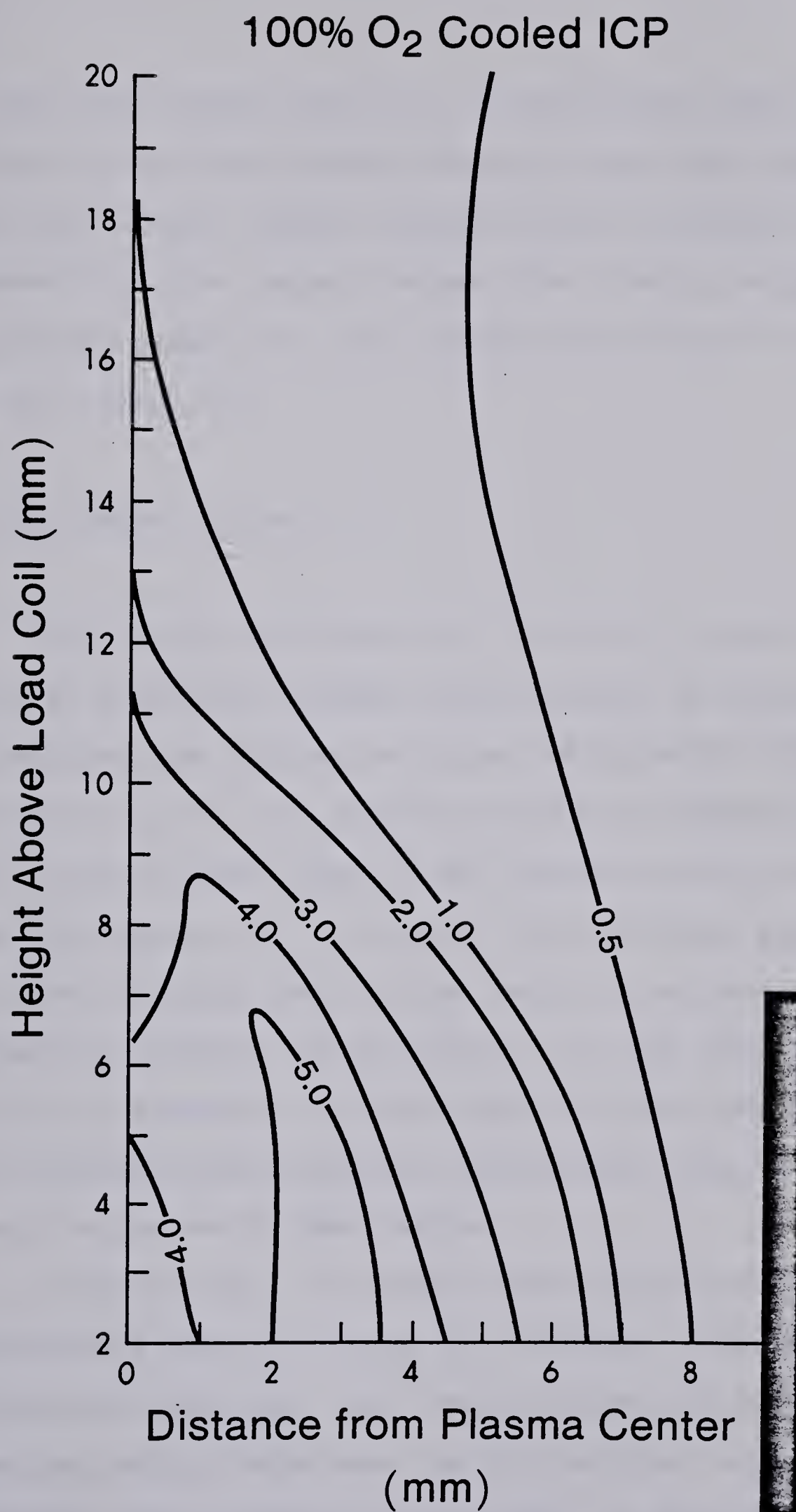


Fig. 78. Electron density map for a 100% O<sub>2</sub> cooled ICP, operated at 2.0 Kw power and 1.0 L/min aerosol flow rate.





of  $O_2$  into the coolant flow of a conventional argon plasma. It is also clear that electron density zones are pushed towards the central aerosol channel when 10% oxygen was introduced into the coolant stream. The density zones of the 10%  $O_2$  cooled plasma are also broader than those of the Ar or 10%  $N_2$  cooled ICP.

#### d. 100% Oxygen Cooled ICP

The electron profiles for the 100%  $O_2$  cooled plasma measured at different heights are presented in Figure 77. These profiles are similar to those indicated for the 100%  $N_2$  cooled ICP, i.e. (a) the profile maximum is pushed towards the central axis when argon in the coolant flow is totally replaced by oxygen, (b) the signal from hydrogen profiles at 20 mm above induction coil is too small to be detected by our present photodiode array detector, so the data for this height is not reported, (c) the absolute magnitude of the electron distribution decreases drastically when the discharge is cooled by 100% oxygen.

A contour plot of electron distribution that was obtained from a 100%  $O_2$  cooled ICP is shown in Figure 78. This figure demonstrates that density zones are being pushed towards the central axis when the conventional argon plasma is converted into a 100%  $O_2$  cooled ICP. It should be noted





that the shapes of the density zones are wider than those of the 100% N<sub>2</sub> cooled discharge. In the middle aerosol channel, the vertical density profile exhibits a "hump" shaped characteristic with the maximum density occurring at 6 mm above the load coil.

#### D. Conclusions

It is clear that mapping the electron distribution from an ICP source with a photodiode array provides a unique and detailed picture of the spatial characteristics of electron density distribution. From the results discussed in the previous sections, it is quite clear that electron distributions in the ICP are highly dependent on the rf power and plasma physical volume. The experimental data also indicate that electron distributions in the plasma source are somewhat independent of the variation in aerosol flow rate.

Since the presence of N<sub>2</sub> or O<sub>2</sub> in the coolant stream alters the characteristics of the electron distributions in the plasma source, several important conclusions can be drawn from these observations. First of all, the 10% mixed gas plasma increases the electron density which indicates that a mixed gas plasma (10%) is more energetic than the conventional argon discharge. Secondly, as mentioned



previously, the presence of nitrogen or oxygen has a marked effect on both the intensity of the analyte emission signals and the electron densities; therefore, these observations lead one to believe that signal enhancements observed in the mixed gas plasmas may be the result of an increase in electron density. Thirdly, since the vertical profiles of the electrons and emission signals exhibit "hump" shaped characteristics in the aerosol channel, this implies that a correlation may exist between the electron density and the analyte signal in the ICP source. Finally, the similar behaviour of analyte emission signals and electron densities in the aerosol channel also suggests that ionization and excitation processes are probably due to collisions with energetic electrons.

Based on these results, it is probably most important to study the correlation between the electron density and analyte emission signals. Such measurements have been carried out and will be described in the following chapter.



CHAPTER IX  
CORRELATION OF ANALYTE EMISSION WITH  
ELECTRON DENSITY IN MIXED GAS ICPs

A. Introduction

The electron density in Ar-ICP discharges has been measured by several investigators (88,93,94,96,98,103). However, few measurements of the spatial distribution of electron density in the ICP have been made (88,99,94) and no correlation has been made between the spatial distribution of the electron density and that of the analyte emission intensity. It is evident from the preceding chapters that distribution of electron density in the plasma source is greatly influenced by the ICP operating parameters such as plasma power, observation height, aerosol flow rate, and plasma gas composition.

It can be deduced from the preceding chapters that variations in ICP operating parameters cause both magnitude and spatial changes in the analyte emission intensity and electron density. Therefore, it seems reasonable that a correlation may exist between analyte emission intensity and electron density. In this study changes in the emission and structure of both the cadmium neutral atom and ion lines





were monitored as a function of ICP operating parameters and these changes were correlated with those in electron density. It will be seen that a correlation occurs between the distribution of electron density and that of the analyte emission intensity.

For many analytes, ion species are considerably more sensitive than neutral atom species towards the addition of foreign gases into the argon discharge. This is certainly true for all the elements discussed in Chapter IV. It will be seen in this chapter that correlation of analyte emission intensity with electron density in mixed gas ICPs provides a rational explanation on the nature of ion line advantages in the mixed gas discharge.

There are several reasons for choosing cadmium neutral atom (228.8 nm) and ion (226.5 nm) emission lines for these studies. First, both lines have about equal sensitivity in the argon plasma source. Second, they are in the same wavelength region so that the monochromator does not need to be calibrated against a standard tungsten filament lamp. Third, the combined energy of the excitation and ionization potentials (14.5 eV) of the cadmium ion line is greater than excited energies of argon metastables (11.5 eV); therefore, argon metastable does not have enough energy to excite and ionize the cadmium species.

Finally, certain qualitative observations have been



employed to assess the role of electrons in the ionization and excitation mechanisms in mixed gas plasma.

## B. Experimental

The plasma system was the Plasma-Therm ICP system discussed in Chapter II. Unless specifically noted, all operating conditions are as listed in Table III.1. The measurement systems were identical to those described in Chapter VII-VIII. Foreign gases such as oxygen and nitrogen were introduced only to the coolant flow of a conventional argon plasma.

The radial distribution of analyte emission intensity was calculated using the Abel inversion technique discussed in Chapter VII. The operating conditions for this experiment were identical to those used for the electron density measurements.

## C. Results and Discussion

### 1. Comparison of Horizontal Lateral and Radial Emission Profiles of Cadmium Neutral Atom and Ion Lines



The horizontal profiles of CdI (228.8 nm) and CdII (226.5 nm) lines are provided in Figures 79 and 80 respectively. The ICP operating conditions were 2.0 Kw rf power, 1.0 L/min aerosol flow rate, and these profiles were observed at 2 mm above the load coil. All gas flows were argon. The measured lateral intensity distribution for the CdI 228.8 nm line is presented in Figure 79, together with the calculated radial profile. The lateral and radial profiles for the CdII 226.5 nm line are provided in Figures 80a and 80b. The different shapes of the lateral and radial emission profiles are clearly illustrated in Figures 79 and 80. The lateral profiles of Figures 79a and 80a imply that there is high emission intensity at the center of the aerosol channel, whereas the radial profiles in Figures 79b and 80b indicate that the emission dips significantly at the center axis. Since the ICP is viewed from the side, the difference in emission intensity in the aerosol channel is due to the fact that the measured lateral intensity is the sum of the total emission intensity contributed from all depths within the source. Hence, after Abel inversion the calculated radial intensity in the center axis is lower than the measured lateral intensity. Another interesting point to note in Figures 79 and 80 is that the radial profile of the neutral atom line dips significantly less than that of the





# Ar - ICP, 2 mm Above Load Coil

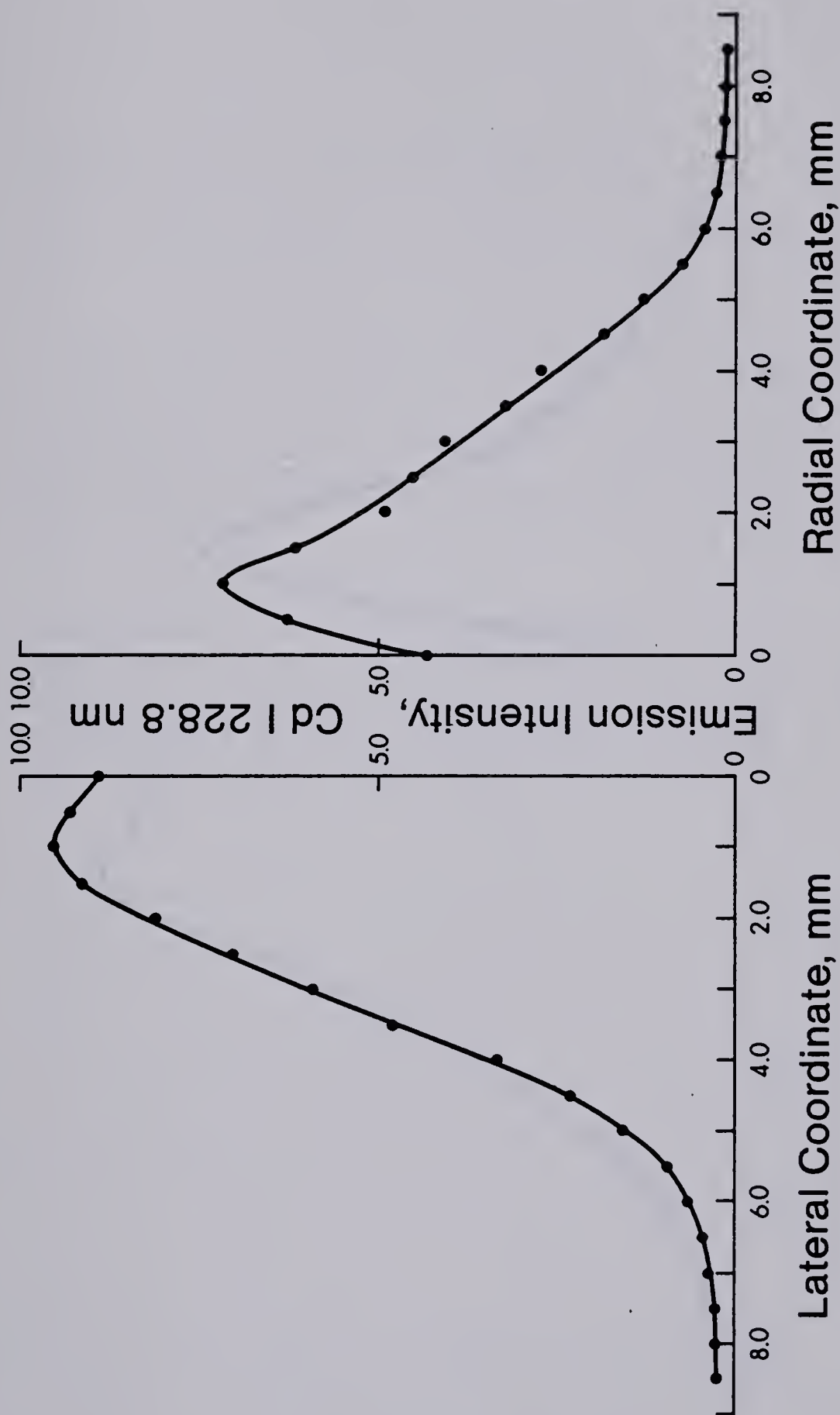


Fig. 79. Lateral and radial emission profiles for CdI 228.8 nm at 2 mm above the load coil.





# Ar - ICP, 2 mm Above Load Coil

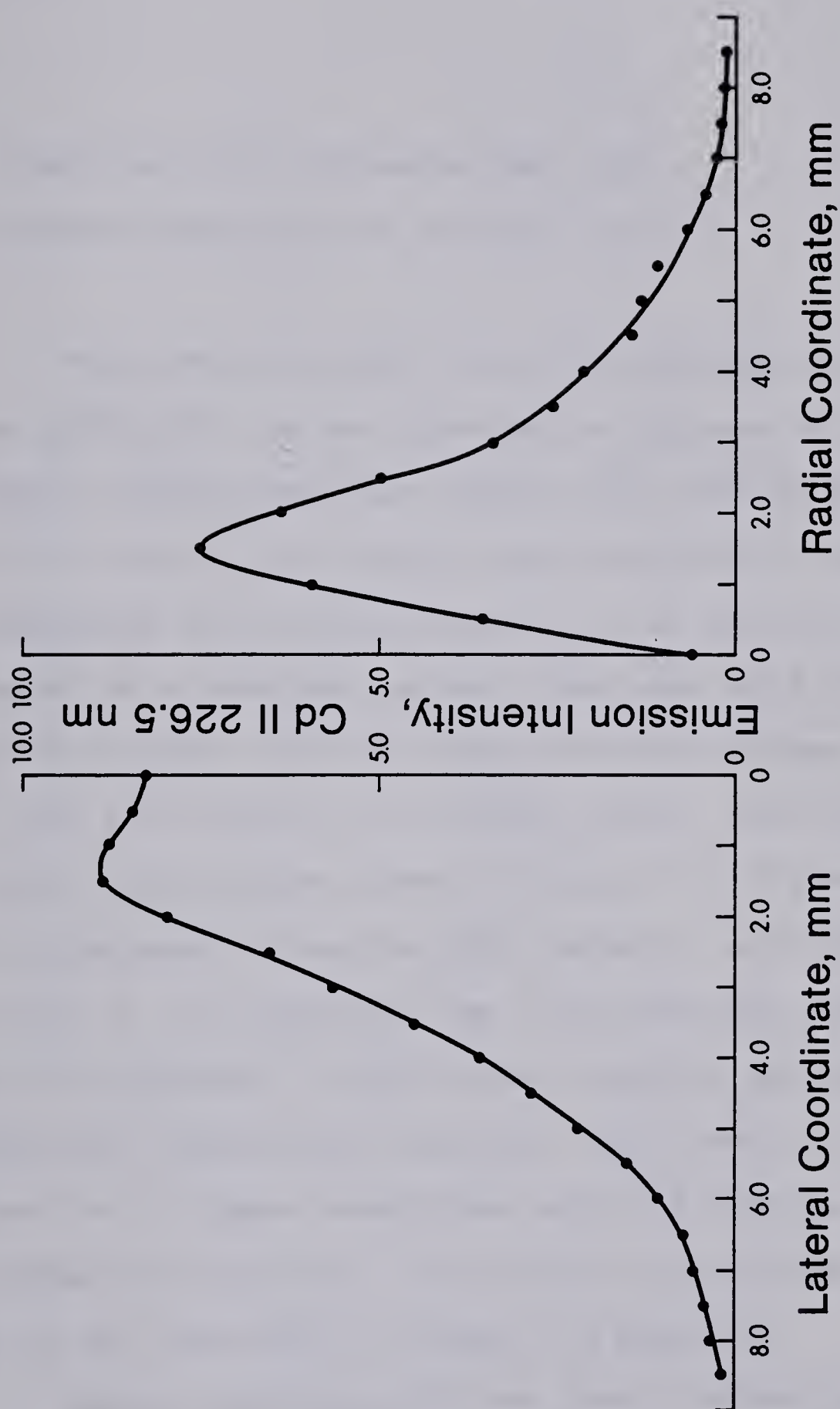


Fig. 80. Lateral and radial emission profiles for CdII 226.5 nm at 2 mm above the load coil.



ion line.

## 2. Complete Radial Emission Maps for Cadmium Neutral Atom and Ion Lines

The complete radial emission profiles for CdI 228.8 nm and CdII 226.5 nm are provided in Figures 81 to 87. A set of spatial radial profiles (Figure 81) will be discussed in detail as most of the spatial data measured in this study are presented in the same format. All of the data were collected at a constant aerosol flow rate (1.0 L/min Ar), constant rf power (2.0 Kw) and a constant volume of coolant flow rate (15 L/min Ar or foreign gases). Two different sets of radial profiles are shown in Figure 81. Figure 81a on the left corresponds to neutral atom emission and Figure 81b on the right to ion emission. The five different profiles on each set correspond to the radial emission profiles measured at different observation heights, i.e. from 2 to 20 mm above the load coil. These conditions hold for Figures 81 to 87. For comparison purposes, the scales as presented in Figures 82 to 87 are identical to those of Figure 81.

Radial emission profiles from a conventional argon plasma are presented in Figure 81. These profiles show several interesting features which seem characteristic of



Ar - ICP (2.0 kw, 1.0  $\ell$ pm Aerosol)

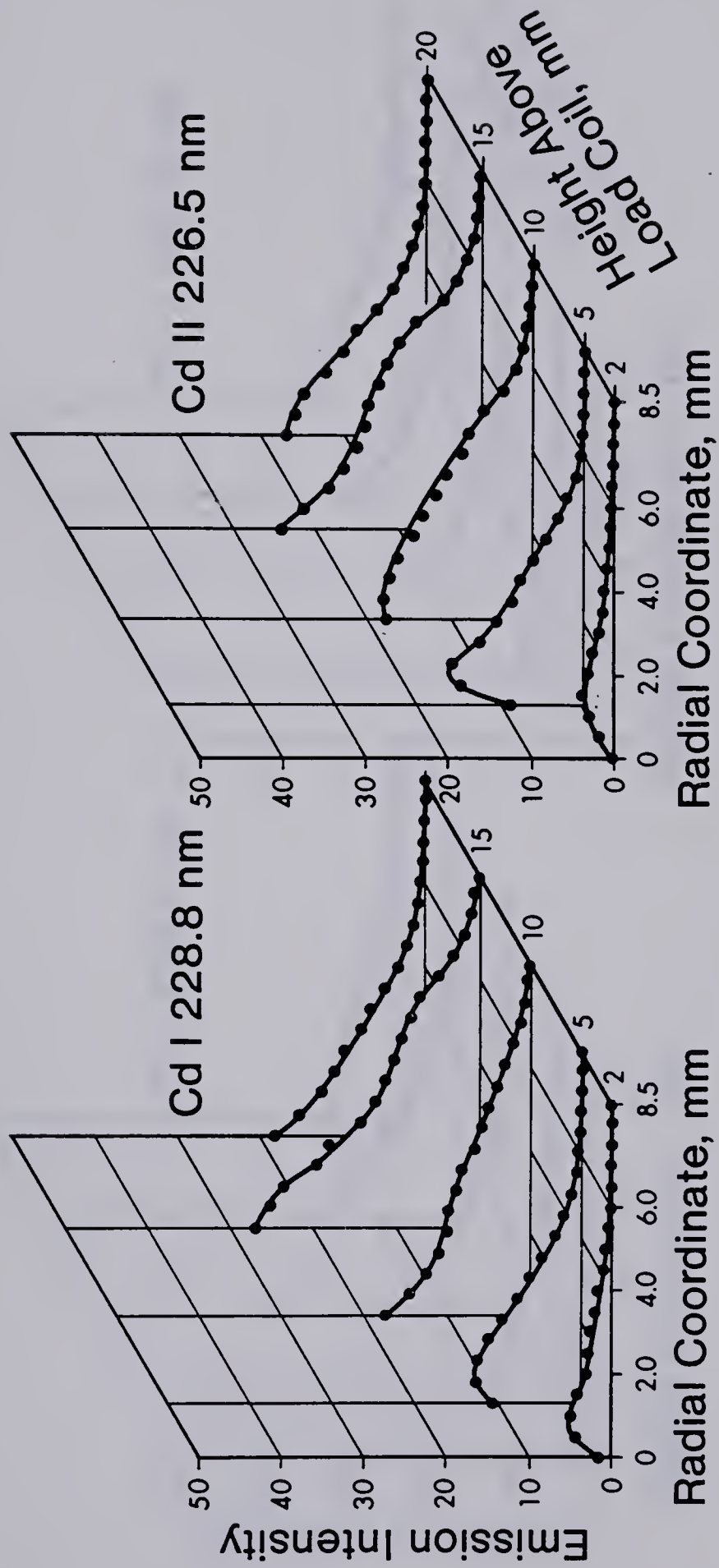


Fig. 81. Complete radial emission map of an Ar-ICP for CdI 228.8 nm and CdII 226.5 nm, operated at 2.0 Kw power and 1.0 L/min aerosol flow rate.





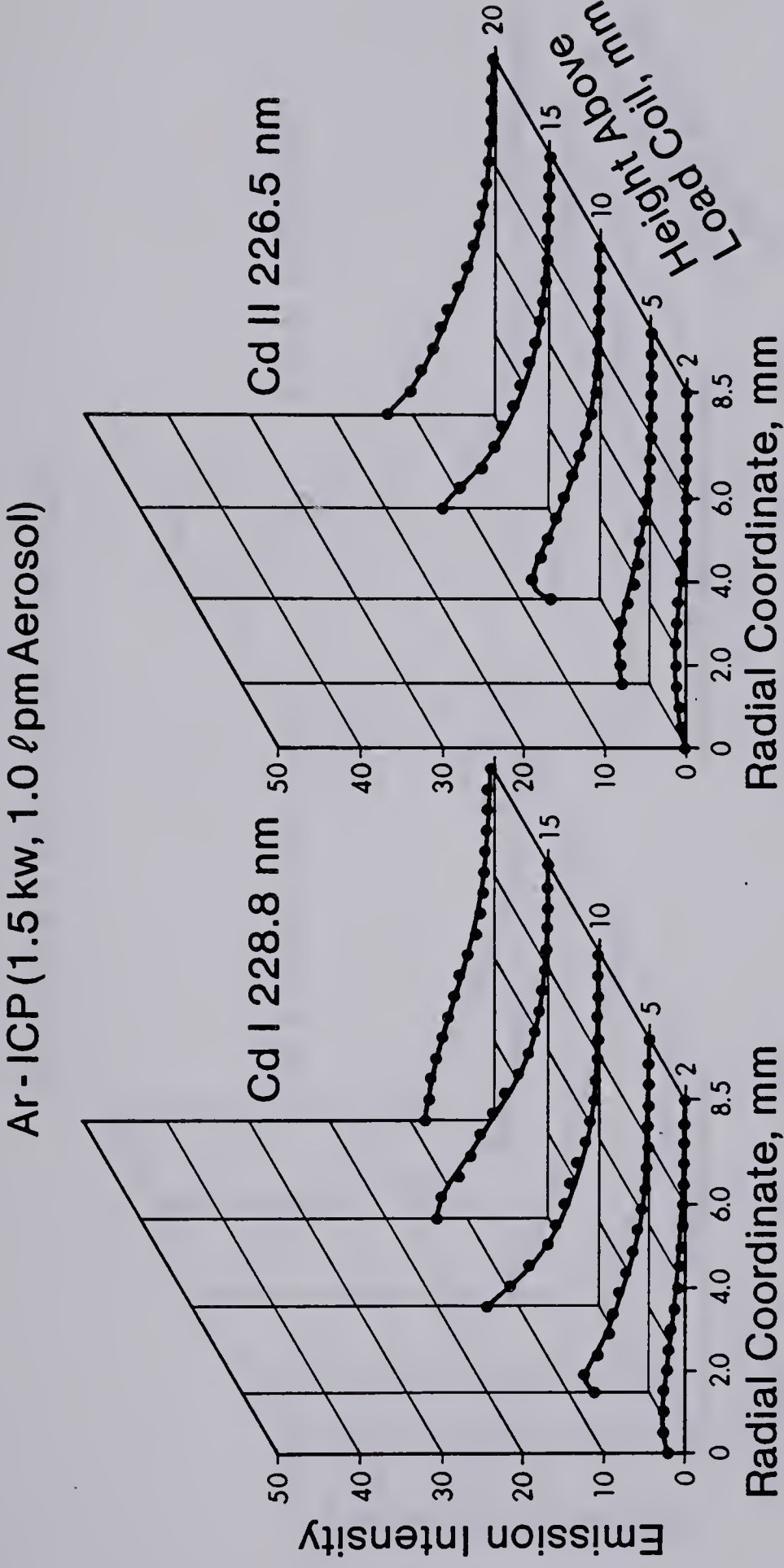


Fig. 82. Complete radial emission map of an Ar-ICP for CdI 228.8 nm and CdII 226.5 nm, operated at 1.5 Kw power and 1.0 L/min aerosol flow rate.



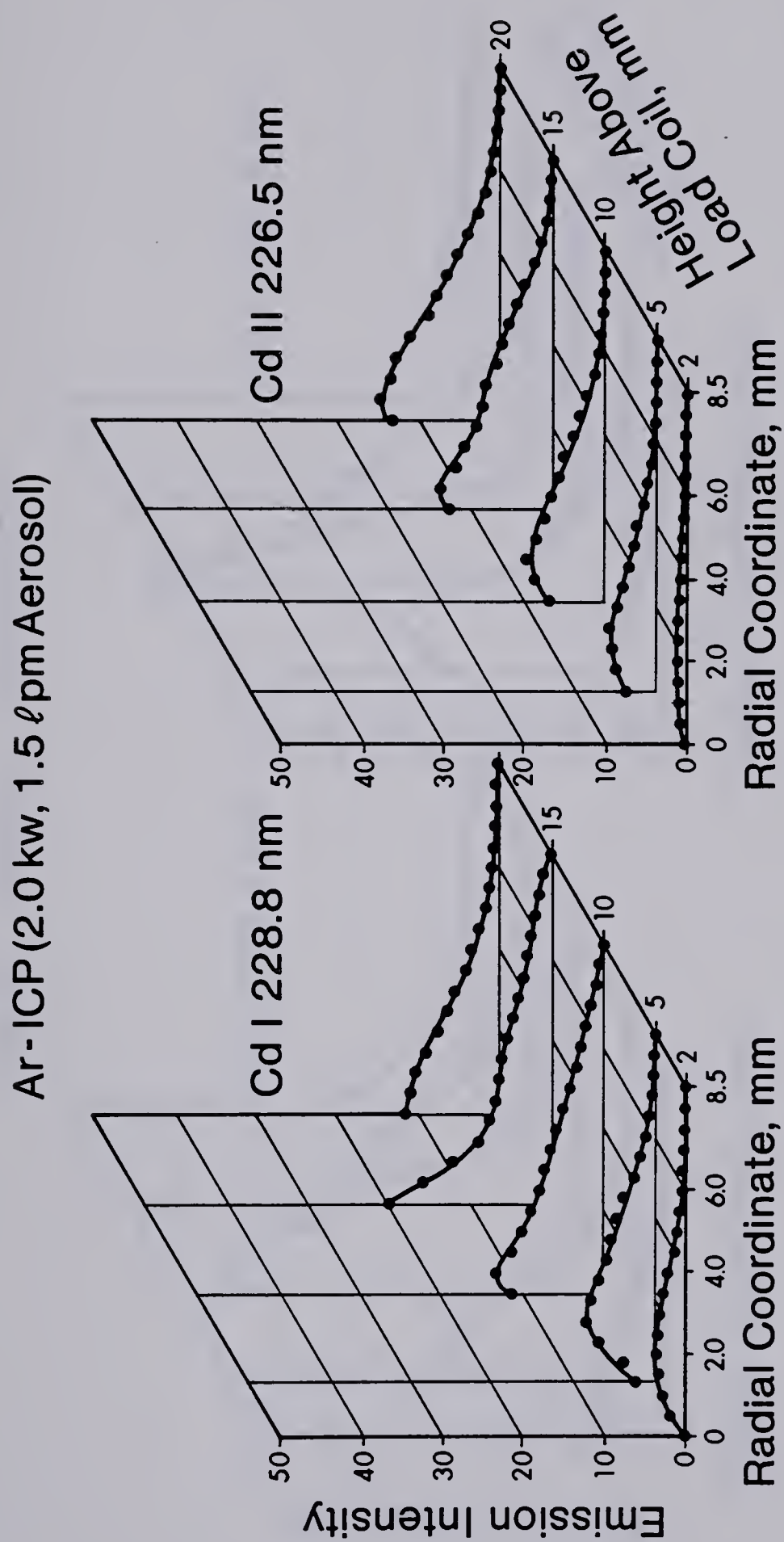


Fig. 83. Complete radial emission map of an Ar-ICP for CdI 228.8 nm and CdII 226.5 nm, operated at 2.0 Kw power and 1.5 L/min aerosol flow rate.



# 10% N<sub>2</sub> - 90% Ar - Cooled ICP

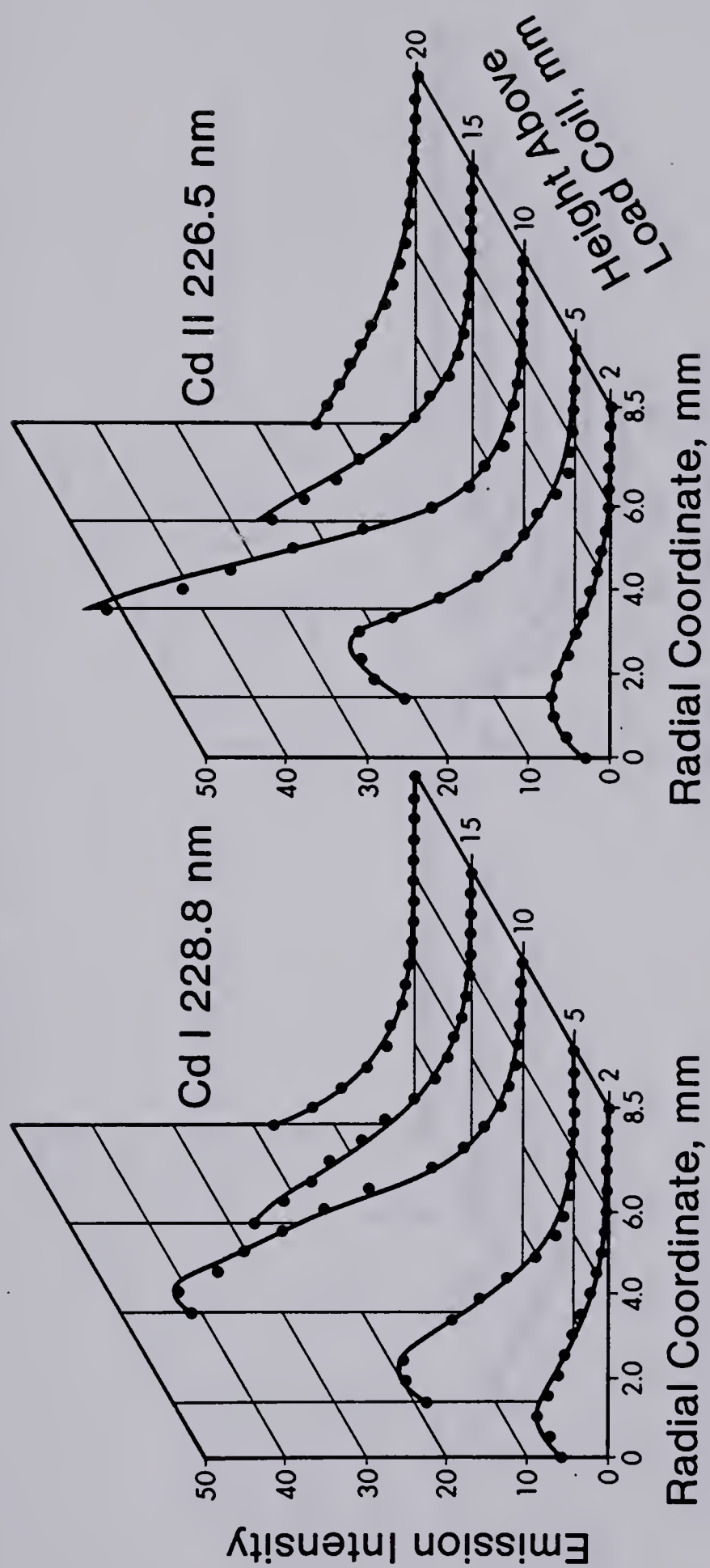


Fig. 84. Complete radial emission map of a 10% N<sub>2</sub> - 90% Ar cooled ICP for Cd I 228.8 nm and Cd II 226.5 nm, operated at 2.0 Kw power and 1.0 L/min aerosol flow rate.





100% N<sub>2</sub> - Cooled ICP

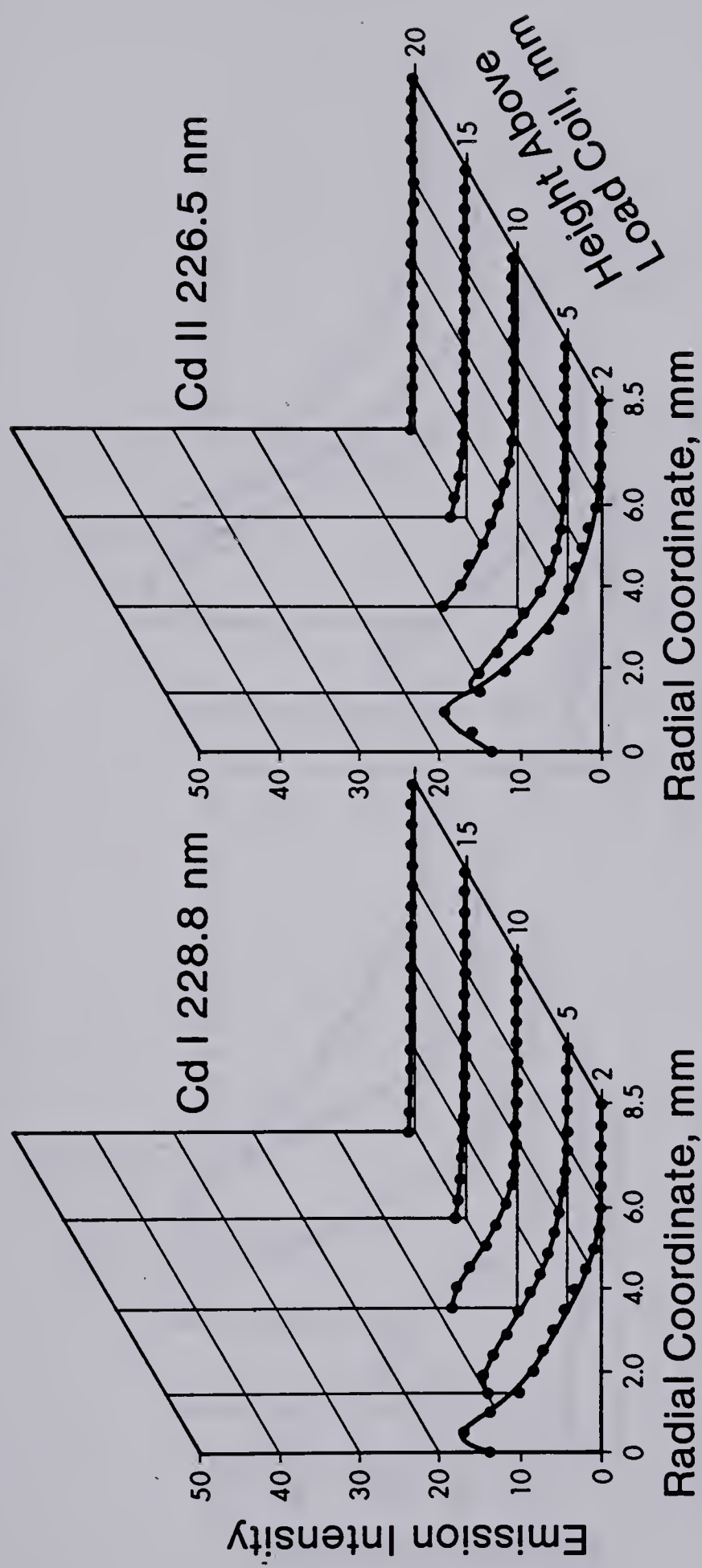


Fig. 85. Complete radial emission map of a 100% N<sub>2</sub> cooled ICP for Cd I 228.8 nm and Cd II 226.5 nm, operated at 2.0 Kw power and 1.0 L/min aerosol flow rate.





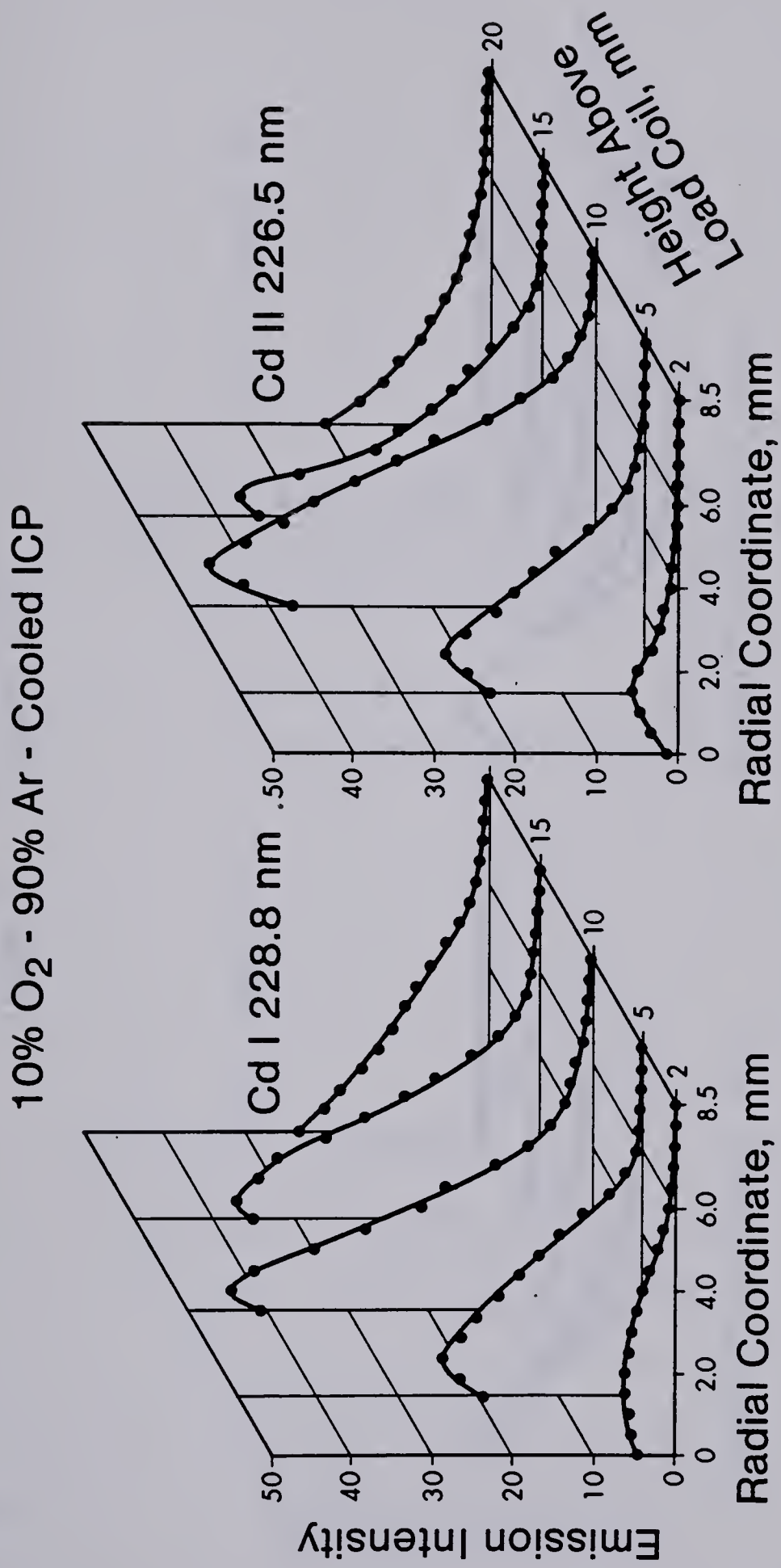


Fig. 86. Complete radial emission map of a 10% O<sub>2</sub> - 90% Ar cooled ICP for Cd I 228.8 nm and Cd II 226.5 nm, operated at 2.0 Kw power and 1.0 L/min aerosol flow rate.



# 100% O<sub>2</sub> - Cooled ICP

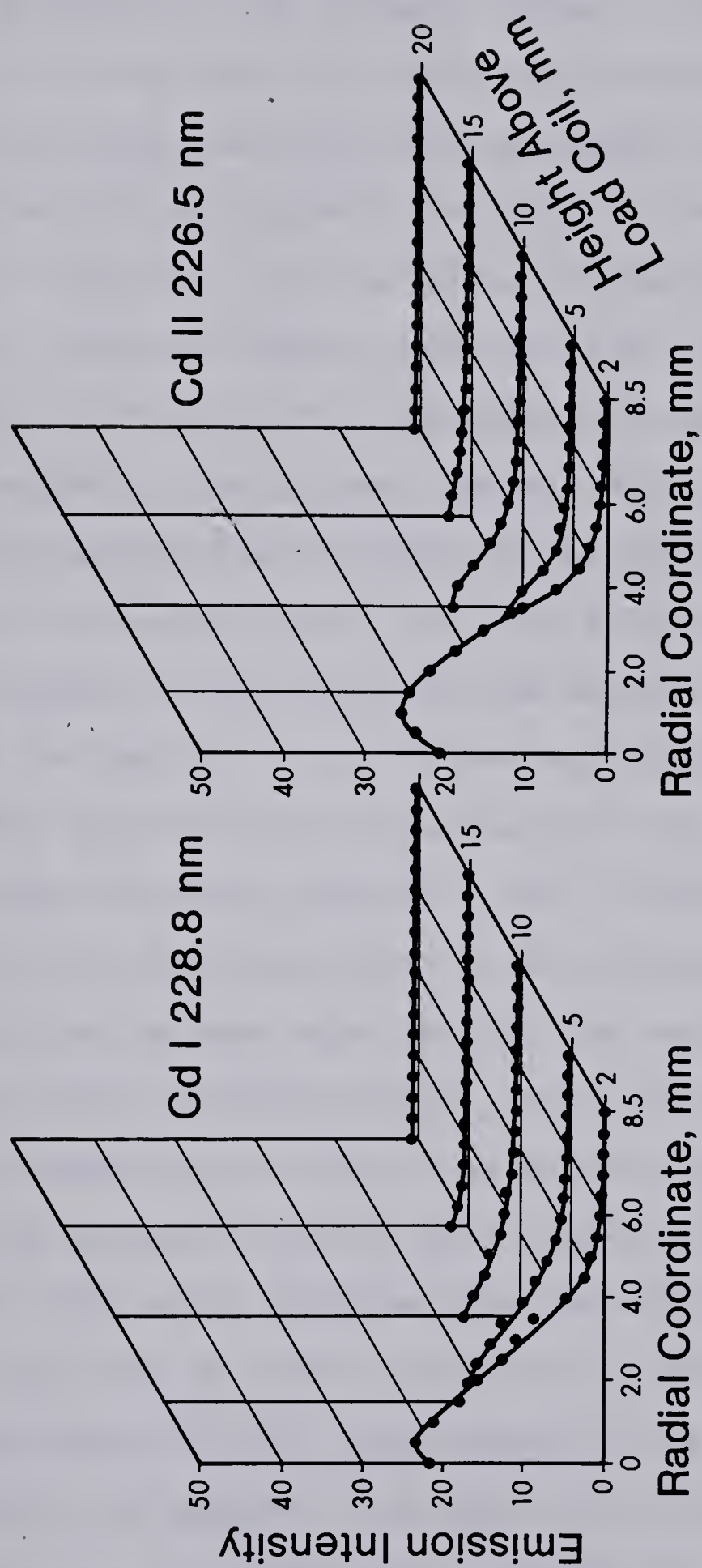


Fig. 87. Complete radial emission map of a 100% O<sub>2</sub> cooled ICP for Cd I 228.8 nm and Cd II 226.5 nm, operated at 2.0 Kw power and 1.0 L/min aerosol flow rate.



analyte emission in the aerosol channel. First, low in the plasma (2 to 5 mm above the load coil) emission peaks off-axis with peak emission corresponding roughly to the edge of the analyte channel, and also to the plasma "doughnut" boundary. This is evidence, perhaps, that the excitation of these neutral atom and ion lines is related to interaction with energetic electrons originated from the annular region of the plasma. Second, with an increase in observation height the position of the peak maximum shifts closer to the central axis, until at a height of 10 mm, the emission peaks in the center of the aerosol channel. As discussed in Chapter VIII, the maximum electron density zones moved towards the central aerosol axis with increasing distance away from the induction coil. Therefore, the above observation can be interpreted as an increase in the amount of interaction between cold aerosol gas and hot energetic electrons with increasing height, such that complete mixing occurs at this height. Third, the emission profile from the ion line is somewhat broader when compared to emission from atom line. The radial profiles observed corresponded closely to those reported by Blades and Horlick (120,121), and Furuta and Horlick (122). This might be the result of diffusion of ion species. A broader ion profile is being observed because the coulombic attraction between ions and electrons is stronger than that of the atoms and electrons;







therefore, ions tend to diffuse more into the main body of the plasma which consists of high concentration of electrons. Fourth, in agreement with the data presented in Chapter IV the radial emission intensities for both ion and neutral atom lines in the aerosol channel peak around 15 mm above the load coil. This emission structure suggests that atom and ion emission can be correlated with the magnitude of electron density in this channel. Such correlation has been carried out and will be discussed later in this chapter. Complete radial emission intensity maps of the ICP under different operating parameters have been measured in order to test the validity of the above discussions.

The complete radial emission maps of the CdI 228.8 nm and CdII 226.5 nm lines for a 1.50 Kw argon discharge are shown in Figure 82. The aerosol flow rate was kept at 1.0 L/min argon. For comparison purposes, the ordinate and abscissa scales as presented in Figure 82 are identical to those of Figure 81. Preliminary studies indicate that the magnitude and the distribution of the overall radial emission depend upon the rf power. Decreasing the plasma power from 2.0 Kw to 1.5 Kw causes the radial intensity to decrease. The radial emission profiles for both lines operated at 1.50 Kw power are somewhat narrower when compared to those of the 2.0 Kw plasma. Also, the maximum emission in the aerosol channel shifts away from the



induction coil when plasma power is decreased from 2.0 Kw to 1.50 Kw.

At fixed plasma power of 2.0 Kw, an increase in aerosol flow rate from 1.0 L/min to 1.50 L/min (Figure 83) results in widening the aerosol channel because of a higher influx of cooler aerosol gas. In addition, the maximum radial emission along the aerosol channel clearly shifts away from the induction coil. Finally, the overall magnitude of radial emission decreases due to the fact that an increase in aerosol flow rate results in a reduction of time that a sample spends in the plasma.

### 3. Effects of Foreign Gases ( $N_2$ or $O_2$ ) in the Coolant Stream on the Complete Radial Emission Maps

In addition to variations in plasma power and aerosol flow rate, variation in coolant gas compositions can also cause both intensity and spatial changes in the analyte emission intensity. It is also to be expected that changes in the gas composition will result in electron density, temperatures and conductivity changes in the plasma discharge. It was established in Chapters IV to VI that nitrogen or oxygen introduced into the coolant flow of a



conventional argon plasma can have a marked effect on the emission intensities and spatial characteristics of the analyte signals. These results are rather limited and mainly concern themselves with the characterization and evaluation of the mixed gas plasmas only in the aerosol channel. A complete radial emission map of the mixed gas ICPs is absolutely necessary in order to assess the physical dependence of analyte emission upon variation in gas composition. From a fundamental point of view it is necessary to monitor changes in the radial emission distribution of the analyte as a function of gas compositions and to correlate these changes with those in the electron density.

#### a. 10% and 100% Nitrogen Cooled ICPs

The complete radial emission profiles for CdI 228.8 nm and CdII 226.5 nm are provided in Figures 84 and 85. The radial emission maps for 10% (Figure 84) and 100% (Figure 85) N<sub>2</sub> cooled ICPs are shown. These plots are analogous to those presented in Figure 83. The mixed gas plasmas were operated at 2.0 Kw and 1.0 L/min aerosol flow rate (Ar). For comparison, note the radial emission maps for the argon plasma presented in Figure 81. As 10% nitrogen is introduced into the coolant flow, the intensities of radial emission of





atom and ion lines at all observation heights (2 mm to 20 mm) are higher than those of the conventional argon discharge (Figure 83). This observation leads one to conclude that 10% N<sub>2</sub> cooled ICP is a more energetic source than the conventional argon discharge. The emission profiles of a 10% N<sub>2</sub> cooled ICP are somewhat narrower than those of the conventional argon discharge. This is certainly true for both the neutral atom and ion lines. In addition, the maximum radial profiles shift in the direction of the load coil. This behaviour appears to be the result of the physical volume of the 10% N<sub>2</sub> cooled discharge. Generally, a similar spatial pattern is also observed for the electron distribution in the 10% N<sub>2</sub> cooled ICP except that the electron distribution peaks lower in the discharge (see Figure 84).

It can be seen from Figures 81, 84 and 85 that the maximum intensity of the radial emission shifts in the direction of the induction coil as the percentage of nitrogen introduced to the coolant increases from 0% to 100%. Previous studies have indicated that the physical size of the mixed gas ICP was constricted to a smaller volume when the argon discharge was converted into a totally 100% N<sub>2</sub> cooled plasma. It can be seen from Figure 85 that the radial emission is constricted to a small volume and the emission maximum shifts towards the load coil as a result of





the reduction in plasma volume. in addition, the radial emission intensity of a 100% N<sub>2</sub> cooled plasma (Figure 85) is considerably smaller than those of the conventional argon and 10% N<sub>2</sub> cooled plasma.

The results presented in this study clearly indicate that spatial position, distribution and magnitude of the radial emission intensity is undoubtedly related to the plasma volume and plasma gas composition. The most interesting point to note is perhaps that the distributions of analyte radial emission follow closely to the spatial distribution patterns observed for the electron density (Chapter VIII).

#### b. 10% and 100% Oxygen Cooled ICPs

In order to verify the above correlation of radial emission and electron density, similar experiments were conducted for the O<sub>2</sub>-Ar mixed gas plasmas. The experimental conditions chosen for this study were identical to those described earlier for the N<sub>2</sub>-Ar mixed gas plasmas. The analogous plots of radial emission maps for the 10% and 100% O<sub>2</sub> cooled plasmas are presented in Figures 86 and 87. Again, the radial emission maps for the argon discharge (Figure 81) should be referred to for comparison.

Several important trends can be seen on the radial



emission maps of the 10% and 100% O<sub>2</sub> cooled ICPs. First, the overall intensity of radial emission obtained from a 10% O<sub>2</sub> cooled ICP (Figure 86) is somewhat higher than that of the conventional discharge (Figure 81) operated under similar experimental conditions. Second, the radial emission is constricted to a smaller volume than the conventional argon discharge. Third, the emission distribution peaks at 10 mm above the load coil. These observations are again due to the fact that 10% O<sub>2</sub> cooled ICP has a smaller volume than the conventional discharge. The radial emission distributions of a 10% O<sub>2</sub> cooled plasma (Figure 86) are wider than those of the 10% N<sub>2</sub> cooled ICP (Figure 84).

In the case of 100% O<sub>2</sub> cooled ICP, the radial emission distributions (Figure 87) are similar to the trends indicated for the 100% N<sub>2</sub> cooled ICP (Figure 85), i.e. (a) the radial emission distributions peak at lower observation heights (around 2 to 5 mm above the load coil); (b) the intensity of the radial emission decreases when the conventional argon discharge is being converted into a 100% O<sub>2</sub> cooled ICP. It should be noted that the radial emission distributions for the mixed gas plasmas are identical in trends and patterns indicated for the electron distributions in the discharges (Figures 71 to 78).





#### 4. Correlation of Analyte Radial Emission with Electron Density Measured at 2, 10, and 20mm Above the Load Coil

The spatial distributions of electron density, and atom (CdI 228.8 nm) and ion (CdII 226.5 nm and 214.4 nm) radial emission measured at 2 mm above the load coil are presented in Figure 88. The plasma operating parameters chosen for this study were 2.0 Kw rf power and 1.0 L/min aerosol flow rate. As mentioned earlier in Chapters VII and VIII, the net electron density increases rapidly and then reaches its maximum at the radial distance of 3.5 mm away from the aerosol axis. After 4.0 mm from the center of the plasma aerosol channel, the net electron density drops drastically. A generally similar type of radial distribution was observed for the cadmium neutral atom and ion lines (Figure 88). However, the position of maximum radial intensity for electron density, and the cadmium emission (ion and neutral atom lines) is different. In particular, the radial emission intensity of the cadmium neutral atom line peaks at about 1 mm off-axis, whereas the ion line peaks at around 2 mm off the aerosol channel. It is interesting to note that the maximum radial emission intensities of the ion lines peak at the region which contains high concentration of electron (see Figure 88). In





addition, the spatial characteristic of the two cadmium ion lines (CdII 226.5 nm and 214.4 nm) at 2 mm above the load coil appears to be similar to each other. It should be noted that all these radial horizontal profiles presented in Figure 88 were measured at 2 mm above the load coil and operated under similar conditions. As mentioned before, in the case of an argon discharge, the emission intensity of the cadmium ion and atom species is considerably stronger at 10 to 20 mm above the load coil (see Figure 81). Therefore, before drawing any definitive conclusions about the emission characteristics of the plasma discharge it is important to study the radial emission profiles at different observation heights in order to see whether these spatial patterns, trends, and correlation of analyte emission with electron density have some generality.

Radial distribution of electron density, cadmium neutral atom and ion lines are provided in Figures 89 and 90. These radial distributions were measured at 10 mm (Figure 89) and 20 mm (Figure 90) above the load coil. These plots are analogous to those presented in Figure 88. Previous studies have indicated that with an increase in observation height the position of the off-axis electron density maximum moved towards the central aerosol channel (see Chapter VIII). The above trend was generally reflected in the radial emission profiles of the cadmium neutral atom



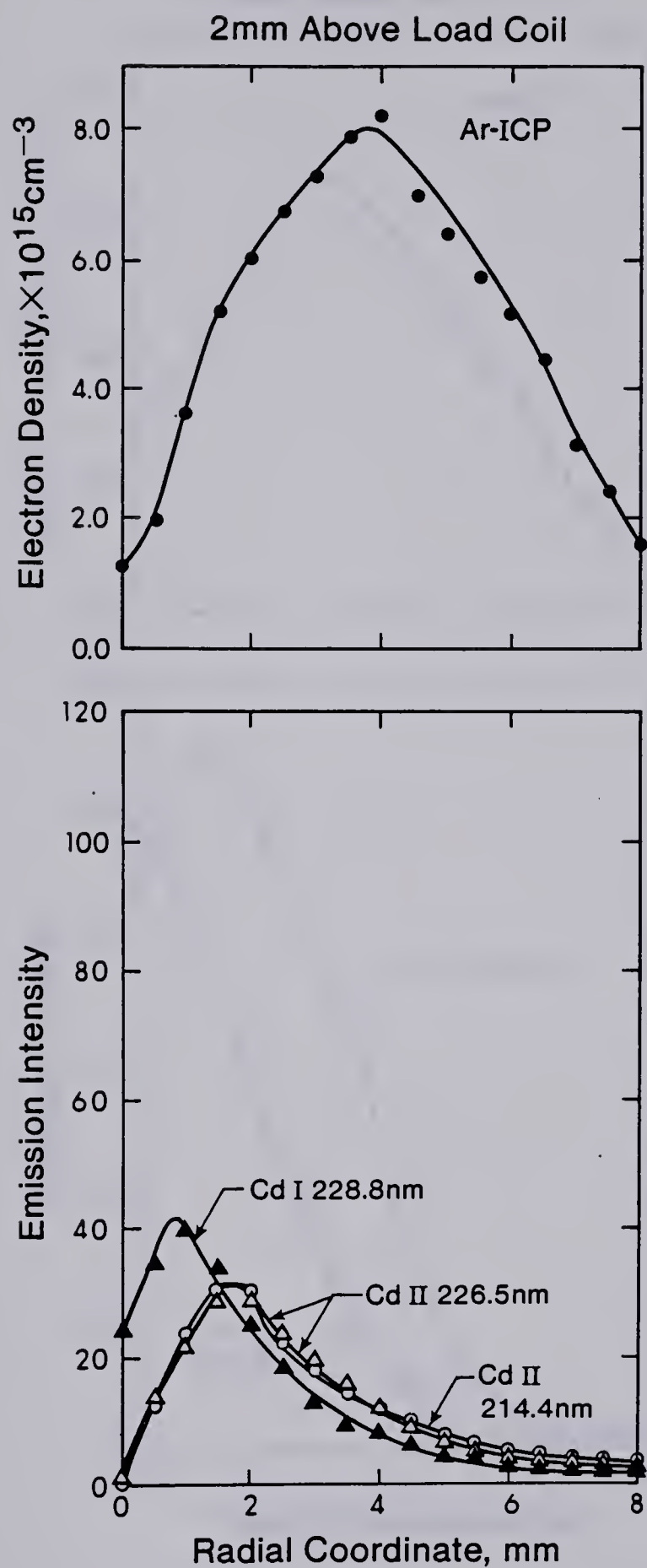


Fig. 88. Correlation of electron density with radial emission for CdI 228.8 nm, CdII 226.5 nm, and CdII 214.4 nm at 2 mm above the load coil.



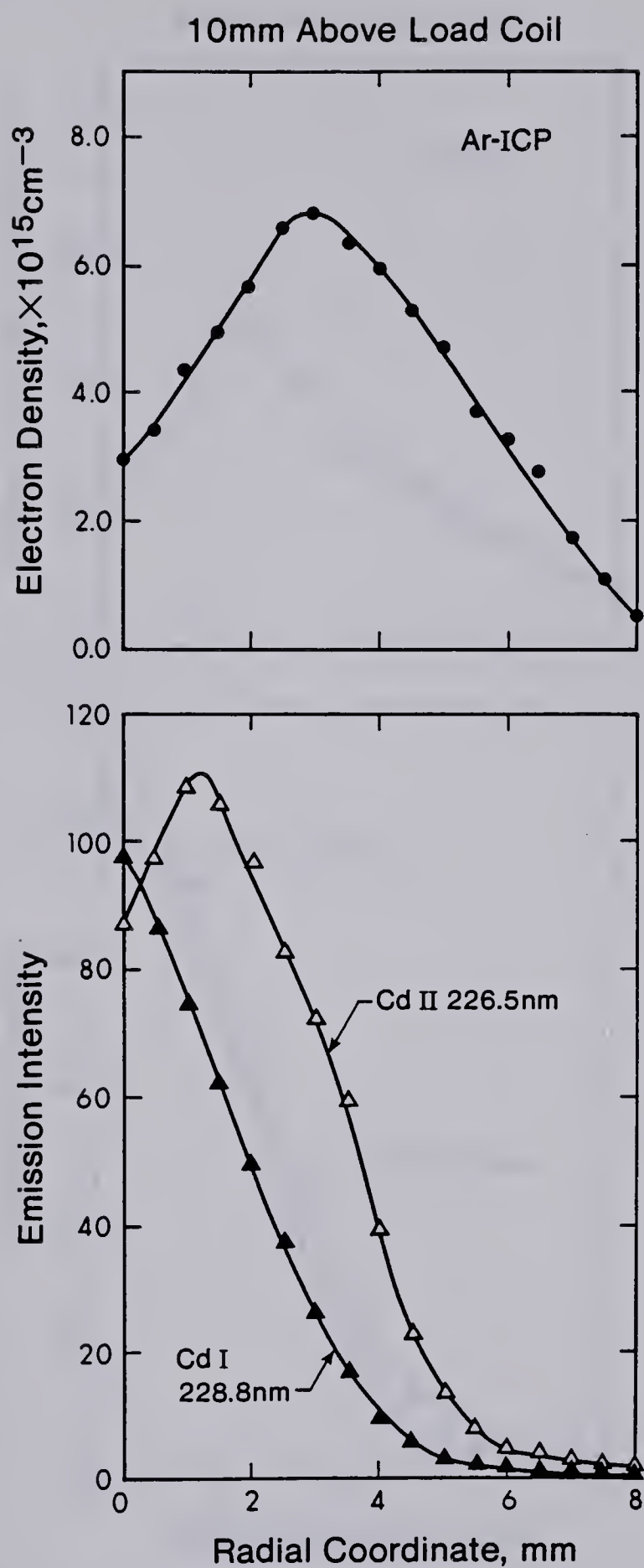


Fig. 89. Correlation of electron density with radial emission for CdI 228.8 nm, CdII 226.5 nm, at 10 mm above the load coil.



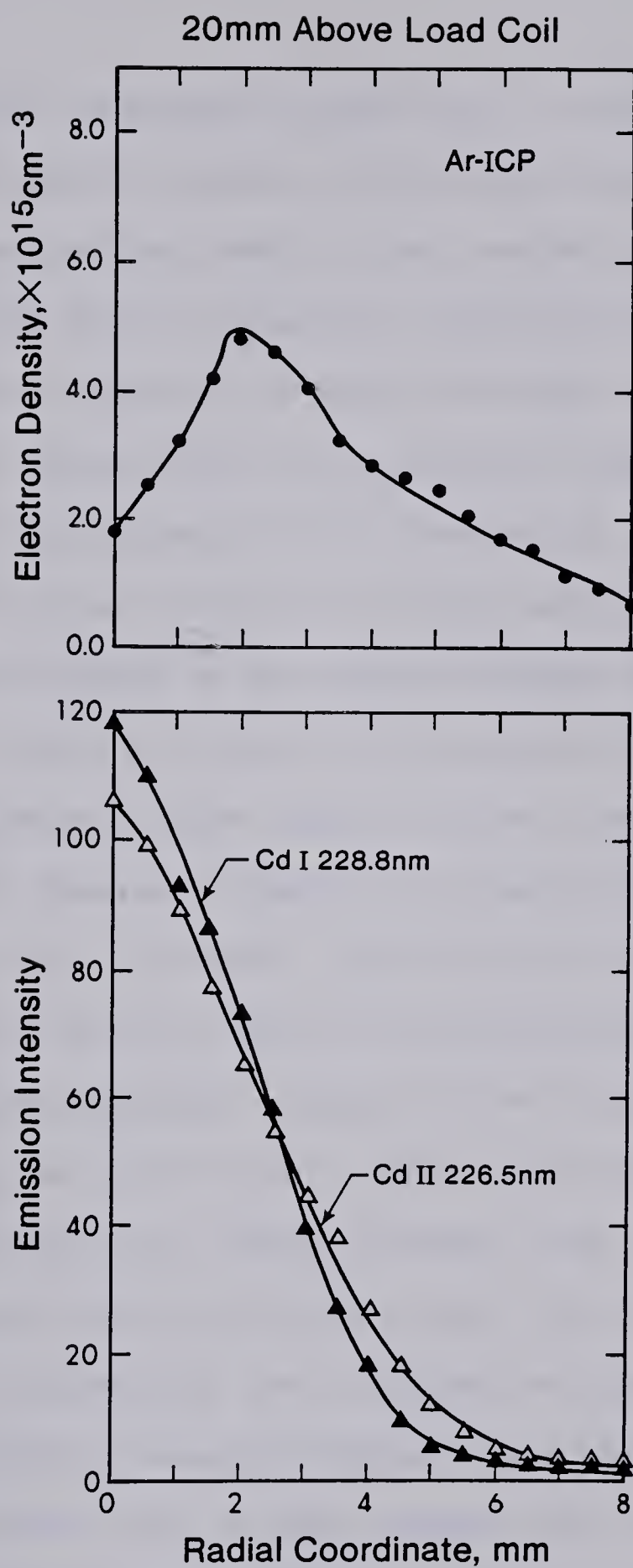


Fig. 90. Correlation of electron density with radial emission for CdI 228.8 nm and CdII 226.5 nm at 20 mm above the load coil.





and ion lines (Figures 89 and 90). It should be noted that at higher viewing heights, the radial emission profiles of the cadmium species peak in the central plasma axis. However, the electron density distributions at higher viewing zones exhibit slightly off-axis maxima. In addition, the overall magnitude of the electron density profiles decreases significantly with increasing observation height, which is in great contrast to the analyte emission signals which peaks higher in the upper viewing zone. Another interesting point to note in Figures 88 to 90 is that the radial emission of the neutral atom line in the middle of the aerosol channel appears to be more sensitive than that of the ion line. However, the off-axis radial emission intensity of the ion line is considerably more sensitive than its corresponding neutral atom line. It is also interesting to note that at all observation heights the cadmium ion emission peaks further into the main body of the plasma (high electron density zone) than the atom emission.

The effect of 10% nitrogen on the radial profiles and magnitude of electron density and cadmium emission are shown in Figure 91. In this figure, the two different profiles within each frame correspond to different types of plasma discharge; the dotted line corresponds to the conventional argon discharge, and the solid line corresponds to the 10% N<sub>2</sub> cooled plasma. In this experiment, the plasmas



were operated at 2.0 Kw and 1.0 L/min aerosol flow rate. These profiles were measured at 10 mm above the load coil.

Note that as the concentration of the nitrogen in the coolant flow is increased from 0% (dotted line) to 10% (solid line), the radial distributions of the cadmium ion emission (lower frame) and the electron density (upper frame) shift towards the central plasma axis. This result is consistent with the visual observation presented in Chapter III that as the amount of nitrogen in the coolant flow is increased, the plasma shrinks in size. Thus, we would expect that the maximum radial emission will occur somewhere nearer to the central aerosol channel. From Figure 91, it is clear that the radial emission of the ion line is more dependent on the electron density than is the neutral atom line. It is also evident that the 10%  $N_2$  cooled plasma increases the electron density along the radial axis. A similar result is also obtained for the cadmium ion and atom line emission along the radial axis.

Several important conclusions can be drawn based on the radial distributions of electron density and analyte species. First, the radial emission of the ion lines peaks closer to the region which contains high concentration of electron than its corresponding neutral atom line. This can be rationalized by considering that the coulombic attraction between the ion and electron is greater than that of the



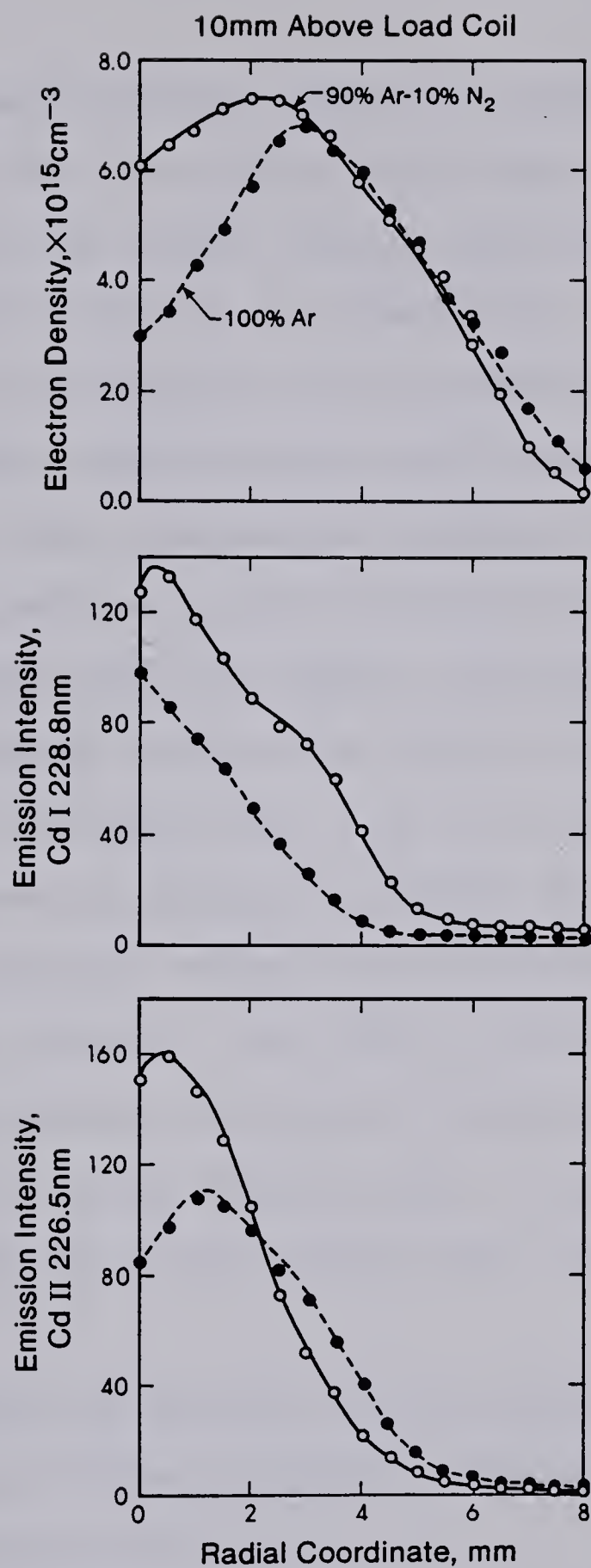


Fig. 91. Correlation of electron density with radial emission for CdI 228.8 nm and CdII 226.5 nm at 10 mm above the load coil. (dotted line = Ar-ICP, solid line = 10%  $\text{N}_2$  cooled ICP).





neutral atom and electron. Second, the radial emission distributions for the conventional argon and mixed gas ICPs closely follow the trends and patterns indicated for the electron distribution in the discharge, i.e., the density and emission distributions move towards the central axis with increasing distance away from the load coil. In addition, at lower observation heights, the electron density and emission profiles exhibit off-axis maxima. Third, the intensity of the electron density and analyte radial emission is pushed towards the central axis as the argon discharge is converted into a 10% N<sub>2</sub> cooled plasma. The result presented in Figure 91 clearly indicates that the density and emission maxima are undoubtedly related to the plasma volume. Finally, the 10% N<sub>2</sub> cooled plasma increases the electron density and analyte emission intensities which implies that a 10% N<sub>2</sub> cooled plasma is perhaps more energetic than the conventional argon discharge.

#### 5. Correlation of Analyte Radial Emission from Mixed Gas ICPs with Electron Density in the Aerosol Channel

As mentioned before, variations in ICP operating parameters, such as plasma power, aerosol flow rate and gas composition, have caused considerable changes in the



magnitude and spatial distributions of both the analyte emission and electron density. In addition, the most interesting point to note is that the distribution of analyte radial emission as a function of ICP operating parameters, closely follows the spatial distribution patterns observed for the electron density.

In most analytical analysis, the usual modes of acquiring analytical data from the ICP are at the center of the aerosol channel. Therefore the data presented here are only concerned with the study of correlation of analyte emission with electron density in this channel.

The radial emission and electron density distributions in the central aerosol channel as a function of various ICP operating parameters, such as plasma power, aerosol flow rate and gas composition, are shown in Figures 92 to 95. The radial emission signals from CdI (228.8 nm) and CdII (226.5 nm) were acquired simultaneously with a 1024 element photodiode array measurement system described in Chapter II. The coolant flow rate was constant at 15 L/min.

Typical spatial distributions of electron density, and atom and ion radial emission in the aerosol channel when the plasma power was varied from 2.0 to 1.50 Kw are shown in Figure 92. The two different profiles within each frame correspond to different plasma power levels. In Figure 92 curve a corresponds to a plasma power level of 2.0 Kw and



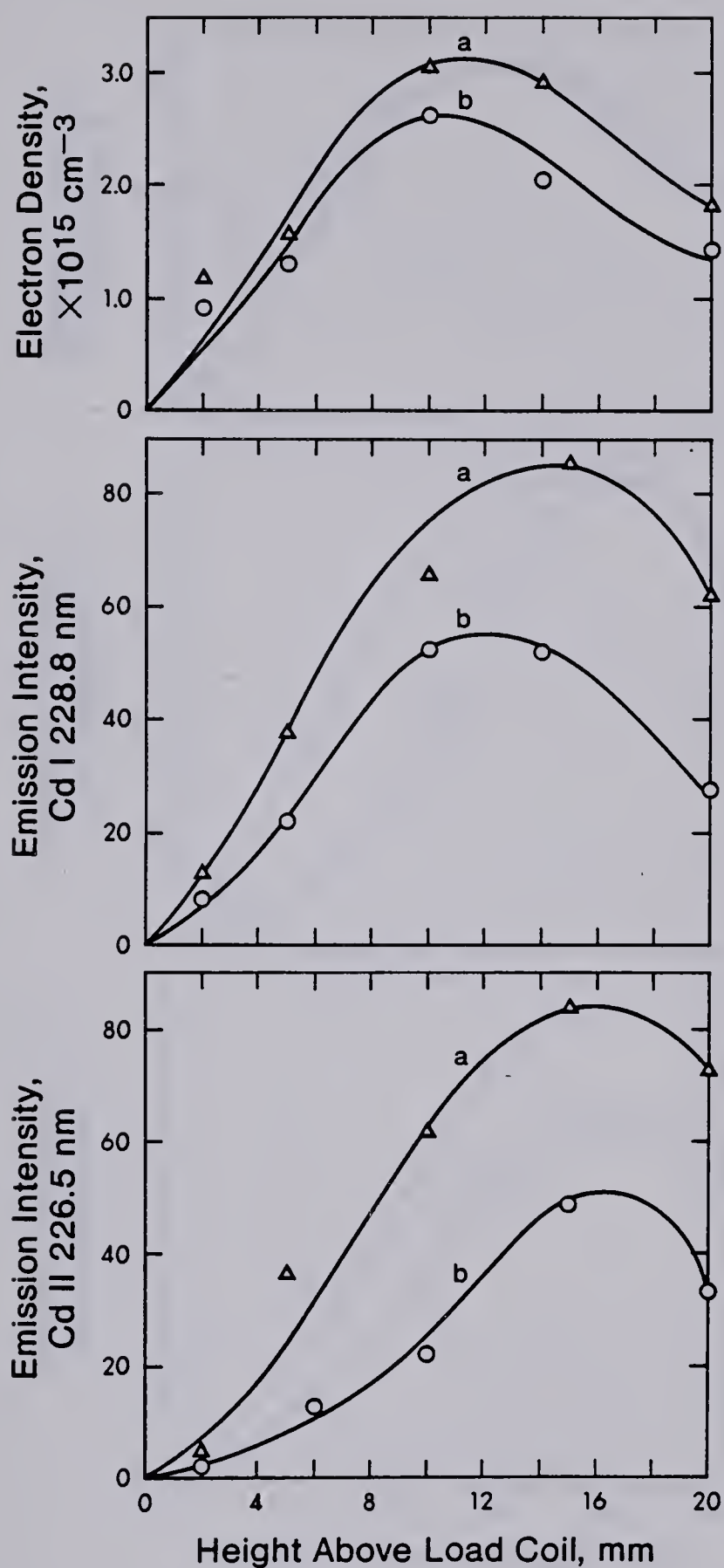


Fig. 92. Correlation of electron density with vertical spatial emission profiles for CdI 228.8 nm and CdII 226.5 nm as a function of plasma power, curve a, 2.0 Kw; curve b, 1.5 Kw.





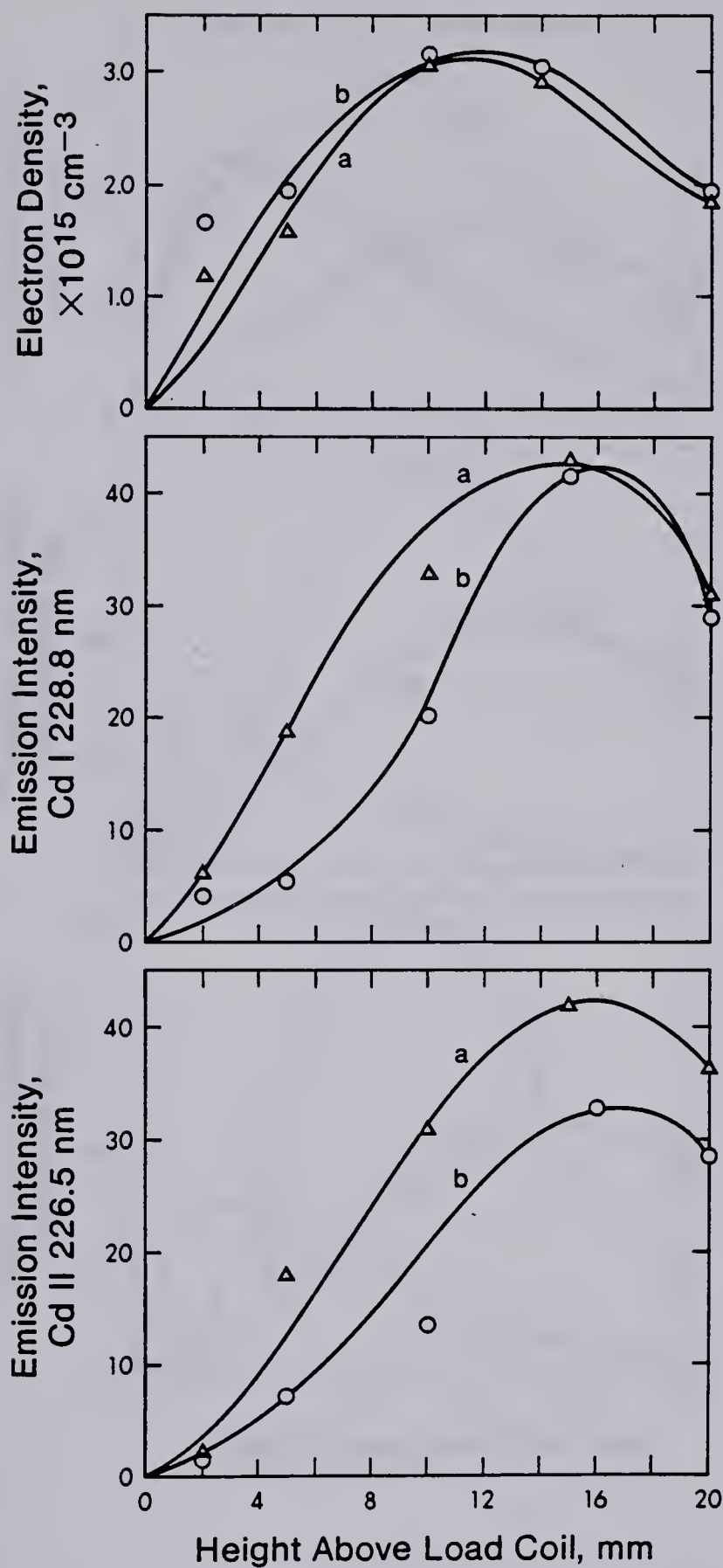


Fig. 93. Correlation of electron density with vertical spatial emission profiles for CdI 228.8 nm and CdII 226.5 nm as a function of aerosol flow rate; curve a, 1.0 L/min curve b, 1.5 L/min.



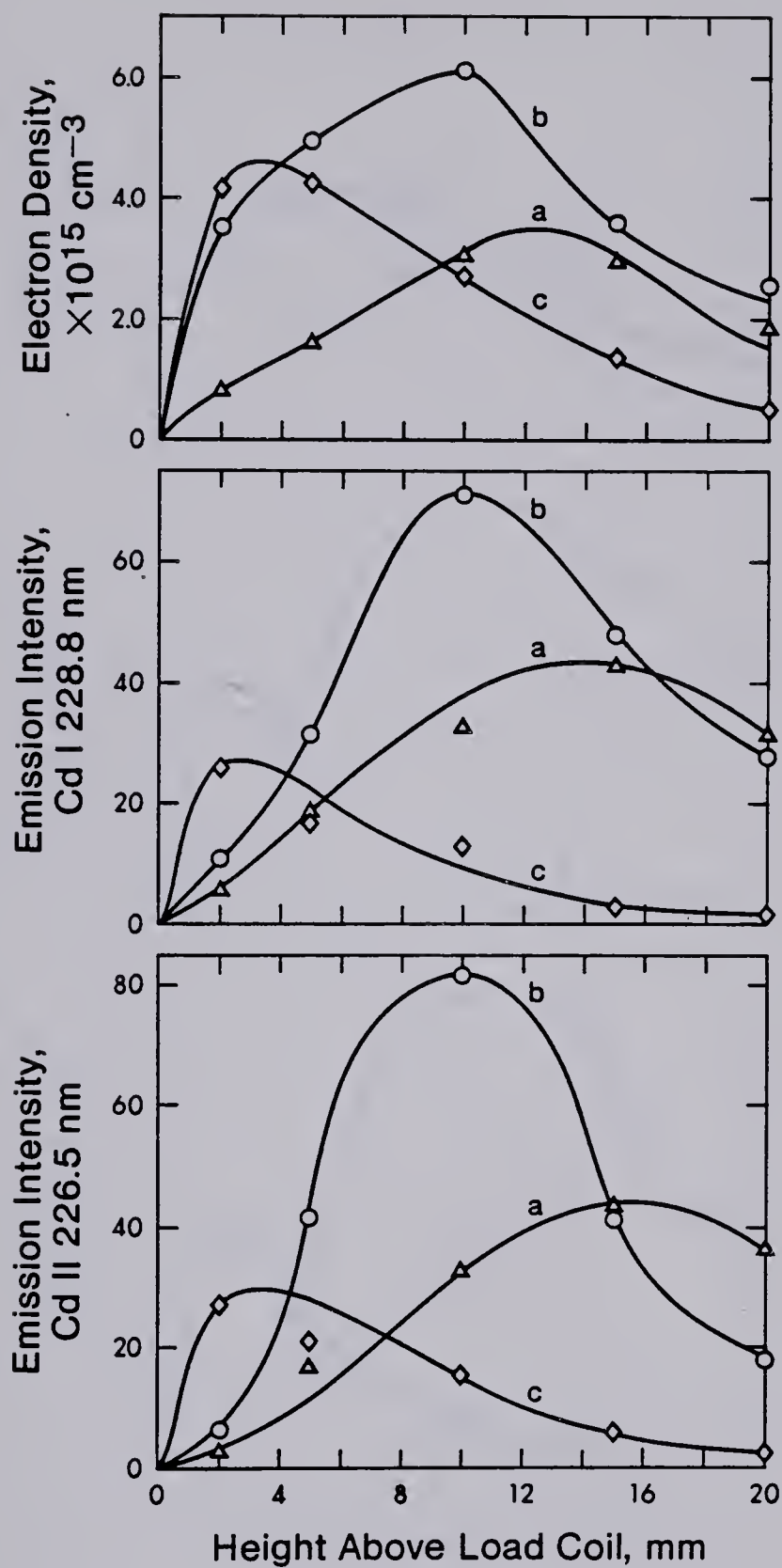


Fig. 94. Correlation of electron density with vertical spatial emission profiles for CdI 228.8 nm and CdII 226.5 nm as a function of gas composition, curve a, 100% Ar; curve b, 10%  $\text{N}_2$  - 90% Ar; curve c, 100%  $\text{N}_2$  cooled ICP.



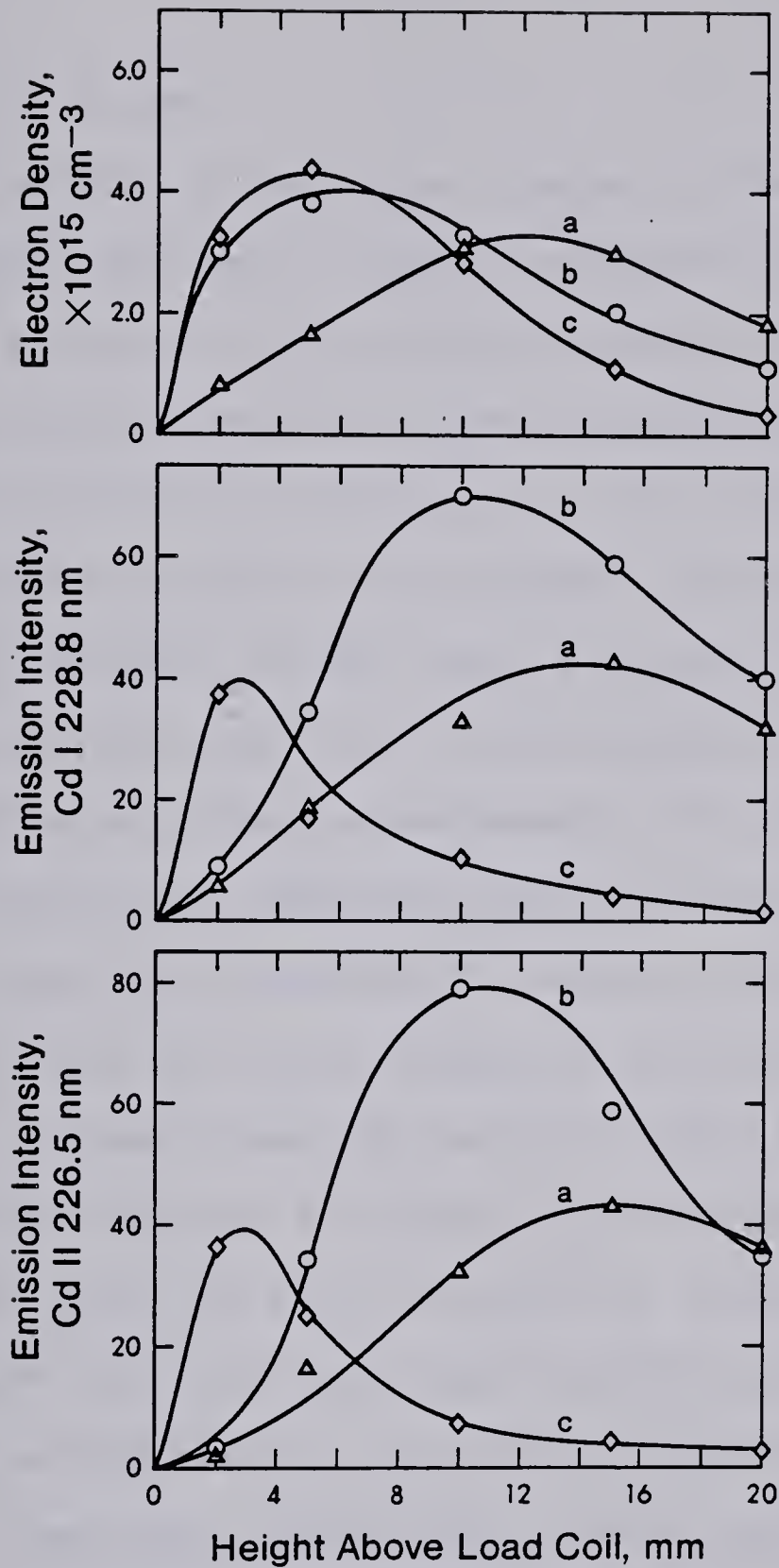


Fig. 95. Correlation of electron density with vertical spatial emission profiles for CdI 228.8 nm and CdII 226.5 nm as a function of gas composition, curve a, 100% Ar; curve b, 10% O<sub>2</sub>-90% Ar; curve c, 100% O<sub>2</sub> cooled ICP.





curve b to 1.50 Kw.

A number of important trends in the correlation of spatial distributions of radial emission with electron density are clearly illustrated in Figure 92. As power is decreased the magnitude of electron density decreases (Frame I) and the position of the peak in the electron density shifts slightly lower in the plasma. The same holds true for the radial emission of CdI line in Frame II except that the intensity of the atom line is more dependent on plasma power than is electron density. Decreasing the plasma power from 2.0 to 1.50 Kw also significantly decreases the ion radial emission intensity (Frame III). However, the spatial position of the ion radial emission profile is less dependent on power than the neutral atom line or electron density distribution. In Figure 92, perhaps, the most interesting point to note is that the radial emission intensity of the ion line clearly peaks higher in the plasma than that of the neutral atom line by about a few mm. Also, the radial emission intensities of both ion and neutral atom lines peak higher in the plasma than that of the electron density.

Several conclusions can be drawn on the distributions of radial emission and electron density along the aerosol channel. First, it seems reasonable to explain the decrease in radial emission as resulting from a decrease



in electron density in the plasma due to the fact that energetic electrons are responsible for the excitation and ionization of the analyte species. Second, the radial emission of the ion line peaks higher in the plasma as the plasma power is decreased because there is less energy available to heat the incoming aerosol gas. Third, a direct correlation of the radial emission and electron density appears to exist in the ICP.

Spatial profiles of radial emission and electron density are shown in Figure 93. With the different profiles within each frame corresponding to different aerosol flow rates; curve a corresponds to an aerosol flow rate of 1.0 L/min and curve b to 1.50 L/min. In this experiment, the plasma was operated at 2.0 Kw power and all gas flows were argon.

It is clear from figure 93 that the electron distributions in the aerosol channel are only slightly dependent on the variations in aerosol flow rate (Frame I). With an increase in aerosol flow rate (from curve a to curve b), electron density is slightly depressed at lower observation heights and enhanced slightly at higher observation heights. However, the spatial patterns of cadmium neutral atom (Frame II) and ion lines (Frame III) are critically dependent on the aerosol flow rate. An increase in aerosol flow rate will have the following



effects on the cadmium neutral atom and ion lines. First, cadmium neutral atom radial emission (Frame II) is depressed at lower observation heights (0 to 14 mm above the load coil). On the other hand the emission is enhanced at higher observation heights. This sequence roughly correlates with the spatial characteristics of electron density. The drastic suppression of atom emission observed at lower observation heights can be interpreted as a higher influx of cooler aerosol gas with an increase in aerosol flow rate. Whereas at higher observation heights, intensity of radial emission is increased because of interactions of neutral atom species with higher concentration of energetic electrons. Second, the radial intensity of the ion line (Frame III) is depressed at all observation heights when the aerosol flow rate is increased from 1.0 L/min to 1.50 L/min. The overall magnitude of the ion emission decreases due to the fact that an increase in aerosol flow rate results in a reduction of time that a sample spends in the plasma. Since the excited energy for the ion lines is greater than its corresponding neutral atom line (Table IX.1), a reduction of time that a sample spends in the plasma in order to reach its excited state will be greatly felt by the ion species than the neutral atom species. Hence, emission suppression is observed only for the ion line but not for the neutral atom line. Third, the radial emission peaks higher in the plasma





TABLE IX.1  
WAVELENGTH, EXCITATION POTENTIALS AND SUM OF EXCITATION  
POTENTIALS AND IONIZATION POTENTIALS FOR CD

Element (wavelength)	EP (eV)	EP + IP (eV)
CdI 228.8 nm	5.41	/
CdII 226.5 nm	5.47	14.46
CdII 214.4 nm	5.78	14.77



when the carrier gas flow is changed from 1.0 L/min to 1.50 L/min. Fourth, the radial emission intensities of both neutral atom and ion lines peak higher in the plasma than that of the electron density.

As mentioned in previous chapters, introduction of foreign gases into the coolant flow of an argon discharge has marked effects on both the intensity and spatial distribution of the electron density in the plasma. The results discussed in the preceding chapters indicate that: (a) the electron density distributions exhibited higher magnitude when 10%  $N_2$  (or  $O_2$ ) - 90% Ar replaced pure Ar as the outer coolant flow; (b) the introduction of 100% nitrogen or oxygen in the outer flow caused a reduction in the magnitude of electron density; and (c) the electron density distributions of the mixed gas plasmas peak at lower heights when compared to the conventional argon discharge.

The above trends are generally reflected in the effects of foreign gases on the spatial distributions of radial emission and electron concentration along the aerosol channel. The spatial profiles of radial emission and electron density in the presence of nitrogen are shown in Figure 94. In this figure, the three different profiles within each frame correspond to different concentrations of nitrogen in the coolant flow; curve a corresponds to 0%, curve b to 10% and curve c to 100%  $N_2$  cooled ICP's. In this



experiment, the plasma was operated at 2.0 Kw power and the aerosol flow rate of 1.0 L/min.

Note that as the concentration of nitrogen in the coolant flow is increased from 0% (curve a) to 10% (curve b) and finally to 100% (curve c) the emission spatial patterns of the neutral atom (Frame II) and ion (frame III) shift towards the load coil. A similar result is obtained for the electron spatial distribution along the aerosol channel. This result is consistent with the visual observation presented in Chapter III that as the amount of nitrogen in the coolant flow is increased the plasma shrinks in size. Thus, we would expect that the maximum emission will occur somewhere nearer to the induction coil. From Figure 94, it is clear that the intensity of the radial emission for the neutral atom and ion lines increase drastically when 10% nitrogen is present in the coolant flow. Similarly, the electron density in the aerosol channel behaves almost identically to the radial emission of the cadmium lines, although for equivalent power and flow rate the electron profile is broader than the emission profiles. Thus we see some trends towards correlation of emission intensity with the electron density. This correlation is further substantiated by the following observation. For equivalent ICP operating parameters, the ion emission is more strongly affected by the addition of nitrogen into the coolant flow





than the neutral atom line. Since electron density is also increased when the argon discharge is converted into a 10%  $N_2$  cooled ICP, the observed high sensitivity of ion line in the mixed gas plasmas may be explained by the large effective cross-sections of charged particles for elastic collisions with electrons. Owing to coulombic interactions, effective cross-sections for ions and electron encounters are large (91), therefore there is a great likelihood that the frequency of ion-electron collisions in the plasma is higher than that of the atom-electron collisions.

The above trends are generally reflected in the study of correlation of analyte emission with electron in  $O_2$ -Ar mixed gas ICP. The spatial profiles of radial emission and electron density in the presence of oxygen are shown in Figure 95. The three different profiles within each frame corresponds to different concentrations of oxygen in the coolant flow; curve a corresponds to 0%, curve b to 10% and curve c to 100%  $O_2$  cooled ICP. The only notable difference between these two studies (Figures 94 and 95) is that the electron density of the 10%  $O_2$  cooled ICP does not increase as much as that of the 10%  $N_2$  cooled ICP. Again, the sequence of the spatial and intensity patterns of radial emission correlates well with those of the electron density.



## D. Conclusions

By considering the information presented in this chapter, it can be seen that changes in any of the ICP operating parameters, such as plasma power, aerosol flow rate and coolant gas composition, will alter the spatial characteristics of the radial emission and electron density. Also, most characteristics of the radial emission data are quite similar to those of the lateral profiles measured by Edmonds and Horlick (106). Changes in any of these operating parameters will undoubtedly influence the conductivity of the plasma and thus the magnitude of the magnetic flux density. In turn, the magnetic flux density determines the magnitude of the plasma gas temperature and electron density. Because electron density changes from point to point in the plasma discharge especially in the aerosol channel (Figures 90 to 93), a study of spatially resolved profiles of both the analyte emission and electron density is absolutely necessary in order to gain an insight into the fundamental processes that control the excitation and ionization mechanisms.

Emission of the analyte lines is made possible by introducing the analyte aerosol gas into the middle channel of the hot plasma discharge, but transporting cool aerosol gas along this channel will undoubtedly decrease the plasma





"temperature". The distribution of the electrons will also be disturbed in the presence of cool aerosol gas. Spatial data presented in this work demonstrates that lower in the plasma the electron density maximum is pushed away from the central axis due to the presence of the aerosol gas. At this position, atom and ion emission also peak off-axis which is a good indication that the excitation of neutral atom and ion species is related to contact with energetic electrons. This mechanism is further substantiated by the diffusion of ions into the high electron density zone due to coulombic attraction which produces significantly broader ion profiles. In addition, the electron density distribution in the center aerosol channel as a function of observation height exhibits a "hump" shape characteristic, which has a striking resemblance to the "hump" shapes of the analytical vertical profiles mentioned earlier. In the case of a conventional argon discharge, the position of the measured electron density maximum is found to be in close proximity with those of the analyte emission profiles which peak around 10 to 15 mm above the induction coil. These observations have undoubtedly demonstrated that the analyte emission intensity and electron density have similar spatial patterns in the ICP.

In general, the addition of 10% foreign gases ( $N_2$  or  $O_2$ ) into the coolant flow of an Ar-ICP enhances the overall





magnitude of analyte emission and electron density in the discharge. This observation leads one to conclude that a 10% mixed gas ICP is a more energetic source than the conventional argon discharge. The characteristics of electron density in the mixed gas plasmas also correlate well with those of the analyte emission intensities, i.e. (a) both distributions shift in the direction of the load coil as the percentage of foreign gases introduced into the coolant increases from 0% to 100%; (b) both profiles are constricted to a smaller volume in the presence of foreign gases; and (c) under similar operating conditions the distribution of electron density and analyte emission peak lower in the plasma than those of the argon discharge. The results presented here clearly indicate that mixed gas ICPs have added a new dimension in unveiling the excitation and ionization processes in the discharge.

A detailed picture of the spatial radial emission structure of the inductively coupled plasma is now emerging. The spatial characteristics of the neutral atom and ion line radial emission can be strongly correlated with those of the electron density. These spatial characteristics lead one to believe that excitation and ionization of the analyte species are the results of collision with energetic electrons. However, the results presented in this work are based on only one element, Cd. Clearly, more data are



required to confirm such correlation but the present data do indicate that the correlation is there.

The overpopulation of very high energy levels (ion line advantage) in the plasma discharge is believed to be due to the direct excitation either by energetic electrons or by metastable argon atoms. The experimental data presented here indicate a tremendous amount of electrons in the inductively coupled plasma. From these measurements, the tendency of metastable atoms towards collisional decay in a high temperature atmospheric plasma, such as ICP, is extremely high. Therefore, the tendency of analyte ionization via Penning ionization with excited argon metastables is not as important in an atmospheric plasma discharge as it would be in a less energetic or low pressure discharge. The emission profile from the ion line is somewhat broader when compared to emission from the neutral atom line. This is probably due to the fact that the coulombic attraction between ions and electrons is stronger than that of the atoms and electrons. Therefore, the population of ion excited states is increased because of a higher collision rate between ion species and energetic electrons.

In conclusion, the physical concept upon which the ionization and excitation mechanisms are based is that the energetic electrons transfer their energies to the



neighboring particles through collisions. This collisional process occurs with great probability and efficiency because there is a tremendous amount of low mass and high mobility electrons in the plasma source, in the order of  $10^{15} \text{ cm}^{-3}$ . The observations of the spatial data seem to be in favor of excitation and ionization by energetic electrons, but extension of research to other elements is necessary before this claim can be justified.





## CHAPTER X

### SUMMARY

The experimental data presented so far support the utilization of mixed gas ICPs as an alternative discharge for the ICP-AES. The results presented in this work clearly indicate that under optimal operating conditions, mixed gas ICPs are comparable or superior to the conventional argon discharge in terms of stability, sensitivity, and freedom from interference effects.

From the experimental results obtained, it is quite clear that profiling the emission with a photodiode array system provides a unique and detailed picture of analyte emission characteristics in mixed gas ICPs. The present investigation has unambiguously demonstrated an overall spatial dependence of analyte emission on the amount of foreign gas in the coolant flow of an argon discharge. The best viewing zones for mixed gas ICPs are somewhat lower than that of the conventional argon plasma. These observations imply that the viewing height has to be lowered in order to fully appreciate the analytical capabilities of mixed gas ICPs. The dependence of analyte emission intensity on the nature of the mixed gas ICP has been verified by the spectral evaluation of the discharge. It is also apparent



that the emission signals and signal-to-noise ratios are strongly dependent on both the concentration of the foreign gas in the coolant flow and the observation height. In particular, both the emission intensity and signal-to-noise ratio increase significantly when the conventional argon discharge is converted into a 10 % mixed gas plasma. The signal-to-noise ratio is slightly deteriorated for a 100 % mixed gas ICP. However, this disadvantage in signal-to-noise ratio is often offset by the advantage of cheaper operating cost and lower background intensity. In certain regions, the mixed gas plasma suffers from molecular bandhead interferences, but these spectral interferences can be avoided by switching to a different set of mixed gas ICPs.

Spatial and spectral studies indicate that mixed gas ICPs affect the emission intensity of the ion line more than its corresponding neutral atom line. The origin of this observation appears to be in the excitation and ionization processes of the discharge. Correlation studies between analyte emission intensities and electron density indicate that the high sensitivity of the ion line in mixed gas ICPs may be explained by the effective cross-sections of charged particles for elastic collisions with energetic electrons. Owing to Coulombic interactions, effective cross-sections for ions and electron encounters are large, therefore the frequency of ion-electron collisions is higher than that of



atom-electron collisions. In addition, the correlation data clearly indicate that the spatial distributions of the electron density and analyte signal behave in a similar pattern towards changes in any of the ICP operating parameters, such as plasma power, aerosol flow rate and gas composition. Spatial data also indicate that the electron density distribution in the central aerosol axis as a function of the observation height exhibits a striking resemblance to the "hump" shape characteristics of analyte spatial emission profiles. These spatial and correlation studies have undoubtedly demonstrated that the excitation and ionization of analyte species in mixed gas plasmas are the results of collision with energetic electrons.

In most temperature measurements, LTE is assumed to exist in the plasma source, hence the ionization temperature measurement using two line method is characterized by the magnitude of electron density in the plasma source. These studies have indicated that distributions of analyte atom and ion species are extremely sensitive to changes in electron density, therefore care should be exercised in reporting results concerning temperature calculations.

There are several areas which could be helpful in unveiling the excitation and ionization mechanisms in the plasma source. One set of study which should be undertaken is the study of distribution of electron energy in the





plasma source. By correlating the analyte emission intensity with electron energy, a detailed picture of spatial distributions for these two variables could be obtained in order to account for the excitation and ionization processes in the plasma discharge. This study should be combined with the measurement of kinetic temperatures or energies of ions and atoms in the discharge, which can be measured by thermal Doppler broadening of suitable lines. Separate measurements of various kinetic temperatures can therefore be helpful in understanding the efficiency for the energy transfer in collisions between analytes of different species, and also between analyte and electron.



## BIBLIOGRAPHY

1. S. Greenfield, J.L. Jones, and C.T. Berry,  
Analyst, 89, 713 (1964).
2. R.H. Wendt and V.A. Fassel,  
Anal. Chem., 37, 920 (1965).
3. V.A. Fassel and R.N. Kniseley,  
Anal. Chem., 46, 1155A (1974).
4. V.A. Fassel and R.N. Kniseley,  
Anal. Chem., 46, 1110A (1974).
5. W. Crookes,  
Phil. Mag., 7, 57 (1879).
6. I. Langmuir,  
Phys. Rev., 33, 954 (1929).
7. Lev A. Arzimovich, "Elementary Plasma Physics",  
Blaisdell Pub. Co., 1965
8. M.Venugopalan, "Reactions under Plasma Condition",  
John Wiley and Son Inc., 1971.
9. Martin A. Uman, "Introduction to Plasma Physics",  
McGraw Hill, Inc., N.Y., 1964.
10. E.J. Hellund, "The Plasma State",  
Reinhold Publishing Corp., N.Y., 1961.
11. D.J. Rose and M. Clark, Jr.,  
"Plasmas and Controlled Fusion", The MIT Press,  
Cambridge, Mass., 1961.
12. R.F. Post,



- Rev. Mod. Phys., 28, 338 (1956).
13. G.I. Babat,  
J. Inst. Elec. Engrs. (London), 94, 27 (1947).
  14. R.K. Skogerboe, I.T. Urasa, and G.N. Coleman,  
Appl. Spectrosc. 30, 500 (1976).
  15. C.D. Kiers and T.J. Vickers,  
Appl. Spectrosc., 31, 273 (1977).
  16. R.K. Skogerboe and I.T. Urasa,  
Appl. Spectrosc., 32, 527 (1978).
  17. G.W. Johnson, H.E. Taylor, and R.K. Skogerboe,  
Spectrochim. Acta, 34B, 197 (1979).
  18. G.N. Coleman, W.P. Braun, and A.M. Allen,  
Appl. Spectrosc., 34, 24 (1980).
  19. R.J. Decker,  
Spectrochim. Acta, 35B, 19 (1980).
  20. C.I.M. Beenakker,  
Spectrochim. Acta, 31B, 483 (1975).
  21. C.I.M. Beenakker and P.W.J.M. Boumans,  
Spectrochim. Acta, 33B, 53 (1978).
  22. C.I.M. Beenakker, B. Bosman, and P.W.J.M. Boumans,  
Spectrochim. Acta, 33B, 373 (1978).
  23. A. Bollo-Kamara and E.G. Coddington,  
Spectrochim. Acta, 36B, 973 (1981).
  24. A. Aziz, J.A.C. Broekaert, and F. Leis,  
Spectrochim. Acta, 37B, 381 (1982).





25. S. Greenfield, H. McD. McGreachin, and P.B. Smith,  
Talanta, 22, 1 (1975).
26. S. Greenfield, H. McD. McGreachin, and P.B. Smith,  
Talanta, 22, 553 (1975).
27. S. Greenfield, H. McD. McGreachin, and P.B. Smith,  
Talanta, 23, 1 (1976).
28. R.M. Barnes,  
C.R.C. Crit. Rev. Anal. Chem.,  
Sept., 1978.
29. R.L. Dahlquist and J.W. Knoll,  
Appl. Spectrosc., 32, 1 (1978).
30. P.W.J.M. Boumans,  
Fresenius Z. Anal. Chem., 299, 337 (1979).
31. G.I. Babat,  
Vestnik Elektropromyshlennosti, No 2,3,1 (1942).
32. T.F. Reed,  
J. Appl. Phys., 32, 821 (1961).
33. T.B. Reed,  
J. Appl. Phys., 32, 2534 (1961).
34. J. Reboux,  
Ingenieurs et Techniciens, 157, 115 (1962).
35. J. Reboux,  
Ingenieurs et Techniciens, 166, 107 (1963).
36. R. Woodriff,  
Appl. Spectrosc., 22, 207 (1968).



37. G.W. Dickinson and V.A. Fassel,  
Anal. Chem., 41, 1021 (1969).
38. G.H. Morrison,  
ICP Inform. Newslett., 3, 165 (1977).
39. R. Nakashima, S. Sasaki, and S. Shibata,  
Anal. Chim. Acta, 77, 65 (1975).
40. R.D. Iron, E.A. Schenk, and R.D. Giaque,  
Clin. Chem., 22, 2018 (1976).
41. A.Aziz, J.A.C. Broekraert, and F. Leis,  
Spectrochim. Acta, 36B, 251 (1981).
42. C.C. Butler, R.N. Kniseley, and V.A. Fassel,  
Anal. Chem., 47, 325 (1975).
43. J.A.C. Broekaert, F. Leis, and K. Laqua,  
Spectrochim. Acta, 34B, 73 (1979).
44. V.A. Fassel, C.A. Peterson, F.W. Abercrombie,  
and R.N. Kniseley, Anal. Chem., 48, 516 (1976).
45. D.L. Windsor and M.B. Denton,  
Appl. Spectrosc., 32, 366 (1978).
46. Kazuko Matsumoto and Keiichiro Fuwa,  
Bunsei Kagaku, 30(3), 188 (1981).
47. B. Phalavanpour, M. Thompson, and L. Thorne,  
Analyst, 106, 467 (1981).
48. S.M. Workman and P.N. Soltanpour  
Soil Sci. Soc. Am. J., 44, 1331 (1980),
49. J.W. Carr and Gary Horlick,



- Spectrochim. Acta, 37B, 1 (1982).
50. A.M. Gunn, D.L. Millard, and G.F. Kirkbright,  
Anal. Chem., 103, 1006 (1978).
  51. G.F. Kirkbright and R.D. Snoak,  
Anal. Chem., 51, 1938 (1979).
  52. D.L. Millard, H.C. Shan, and G.F. Kirkbright,  
Analys, 105, 502 (1980).
  53. D.R. Hull and G. Horlick,  
Pittsburgh Conference, Atlantic City, New Jersey,  
Paper #243, 1980.
  54. ED. Salin and G. Horlick,  
Anal. Chem., 51, 2284 (1979).
  55. R.H. Scott  
Spectrochim. Acta, 33B, 123 (1978):
  56. R. Savage and G. Hieftje,  
Anal. Chem., 51, 408 (1979).
  57. G.R. Kornblum, W. Van der Waa, and L. de Galan,  
Anal.Chem., 51, 2378 (1979).
  58. P.A.M. Ripson and L. de Galan,  
Spectrochim. Acta, 36B, 71 (1981).
  59. L. Ebdon, D.J. Mowthorpe, and M.R. Cave,  
Anal. Chim. Acta, 115, 171 (1980).
  60. S.P. Terblanche, K. Visser, and P.B. Zeeman,  
Spectrochim. Acta, 36B, 293 (1981).
  61. R.M. Barnes and G.A. Meyer,





- Anal. Chem., 46, 75 (1980).
62. R.M. Barnes and S. Nikdel,  
Appl. Spectrosc., 30, 310 (1976).
63. B. Meddings, H. Kaiser, and H. Anderson,  
International Winter Conf. San Juan, Puerto Rico,  
(1980).
64. S. Greenfield,  
Proc. Soc. Anal. Chem., 2, 111 (1965).
65. S. Greenfield, P.B. Smith, A.E. Breeze, and N.M.D.  
Chilton, Anal. Chim. Acta, 41, 385 (1968).
66. S. Greenfield and P.B. Smith,  
Anal. Chim. Acta, 57, 209 (1971).
67. R.M. Dagnall, D.J. Smith, T.S. West, and S. Greenfield,  
Anal. Chim. Acta, 54, 397 (1971).
68. S. Greenfield, I.L. Jones, H.M. McGeachin, and P.B.  
Smith, Anal. Chim. Acta, 74, 225 (1975).
69. S. Greenfield,  
Proc. Anal. Div. Chem. Soc., 13(8), 223 (1976).
70. S. Greenfield and H.M. McGreachin,  
Anal. Chim. Acta., 100, 101 (1978).
71. S. Greenfield and D.T. Burns,  
Anal. Chim. Acta, 113, 205 (1980).
72. Charly D. Allemand and Ramon M. Barnes  
Spectrochim. Acta, 33B, 513 (1978).
73. L. Ebdon, M.R. Cave, and D.J. Mowthorpe,



- Anal. Chim. Acta, 115, 179 (1980).
74. A. Montaser and J. Mortazavi,  
Anal. Chem., 52, 225 (1980).
75. J. Zalewski,  
Dissertation, Dept. of Chemistry,  
Iowa State University, Ames, 1978.
76. A. Montaser, V.A. Fassel, and J. Zalewski,  
Appl. Spectrosc., 35, 292 (1981).
77. K. Ohls and D. Sommer,  
Fresenius Z. Anal. Chem., 295, 337 (1979).
78. K. Ohls and D. Sommer,  
ICP Inform. Newlett., 4, 532 (1979).
79. P.W.J.M. Boumans and F.J. de Boer,  
Spectrochim. Acta, 32B, 365 (1977).
80. D. Truitt and J.W. Robinson,  
Anal. Chim. Acta, 49, 401 (1970).
81. D. Truitt and J.W. Robinson  
Anal. Chim. Acta, 50, 61 (1970).
82. E.H. Choot and G. Horlick,  
63rd Canadian Chemical Conference, Ottawa,  
Ontario, Paper #AN12, 1980.
83. E.H. Choot and G. Horlick,  
Pittsburgh Conference, Atlantic City, New Jersey,  
Paper #124 (1981).
84. M.P. Lau,



- Dissertation, Dept. of Chem., University of Alberta,  
Edmonton, Alberta, 1981.
85. R.C.L. Ng,  
Dissertation, Dept. Of Chem., University of Alberta,  
Edmonton, Alberta, 1982.
86. J.F. Alder, R.M. Bombelka, and G.F.Kirkbright,  
Spectrochim. Acta, 35B, 163 (1980).
87. A. Batal and J.M. Mermet  
Can. J. of Spectrosc., 27, 37 (1982).
88. G.R. Kornblum and L. De Galan,  
Spectrochim. Acta, 32B, 71 (1977).
89. J.F. Alder and J.M. Mermet,  
Spectrochim. Acta, 28B, 421 (1973).
90. P.W.J.M. Boumans and F.J. de Boer,  
Spectrochim. Acta, 31B, 355 (1976).
91. P.W.J.M. Boumans,  
" Theory of Spectrochemical Excitation",  
Plenum Press, New York, 1966.
92. H.R. Griem, "Plasma Spectroscopy",  
McGraw Hill, New York, 1964.
93. J.M. Mermet,  
Spectrochim. Acta, 30B, 383 (1975).
94. D.J. Kalnicky, V.A. Fassel, and R.N. Kniseley,  
Appl. Spectrosc., 31, 137 (1977).
95. J. Jarosz, J.M. Mermet, and J.P. Robin,





- Spectrochim. Acta, 35B, 163 (1980).
96. J.F. Alder, R.M. Bombelka, and G.F. Kirkbright,  
Spectrochim. Acta, 35B, 163 (1980).
97. J. Jarosz and J.M. Mermet,  
J.Q.S.R.T., 17, 237 (1977).
98. G.R. Kornblum and L. De Galan,  
Spectrochim. Acta, 29B, 249 (1974).
99. P.W.J.M. Boumans, H.C. Wagenaar, and F.J. De Boer,  
17th Coll. Spectrosc. Int., Florence, pg. 114 (1973).
100. H.U. Eckert, F.L. Kelly, and H.N. Olsen,  
J. Appl. Phys., 39, 1846 (1968).
101. J.M. Mermet,  
C.R. Acad. Sci. Ser. B, 281, 273 (1975).
102. J.L. Delcrois, C.M. Ferreira, and A. Ricard,  
"Principles of Laser Plasmas",  
J. Wiley, New York, 1976.
103. W.H. Gunter, K. Visser, and P.B. Zeeman,  
Spectrochim. Acta, 37B, 571 (1982).
104. Gary Horlick,  
Appl. Spectrosc., 30, 113 (1976).
105. M. Franklin, H. Amenson, and S.R. Koirtyohann,  
Spectrochim. Acta, 31B, 489 (1976).
106. T. Edmonds and G. Horlick,  
Appl. Spectrosc., 31, 536 (1977).
107. G. Horlick and M. Blades,



- Appl. Spectrosc., 34, 229 (1980).
108. H. Kawaguchi, T. Ito, K. Ota, and A. Mizuike,  
Spectrochim. Acta, 35B, 199 (1980).
109. R.H. Scott, V.A. Fassel, R.. Kniseley, and D.E. Nixon,  
Anal. Chem., 46, 75 (1974).
110. D.M. Coleman and J.P. Walters,  
Spectrochim. Acta, 33B, 127 (1978).
111. J.P. Walters,  
"Comtemporary Topics in Analytical and Clinical  
Chemistry", pg. 91 Plenum Press, N.Y. (1978).
112. G. Horlick and E. G. Coddling,  
Appl. Spectrosc., 29, 167 (1975).
113. E.G. Coddling and G. Horlick,  
Spectrosc. Lett., 7(1), 33 (1974).
114. G. Horlick, E.G. Coddling, and S.T. Leung,  
Appl. Spectrosc., 29, 48 (1975).
115. G. Horlick,  
Anal. Chem., 47, 352 (1975).
116. E.G. Coddling and G. Horlick,  
Appl. Spectrosc., 27, 366 (1973).
117. G. Horlick and E.G. Coddling,  
Anal. Chem., 46, 133 (1974).
118. M.W. Blades,  
Dissertation, Dept. of Chem., Univ. of Alberta,  
Edmonton, Alberta, 1981.



119. J.W. Carr,  
Dissertation, Dept. of Chem., Univ. of Alberta,  
Edmonton, Alberta, 1980.
120. M.W. Blades and G. Horlick,  
Spectrochim. Acta, 36B, 861 (1981).
121. M.W. Blades and G. Horlick  
Spectrochimica Acta, 36B, 881 (1981).
122. N. Furuta and G. Horlick,  
Spectrochim. Acta, 37, 53 (1982).
123. H. Kawaguchi, T. Ito, and A. Mizuike,  
Spectrochim. Acta, 36B, 615 (1981).
124. A.N. Zaidel, V.K. Prokof'ev, V.A. Slavnyi,  
and E.Ya. Schreider, "Tables of Spectral Lines",  
IFI/Plenum, New York, 1970.
125. J.W. Robinson, Ed.,  
"Handbook of Spectroscopy", CRC Press, Cleveland,  
Vol. I., 1974.
126. R.M. Barnes and S. Nikdel,  
J. Appl. Phys., 47, 3929 (1976).
127. E.D. Salin and G. Horlick,  
Anal. Chem., 52, 1578 (1980).
128. H.V. Malmstadt, C.G. Enke, S.R. Crouch, and  
G. Horlick, "Electronic Measurements for Scientists",  
W.A. Benjamin, Inc., 1974.
129. R.M. Belchamber,





Dissertation, Dept. of Chem., University of Alberta,  
Edmonton, Alberta, 1981.

130. H.N. Olsen,  
Phys. Rev., 124, 1703 (1961).
131. A. Batal, J. Jarosz, and J.M. Mermet,  
Spectrochim. Acta, 36B, 983 (1982).
132. P.W.J.M. Boumans and F.J. deBoer,  
Spectrochim. Acta, 32B, 365 (1977).
133. R.M. Ajhar, P.D. Dalager, and A.L. Davison,  
Am. Lab., 8(3), 71 (1976).
134. R.K. Winge, V.J. Peterson, and V.A. Fassel,  
Appl. Spectrosc., 33, 206 (1979).
135. P.W.J.M. Boumans and M. Bosveld,  
Spectrochim. Acta, 34B, 59 (1979).
136. G. Horlick,  
Ind. Research Development, p.73, Aug., (1978).
137. G.R. Kornblum and L. De Galan,  
Spectrochim. Acta, 32B, 455 (1977).
138. G.F. Larson, V.A. Fassel, R.H. Scott, and  
R.N. Kniseley, Anal. Chem., 47, 238 (1975).
139. S.R. Koirtyohann and E.E. Pickett,  
Spectrochim. Acta, 28B, 139 (1968).
140. S.R. Koirtyohann, J.S. Jones, C.P. Jester, and  
D.A. Yates, Spectrochim. Acta, 36B, 49 (1981).
141. W.H. Gunter, K. Visser, and P.B. Zeeman,



- Spectrochim. Acta, 37B, 571 (1982).
142. J.E. Roederer, G.J. Bastiaans, M.A. Fernandez, and K.J. Fredeen, Appl. Spectrosc., 36, 383 (1982).
143. R. Herrman and C.T.J. Alkemade, "Chemical Analysis by Flame Photometry", Wiley-Interscience, New York, 1963.
144. G.F. Kirkbright, A.F. Ward, and T.S. West, Anal. Chim. Acta, 62, 241 (1972).
145. G.F. Kirkbright, A.F. Ward, and T.S. West, Anal. Chim. Acta, 64, 353 (1973).
146. A.E. Watson and T.W. Steele, ICP Information Newslett., 5, 553 (1980).
147. J.M. Mermet and C. Trassy, Rev. Phys. Appl., 12, 1219 (1977).
148. J. Jolly and M. Touzeau, J.Q.S.R.T., 15, 863 (1975).
149. S. Vacquie, J.P. Dinguirard, H. Kafrouni, and I. Page, J.Q.S.R.T., 17, 755 (1977).
150. R.R. Williams, Dissertation, Dept. of Chem., University of Georgia, Athen, Georgia, 1981.
151. R.H. Huddleston and S.L. Leonard, "Plasma Diagnostic Techniques", Academic Press, New York, 1965.
152. A.J. Bearden, F.J. Ribe, G.A. Sawyer, and



- T.F. Stratton, *Phys. Rev.*, 6, 257 (1961).
153. C.R. Vidal,  
*J.Q.S.R.T.*, 6, 461 (1966).
154. C.R. Vidal,  
*J.Q.S.R.T.*, 6, 575 (1966).
155. A. Montaser, V.A. Fassel, and G. Larsen,  
*Appl. Spectrosc.*, 35, 385 (1981).
156. W.L. Wiese, D.E. Kelleher, and D.R. Paquette,  
*Phys. Rev. A*, 6, 1132 (1972).
157. M.P. Freeman and S. Katz,  
*J. Opt. Soc. Am.*, 53, 1172 (1963).
158. C.J. Cremers and R.C. Birkebak,  
*Appl. Opt.*, 5, 1057 (1966).
159. M.W. Blades and G. Horlick,  
*Appl. Spectrosc.*, 34, 697 (1980).
160. B.S. Choi and H. Kim,  
*Appl. Spectrosc.*, 36, 71 (1982).
161. K. Bockasten,  
*J. Opt. Soc. Am.*, 51, 943 (1961).
162. M.M. Prost,  
*Spectrochim. Acta*, 37B, 541 (1982).
163. O.N. Nestor and H.N. Olsen,  
*S.I.A.M. Rev.*, 2, 200 (1960).
164. P.D. Willson and T.H. Edwards,  
*Appl. Spectrosc. Rev.*, 12, 1 (1976).





165. A. Savitky and M.J.E. Golay,  
Anal. Chem., 36, 1627 (1964).



## APPENDIX A

This appendix will provide a description of the software programs used for electron density measurements. It is divided into three major programs. All programs run on an Apple /// (128 K RAM) microcomputer with an SOS operating system. They are written in UCSD-Pascal. Detailed documentation will be provided within the program listing.

The first program is used to perform the following tasks;

- (1) requires the operator to input the lateral data set collected from a PDP-8 minicomputer into the memory of the Apple /// microcomputer,
- (2) performs background subtraction using the "Slope" method,
- (3) normalizes the background subtracted lateral intensity data,
- (4) stores the lateral data set onto the floppy disk under a given file name.



```
PROGRAM LATERAL;
```

```
VAR DIOINT, INT : ARRAY [1..50,1..35] OF REAL;
    X, Y, SEG, NUM, DL, DR, START, XCORD: INTEGER;
    AMIN, C, SLOPE, INTR, INTL, SF : REAL;
    OFN, YES : STRING;
```

```
PROCEDURE CONDITIONS;
```

```
BEGIN
```

```
    WRITELN;
```

```
    WRITELN('Set no.....',X);
```

```
    WRITE('Scaling factor      :');READLN(SF);WRITELN;
```

```
    WRITE('Left diode #        :');READLN(DL);
```

```
    WRITE('Left diode intensity :');READLN(INTL);WRITELN;
```

```
    WRITE('Right diode #       :');READLN(DR);
```

```
    WRITE('Right diode intensity :');READLN(INTR);WRITELN;
```

```
    WRITE('Starting diode number      :');READLN(START);WRITELN;
```

```
END;    (* Conditions *)
```

```
PROCEDURE INPUTDATA;
```

```
VAR S, DIO, CORR : INTEGER;
```

```
    NO : STRING;
```

```
BEGIN
```

```
    WRITELN('Diode #      Intensity');
```

```
    FOR Y := 1 TO NUM DO BEGIN
```

```
        S := START + Y - 1;
```

```
        WRITE(S:4,' ':10);READLN(INT[X,Y])
```

```
    END;
```

```
(* Make sure all input values are correct *)
```

```
WRITE('Any corrections (Y/N) ?');READLN(NO);
```

```
WHILE ( NO = 'Y' ) OR ( NO = 'y' ) DO BEGIN
```

```
    WRITELN;
```

```
    WRITE('Enter diode # to be corrected :');READLN(DIO);
```

```
    CORR := DIO - START +1;
```

```
    WRITE('Enter new diode intensity :');READLN(INT[X,CORR]);
```

```
    WRITE('Any corrections (Y/N) ?');READLN(NO)
```

```
END
```

```
END;    (* Inputdata *)
```





```

PROCEDURE BACKSUBTRACT;
VAR  BACK, COMP : REAL;
BEGIN
  FOR Y := 1 TO NUM DO BEGIN
    BACK := SLOPE * XCORD + C;
    DIOINT[X,Y] := INT[X,Y] - BACK;
    XCORD := XCORD + 1
  END;
  AMIN := DIOINT[X,1];
  FOR Y := 2 TO NUM DO BEGIN
    COMP := DIOINT[X,Y] - AMIN;
    IF COMP < 0 THEN AMIN := DIOINT[X,Y]
  END
END;  (* Background subtractions *)

```

```

PROCEDURE STOREDATA;
VAR  DISK, OUTFILE : STRING;
     LATINT : FILE OF REAL;
BEGIN
  DISK := '.D2/';
  OUTFILE := CONCAT ( DISK, OFN );
  REWRITE ( LATINT, OUTFILE );
  FOR X := 1 TO SEG DO BEGIN
    FOR Y := 1 TO NUM DO BEGIN
      LATINT^ := DIOINT[X,Y];
      PUT ( LATINT )
    END
  END;
  CLOSE ( LATINT, LOCK )
END;  (* Storedata *)

```



```

BEGIN      (* Main program *)

  (* Initialization *)

  WRITE('Output filename      :'); READLN(OFN);
  WRITE('Total # of segments  :'); READLN(SEG); WRITELN;
  WRITE('Total # of diodes    :'); READLN(NUM); WRITELN;

  FOR X := 1 TO SEG DO BEGIN

    (* Input running conditions *)
    (* Check input data, correct if necessary *)

    YES := 'Y';
    WHILE ( YES = 'Y' ) OR ( YES = 'y' ) DO BEGIN
      CONDITIONS;
      WRITE('Any corrections (Y/N) ?'); READLN(YES)
    END;

    (* Input diode intensities collected by PDP-8 *)

    INPUTDATA;

    (* Perform background subtractions using slope method *)

    SLOPE := ( INTR - INTL ) / ( DR - DL );
    C      := INTL - SLOPE * DL;
    XCORD := START;

    BACKSUBTRACT;

    (* Normalization of background subtrated intensities *)

    FOR Y := 1 TO NUM DO BEGIN
      DIOINT[X,Y] := ( DIOINT[X,Y] - AMIN ) / SF
    END
  END;

  (* Store data to floppy disk *)

  STOREDATA

END.      (* Main *)

```



The second program is used to transform the lateral data set into the radial data set by Abel inversion. This program is divided into a series of procedures, namely,

- (1) the program reads the lateral data set from the floppy disk into the memory,
- (2) Savitzky-Golay filter is used to smooth the hydrogen-beta line profile,
- (3) midpoint reconstruction procedure is used to double the number of data points,
- (4) Savitzky-Golay filter is used to smooth the constructed lateral data points,
- (5) lateral data set is converted into the radial data set by Abel inversion procedure,
- (6) the calculated radial data set is stored onto the floppy disk under a different file name.





```
PROGRAM ABELINVERSE;
```

```
USES REALMODES;
```

```
VAR DIOINT : ARRAY [1..50,1..50] OF REAL;
    RINT, L : ARRAY [1..50,1..35] OF REAL;
    SN : ARRAY [1..70,1..35] OF REAL;
    Y, X, NUM, SEG, NEW : INTEGER;
    IFN, OFN, DISK : STRING;
```

```
PROCEDURE CONDITIONS;
```

```
BEGIN
```

```
    WRITE('Input filename :');READLN(IFN);
```

```
    WRITELN;
```

```
    WRITE('Output filename :');READLN(OFN);
```

```
    WRITELN;
```

```
    WRITE('Total # of diodes to be read :');READLN(NUM);
```

```
    WRITELN;
```

```
    WRITE('Total segments :');READLN(SEG);
```

```
END;    (* Conditions *)
```

```
(*   Input data from floppy disk.                                *)
(*   Data were originally input to Lateral Program for            *)
(*   background subtraction, normalization and then stored       *)
(*   onto the floppy disk.                                         *)
```

```
PROCEDURE INPUTDATA;
```

```
VAR LATINT : FILE OF REAL;
```

```
    INFILE : STRING;
```

```
BEGIN
```

```
    INFILE := CONCAT( DISK, IFN );
```

```
    RESET ( LATINT, INFILE );
```

```
    FOR X := 1 TO SEG DO BEGIN
```

```
        FOR Y := 1 TO NUM DO BEGIN
```

```
            DIOINT [X,Y] := LATINT^;
```

```
            GET ( LATINT )
```

```
        END
```

```
    END
```

```
END;    (* Inputdata *)
```



```

(*) The following procedure is used to smooth the hydrogen *)
(*) beta line profile. *)
(*) The smoothing routine is based on the Savitzky-Golay *)
(*) least squares method, first three and last three pts *)
(*) are not smoothed. *)

```

```
PROCEDURE SMPROFILE;
```

```

VAR P0, P1, P2, P3, A, B, C, D, E, F, G, H : INTEGER;
    M1, M2, M3 : REAL;
    ADD : ARRAY [1..60] OF REAL;

```

```
PROCEDURE ADD10;
```

```
BEGIN
```

```
  FOR Y := 1 TO NUM DO BEGIN
```

```
    G := Y + 10;
```

```
    ADD[G] := DIOINT[X,Y]
```

```
  END;
```

```
  FOR Y := 1 TO 10 DO BEGIN
```

```
    G := 11 - Y;
```

```
    ADD[G] := DIOINT[X,Y]
```

```
  END
```

```
END;
```

```
PROCEDURE SMOOTHPF;
```

```
BEGIN
```

```
P0 := H; P1 := H - 1; P2 := H - 2; P3 := H - 3;
```

```
  FOR Y := 4 TO P3 DO BEGIN
```

```
    A := Y - 3; B := Y + 3;
```

```
    C := Y - 2; D := Y + 2;
```

```
    E := Y - 1; F := Y + 1;
```

```
    M1 := ADD[A] + ADD[B];
```

```
    M2 := ADD[C] + ADD[D];
```

```
    M3 := ADD[E] + ADD[F];
```

```
    DIOINT[X,Y] := -2 * M1 + 3 * M2 + 6 * M3 + 7 * ADD[Y];
```

```
    DIOINT[X,Y] := DIOINT[X,Y]/21
```

```
  END
```

```
END;
```

```
PROCEDURE SUB10;
```

```
BEGIN
```

```
  FOR Y := 1 TO NUM DO BEGIN
```

```
    G := Y + 10;
```

```
    DIOINT[X,Y] := DIOINT[X,G]
```

```
  END
```

```
END;
```



BEGIN

FOR X := 1 TO SEG DO BEGIN

ADD10;

WRITELN('OK.....1');

H := NUM + 10;

WRITELN('OK.....2');

SMOOTHPF;

WRITELN('OK.....3');

DIOINT[X,1] := ADD[1]; DIOINT[X,2] := ADD[2];

DIOINT[X,3] := ADD[3];

DIOINT[X,P2] := ADD[P2]; DIOINT[X,P1] := ADD[P1];

DIOINT[X,P0] := ADD[P0];

SUB10;

WRITELN('OK.....4');

END

END; (\* SMPProfile \*)





```

(*) This Midpoint Procedure is used to double the number (*)
(*) of data points by reconstructing the midpoints. (*)
(*) Paul D. Wilson and T.H. Edwards, (*)
(*) " Sampling and Smoothing of Spectra " (*)
(*) Applied Spectroscopy Reviews, 12(1), 1-81, 1976. (*)

```

```

PROCEDURE MIDPOINT;

```

```

  VAR INT : ARRAY[1..300] OF REAL;
  NP : INTEGER;

```

```

  PROCEDURE CLEAR;

```

```

  BEGIN

```

```

    FOR X := 1 TO 300 DO INT[X] := 0.0
  END;

```

```

  PROCEDURE MIRROR;

```

```

  VAR X1, X2 : INTEGER;

```

```

  BEGIN

```

```

    FOR X := 1 TO SEG DO BEGIN
      X1 := ( 49 + X ) * 2; X2 := X1 - NP;
      INT[X1] := DIOINT[X,Y];
      INT[X2] := INT[X1];
      NP := NP + 4
    END

```

```

  END;

```

```

  PROCEDURE MIDCALC;

```

```

  VAR N1, N2, MID, R, X11, X12, X21, X22 : INTEGER;
  SUM1, SUM2 : REAL;

```

```

  BEGIN

```

```

    FOR X := 1 TO SEG DO BEGIN
      N1 := 1; N2 := 3;
      MID := ( 49 + X ) * 2 + 1;
      FOR R := 1 TO 20 DO BEGIN
        X11 := MID - N1; X12 := MID + N1;
        X21 := MID - N2; X22 := MID + N2;
        SUM1 := INT[X11] + INT[X12];
        SUM2 := INT[X21] + INT[X22];
        INT[MID] := INT[MID] + ( SUM1/N1 - SUM2/N2 ) * 0.6366;
        N1 := N1 + 4; N2 := N2 + 4
      END
    END

```

```

  END;

```



```

PROCEDURE REASSIGN;
VAR X1, X2, N1, N2 : INTEGER;
BEGIN
  FOR X := 1 TO SEG DO BEGIN
    X1 := ( 49 + X ) * 2; X2 := X1 + 1;
    N2 := X * 2; N1 := N2 - 1;
    L[N1,Y] := INT[X1];
    L[N2,Y] := INT[X2];
  END
END;

```

```

BEGIN

```

```

  FOR Y := 1 TO NUM DO BEGIN

```

```

    CLEAR;
    WRITELN('Clear.....ok');
    NP := 2;
    MIRROR;
    WRITELN('Mirror.....ok');
    MIDCALC;
    WRITELN('Midpoint calc...ok');
    REASSIGN

```

```

  END

```

```

END;  (* Midpoint *)

```



```

(*) Savitzky-Golay method for smoothing data by Simplified  (*)
(*) Least Squares procedures,                                (*)
(*) Abraham Savitzky and Marcel J.E. Golay,                 (*)
(*) Anal. Chem.,36,1627(1964).                               (*)
(*)                                                           (*)
(*) Seven points Quadratic Smoothing Routine, first three  (*)
(*) and last three points are not smoothed.                 (*)
(*) Normalization factor = 21                                (*)

```

```
PROCEDURE SMOOTHING;
```

```

VAR  P0, P1, P2, P3, A, B, C, D, E, F, G, H : INTEGER;
     M1, M2, M3 : REAL;
     ADD : ARRAY [1..100] OF REAL;

```

```
PROCEDURE ADDDATA;
```

```
BEGIN
```

```
  FOR X := 1 TO NEW DO BEGIN
```

```
    G := X + 10;
```

```
    ADD[G] := L[X,Y]
```

```
  END;
```

```
  FOR X := 1 TO 10 DO BEGIN
```

```
    G := 11 - X;
```

```
    ADD[G] := L[X,Y]
```

```
  END
```

```
END;
```

```
PROCEDURE SMROUTINE;
```

```
BEGIN
```

```
P0 := H; P1 := H - 1; P2 := H - 2; P3 := H - 3;
```

```
FOR X := 4 TO P3 DO BEGIN
```

```
  A := X - 3; B := X + 3;
```

```
  C := X - 2; D := X + 2;
```

```
  E := X - 1; F := X + 1;
```

```
  M1 := ADD[A] + ADD[B];
```

```
  M2 := ADD[C] + ADD[D];
```

```
  M3 := ADD[E] + ADD[F];
```

```
  SN[X,Y] := -2 * M1 + 3 * M2 + 6 * M3 + 7 * ADD[X];
```

```
  SN[X,Y] := SN[X,Y]/21
```

```
END
```

```
END;
```





```

PROCEDURE SUBDATA;
BEGIN
  FOR X := 1 TO NEW DO BEGIN
    G := X + 10;
    SN[X,Y] := SN[G,Y]
  END
END;

BEGIN

  FOR Y := 1 TO NUM DO BEGIN

    ADDDATA;

    H := NEW + 10;

    SMROUTINE;

    SN[1,Y] := ADD[1]; SN[2,Y] := ADD[2]; SN[3,Y] := ADD[3];
    SN[P2,Y] := ADD[P2]; SN[P1,Y] := ADD[P1]; SN[P0,Y] := ADD[P0];

    SUBDATA;

  END

END;  (* Smoothing *)

```



```

(* This procedure performs Abel Transformation routine *)

PROCEDURE ABEL;
CONST NORM = -25.4648;
VAR A, N : INTEGER;
    B, SUM1, SUM2, M1, M2, M3, A2, BK : REAL;

FUNCTION AKK( K : INTEGER ) : REAL;
BEGIN
    AKK := 1.0 / SQRT( 2 * K - 1.0 )
END;

BEGIN
    FOR Y := 1 TO NUM DO BEGIN
        FOR X := 1 TO NEW DO BEGIN
            WRITELN(X,':5,Y);
            B := AKK(X);
            A := X + 1;
            SUM1 := SN[X,Y]*(-B);
            SUM2 := 0.0;
            IF A <= NEW THEN BEGIN
                FOR N := A TO NEW DO BEGIN;
                    M1 := SQR(N) - SQR(X-1);
                    M2 := SQR(N-1) - SQR(X-1);
                    M3 := 2 * N - 1;
                    A2 := ( SQRT(M1) - SQRT(M2) ) / M3;
                    BK := B - A2;
                    SUM2 := SUM2 + SN[N,Y]*BK;
                    B := A2
                END
            END;
            RINT[X,Y] := NORM * ( SUM1 + SUM2 )
        END
    END
END; (* Abel *)

(* Store radial data onto floppy disk *)

PROCEDURE STOREDATA;
VAR RADINT : FILE OF REAL;
    OUTFILE : STRING;

BEGIN
    OUTFILE := CONCAT( DISK, OFN );
    REWRITE ( RADINT, OUTFILE );
    FOR X := 1 TO NEW DO BEGIN
        FOR Y := 1 TO NUM DO BEGIN
            RADINT^ := RINT[X,Y];
            PUT ( RADINT )
        END
    END;
    CLOSE ( RADINT, LOCK )
END; (* Storedata *)

```



```
BEGIN          (* Main program *)

CONDITIONS;    (* Input initial conditions      *)
WRITELN('Conditions.....ok');

(* Store and retreat data from the second disk only *)

DISK := '.D2/';

INPUTDATA;     (* Input lateral data from disk #2 *)
WRITELN('Input data.....ok');

NEW := SEG * 2;

SMPROFILE;     (* Smooth the hydrogen profiles    *)
WRITELN('Profile smooth....ok');

MIDPOINT;      (* Increase number of data points  *)
WRITELN('Midpoint.....ok');

SMOOTHING;     (* smooth data points          *)
WRITELN('Smoothing.....ok');

ABEL;          (* Perform Abel Inversion      *)
WRITELN('Abel inversion....ok');

STOREDATA;     (* Store radial data onto disk #2 *)
WRITELN('Store data.....ok');

END.           (* Main *)
```





The third program is used to list the radial data set to output devices, such as screen monitor or printer. Refer to Apple /// Pascal manuals for further information.



```
PROGRAM DATALIST;
```

```
VAR DATAFILE : FILE OF REAL;
    INFILE, DISK, IFN : STRING;
    NUM, SEG, X, Y, Z, A : INTEGER;
    INT          : ARRAY [1..50,1..50] OF REAL;
```

```
BEGIN
```

```
    WRITE('Input filename :');READLN(IFN);WRITELN;
    WRITE('Total # of segments      :');READLN(SEG);WRITELN;
    WRITE('Total # of diodes to be read :');READLN(NUM);WRITELN;
```

```
    DISK := '.D2/';
```

```
    INFILE := CONCAT( DISK, IFN );
    RESET ( DATAFILE, INFILE );
    FOR X := 1 TO SEG DO BEGIN
        FOR Y := 1 TO NUM DO BEGIN
            INT [X,Y] := DATAFILE^;
            GET ( DATAFILE )
        END
    END;
END;
```

```
    A := SEG +1;
    FOR Y := 1 TO NUM DO BEGIN
        WRITELN('Diode # ',Y:2);
        WRITELN('Coordinate   vs.   Intensity');WRITELN;
        X := 1 ; Z := 1;
        REPEAT
            WHILE (Z < 6) AND ( X < A ) DO BEGIN
                WRITE('(',X:2,',')',INT[X,Y]:8:2,',':3);
                X := X + 1;
                Z := Z +1
            END;
            WRITELN;
            Z := 1;
        UNTIL ( X > SEG );
        WRITELN
    END
```

```
END.
```







**B30371**